Kazan Federal University
Zavoiskii Physical-Technical Institute
Russian Academy of Sciences
Bruker Ltd (Moscow)
"Dynasty" Foundation
Russian Foundation for Basic Reserch

ACTUAL PROBLEMS OF MAGNETIC RESONANCE AND ITS APPLICATION

XV International Youth Scientific School

ACTUAL PROBLEMS OF MAGNETIC RESONANCE AND ITS APPLICATION
KAZAN

Program
Lecture Notes
Proceedings

Kazan
22 - 26 October 2012

Kazan Federal University
Zavoiskii Physical-Technical Institute
Russian Academy of Sciences
Bruker Ltd (Moscow)
“Dynasty” Foundation
Russian Foundation for Basic Reserch

ACTUAL PROBLEMS OF MAGNETIC RESONANCE AND ITS APPLICATION

XV International Youth Scientific School

Program
Lecture Notes
Proceedings

Kazan
22 – 26 October 2012

KAZAN UNIVERSITY

2012

Proceedings of the XV International Youth Scientific School “Actual problems of magnetic resonance and its application”, 22 – 26 October 2012, Kazan. Edited by professor M.S. Tagirov (Kazan Federal University) and professor V.A. Zhikharev (Kazan State Technological University). – Kazan: Kazan Federal (Volga Region) University, 2012. – 210 p.

The reports of young scientists submitted on XV International Youth Scientific School “Actual problems of magnetic resonance and its application” carry out by Kazan Federal (Volga Region) University and Zavoiskii Physical-Technical Institute are included in the present collection.

ISBN 978-5-905787-85-0

Program

Monday, October 22

Institute of Physics

9:00 **Registration**

Auditorium 212. Institute of Physics.

10:00 – 10:15 **Opening Ceremony of School-2012**

Lectures

Auditorium 212. Institute of Physics.

10:15 – 11:00 **Yu.M. Bunkov** (Institut Neel, CNRS, Grenoble, France), "Spin superfluidity and magnon Bose – Einstein condensation"

11:00 – 11:25 **Coffee break**

Conference Hall 1. Institute of Physics.

11:25 – 12:10 **S.B. Orlinskii** (Kazan Federal University, Kazan, Russia), "Atherosclerotic Plaque and nanostructures"

12:10 – 12:55 **R.M. Rakhmatullin** (Kazan Federal University, Kazan, Russia), "Coupling Design for Pulse High frequency EPR Spectroscopy"

13:00 – 14:00 **Lunch**

Oral Session

Conference Hall 1. Institute of Physics.

14:00 – 14:15 **L.F. Galiullina,** "Investigation of cholesterol+model of biological membrane complex by NMR spectroscopy"

14:15 – 14:30 **R.R. Gazizulin,** "The magnon Bose-Einstein condensation in single crystal $CsMnF_3$"

14:30 – 14:45 **D.S. Blokhin,** "Methods to control formation of micellar systems of sodium dodecyl sulfate in solution"

14:45 – 15:00 **K.R. Sharipov,** "Superparamagnetic properties in hole doped manganites"

15:00 – 15:15 **G.A. Tokarev,** "Double doping nanoparticles of hydroxyapatite"

15:15 – 15:30 **V.S. Iyudin,** "Electron spin polarization of supramolecules based on metalporphyrins"

15:30 – 15:45 **I.A. Irisova,** "Mechanochemically-doped Er^{3+} and Yb^{3+} cubic symmetry centers at the surface of fluorite nanoparticles"

15:45 – 16:00 **R.R. Gainov,** "Preliminary studies of chalcopyrite ($CuFeS_2$) by NMR and Mössbauer effect"

16:00 – 16:30 **Coffee break**

16:30 – 16:45 **A.Yu. Orlova,** "Investigations of antimony-containing chalcogenides Ag_5SbS_4 and $CuPbSbS_3$ by Sb NQR spectroscopy"

16:45 – 17:00 **S.V. Efimov**, "NMR Studies and Molecular Dynamics Simulation of Cyclosporin in Complex with Detergent Micelles"

17:00 – 17:15 **A.V. Khaliullina,** "Structural and dynamic properties of a channel protein transmembrane segment studied using solid-state NMR"
17:15 – 17:30 **I.A. Evlampiev,** "Preliminary NQR studies of Cu_3SbS_3"
17:30 – 17:45 **N.A. Krylatykh,** "Low-field NMR studies of gadolinium based contrast agents"
17:45 – 18:00 **K.R. Safiullin,** "Imaging using polarised ^3He at low magnetic fields"
18:00 – 18:15 **V.O. Sakhin,** "EPR study of the spatial modulation of magnetization in $La_{2-x}Sr_xCuO_4$"
18:15 – 18:30 **J.V. Mamedov,** "Magnetic resonance of $GdMnO_3$"

Tuesday, October 23

Lectures

Conference Hall 1. Institute of Physics.

9:30 – 10:15 **V.V. Kachala** (Zelinskii Institute of Organic Chemistry, Moscow, Russia), **"**1D and 2D NMR for reaction monitoring and molecule analysis in ionic liquids"
10:15 – 11:00 **M.R. Gafurov** (Bruker Ltd, Moscow, Russia), "Overview Bruker BioSpin report"

11:00 – 11:25 **Coffee break**

11:25 – 12:10 **M.V. Eremin** (Kazan Federal University, Kazan, Russia), "Collective spin excitations in HTSC cuprates"
12:10 – 12:55 **S.N. Lukin** (Institute of Semiconductor Physics, Kiev, Ukraine), "Capabilities of HF/HF EPR"

13:00 – 14:00 **Lunch**

Oral Session

Conference Hall 1. Institute of Physics.

14:00 – 14:15 **S.O. Rabdano,** "Hydration properties of organic molecules functional groups as studied by NMR-relaxation and quantum chemical calculations"
14:15 – 14:30 **S.S. Zalesskiy,** "Determination of Tris(dibenzylideneacetone)dipalladium Structure and Purity in Solution by Modern NMR Techniques"
14:30 – 14:45 **Yu.A. Savina,** "ESR study of antiferromagnetic zigzag chain system β-$TeVO_4$"
14:45 – 15:00 **K.A. Kozhanov,** "Versatile coordination sphere dynamics in o-semiquinonic pincer nickel complexes: an EPR study and mechanistic aspects"
15:00 – 15:15 **M.N. Uvarov,** "EPR Study of Dynamics of Triplet Fullerenes in Glassy and Polymer Matrices"
15:15 – 15:30 **E.M. Zubanova,** "EPR study of kinetics and mechanism of phototransformations of tetraalkylammonuim tetrachlorocuprates in low-temperature matrices"
15:30 – 15:45 **D.A. Pomogailo,** "Determination of the translational order of spin probe in smectic liquid crystal"
15:45 – 16:00 **O.V. Kravchyna,** "Charge ordering in $Nd_{2/3}Ca_{1/3}MnO_3$: evidence for ferromagnetic correlations"

16:00 – 16:30 **Coffee break**

16:30 – 16:45 **I.A. Khodov,** "Spatial structure of felodipine in DMSO-d6 solution by 1-D NOE and 2-D NOESY NMR spectroscopy"
16:45 – 17:00 **S.E. Kurnikov,** "Hydration properties of the Na^+ in aqueous solutions studied by NMR relaxation and quantum chemical calculations"
17:00 – 17:15 **E.A. Samohvalov,** "New mixed-valence tellurates $Li_{1-x}Mn_{2+x}TeO_6$ and $LiMn_{2-x}Fe_xTeO_6$: magnetization and EPR studies"
17:15 – 17:30 **A.A. Pavlov,** "Spin crossover in cobalt(II) tris-dioximate complexes by EPR and NMR spectroscopy"
17:30 – 17:45 **G.V. Rodchenkov,** "Static and dynamic magnetic properties of $Eu_{1-x}Ca_xCoO_{3-\delta}$"
17:45 – 18:00 **D.A. Ovchinnikov,** "Structure of the 4-aminononafluorobiphenyl radical anion. Study by optically detected ESR"
18:00 – 18:15 **O.V. Zakiryanova,** "An examination of complexing between copper chloride (II) and 5-aminouracil in aqueous solutions using UV-visible spectrometry and NMR ^{13}C spectroscopy methods"
18:15 – 18:30 **A.V. Bogdanov,** "ESR study of photoorientation in azobenzene-containing liquid-crystalline polymer"
18:30 – 18:45 **V.G. Bayev,** "Palladium influence on magnetic anisotropy of Ni-Pd nanowire arrays chemically electrodeposited in porous anodized alumina"

Wednesday, October 24

Lectures

Conference Hall 1. Institute of Physics.

9:00 – 9:45 **F.S. Dzheparov** (Alikhanov Institute for Theoretical and Experimental Physics, Moscow, Russia), "Interplay of classical and quantum spin dynamics"
9:45 – 10:30 **V.A. Atsarkin** (Kotel'nikov Institute of Radio Engineering and Electronics, Moscow, Russia), "Ferromagnetism in terms of EPR spectroscopy"

10:30 – 10:55 **Coffee break**

Oral Session

Conference Hall 1. Institute of Physics.

10:55 – 11:10 **T.V. Frantsuzenko,** "Spin dynamics in new layered antimonate Na_4FeSbO_6"
11:10 – 11:25 **M.I. Stratan,** "Spin dynamics in one-dimensional magnet vanadyl acetate $VO(CH_3COO)_2$"
11:25 – 11:40 **S.F. Petrova,** "Aerobic oxidation of 5-hydroxy-6-methyluacil in alkaline solutions"
11:40 – 11:55 **A.V. Fokin,** "Investigations of the locally compensated triclinic Fe^{3+} EPR centers in lead germinate"
11:55 – 12:10 **I.N. Razmyslov,** "Investigation of the magnetic resonance spectra of the nanocomposite thin films"
12:10 – 12:25 **D.V. Kurzhunov,** "EPR-monitored redox titration of RcXDH and mAOH1 variants"
12:25 – 12:40 **O.I. Gromov,** "Structure of Cu(II) Alkyl Chlorocomplexes formed via tetrachlorocuprates photolysis: EPR, UV-Vis and DFT study"
12:40 – 12:55 **R.G. Dzhambulatov,** "Hydrophobic and hydrophilic interactions in carboxylic acid aqueous solutions"

13:00 – 14:00 **Lunch**

Assembly Hall of Kazan Federal University

14:00 – 18:00 Awarding Ceremony of Zavoisky Youth Scientific Prize Winners

Thursday, October 25

Lectures

Conference Hall 1. Institute of Physics.

9:00 – 9:45 **E.B. Fel'dman** (Institute of Problems of Chemical Physics, Chernogolovka, Russia), "Classical and Quantum Correlations in Spin Systems in Multiple Quantum NMR in Solids"

9:45 – 10:30 **O.A. Anikeenok** (Kazan Federal University, Kazan, Russia), "The secondary-quantization representation with a basis of partially nonorthogonal orbitals: transferred hyperfine interactions"

10:30 – 10:55 **Coffee break**

Oral Session

Conference Hall 1. Institute of Physics.

10:55 – 11:10 **N.V. Orlov,** "Development of New Se-based Chiral Derivatization Reagent for Determination of Enantiomeric Purity of α-Chiral Carboxylic Acids by NMR Spectroscopy"

11:10 – 11:25 **Yu.S. Kutin,** "Study of electric field gradients in ZnO by means of high-frequency EPR/ENDOR spectroscopy"

11:25 – 11:40 **A.S. Alexandrov,** "Nuclear pseudo quadrupole resonance of ^{141}Pr in Van Vleck paramagnet PrF_3"

11:40 – 11:55 **T.R. Safin,** "Magnetic system for NMR logging tool using cryogenic technologies"

11:55 – 12:10 **D.A. Sunyaev,** "Temperature dependence of the magnetic penetration depth and multicomponent order parameter in the $YBa_2Cu_3O_{7-\delta}$"

12:10 – 12:25 **I.V. Romanova,** "Magnetic and magnetoelastic properties of lithium-rare-earth tetra-fluoride single crystals"

12:25 – 12:40 **E.M. Alakshin,** "NMR of ^{141}Pr, ^{19}F and ^{3}He of PrF_3 nanoparticles at low temperature"

12:40 – 12:55 **M.A. Volodin,** "Study of the exchange interaction in relation to the concentration of spin labels in different solutions"

13:00 – 14:00 **Lunch**

14:00 – 18:00 **Excursion** to the G.R. Derzhavin's village

Friday, October 26

Lectures

Conference Hall 1. Institute of Physics.

P R O G R A M

9:15 – 10:00 **A.V. Klochkov** (Kazan Federal University, Kazan, Russia), "NMR of ^{3}He in porous media"

10:00 – 10:45 **A.N. Yudin** (Kapitza Istitute for Physical Problems, Moscow, Russia), "The use of NMR methods for investigation of new phases in superfluid ^{3}He"

10:45 – 11:15 **Coffee break**

11:15 – 12:00 **K.M. Salikhov,** (Zavoisky Physical-Technical Institute, Kazan, Russia), **"**Quantum computing"

12:00 – 13:00 **Closing Ceremony of School-2012**

13:00 – 14:00 **Lunch**

Spin superfluidity and magnon Bose – Einstein condensation

Yu.M. Bunkov

Institut Neel, CNRS, Grenoble, France

e-mail: yuriy.bunkov@grenoble.cnrs.fr

The superfluid current of spins—spin supercurrent —is one more representative of superfluid currents, such as the superfluid current of mass and atoms in superfluid 4He; superfluid current of electric charge in superconductors; superfluid current of hypercharge in the Standard Model of particle physics; superfluid baryonic current and current of chiral charge in quark matter; etc. Spin superfluidity manifests as the spontaneous phase-coherent precession of spins first discovered in 1984 in 3He-B, and can be described in terms of the Bose condensation of spin waves—magnons.We discuss different phases of magnonsuperfluidity, including those in a magnetic trap; and signatures of magnonsuperfluidity: (i) spin supercurrent, which transports the magnetization for a macroscopic distance (up to 1 cm); (ii) spin current Josephson effect, which shows the interference between two condensates; (iii) spin current vortex—a topological defect which is an analog of a quantized vortex in superfluids, of an Abrikosov vortex in superconductors, and cosmic strings in relativistic theories; (iv) Goldstone modes related to broken $U(1)$ symmetry—phonons in the spin-superfluidmagnongas; etc. We also touch the topic of spin supercurrentin general, including spin-Hall and intrinsic quantum spin-Hall effects.

Bose–Einstein condensations (BEC) of quasiparticles whose numbers are not conserved is presently one of the debated phenomena of condensed matter physics. In thermal equilibrium the chemical potential of excitations vanishes and, as a result, their condensate does not form. The only way to overcome this situation is to create a non-equilibrium but dynamically steady state, in which the number of excitations is conserved, since the loss of quasiparticles owing to their decay is compensated by pumping of energy. Thus the Bose condensation of quasiparticles belongs to the phenomenon of second class, when the emerging steady state of the system is not in a full thermodynamic equilibrium. Formally BEC requires conservation of charge or particle number. However, condensation can still be extended to systems with weakly violated conservation. For sufficiently long-lived quasiparticles their distribution may be close to the thermodynamic equilibrium with a well-defined finite chemical potential, which follows from the quasi-conservation of numbers of quasiparticles, and the Bose condensation becomes possible. Several examples of Bose condensation of quasiparticles have been observed or suggested, including phonons [1], excitons [2], exciton–polaritons [3], photons [4], and rotons [5]. The BEC of quasi-equilibrium magnons—spin waves— in ferromagnets has been discussed in Ref. [6] and investigated in [7–9].

Magnons are magnetic excitations in magnetic materials, such as magnetically ordered systems, like ferromagnets, antiferromagnets, etc., and paramagnetic systems with external magnetic ordering such as Fermi liquids. The most suitable systems for studying the phenomenon of magnon BEC are superfluid phases of helium-3. The absolute purity, long lifetime of magnons, different types of magnon–magnon interactions and well controlled magnetic anisotropy make antiferromagnetic superfluid phases of 3He a basic laboratory of magnonBEC. The first BEC state of magnons was discovered in 1984 in 3He-B as a coherent spin precession, and it was baptized as Homogeneously PrecessingDomain (HPD) [10, 11]. This is the spontaneously emerging steady state ofprecession, which preserves the phase coherence across the whole sample even in an inhomogeneous external magnetic field and

even in the absence of energy pumping. This is equivalent to the appearance of a coherent superfluid Bose–Einstein condensate.In the absence of energy pumping this HPD state slowly decays, but during the decay the system remains in the coherent state of BEC: the volume of the Bose condensate (the volume of HPD) gradually decreases with time without violation of the observed properties of the spin-superfluid phase-coherent state. A steady state of phase-coherent precession can be supported by pumping.HPD is very close to the thermodynamic equilibrium of the magnon Bose condensate and exhibits all the superfluid properties which follow from the offdiagonallong-range order (ODLRO) of the coherent precession. Following the discovery of HPD, several other states of magnon BEC have been observed in superfluid phases of 3He, which we discuss in this review, including finite magnon BEC states in magnetic traps. Very similar BEC states were recently observed in antiferromagnets with the so-called Suhl–Nacamura interaction, the long-range nuclear–nuclear interaction via a magnetically ordered electronic subsystem [12, 13].The full review of this subject will be published in the book[14].

The past decade was marked by fundamental studies of mesoscopic quantum states of dilute ultra-cold atomic gases in the regime where the de Broglie wavelength of the atoms is comparable with their spacing, giving rise to the phenomenon of Bose–Einstein condensation (see reviews [15, 16]). Formation of the Bose–Einstein condensate (BEC)—accumulation of the macroscopic number of particles in the lowest energy state—was predicted by Einstein in 1925 [17]. In an ideal gas, all atoms are in the lowest energy state in the zero temperature limit. In dilute atomic gases, weak interactions between atoms produce a small fraction of non-condensed atoms. In the only known bosonic liquid 4He, which remains liquid at zero temperature, BEC is strongly modified by interactions. Depletion of the condensate due to interactions is very strong: in the limit of zero temperature only about 10% of particles occupy the state with zero momentum. Nevertheless, BEC still remains the key mechanism for the phenomenon of superfluidity in liquid 4He: because of BEC the whole liquid (100% of 4He atoms) forms a coherent quantum state at $T = 0$ and participates in non-dissipative superfluid flow. Superfluidity is a very general quantum property of matter at low temperatures, with a variety of mechanisms and possible non-dissipative superfluid currents. These include the supercurrent of electric charge in superconductors and mass supercurrent in superfluid 3He, where the mechanism of superfluidityis the Cooper pairing; hypercharge supercurrent in the vacuum of the Standard Model of elementary particle physics, which comes from the Higgs mechanism; supercurrent of color charge in a dense quark matter in quantum chromo - dynamics; etc. All these supercurrents have the same origin: spontaneous breaking of the $U(1)$ or higher symmetry related to conservation of thecorresponding charge or particle number, which leads to so-called off-diagonal long-range order. This spin supercurrent—the superfluid current of spins—is one more representative of superfluid currents. Here the $U(1)$ symmetry is the approximate symmetry of spin rotation, which is related to the quasi-conservation of spin. It appears that the finite lifetime of magnons, and non-conservation of spin due to spin–orbital coupling do not prevent coherence and superfluidity of magnonBEC in 3He-B. The non-conservation leads to a decrease in the number of magnons until the HPD disappears completely, but during this relaxation, thecoherence of magnon BEC is preserved with all the signatures of spin superfluidity.

The magnetic $U(1)$ symmetry is also broken spontaneously in some static magnetic systems. Sometimes this symmetry breaking is described in terms of BEC of magnons [18–22]. Let us stress from the beginning that there is a principal difference between the magnetic ordering in equilibrium and the BEC of quasiparticles which we are discussing in this review. In these magnetic systems, symmetry breaking phase transition starts when the system becomes softly unstable towards the growth of one of the magnonmodes.

Condensation of this mode can be used for a description of the soft mechanism of formation of ferromagnetic and antiferromagnetic states (see e.g. [23]). However, the final outcome of the condensation is the true equilibrium ordered state. In the same manner, the Bose condensation of phonon modes may serve as a soft mechanism of formation for the equilibrium solid crystals [24]. But this does not mean that the final crystal state is the Bose condensate of phonons. On the contrary, BEC of quasiparticles is in principle a non-equilibrium phenomenon, since quasiparticles (magnons) have a finite lifetime. In our case, magnons live long enough to form a state very close to thermodynamic equilibrium BEC, but still it is not an equilibrium. In the final equilibrium state at $T = 0$ all of the magnons will die out. In this respect, the growth of a single mode in the nonlinear process after a hydrodynamic instability [27], which has been discussed in terms of the Bose condensation of classical sound or surface waves [28], is more close to magnon BEC than equilibrium magnets with spontaneously broken $U(1)$ symmetry. The other difference is that the ordered magnetic states are states with diagonal long-range order. The magnon BEC is a dynamic state characterized by off-diagonal long-range order which is the main signature of spin superfluidity.

References

[1] Kagan, Yu., et al. Condensation of phonons in an ultracold Bose gas, *Phys. Lett.* A **361**, 401 (2007).

[2] Butov, L.V., Ivanov, A. L., Imamoglu, A., Littlewood, P. B., Shashkin, A. A., Dolgopolov, V. T., Campman, K. L., and Gossard, A. C. Stimulated scattering of indirectexcitons in coupled quantum wells: Signature of a degenerate Bose-gas ofexcitons, *Phys. Rev. Lett.* **86**, 5608 (2001).

[3] Kasprzak, J., Richard, M., Kundermann, S., Baas, A., Jeambrun, P., Keeling, J.M.J., Marchetti, F.M., Szymaska, M.H., Andre, R., Staehli, J.L., Savona, V., Littlewood, P.B., Deveaud, B., and Dang, Le Si. Bose–Einstein condensation of excitonpolaritons, *Nature* **443**, 409–414 (2006); B. Deveaud-Pledran, On the condensation of polaritons*J. Opt. Soc. Am.* B **29**, A138–A145 (2012).

[4] Klaers, J., Schmitt, J., Vewinger, F., and Weitz, M. Bose–Einstein condensation of photons in an optical microcavity*Nature* **468**, 545 (2010); Schmitt, J., Damm, T., Vewinger, F., and Weitz, M. Bose–Einstein condensation of paraxial light, *Appl. Phys.* B Laser Opt. **105**, 17–33 (2011); arXiv:1109.4023.

[5] Melnikovsky, L.A. Bose–Einstein condensation of rotons, *Phys. Rev.* B **84**, 024525 (2011).

[6] Kalafati, Yu. D., and Safonov, V.L. Possibility of Bose condensation of magnons excited by incoherent pump, *JETP Lett.* **50**, 149–151 (1989).

[7] Demokritov, S.O., Demidov, V.E., Dzyapko, O., Melkov, G.A., Serga, A.A., Hillebrands, B., and Slavin, A.N. Bose–Einstein condensation of quasiequilibrium magnons at room temperature under pumping, *Nature* **443**, 430–433 (2006).

[8] Demidov, V.E., et al. Observation of spontaneous coherence in Bose–Einstein condensate of magnons, *Phys. Rev. Lett.* **100**, 047205 (2008).

[9] Chumak, A.V., Melkov, G.A., Demidov, V.E., Dzyapko, O., Safonov, V.L., and Demokritov, S.O. Bose–Einstein condensation of magnons under incoherent pumping, *Phys. Rev. Lett.* **102**, 187205 (2009).

[10] Borovik-Romanov, A.S., Bunkov, Yu.M.,Dmitriev, V.V., and Mukharskiy, Yu.M. Long-lived induction decay signal investigations in 3He, *JETP Lett.* **40**, 1033, (1984); Stratification of 3He spin precession in two magnetic domains, *Sov.Phys. JETP* **61**, 1199, (1985).

[11] Fomin, I.A. Long-lived induction signal and spatially nonuniform spin precession in 3He-B, *JETP Lett.* **40**, 1037 (1984).

[12] Bunkov, Yu.M.,Alakshin, E.M., Gazizulin, R.R., Klochkov, A.V., Kuzmin, V.V., Safin, T.R., and Tagirov, M.S. Discovery of the classical Bose–Einstein condensation of magnons in solid antiferromagnets, *JETP Lett.*, **94**, 68–72 (2011).

[13] Bunkov, Yu. M., Alakshin, E. M., Gazizulin, R. R., Klochkov, A.V., Kuzmin, V.V., L'vov, V.S., and Tagirov, M.S. High T*c*spinsuperfluidity in antiferromagnets, *Phys. Rev. Lett.* **108**, 177002 (2012).

[14] Yu. M. Bunkov and G. E. Volovik"Spin superfluidity and magnon Bose–Einstein Condensation" pages 253 -312 in "Novel Superfluids"ed by K. H. Bennemannand J. B. Ketterson, Oxford University press, 2012. Preprint **http://arxiv.org/pdf/1003.4889.pdf**

[15] Pethick, C.J., and Smith, H. *Bose–Einstein Condensation in Dilute Gases*, Ed. by Cambridge University Press (2002); Leggett, A.J. *Rev. Mod. Phys.* **73**, 307 (2001).

[16] Pitaevskii, L., and Stringari, S. *Bose–Einstein Condensation* (Clarendon Press, Oxford, 2003).

[17] Einstein, A. Quantentheorie des einatomigenidealen Gases, Sitzungsberichte der PreussischenAkademie der Wissenschaften**1**, 3 (1925).

[18] Ruegg, C. *Nature* **423**, 63 (2003).

[19] Della Torre, E., Bennett, L.H., and Watson, R.E. Extension of the Bloch *T*3/2 law to magnetic nanostructures: Bose–Einstein condensation, *Phys. Rev. Lett.*, **94**, 147210 (2005).

[20] Radu, T., Wilhelm, H., Yushankhai, V., Kovrizhin, D., Coldea, R., Tylczynski, Z., Lhmann, T., and Steglich, F. Bose–Einstein condensation of magnons in *Cs*2*CuCl*4, *Phys. Rev. Lett.*, **95**, 127202 (2005).

[21] Giamarchi, T., Rüegg, Ch., and Tchernyshyov, O. Bose–Einstein condensation in magnetic insulators, *Nature Phys.* **4**, 198–204 (2008).

[22] Kaul, S.N., and Mathew, S.P. Magnons as a Bose–Einstein condensate in nanocrystalline gadolinium, *Phys. Rev. Lett.* 106, 247204 (2011).

[23] Nikuni, T., Oshikawa, M., Oosawa, A., and Tanaka, H. Bose–Einstein condensation of dilute magnons in TlCuCl3, *Phys. Rev. Lett.* **84**, 5868–5871 (2000).

[24] Kohn, W., and Sherrington, D. Two kinds of bosons and Bose condensates, *Rev. Mod.Phys.* **42**, 1–11 (1970).

[25] Radu, T., Wilhelm, H., Yushankhai, V., Kovrizhin, D., Coldea, R., Tylczynski, AQ7 Z., Lühmann, T., and Steglich, F., Radu et al. reply, *Phys. Rev. Lett.* **98**, 039702 (2007).

[26] Mills, D.L. A comment on the letter by Radu T. et al., *Phys. Rev. Lett.***98**, 039701 (2007).

[27] Landau, L.D., and Lifshitz, E.M. *Fluid Mechanics*, Pergamon, Oxford (1959).

[28] Zakharov, V.E., and Nazarenko, S.V. Dynamics of the Bose–Einstein condensation, *Physica***D 201**, 203–211 (2005)

Atherosclerotic Plaque and nanostructures

B.V. Yavkin[1], T.B. Biktagitov[1], G.V. Mamin[1], S.B. Orlinskii[1], M.R. Gafurov[1], M.Kh. Salakhov[1], E.S. Klimashina[2], V.I. Putlayev[2], V.A. Abdul'yanov[3], I.M. Ignatjev[3], R.N. Khairullin[3], A.V. Zamochkin[3], Yu.A. Chelyshev[4]

Kazan Federal University, Federal Center of Shared Usage for Physicochemical Measurements, ul. Kremlevskaya 18, Kazan, 420008 Russia

Department of Chemistry, M. V. Lomonosov Moscow State University, Lenniskie Gory 1, Moscow, 119992 Russia

Interregional Clinic and Diagnostic Center, Kazan, 420101 Russia

Kazan State Medical University, Kazan, 420012 Russia

e-mail: Sergei.Orlinskii@ksu.ru

The nature of the calcification of vessel walls is one of the most urgent problems of cardiovascular pathology. Calcification accompanies the formation of an atherosclerotic plaque, complicates the course of the atherosclerotic process, and results in myocardial infarction, stroke, and acute ischemia of tissue. Calcification is an indicator of the instability of the atherosclerotic plaque.

The mortality rate in Russian Federation from the diseases of the blood circulatory system is about 800 on 100 000 (2000). Arteriosclerotic vascular disease (Atherosclerosis, ASVD) is a condition in which an artery wall thickens as a result of the accumulation of fatty materials. The calcified atherosclerotic **plaque** is an organomineral aggregate in which formation **hydroxyapatite** is significantly involved (fig.1). The spectral and relaxation characteristics of the organomineral radicals correlate with the calcification degree of the atherosclerotic plaque and can be used for diagnostics (fig.2).

A high sensitivity of EPR spectroscopy in the *W* range for small samples provides the

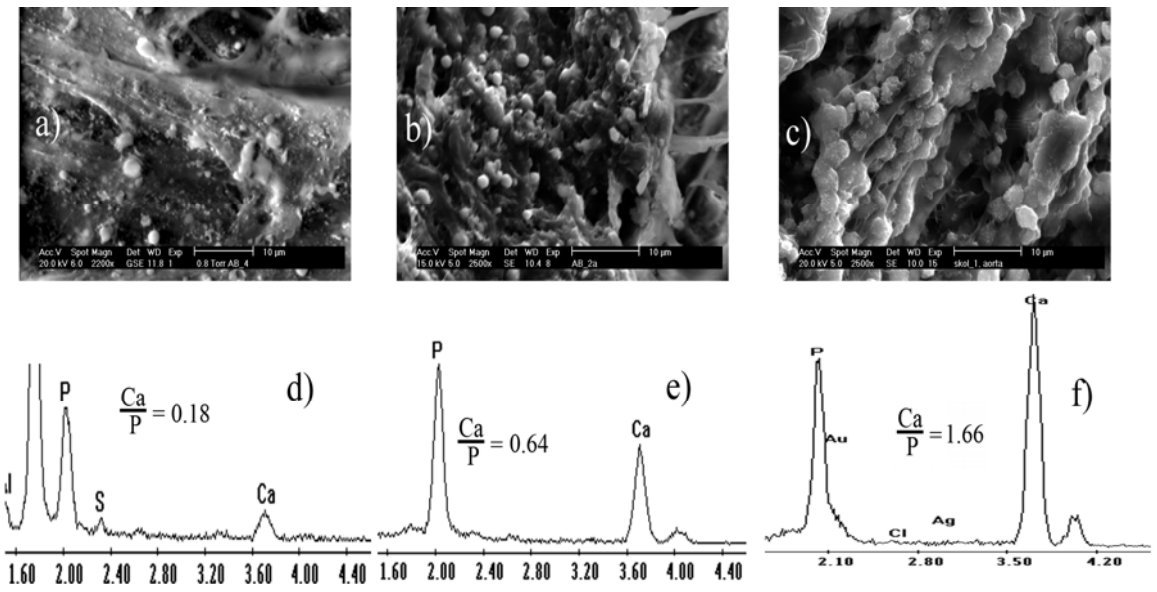

Fig.1. (a–c) Reliefs of the section of the inner aorta wall of patients with atherosclerosis and (d–f) the x-ray spectra of the globular fragments of the cut obtained using the microprobe analysis for low, intermediate, and high calcification degrees Ca/P = (a, d) 0.18, (b, e) 0.64, and (c, f) 1.66, respectively.

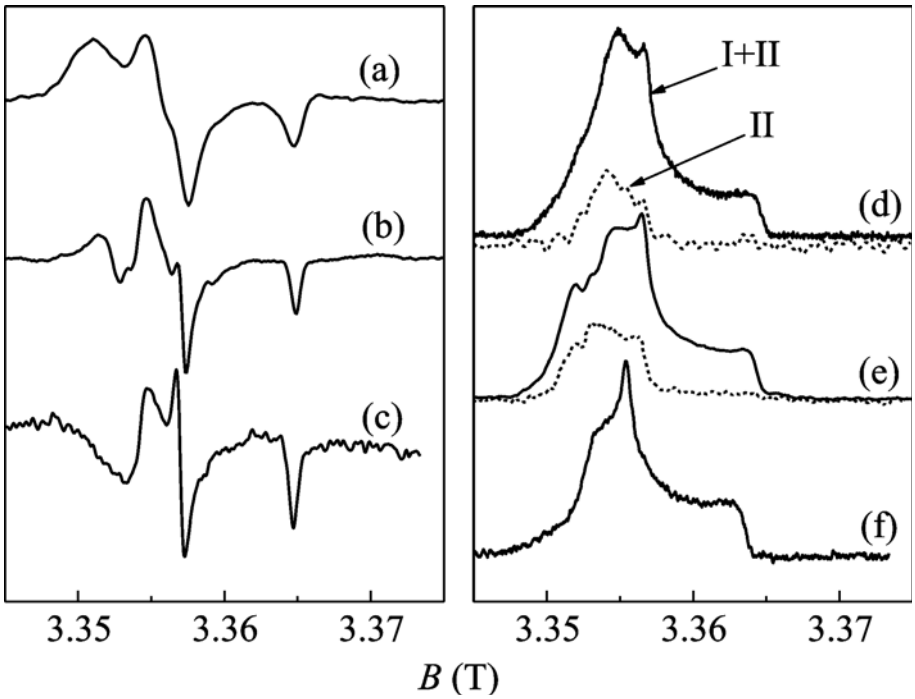

Fig.2. (a–c) Stationary EPR spectra and (d–f) spin echo spectra in the *W* range for the samples of (a, d) the atherosclerotic plaque with the maximum calcification degree, (b, e) enamel, and (c, f) mammoth tusk. The dashed line shows the EPR spectral component of center II.

premises for creating new, including low-invasive diagnostic methods for atherosclerosis and other diseases [1, 2].

The fabricated nano biomaterials with biomimetic structures and functions are expected to bear high bioactivities and unexpected biological effects, and ultimately can well serve as biomedicinal devices for human disease treatment. Many commercial substitute materials now have been developed, including natural and synthetic polymers, human bones, synthetic ceramics and composites especially hydroxyapatite [3].

Hydroxyapatite (HAp) is one of basic materials used in bone implant surgery. Due to such features as high biocompatibility, osteoconductivity, very good adaptation under *in vivo* conditions and chemical composition mirroring that of bone mineral and teeth enamel it is widely applied to fill bone defects in orthopedics, maxillofacial surgery as well as in stomatology. HAp nanoparticles have the potential to improve current disease diagnosis due to their ability to circulate in the blood and distribute in the body to image tissues and cells or to deliver a payload for bio-imaging and therapeutical applications. Sorption activity to a number of ions including those of some heavy metals and radio nucleotides makes the HAp based substances important not only in the biomedical area but also for waste management and in catalysts production [3, 4].

Conventional continuous-wave (cw) X-band EPR (frequency of about 9 GHz) is widely used for the detection, structure localization, qualitative and quantitative analyses of radiation defects (which are usually ascribed to the different carbonate, phosphorous, hydroxyl and oxygen radicals) created by X-ray, UV or gamma irradiation, for the detection of the intrinsic paramagnetic impurities, investigation of interaction with some paramagnetic ions such as Gd^{3+} or Mn^{2+} sorbed on hydroxyapatite or embedded into the lattice, etc [5 – 8]. In this work we demonstrate that the abilities of the modern conventional and pulsed EPR techniques, higher sensitivity and spectral resolution of the high-field EPR spectrometers could

significantly extend the boundaries of EPR for the investigations of the HAP based tissues in very small amounts including nanoparticles.

In light of the long history of therapeutic application of HAp, it hypothesized that this compound may be of interest in the management of heavy metal-induced disease [4]. But little is known about the physicochemical background of the interaction of the impurities (including lead ions) even with the calcified bulk tissues and very few structural studies have been reported. Hydroxyapatite is a hexagonal material with 44 atoms per unit cell. Because of this large unit cell size, it is only recently that HAP has been studied using quantum mechanical methods.

Two nonequivalent calcium positions Ca(1) and Ca(2) are distinguishable in the HAP structure. The Ca(1) ions lie along a line parallel to the crystal c-axis and connected to each other by three shared oxygen ions resulting in a “Ca(1) channel”. The Ca(2) ions form perpendicular to the c-axis triangles with two hydroxyl groups. This scheme forms an “OH channel”. The 9-fold 4f Ca(1) and 7-fold 6h Ca(2) sites are both available for cationic substitution. The “hand-made” rule that the ions with the larger ionic radii and higher than Ca^{2+} electronegativity readily occupy Ca(2) positions seems to be not true at least in the investigated HAp nanomaterials (fig.3, [9]).

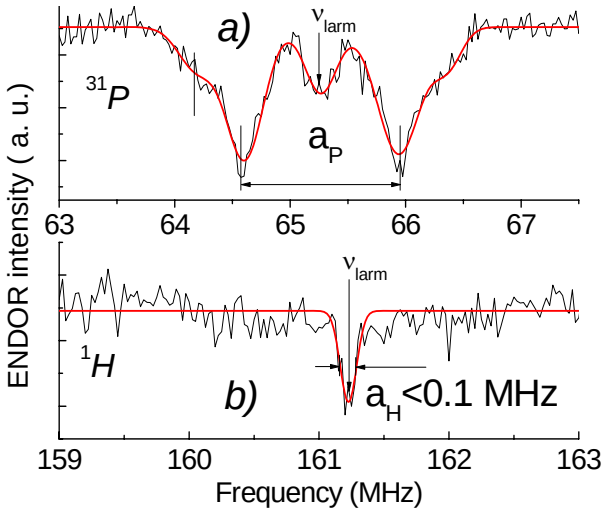

Fig.3. W-band ENDOR investigations of X-ray irradiated nanoparticles (20 nm and larger) of synthetic hydroxyapatite $Ca_9Pb(PO_4)_6(OH)_2$ show that the lead ions probably replace Ca(1) position in the hydroxyapatite structure while in calculations and bulk experiments Ca(2) site is preferable [8].

Among the diversity of the methods of the synthesis of the hydroxyapatites’ powders and nanoparticles the wet (precipitation) chemical procedure involving the aqueous solutions of calcium nitrate, diammonium hydrogen phosphate and ammonium hydroxide is the most commonly in use. The main advantages of the process are that its by-product consists primarily of water and the probability of contamination during processing is very low, fast production rate and low processing costs. Its disadvantages are that it requires washing of the precipitate to remove nitrates and ammonium hydroxide and that the resulting product can be greatly affected by even a slight difference in the reaction conditions. For example, by means of EPR ad ENDOR techniques it is shown that during the wet chemical precipitation synthesis process nitrate anions from the reagents (by-products) could incorporate into the OH channels of the hydroxyapatite structure [10].

Conclusion

New possibilities of applying multifrequency (high-frequency) electron paramagnetic resonance approaches in medicine are demonstrated on an example of the investigation of a calcified atherosclerotic plaque. W-band pulsed EPR and ENDOR investigations of X-ray irradiated nanoparticles of synthetic hydroxyapatite $Ca_9Pb(PO_4)_6(OH)_2$ are performed. Incorporation of nitrates into the OH channels of HAp nanostructures is detected.

References

[1] V. A. Abdul'yanov et al., *JETP Lett.*, 2008, **88**, 69.

[2] N. I. Silkin et al., Russian Patent, Pat. Appl. No. 201112522.

[3] R Z LeGeros and J P LeGeros Hydroxyapatite Ch.16 (pp. 367-394) in Bioceramics and their clinical applications T. Kokubo (Ed.) Woodhead Pub. and Maney Pub. Cambridge (2008) - 760 pages.

[4] E. I. Abdel-Gawad and S. A. Awwad. *Journ. Am. Sci.* 2011;7(1):105-119.

[5] F. Callens et al.. *Appl. Magn.Reson.*, 1998, **14**, 235.

[6] P. Moens et al. *Phys. Rev. B*, 1996, **53**, 5190.

[7] D. U. Schramm, et al. *Phys. Rev. B*, 2000, **63**, 024107.

[8] D. U. Schram and A. M. Rossi, *Appl. Radiat. Isotopes*, 2000, **52**, 1085.

[9] D. U. Schram and A. M. Rossi, *Appl. Radiat. Isotopes*, 2000, **52**, 1085.

[10] N. I. Silkin et al., Russian Patent, Pat. Appl. No. 2011125295.

Coupling Design for Pulse High frequency EPR Spectroscopy

R. Rakhmatullin[1], Yu. Grishin[2,3], A. Savitsky[2], E. Reijerse[2], W. Lubitz[2]

[1]Kazan Federal University, 420008, Kremlevskaya 18, Kazan, Russia

[2]Max Planck Institut fur Bioanorganische Chemie, 45470, Stiftstr 34-36, Mulheim an der Ruhr, Germany

[3]Institute of Chemical Kinetics & Combustion, 630090, Institutskaya 3, Novosibirsk, Russia

e-mail: rrakhmat@gmail.com

The sensitivity and the bandwidth of pulsed EPR spectrometer are defined to a great extent by the resonator. The performance of the resonator is characterized by the valueη·η·Q, where Q is a figure of merit (Q-factor) of the resonator, and η is the filling factor [1]. The resonator is connected to the transmission line with the coupling device and resulting loaded Q_L — "Loaded Q-factor" is related to the bandwidth $\Delta\omega$ of the resonator by $\Delta\omega = \Delta\omega_0 / Q_L$, $Q_L = Q_0 / (1 + \beta)$, where Q_0 is the unloaded quality factor and β is the coupling parameter. The advanced pulsed techniques require wide range of the loaded quality change that can be done with the appropriate coupling device.

In this report an example of high frequency coupler construction is presented with the circular coupling hole and a spherical movable element [2]. The combination of "sphere – circular hole" acts as a broadband impedance transformer, which greatly facilitates its use. This device has less number of degrees of freedom in choosing of the device dimensions as compared to used in commercial instruments (two parameters of change – sphere diameter and distance to "iris hole" only), greatly facilitates its manufacture and reproducibility, and, finally, enables one to obtain the fine adjustment of β from undercoupling ($\beta << 1$) to strong overcoupling ($\beta >> 1$).

The probehead design for Q- and W-band EPR as well as results of electromagnetic simulation and measurements is presented.

References

[1] Poole C.P., Electron Spin Resonance: A Comprehensive Treatise on Experimental Techniques, 2nd Edition, Dover Publications, 1997

[2] O. Burghaus, M. Rohrer, T. Gotzinger, M. Plato and K. Möbius, Meas. Sci. Technol. **3**, 765 (1992).

1D and 2D NMR for reaction monitoring and molecule analysis in ionic liquids

V.V. Kachala[1,2], E.A. Khokhlova[1], V.P. Ananikov[1]

[1]N.D. Zelinkskii Institute of Organic Chemistry RAS, 119991, Leninskii pr., 47, Moscow, Russia
[2]Bruker ltd, 119017, Pyatnitskaya 50/2 str. 1, Moscow, Russia

email: kachala@bruker.ru

Introduction

The ionic liquids (IL) are promising solvents for many chemical reactions, as well as for industrial processes because of their unique physical properties: They are high-polar solvents with low vapor pressure and excellent thermal stability.

Developing methods of product extraction, purification and recycling of ionic liquids allowed to fulfill high standards of Green chemistry. A good way of tuning physical and chemical properties of ionic liquids is combination of cation and anion pairs. In order to perform studies of chemical reactions, extraction, quality control, we need a non-destructive method which allows monitoring of chemical transformations. One of actual chemical processes observed in ionic liquids, is conversion of carbohydrates into 5-hydroxymethylfurfural (5-HMF) as shown on fig.1, which has diverse range of chemical and industrial applications.

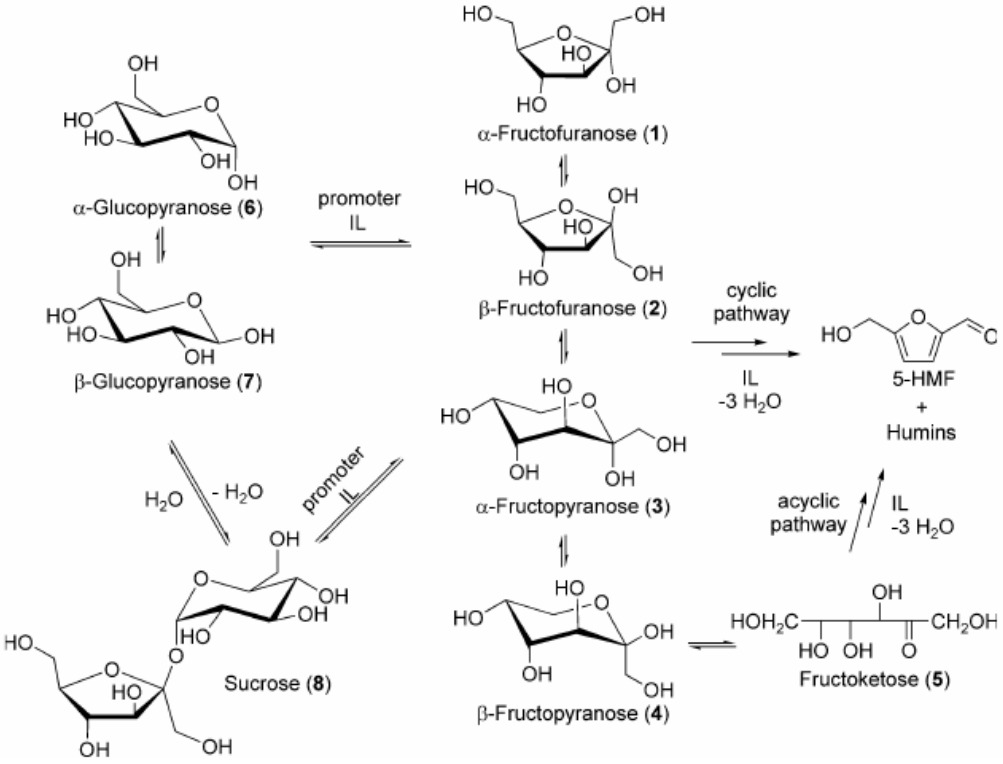

Fig.1. Interconversion of carbohydrates and formation of 5-HMF

Development of NMR experiments for IL systems

There was common belief than NMR measurements in ionic liquids are impossible due to RF power dissipation and bad homogeneity of media. We have found a way of NMR

measurements in this solvents. Most of ionic liquids are very viscous in normal conditions, so the temperatures of 60-120 Celsius are usual for reactions in these systems, elevated temperature was set also during NMR experiments.

The next issue is shimming. All Z-shims can be easily adjusted using Z-gradient shimming based on IL signals. X- and Y- shims were tuned manually by FID area. In order to achieve proper spectral results, we needed precise 90-degree pulses. As the rule of thumb, ^{13}C and ^{1}H pulses for IL are 1.5 times longer than for organic solvents.

The chemical shifts of ionic liquids depend on temperature, reaction mixture composition and other factors. We used DMSO-d6 in glass capillary – an external standard which didn't affect our IL system and provided stable chemical shifts regardless the temperature.

More serious problems were caused by sample inhomogeneity, which was essential for acquisition of good spectra. A detailed study has shown that microheterogeneity of the sample causes the problems in observation of NMR spectra in IL. We developed new approach that helped us to avoid the problems. The reaction takes place directly in NMR tube, equipped with special stirrer. The reaction mixture is stirred mechanically, destroying heterogeneity of sample. Then sample quickly transferred to NMR spectrometer, remaining hot, and high-quality spectra can be recorded then within several hours if the temperature is stable (fig.2).

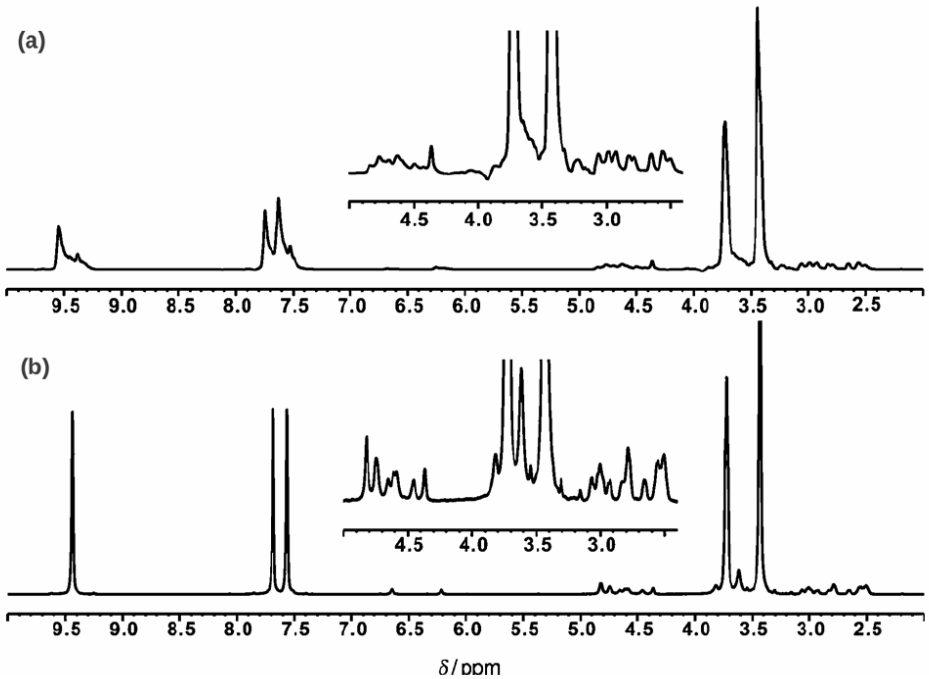

Fig.2. (a) 1H NMR spectrum of glucose in [BMIM]Cl with conventional sample preparation; (b) the same sample after treatment in our NMR reactor, which is shown in fig.2. Conditions: 80 8C, 600 MHz. The inserts show the magnified region containing the glucose signals.

The elimination of micro heterogeneity made it possible to record high-resolution NMR spectra for a broad range of IL Systems. This approach is useful for conducting mechanistic studies in native-state IL systems. The NMR setup developed in the present study can be easily assembled and utilized with standard NMR hardware for both 1D and 2D experiments like heteronuclear multiple-bond correlation (HMBC), heteronuclear single-quantum correlation (HSQC), and COSY.

Reaction monitoring in ionic liquids

The primary task of the study was the identification and quantification of reaction components. 1H spectra, even well resolved, contain lots of overlapped signals, making them almost impossible to integrate. Carbon-13 spectra were optimal for our task as they have wide signal spread and extra loss overlap, as well as better reproducibility of chemical shifts.

The idea to use IL signal for quantification required research of T1 relaxation times for carbon-13 of ionic liquid media and solutes in order to optimize experimental conditions. The measured values indicate that aromatic carbons of ionic liquid cation can be utilized for referencing in quantity measurement (fig.3).

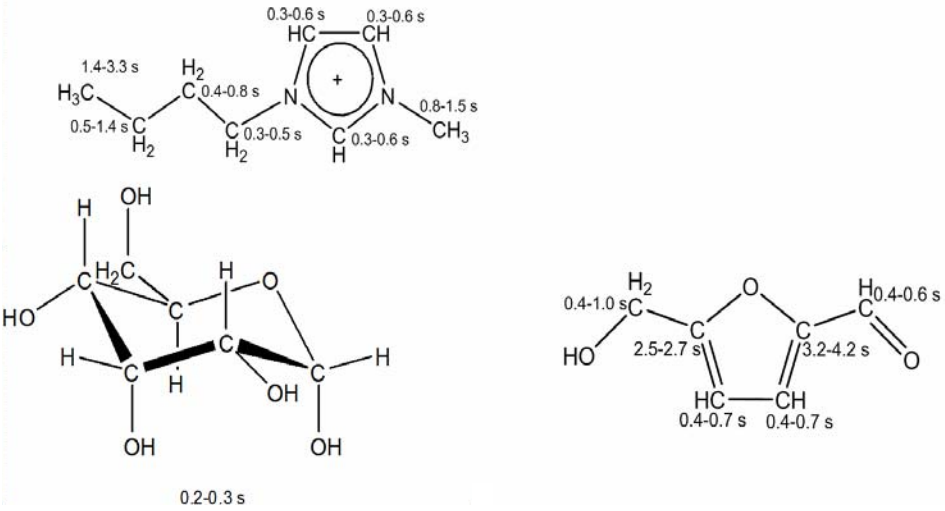

Fig.3. ^{13}C T1 relaxation times of glucose, 5-HMFand ionic liquid, [BMIM]Cl

^{13}C NMR allowed monitoring the reaction with sufficient signal-to-noise ratio in a reasonable time. The results were confirmed by chromatography measurements.

The mechanism of the conversion of carbohydrates to 5-hydroxymethylfurfural (5-HMF) was studied at the molecular level with the detection of anomers and intermediate species (fig.4).

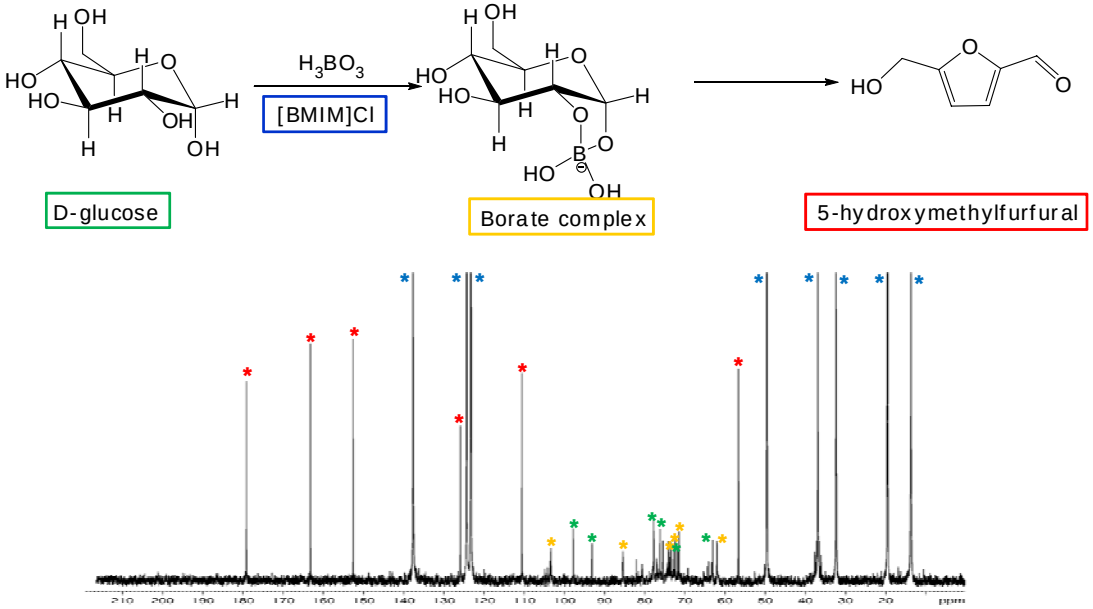

Fig.4. ^{13}C NMR glucose conversion monitoring

Molecule structure analysis in ionic liquids

Alpha-glucopyranose-1,2-borate intermediate complex was characterized by 1D and 2D NMR methods. Another interesting fact that we discovered, is the existence of fructose in unusual open form (fructoketose) in IL. The structure of fructoketose was approved by 13C, HSQC and HMBC spectra (fig.5).

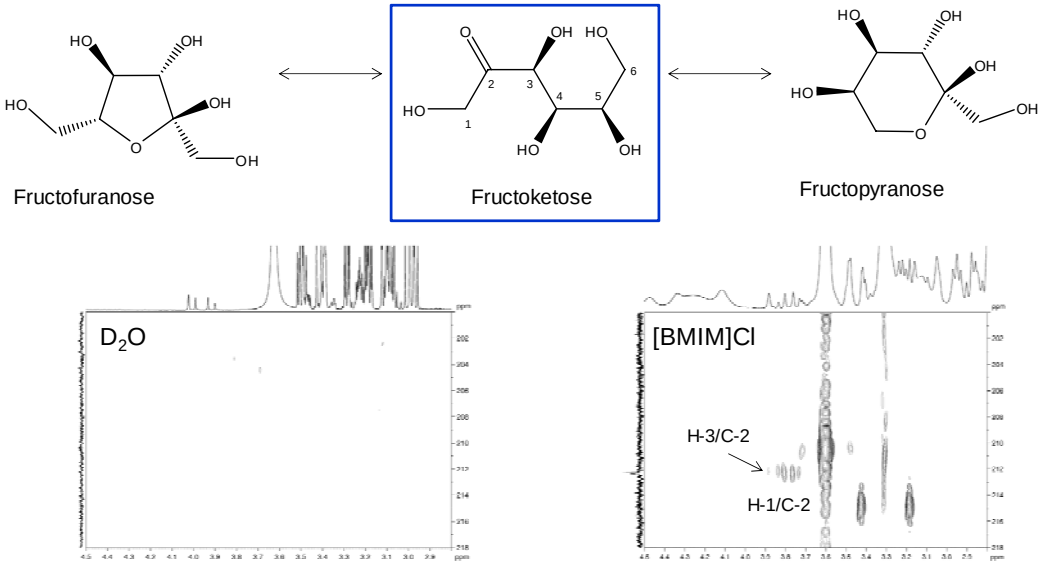

Fig.5. Fructoketose open form, nonexistent in D2O

Summary

A new NMR procedure has been developed to investigate molecular structures and chemical reactions directly in ionic liquids. The elimination of micro heterogeneity by mechanical stirring allowed recording high-resolution 1D and 2D NMR spectra for a broad range of IL systems. This approach was useful for conducting mechanistic studies in native-state ionic liquids.

References

[1] Khokhlova E. A., Kachala V. V., Ananikov V. P., ChemSusChem, 2012, 5, 783-789.

[2] Ananikov V. P., Chem. Rev., 2011, 111, 418-454.

Overview Bruker BioSpin report

M.R. Gafurov

Bruker Ltd Moscow, Russian Federation.

e-mail: kazan@bruker.ru

Established in 1960 Bruker Corporation nowadays is a worldwide leader in research and development (R&D) of the analytical instruments for science, high schools, and industry not only in magnetic resonance area but in mass spectrometry, IR and Raman spectroscopy, X-ray analysis, etc., as a result of merging other hi-tech companies and continuous progress in the technologies and materials used.

The Talk is devoted to the last achievements of Bruker Corp. with a stress on the NMR, EPR and MRI equipment and accessories.

For more information you are welcome to visit our Internet Portals **http://www.bruker.ru/** in Russian or **http://www.bruker.com/** in English.

Collective spin excitations in HTSC cuprates

M.V. Eremin

Kazan (Volga region) federal university, Institute of Physics, 420008, Kremlevskaya 18, Russian Federation.

e-mail: Mikhail.Eremin@ksu.ru

Theoretical studies of layered cuprates can be broadly separated into two parts depending on whether the point of consideration is Mott insulator or a metal. Theories of Mott insulators depart from a Mott insulator/Heisenberg antiferromagnet (AFM) at half-filling, and addresses the issue how superconductivity (SC) and metallicity arise upon doping. Another class of theories explores the idea that the system's behavior is primarily governed by interactions at energies smaller than the fermionic bandwidth, while contributions from higher energies account only for the renormalizations of the input parameters. For the cuprates, the point of departure for such theories is a Fermi liquid (FL) at large doping, and the issue these theories address is how non-Fermi liquid physics and unconventional pairing arise upon reducing the doping.

Correspondingly, two approaches are also used for the description of dynamic spin susceptibility. In the itinerant case usually one employs the random phase approximation (RPA) and in a proximity to the AFM state, the spin response above Tc is governed by the continuum of the antiferromagnetic spin fluctuations (paramagnons). In the superconducting d_{x²-y²}-wave state there is a feedback effect of superconductivity on the spin response which yields a formation of the spin resonance below Tc. While the behaviour of the spin response in the superconducting state of optimally and overdoped cuprate superconductors can be qualitatively and even quantitatively understood within this approach, the normal state data are not entirely captured by the RPA where the excitations are completely damped and structureless at high energies.

Within the localized type of approaches the situation is opposite. In this case one starts from the undoped situation of a two-dimensional antiferromagnet and studies how the spin excitations evolve upon introducing the finite amount of carriers. Here the spin response remains dual in nature as it assumes a mixture of the local spins described by the superexchange interaction J and the itinerant carriers with tight-binding energy dispersion. This scenario seems to be quite efficient in describing the normal state spin dynamics, but so far its application to the superconducting state was rather limited. So called downward dispersion of neutron scattering intensity is not reproduced in this approach.

Note, the hour-glass-shape dispersion observed in neutron scattering below Tc naturally calls for the explanation of the spin response in terms of dual character of the excitations [1]. While the upward dispersion resembles the collective spin wave-like branch as in quasi-two dimensional antiferromagnet with short range spin fluctuation, the downward dispersion in the superconducting state can be nicely attributed to the feedback effects of the d-wave order parameter on the itinerant component. In this comutication I will discuss the possible way how to describe both components (local and itinerant) on equal footing based on t-J-G model.

References

[1] M.V. Eremin, I.M. Shigapov and I.M. Eremin. Dual features of magnetic susceptibility in superconducting cuprates: A comparison to inelastic neutron scattering**.** Eur. Phys. J. B (2012) **85**: 131 (9 pp).

Capabilities of HF/HF EPR

S.N. Lukin

Institute of Semiconductor Physics NAS of Ukraine, 41, pr.Nauki, Kiev, 03028, Ukraine

e-mail: s.lukin@mail.ru

The Lecture concerns the features of the High Field/High Frequency EPR (**HF/HF EPR**).

In contrast to the traditional X-band (3cm or 9GHz range) technique, **HF/HF EPR** allows among other factors

- ✓ to measure the value of spectroscopic splitting factor (g-factor) of radicals with great accuracy, i.e., to determine the symmetry of the paramagnetic centers;
- ✓ to minimize the influence of the second order effects of HFS (hyperfine structure) on the shape of the spectrum;
- ✓ to reduce the intensity of the "forbidden" transitions;
- ✓ to investigate the systems with a large initial splitting (10 cm^{-1} or more) inaccessible to traditional X-band, *etc*.

The material is illustrated by the variety of results obtained in 1970's - 1980's which initiated the development and the start of the production in 1996 by **BRUKER** company the first and the only one obtainable now on the market commercial instrument **Elexsys E680** operating at 94 GHz.

The names of the researchers and groups who are considered to be the legends of the “short millimeter range” (original name) and those who reached the best results nowadays are underlined.

Interplay of classical and quantum spin dynamics

F.S. Dzheparov

ITEP, 117258, B. Cheremushkinskaya 25, Moscow, Russia

e-mail: dzheparov@itep.ru

Quantum and classical spin dynamics have more similarity than difference in theoretical part. Many processes can be described within general formalism where the type of dynamics became important at final steps only. The thesis is illustrated by consideration of operator perturbation theory and multi-spin resonance transitions.

Classical spins behavior becomes of interest in connection with modern studies of magnetic resonance in magnetic nanoparticles (see for example [1-4] and references therein).

Traditional consideration of quantum spin transitions in NMR and EPR [5, 6] was very different from analysis of ferromagnetic resonance [7], where motion of huge classical moment of total sample was used. The difference produces difficulties in comparison of corresponding results, especially for complex multi-spin and “multi-quantum” transitions.

Modern theory of multi-spin transitions starts, probably, with treating of two-spin transitions in the book [8]. Most extensive consideration was fulfilled in [9], where several versions of the theory were constructed, and intensities of many transitions were calculated and compared with precision results of beta-NMR spectroscopy [10, 11]. The theory can be characterized as a quantum mechanical unitary operator perturbation theory, constructed in commutator form. It has many common properties with treating of multi-pulse narrowing methods of solid-state NMR [12, 13]. Main aim of the lecture consists in concentrated description of the theory in application to multi-spin transitions, which is equally applicable both to quantum and classical spin systems. The description produces shortest way to separation of quantum and classical effects in results of measurements.

It should be stressed, that construction of quantum mechanical unitary operator perturbation theory started in first half of 20-th century. Probably it was initiated both internal requirements of quantum mechanics and analogies with canonical perturbation theory of classical mechanics (see Ref. [14] as an introduction for example). The influence of canonical classical mechanics was very strong from the beginning of the quantum theory. For example, quantum theory introduces new space of states, instead of classical trajectories, but definition of operators in this space is strictly connected with Hamiltonian classical mechanics in Cartesian coordinates and prescribes a substitution of canonical momentum $\mathbf{p} = \partial L(\mathbf{q}, \dot{\mathbf{q}}) / \partial \dot{\mathbf{q}}$ (not kinematical one $m\dot{\mathbf{q}}$!) by the operator $\hat{\mathbf{p}} = -i\dfrac{\partial}{\partial \mathbf{q}}$ as a quantization rule. Here $L(\mathbf{q}, \dot{\mathbf{q}})$ is a Lagrangian as a function of Cartesian coordinate $\mathbf{q}$ and velocity $\dot{\mathbf{q}}$. We will use presumably units with $\hbar = 1$ and $c = 1$. From mathematical point of view the quantum mechanical states form a Hilbert space, it will be referred to as Schrödinger space here in order to separate from Liouville space, discussed below.

Separation of canonical and kinematical momentums gives a possibility to take into account magnetic field, because (in simplest case) the Hamiltonian

$$H(\mathbf{p}, \mathbf{q}) = \dot{\mathbf{q}}\mathbf{p} - L = \frac{1}{2} m \left(\dot{\mathbf{q}} \right)^2 + U(\mathbf{q}) = \frac{1}{2m} \left(\mathbf{p} + e\mathbf{A}(\mathbf{q}) \right)^2 + U(\mathbf{q}) .$$

Here **A**(**q**) is a vector-potential, *e* is electrical charge, and *U*(**q**) is scalar potential energy. With more general definition we have canonical momentum as $p_\mu = \partial S(q)/\partial q^\mu$, where

$$S(q) = \int_0^{\mathbf{q}} \mathbf{p} d\mathbf{q} - \int_0^t H(\mathbf{p},\mathbf{q}) dt = -\int_0^q p_\mu dq^\mu$$

is an action as a function of final 4-dimentional coordinate $q^\mu = (t,\mathbf{q})$ and integration is carried out along real trajectory. This definition produces the same space components **p** of the 4-momentum p^μ, and new component $p^0 = -H(\mathbf{p},\mathbf{q})$. Therefore, applying the same quantization rule to canonical momentum $p^0 = p_0 = -H(\mathbf{p},\mathbf{q})$. we have two different definitions for corresponding momentum operator: $\hat{p}_0 = -i\dfrac{\partial}{\partial t}$ and $\hat{p}_0 = -H(\hat{\mathbf{p}},\mathbf{q})$. For compatibility we should require their coincidence in action on realizable state $|\psi\rangle$, that produce the main equation of the quantum theory – Schrödinger equation $i\dfrac{\partial}{\partial t}|\psi\rangle = H(\hat{\mathbf{p}},\mathbf{q})|\psi\rangle$. This short excursion demonstrates exclusive importance of canonical classical mechanics for foundations of the quantum theory.

Unitary transformations form one of the most important sections of quantum mechanics. Nowadays workers know and understand it, as a rule, much better than canonical transformations in classical theory. Similar education effect is known for a long time; it was indicated, see for example, in the “Introduction” in Ref. [15]. Therefore our consideration will be based on unitary transformations in Liouville space, which can be considered as necessary and usual extension of standard Schrödinger quantum mechanical space or natural space for classical dynamics, based on Liouville equation for distribution functions. In quantum mechanics Liouville space is formed by density matrices or by usual operators of Schrödinger space.

Perturbation theory. General outlines

Absolute majority of interesting theoretical problems have no exact solutions. Perturbation theory produces a possibility to receive approximate (and verifiable in an experiment) result starting from exactly solvable simplified problem. From my point of view the best perturbation theory for spin dynamics consists of two very different parts. First part is directed on simplification of the Hamiltonian up to form, suitable for application in derivation of a master equation, which produces description of evolution of observables. The master equation derivation forms second part of the perturbation theory. This strategy has long history, and its elements can be found, for example, in Refs. [8] and [16].

Evolution both quantum and classic systems is governed by Liouville equation

$$\frac{\partial}{\partial t}\rho = -iL\rho\,, \tag{1}$$

where ρ is density matrix or distribution function in quantum and classical theory respectively. In quantum case the Liouville operator *L* (Liouvillian) is defined as

$$L\rho = [H,\rho] = H\rho - \rho H, \tag{2}$$

while in classical mechanics

$$L\rho = -i\{H,\rho\} = -i\left(\frac{\partial H}{\partial p}\frac{\partial \rho}{\partial q} - \frac{\partial H}{\partial q}\frac{\partial \rho}{\partial p}\right) = -i\sum\nolimits_{j=1}^{N}\sum\nolimits_{\alpha=1}^{d}\left(\frac{\partial H}{\partial p_j^\alpha}\frac{\partial \rho}{\partial q_j^\alpha} - \frac{\partial H}{\partial q_j^\alpha}\frac{\partial \rho}{\partial p_j^\alpha}\right). \tag{3}$$

Here N is a number of considered particles, while d is space dimension.

Eqs. (1)-(3) unify main equations of motion of quantum and classical theory. A tendency to such unification existed from the beginning of quantum mechanics. Partially one of form of main quantization postulate consists in substitution of Poisson bracket of canonical variables by the operator commutator according the same rule $\left\{p_j^\alpha, q_k^\beta\right\} = \delta_{jk}\delta_{\alpha\beta} \rightarrow$ $\rightarrow i\left[\hat{p}_j^\alpha, q_k^\beta\right] = \delta_{jk}\delta_{\alpha\beta}$. Heisenberg equations of motion have the same similarity to Hamilton equations.

From operator point of view the Liouvillian L is a Hermite operator in a new (relative to Schrödinger space) Hilbert space (Liouville space), where density matrices and other quantum mechanical operators works as vectors, while in classical theory Liouville space is formed by distribution functions and other functions in the same way. The Liouville operator is hermitian relative to scalar production $(a,b) = \mathrm{Tr}(a^+ b)$ or $(a,b) = \int dpdq \cdot a^+ b$ in quantum and classical theory respectively.

Formal Nakajima-Zwanzig derivation of master equation starts from separation of a small, but important part ρ_1 of ρ, which is sufficient for calculation of observables. In simplest case this operation is introduced by a time-independent projection operator P and

$$\rho_1 = P\rho, \quad P^2 = P\,. \tag{4}$$

Multiplying Eq. (1) on P we have

$$\frac{\partial}{\partial t}\rho_1 = \frac{\partial}{\partial t}P\rho = -iPL\left(P+\bar{P}\right)\rho = -i\left(PLP\rho_1 + PL\bar{P}\rho_2\right), \tag{5}$$

where

$$\rho_2 = \bar{P}\rho, \quad \bar{P} = 1 - P, \quad \left(\bar{P}\right)^2 = \bar{P} \tag{6}$$

and, evidently,

$$\frac{\partial}{\partial t}\rho_2 = -i\bar{P}L\left(P+\bar{P}\right)\rho = -i\left(\bar{P}LP\rho_1 + \bar{P}L\bar{P}\rho_2\right) \tag{7}$$

Solving Eq.(7) with initial condition $\rho_2(t=0) = 0$ and substituting the solution into Eq. (5) we receive a master equation

$$\frac{\partial}{\partial t}\rho_1 = -i\Omega\rho_1 - \int_0^t d\tau M\left(t,\tau\right)\rho_1\left(\tau\right) \tag{8}$$

with definitions of frequency matrix Ω and memory kernel $M(t,\tau)$:

$$\Omega = PLP, \quad M(t,\tau) = PL\bar{P}\cdot T\exp\left(-i\int_\tau^t d\tau_1 \bar{P}L\left(\tau_1\right)\bar{P}\right)\cdot \bar{P}LP\,. \tag{9}$$

Here standard chronological exponent (Texp) is introduced.

These formal operations are well known and equally applicable both for quantum and classical theory. Real calculations require reasonable approximations for memory kernel which can depend on type of dynamics and we will not discuss them later.

We will concentrate our attention on the first part of perturbation theory consisting of simplification of the Hamiltonian. We will consider the Hamiltonian of the form

$$H = \sum\nolimits_m H_m e^{i\omega_m t}, \quad H_m^+ = H_{-m}\,. \tag{10}$$

As a rule the representation (10) is a consequence of application of so called representation of interaction, when strong but exactly solvable part of the evolution is excluded from the

equation of motion, and all terms in (10) have the same order of value, while many of frequencies ω_m are large.

We come to this representation, for example, in discussion of resonances at frequencies, obeying the condition $k\omega = m\omega_I$. Here *k* and *m* are integer, and ω_I and ω are Larmor frequency and frequency of alternating field. The transitions can take place, for example, in homo-spin system formed by spins I, placed in strong static magnetic field (directed along *z*-axis with value ω_I) and orthogonal it radio-frequency field with value ω_{1I} (we use frequency units for magnetic fields) in presence of dipole-dipole interactions. The terms H_m at that represent so called Van Vleck' alphabet [5, 7] (with corresponding frequencies $\{\omega_m\} = 0, \pm\omega_I, \pm 2\omega_I$) and rf-interaction (with frequencies $\pm(\omega_I - \omega)$) in the system, rotating with the frequency ω_I around the static field. Other example is produced by nuclear or electron spins in presence of quadrupole interaction

$$H_Q = \omega_Q \left((\mathbf{nI})^2 - \frac{1}{3} I(I+1) \right) \tag{11}$$

and static magnetic field, if $\omega_Q \ll \omega_I$. The Hamiltonian (11) produces the same set of primary frequencies ω_m as homo-spin dipole interaction. More complex examples together with solutions can be found in Ref. [9-11].

The aim of considered perturbation theory consists in such transformation of the Liouville equation, which conserve Hamilton form (2) of the main equation (with a new Hamiltonian) and suppress fast oscillating terms of the Hamiltonian. Slow oscillating terms should be treated via master equation.

Very important property of the theory consists in the fact, that new (transformed) Hamiltonian is constructed from powers of commutations (or Poisson brackets) that automatically produce no volume divergences.

Other important property is specific for spin dynamics, where spin variables are included only instead of full set of coordinates and momenta, and main quantum mechanical (QM) commutators are in exact agreement with Poisson brackets of classical mechanics (CM) again:

$$\left[I_j^\alpha, I_k^\beta \right] = i\delta_{jk} e_{\alpha\beta\gamma} I_k^\gamma . \tag{12}$$

Here I_j^α is α component of *j*-th spin, and $[a,b]$ means the commutator of operators *a* and *b* in quantum mechanics, or $[a,b] = -i\{a,b\}$ in classical theory. A summation is meant in (12) over index γ on right side, which is absent on left side. With these notations Eqs. (1)-(3) can be written as

$$\frac{\partial}{\partial t}\rho = -iL\rho = -i[H,\rho] = -iH^\times \rho \tag{13}$$

both in quantum and in classical theory, and the operation $[a,b]$ will be referred as commutator in both theories, if it will not require additional refinement. Last relation in (13) can be written as $L = H^\times$, and it indicates that operator *L* in Liouville space (superoperator) is formed by *H* via commutator that is rather special form for superoperators.

Unitary operator perturbation theory

We can separate the Hamiltonian (10) and (corresponding Liouvillian) into fast (F) and slow (S) oscillating parts:

$$H(t) = H_S(t) + H_F(t), \quad H_S(t) = \sum\nolimits_{|\omega_m|<\Omega} e^{i\omega_m t} H_m, \quad H_F(t) = \sum\nolimits_{|\omega_m|>\Omega} e^{i\omega_m t} H_m . \tag{14}$$

The boundary frequency Ω should be defined later from the requirement of self-consistency of calculations.

We can introduce a new variable $\rho^{(1)}(t)$ via unitary transformation in Liouville space

$$\rho(t) = U(t)\rho^{(1)}(t) = \exp\left(-iS^{\times}(t)\right)\rho^{(1)}(t), \;\; S^{\times}(t) = \sum\nolimits_{|\omega_m|>\Omega} \frac{1}{i\omega_m} e^{i\omega_m t} H_m^{\times} . \tag{15}$$

In action on typical states, for example on I_j^{α} or $I_j^{\alpha} I_k^{\beta}$, the superoperator $H_m^{\times}$ produces finite result even for infinite systems, when number of spins $N \to \infty$. Therefore

$$S^{\times}(t) \sim H_F^{\times} / \Omega \sim \varepsilon \tag{16}$$

can be considered as small value proportional to small parameter ε.

It is evident that $\partial S^{\times}(t) / \partial t = H_F^{\times}(t)$, and equation of motion for $\rho^{(1)}(t)$ does not contain fast oscillating terms in main order in ε:

$$\frac{\partial}{\partial t}\rho^{(1)} = -iH_S^{\times}\rho^{(1)} + O(\varepsilon) . \tag{17}$$

More exactly

$$\frac{\partial}{\partial t}\rho^{(1)} = -iL^{(1)}\rho^{(1)}, \quad L^{(1)} = U^{+}LU + i\dot{U}^{+}U . \tag{18}$$

It is evident, that

$$U^{+}LU\rho^{(1)} = U^{+}\left[H, \left(U\rho^{(1)}\right)_0\right] = \left[\left(U^{+}H\right)_0, \rho^{(1)}\right]. \tag{19}$$

Here a symbol $\left(U\rho^{(1)}\right)_0$ (or $\left(U^{+}H\right)_0$) means, that action of superoperators U (or U^{+}) is concentrated within the bracket, and the result is a vector in Liouville space.

Differentiation of the exponential operator $U(t)$ is a standard action (see for example [9] or Appendix in [17]) with a result

$$\frac{\partial}{\partial t} e^{iS^{\times}} = i\int_0^1 d\alpha e^{i\alpha S^{\times}} \dot{S}^{\times} e^{i(1-\alpha)S^{\times}} \tag{20}$$

Therefore

$$\dot{U}^{+}U\rho^{(1)} = i\int_0^1 d\alpha e^{i\alpha S^{\times}} \dot{S}^{\times} e^{-i\alpha S^{\times}} \rho^{(1)} = i\int_0^1 d\alpha e^{i\alpha S^{\times}} H_F^{\times} e^{-i\alpha S^{\times}} \rho^{(1)} =$$

$$= i\int_0^1 d\alpha e^{i\alpha S^{\times}} \left[H_F, \left(e^{-i\alpha S^{\times}}\rho^{(1)}\right)_0\right] = i\int_0^1 d\alpha \left[\left(e^{i\alpha S^{\times}} H_F\right)_0, \rho^{(1)}\right] = i\left[\left(\frac{e^{iS^{\times}} - 1}{iS^{\times}} H_F\right)_0, \rho^{(1)}\right]. \tag{21}$$

We see that new Liouvillian $L^{(1)} = H^{(1)\times}$ is formed of new Hamiltonian according to relations (18), (19) and (21) as

$$L^{(1)}\rho^{(1)} = H^{(1)\times}\rho^{(1)} = \left[H^{(1)}, \rho^{(1)}\right], \quad H^{(1)} = e^{iS^{\times}} H - \frac{e^{iS^{\times}} - 1}{iS^{\times}} H_F . \tag{22}$$

The transformation from Eqs. (13) and (14) to (18) and (22) defines an iteration method, which can be continued later. At every step of iterations fast oscillating term of the Hamiltonian is suppressed, and new slow oscillating terms are created. After *n* steps the fast

oscillating term has an order $H_F^{(n)} \sim \varepsilon^{2^n}$ as in super-convergent classical Kolmogorov-Arnol'd-Moser theory. But, for typical conditions, relaxation speed $w_F^{(n)}$, produced by $H_F^{(n)}$, is not smaller than the speed $w_F = w_F^{(n=0)}$, calculated directly from $H_F \sim \varepsilon^0$ [8, 9]. There is no contradiction here, because, as a rule, $|\ln w_F^n| \sim 1/\varepsilon,$ while the iterations display the power accuracy $\sim \left(\varepsilon^{2^n}\right)^2$ for $w_F^{(n)}$ only [9].

Main result for applications is concentrated in effective Hamiltonian of slow motions H_S^{eff} presented by slow part of the new Hamiltonian, because it contains new terms relative to initial H_S. Two iterations produce accuracy up to ε^3 and [9]

$$\begin{aligned} H_S^{eff} = H_S^{(2)} + O\left(\varepsilon^4\right) = \left(\left(1 - \tfrac{1}{2}S^{\times 2} - \tfrac{i}{6}S^{\times 3}\right)H_S + \left(\tfrac{i}{2}S^{\times} - \tfrac{1}{3}S^{\times 2} - \tfrac{i}{8}S^{\times 3}\right)H_F\right)_S - \\ - \tfrac{i}{2}\left(\left[\widetilde{\left(S^{\times}\left(H_S + \tfrac{1}{2}H_F\right)\right)_{0F}}, \left(S^{\times}\left(H_S + \tfrac{1}{2}H_F\right)\right)_{0F}\right]\right)_S + O\left(\varepsilon^4\right). \end{aligned} \tag{23}$$

Here $\widetilde{A} = \sum_m A_m \exp\left(i\omega_m t\right)/\left(i\omega_m\right)$ for $A = \sum_m A_m \exp\left(i\omega_m t\right)$, the symbol $\left(\bullet\bullet\bullet\right)_0$ is introduced in (19), and subscripts *S* and *F* indicate separation of slow and fast oscillating parts, as in (14). Main attention of many workers was attracted to situations, where instead of separation of slow part of the Hamiltonian the time averaging can be used. Corresponding result with accuracy up to ε^2 was received in Refs. [18, 19], it was repeated for spin dynamics in [13], and the accuracy was refined up to ε^5 in Ref. [20].

An example

Let us consider a resonance at the frequency $\omega = 2\omega_I$ in homo-spin system, produced by dipole interactions as an example. The Hamiltonian can be written as

$$H = H_Z + H_D + H_{rf}(t). \tag{24}$$

Here $H_Z = \omega_I I_z$ is Zeeman interaction, H_D is dipole-dipole Hamiltonian and

$$H_{rf}(t) = \tfrac{1}{2}\omega_{1I}\left(I_+ e^{-i\omega t} + I_- e^{i\omega t}\right) \tag{25}$$

represents the action of resonance alternating field. Main influence on resonance at the frequency $\omega = 2\omega_I$ is produced by so called C-term of H_D:

$$\begin{aligned} H_{DC} = \tfrac{1}{2}\sum_{jk}\left(c_{jk}\left(I_j^z I_k^+ + I_j^+ I_k^z\right) + H.C.\right) = H_C^+ + H_C^+, \\ c_{jk} = -\tfrac{3}{4}\tfrac{\gamma^2\hbar^2}{r_{jk}^3}\sin\left(2\vartheta_{jk}\right)e^{i\phi_{jk}}, \quad \left[H_Z, H_C^{\pm}\right] = \pm\omega_I H_C^{\pm}, \end{aligned} \tag{26}$$

where polar angles ϑ_{jk} and ϕ_{jk} define direction of the interspin vector $\mathbf{r}_{jk}$.

Effective Hamiltonian of slow motion will include secular part of dipole interactions H_{D0} and, according to (22), a resonance term

$$\begin{aligned} H_{res}(t) = \frac{i}{2}\left[S, H_F\right]_S, \quad H_F = H_C^+ e^{i\omega_I t} + H_C^- e^{-i\omega_I t} + \frac{1}{2}\omega_{1I}\left(I_+ e^{i(\omega_I - \omega)t} + I_- e^{-i(\omega_I - \omega)t}\right), \\ S = \widetilde{H}_F = H_C^+\frac{e^{i\omega_I t}}{i\omega_I} - H_C^-\frac{e^{-i\omega_I t}}{i\omega_I} + \frac{\omega_{1I}}{2i\left(\omega_I - \omega\right)}\left(I_+ e^{i(\omega_I - \omega)t} - I_- e^{-i(\omega_I - \omega)t}\right). \end{aligned} \tag{27}$$

After simplifying

$$H_{res}(t)=\frac{\omega_{1I}\omega}{4\omega_I\left(\omega-\omega_I\right)}e^{i(2\omega_I-\omega)t}\sum_{jk}c_{jk}I_j^+I_k^+ + H.C. = H_r^+(t)+H_r^-(t),$$
$$H_r^+(t)\approx\frac{\omega_{1I}}{2\omega_I}e^{i(2\omega_I-\omega)t}\sum_{jk}c_{jk}I_j^+I_k^+,\ \ H_r^-(t)=\left(H_r^+(t)\right)^+. \tag{28}$$

In the simplest theory (neglecting the influence of dipole order) important part of the density matrix can be chosen as a function of I_z only and master equation (8) after standard transformations became a form

$$\frac{\partial}{\partial t}\rho_1=-\int_0^\infty d\tau\left[H_{res}(t,t),\left[H_{res}(t-\tau,t-\tau),\rho_1(t)\right]\right],$$
$$H_{res}(t,\tau)=e^{iH_{D0}t}H_{res}(\tau)e^{iH_{D0}t}. \tag{29}$$

Correspondingly

$$\frac{\partial}{\partial t}\langle I_z\rangle=\frac{\partial}{\partial t}(I_z,\rho_1)=-\int_0^\infty d\tau\left(I_z,\left[H_{res}(t,t),\left[H_{res}(t-\tau,t-\tau),\rho_1(t)\right]\right]\right)=$$
$$=-2\int_{-\infty}^{\infty}d\tau e^{i(2\omega_I-\omega)\tau}\left(\left[H_r^+(\tau,0),H_r^-\right],\rho_1\right). \tag{30}$$

Here scalar production in Liouville space is applied and the relation $\left[H_Z,H_r^\pm\right]=\pm2\omega_IH_r^\pm$ is taken into account.

One of most representative parameter of resonance at combination frequency $\omega=k\omega_I$ is its forbidding factor $A(\omega=k\omega_I)$. To define it we can introduce a measurable parameter

$$W_0(\omega=2\omega_I)=-\lim_{t\to0}\int d\omega\frac{\partial}{\partial t}\ln\langle I_z\rangle=\frac{\pi\left\langle\left[H_r^+,H_r^-\right]\right\rangle_0}{\langle I_z\rangle_0}, \tag{31}$$

which presents intensity of the resonance. Here $\langle F\rangle_0=\left(F,\rho_1(t=0)\right)$ for any $F=F^+$. The argument $\omega=2\omega_I$ on the left side in (30) indicates type of the resonance, while frequency integration in second term is fulfilled near the resonance frequency $2\omega_I$ and does not include resonances of other types, which are supposed as well separable. The limit $t\to0$ in (31) implies small $t\gg T_2$, according to applicability of Eq. (29). Similar parameter for Larmor resonance is

$$W_0(\omega=\omega_I)=\pi\omega_{1I}^2. \tag{32}$$

The forbidding factor is

$$A(\omega=2\omega_I)=W_0(\omega=2\omega_I)/W_0(\omega=\omega_I). \tag{33}$$

We see that it depends on equilibrium properties of the system. Of course results will be very different for large classical spins and for small quantum spins with the same gyromagnetic ratio. Direct calculation produces

$$W_0(\omega=2\omega_I)=8\pi\left(\frac{\omega_{1I}}{2\omega_I}\right)^2\frac{1}{N}\sum_{jk}\left(\mathrm{Re}\,c_{jk}\right)^2\left\langle I(I+1)-\left(I_k^z\right)^2\right\rangle. \tag{34}$$

It is evident that $W_0(\omega=\omega_I)$ does not depend on spin value at all. Contrary that $W_0(\omega=2\omega_I)$ has strong corresponding dependence, and “extra”-quantum case $I=1/2$ has no dependence on initial state, while classic limit has strong corresponding dependence.

Conclusion

The analysis indicates that description of classical and quantum spin dynamics can be carried out in general way, where difference between these theories go into action at last steps in calculations of such values as forbidding factor or resonance form function for example. These exist strong indications, that dipole resonance form function for classical and quantum theories are very close as well, see for example [21].

I am grateful to Prof. V.A. Atsarkin for stimulating discussions. The work was supported by RFBR (project # 11-02-00880).

References

[1] N. Noginova, T. Weaver, E.P. Giannelis, A.B. Bourlinos, V.A. Atsarkin, V.V. Demidov. Phys. Rev. **B** 77, 014403, 2008.

[2] N. Noginova, Yu.Barnakov, A.Radocea, V.A.Atsarkin. J. Magn. Mag. Mater. **323**, 2264, 2011.

[3] F.S. Dzheparov, O.N. Sorokina, A.L. Kovarski. JETP Lett. **89**, 563, 2009.

[4] O.N. Sorokina, A.L. Kovarski, M.A. Lagutina, S.A. Dubrovskii, F.S. Dzheparov. Appl.Sci. **2**, 342, 2012.

[5] A. Abragam. The principles of nuclear magnetism. Oxford, Clarendon Press 1961.

[6] A. Abragam and B. Bleaney. Electron Paramagnetic Resonance of Transition Ions. Clarendon, Oxford, 1970.

[7] A.G. Gurevich, G.A. Melkov. Magnetic oscillations and waves. Moscow, Fizmatlit 1994 (in Russian).

[8] M. Goldman. Spin temperature and nuclear magnetic resonance in solids. Oxford, Clarendon Press 1970.

[9] F.S. Dzheparov, and S.V. Stepanov. On multi-spin nuclear magnetic resonance with participation of polarized beta-active nuclei. Preprint ITEP-139, Moscow 1982 (in Russian).

[10] Yu.G. Abov, M.I.Bulgakov, A.D. Gul'ko, F.S. Dzheparov, S.S. Trostin, S.P.Borovlev, V.M. Garochkin. JETP Lett. **35**, 424, 1982.

[11] Yu.G. Abov, M.I.Bulgakov, S.P.Borovlev, A.D. Gul'ko, V.M. Garochkin, F.S. Dzheparov, S.S. Trostin, V.E. Shestopal. Izv. AN SSSR, ser fiz. **47**, 2299, 1983.

[12] Yu.N. Ivanov, B.N.Provotorov, E.B. Feldman. Sov. Phys. JETP **48**, 930, 1978.

[13] L.L. Buishvili, E.B.Volzhan, M.G. Menabde. TMF **46**, 251, 1981.

[14] V.I. Arnol'd. Mathematical Methods of Classical Mechanics. Springer 1989.

[15] R.G. Newton. Scattering theory of waves and particles. McGraw-Hill, New York 1966.

[16] S.A. Altshuler, B.M. Kozyrev. Electron paramagnetic resonance. Nauka, Moscow 1972 (in Russian).

[17] D.A. Kirzhnits. Field methods of many particle theory. Atomizdat, Moscow 1963 (in Russian)

[18] E.L. Burshtein, L.S. Soloviev. DAN SSSR **139**, 855,1961.

[19] N.N. Bogoliubov, Yu.A. Mitropolski. Asymptotic methods in the theory of non-linear oscillations. Nauka, Moscow 1974.

[20] V.L. Bodneva, A.A. Milyutin, E.B. Feldman. Sov. Phys. JETP **65**, 773, 1987.

[21] A.A. Lundin, V.E. Zobov. J. Magn.Res. **26**, 229, 1977.

Ferromagnetism in terms of EPR spectroscopy

V.A. Atsarkin

Kotel'nikov Institute of Radio Engineering and Electronics of the RAS, 125009, 11 Mokhovaya Str., Moscow, Russia

e-mail: atsarkin@mail.cplire.ru

Quantal ("EPR-style") description based on the spin-Hamiltonian fomalism is extended to the molecular magnets, magnetic nanoparticles and, finally, ferromagnets regarded as giant exchange-coupled spin clusters. Only the lowest spin multiplet is considered, providing the fixed (maximum) spin value ($S = const$.) The model is consistent with the Landau-Lifshits-Gilbert Equation where the magnon excitations are neglected. Recent experimental data on the magnetic-resonance spectra of superparamagnetic nanoparticles and molecular magnets are reviewed [1 – 5]. Main attention is focused on remarkable similarities in specific quantum features, such as thermally activated narrow spectral component related to the "central" transitions with low m-values and multiple-quantum "forbidden" lines.

The model is violated at elevated temperatures approaching the Curie point (T_C). In the vicinity of the phase transition, the absolute value of the ferromagnetic moment is no longer conserved, and spin dynamics is described by the Landau-Lifshits-Bloch Equation [6]. The experimental verification of this concept is presented, using the effect of resonance magnetoresistance observed on the manganite thin films [7].

References

[1] N. Noginova, F. Chen, T. Weaver, E.P. Giannelis, A.B. Bourlinos, V.A. Atsarkin, J. Phys.: Condens. Matter **19**, 246208 (2007).

[2] N. Noginova, T. Weaver, E.P. Giannelis, A.B. Bourlinos, V.A. Atsarkin, V.V. Demidov, Phys. Rev. B **77**, 014403 (2008).

[3] N. Noginova, Yu. Barnakov, A. Radocea, V.A. Atsarkin, J. Magn. Magn. Mater. **323**, 2264 (2011).

[4] M. Fittipaldi et al., Phys. Chem. Chem. Phys. **11**, 6555 (2009).

[5] L. Castelli et al., Dalton Trans. **40**, 8145 (2011).

[6] D.A. Garanin, Phys. Rev. B **55**, 3050 (1997)

[7] V.A. Atsarkin, V.V. Demidov, L.V. Levkin, A.M. Petrzhik, Phys. Rev. B **82**, 144414 (2010).

Classical and Quantum Correlations in Spin Systems in Multiple Quantum NMR in Solids

E.B. Fel'dman

Theoretical Department, Institute of Problems of Chemical Physics, Chernogolovka, 142432, Russia

email: efeldman@icp.ac.ru

Quantum correlations in many-particle systems are responsible for effective work of quantum devices (in particular, quantum computers) and give them significant advantages over their classical counterparts. Theoretical and experimental investigations of entanglement and quantum discord which describes correlations in different many-particle systems are very important for a development of new quantum technologies.

In order to investigate entanglement and quantum discord we focus on the simplest relevant system, a pair of spins $s = 1/2$ coupled by the dipole–dipole interaction in the conditions of an MQ NMR experiment. Here, the spin system is initially described by a thermodynamic equilibrium density matrix for the spins in a strong external magnetic field. Subsequently, the system is subjected to the irradiation by a specially tailored sequence of resonant rf pulses. The anisotropic dipolar Hamiltonian oscillates rapidly when the period of the sequence is less than the inverse dipolar frequency. The spin dynamics of the system is described by an averaged Hamiltonian, which is responsible for the emergence of the MQ coherences of the zeroth and plus/minus second orders. It is evident that the initial state of the system is separable. However, we show with the Wootters criterion that an entangled state emerges when the intensity of the MQ coherence of order 2 (–2) exceeds the exactly calculated threshold depending on the external magnetic field and the temperature. Thus, the intensity of the MQ coherence of the second order which is the observable in MQ NMR experiments serves as an entanglement witness for the spin systems in the conditions of the MQ NMR experiment.

We consider also an analogous model taking into account the effect of spin-lattice relaxation. We have found that the temperature of the emergence of entangled states is getting less when the spin-lattice relaxation of MQ NMR coherences is getting faster.

We have found a critical value of the intensity of the MQ NMR coherence of the second order for entanglement. However discord does not equal zero at an arbitrary intensity of MQ NMR coherence of the second order.

We have also determined the temperature behavior of discord for a number of materials. In particular, entanglement and quantum discord for a couple of $s = 1/2$ spins in a nanopore filled with a gas of spin-carrying molecules (atoms) have been studied.

The secondary-quantization representation with a basis of partially nonorthogonal orbitals: transferred hyperfine interactions

O.A. Anikeenok

Kazan (Volga region) Federal University, 420008 Kazan, Russia

e-mail: Oleg.Anikeenok@ksu.ru

Calculations with nonorthogonal basis has a long story. V. Fok [1] pointed out its advantages in calculations when helium excited states are taken into account. The nonorthogonal basis was used in Ref. [2] for number of atomic configurations. Well known Hitler-London theory of the hydrogen molecule. In Ref. [3] the nonorthogonal basis was exploited for crystals like LiF, LiCl. In Ref.[4, 5] the secondary-quantization method was developed on the basis of partially non-orthogonal orbitals. However this technique is not widely accepted, because the expressions for one-particle and two-particle operators in this representation are non-Hermitian.The quantum mechanical averaging of these operators in order to reduce the Hamiltonian of the admixture center to the spin Hamiltonian is impossible because all operators in the spin Hamiltonian used to describe the experiment are Hermitian.

Thus, the problem to build the Hermitian operators in the secondary-quantization representation with the basis of partially non-orthogonal orbitals arises. Some progress in this direction was achieved in [6, 7]. However, the form of the operator was determined only with the accuracy up to the squares of the overlap integrals of the orbitals. As a consequence, in the usage of the perturbation theory the contribution of the nonorthogonality effects higher than of the second order remained unclear. At the same time, the advantage of the approach proposed in [6, 7] is that the quantum numbers of the creation and annihilation operators are the quantum numbers of the ion orbitals allowing one to use the developed technique of the irreducible tensor operators and the secondary-quantization method in the atomic spectroscopy [8].

In [9, 10] the part processes resulting in the appearance of the hyperfine fields on the ligand nuclei in the RE admixture centers were determined by the perturbation theory method in the framework of [6, 7]. However, the amplitudes of the electron transfer were the fitting parameters with their order determined by the relevant overlap integrals. This is justified in agreement with the numerous results of the papers on the theory of iron-group admixture centers. In [11], an expression for an arbitrary operator in the orthonormalized multi-particle basis in the secondary-quantization representation with the basis of the partially non-orthogonal orbitals with the creation and annihilation operators satisfying the conventional Fermi relations was obtained.

In [11] it was shown that an expression for an arbitrary operator H_Ψ in the basis set of partially nonorthogonal orbitals may be presented in the form of a series. In this case, under the assumption of the existence of the $(I+S)^{-1}$ matrix with I being a unit operator and S being the overlap matrix for one-electron orbitals, the effects of nonorthogonality are exactly taken into account in each term of the above series. Then according to [11]

$$H_\Psi = \sum_{n=0}^{\infty} c_n \left[Q, \bar{H} \right]^{(2n)}, \qquad c_n = \frac{E_{2n}}{2^{2n} \times (2n)!} \tag{1}$$

where H_Ψ is determined on the functions

$$\left| \{\xi\} \right\rangle = \prod_{\xi} a_\xi^+ \left| 0 \right\rangle$$

The $a_\xi^+ \left(a_{\xi'}\right)$ operators are the creation (annihilation) operators of the electrons of the ion orbitals.

$$a_\xi a_{\xi'} + a_{\xi'} a_\xi = a_\xi^+ a_{\xi'}^+ + a_{\xi'}^+ a_\xi^+ = 0, \qquad a_{\xi'} a_\xi^+ + a_\xi^+ a_{\xi'} = \delta_{\xi\xi'}.$$

Note that the operator of the particle number in our approach is

$$N_\Psi = \sum a_\xi^+ a_\xi$$

The careful consideration showed that E_{2n} in (1) are **Euler numbers** ($E_0 = 1$, $E_2 = -1$, $E_4 = 5$, $E_6 = -61$, $E_8 = 1385$, $E_{10} = -50521$, ….). It follows from the properties of the series with c_n coefficients in the case of boundedness of the matrix elements of the $\left[Q, \bar{H}\right]^{(2n)}$ operators that they are convergent.

$$\bar{H} = \sum a_\xi^+ a_{\xi'} \left\langle \xi \middle| \bar{h} \middle| \xi' \right\rangle + \frac{1}{2} \sum a_\xi^+ a_\eta^+ a_{\eta'} a_{\xi'} \left\langle \xi\eta \middle| \bar{g} \middle| \xi'\eta' \right\rangle,$$

$$\left\langle \xi \middle| (I+S)^{-1} \middle| \theta \right\rangle \equiv \left\langle \xi \middle\| \theta \right\rangle, \qquad \left\langle \xi \middle| (I+S)^{-1} \middle| \theta \right\rangle \left\langle \eta \middle| (I+S)^{-1} \middle| \varsigma \right\rangle \equiv \left\langle \xi\eta \middle\| \theta\varsigma \right\rangle,$$

$$\left\langle \xi \middle| \bar{h} \middle| \xi' \right\rangle = \frac{1}{2} \sum \left\langle \xi \middle\| \theta \right\rangle \left\langle \theta \middle| h \middle| \xi' \right\rangle + \frac{1}{2} \sum \left\langle \xi \middle| h \middle| \theta \right\rangle \left\langle \theta \middle\| \xi' \right\rangle,$$

$$\left\langle \xi\eta \middle| \bar{g} \middle| \xi'\eta' \right\rangle = \frac{1}{2} \sum \left\langle \xi\eta \middle\| \theta\varsigma \right\rangle \left\langle \theta\varsigma \middle| g \middle| \xi'\eta' \right\rangle + \frac{1}{2} \sum \left\langle \xi\eta \middle| g \middle| \theta\varsigma \right\rangle \left\langle \theta\varsigma \middle\| \xi'\eta' \right\rangle,$$

where the operator $Q = \sum a_\xi^+ a_{\xi'} \left\langle \xi \middle| q \middle| \xi' \right\rangle$, $q = \ln(I+S)$, h and g are one-particle and two-particle operators, respectively,

$$\left[Q, \bar{H}\right]^{(n)} \equiv \left[Q, \left[Q, \ldots \left[Q, \bar{H}\right] \ldots\right]\right], \tag{2}$$

where $\left[Q, \bar{H}\right]$ is the commutator and the expression in the right-hand side of (2) denotes n commutators.

Let us consider the operator $q = \ln(I + S)$. Its matrix elements in the case of a convergent logarithmic series may be calculated from

$$\ln(I+S) = S - \frac{S^2}{2} + \frac{S^3}{3} - \ldots \tag{3}$$

It is possible to formally present the left-hand side of equality (3) as an integral

$$\ln(I+S) = S \int_0^1 (I + \alpha S)^{-1} d\alpha \approx S \sum_{i=1}^{N} (I + \alpha_i S)^{-1} \Delta\alpha \tag{4}$$

where $(I + \alpha_i S)^{-1}$ is a matrix reciprocal to the matrix $(I + \alpha_i S)$. However, the expression on the left from the sign of approximate equality is an integral sum of this integral. It exists always when the matrix $(I+S)^{-1}$ exists. It is easy to check by the direct calculation that if the series (3) is convergent, the integral sum in (4) already at $N = 10^6$ and $\Delta\alpha = 10^{-6}$ coincides with (3) with great accuracy. Calculations show that if the series (3) is divergent, the matrix calculated according to (4) exists. For overlap integrals which are sufficiently small the corresponding matrix elements (4) have the same sign and order of magnitude as the values of these integrals. Therefore further the matrix elements of the operator $q = \ln(i+S)$ will be understood in the sense of the equality (4). Thus, in the general case the value of the overlap integrals can be arbitrary.

Let us consider some processes leading to the appearance of the hyperfine fields on the ligand nuclei. The contribution from the transition of the electron to the partially filled central ion shell is found as follows. The operator V_1 corresponding to these processes is written in the secondary-quantization presentation [8]. Then by restricting to the second-order perturbation terms, we get

$$V_1 = \sum a_{\xi}^{+} a_{\xi'} \left[\frac{1}{4} \langle \xi | q | \varsigma \rangle \langle \theta | q | \xi' \rangle - \frac{1}{2} \overline{\gamma}_{\xi\varsigma} \langle \theta || \xi' \rangle - \frac{1}{2} \langle \xi || \varsigma \rangle \overline{\gamma}_{\theta\xi'} + \overline{\gamma}_{\xi\varsigma} \overline{\gamma}_{\theta\xi'} \right] \langle \varsigma | v | \theta \rangle, \qquad (5)$$

where v is the operator of the hyperfine interaction, ξ, η and θ, ς are quantum numbers of the central ion and ligand orbitals, respectively,

$$\overline{\gamma}_{\xi\varsigma} = -\frac{\langle \xi | G | \varsigma \rangle}{\left| \Delta_{\{\xi\},\{\varsigma\}} \right|},$$

$\langle \xi | G | \varsigma \rangle$ is the amplitude of the electron transition from the ligand to the central ion, ς is the ligand orbital, ξ is the central ion orbital, $\left| \Delta_{\{\xi\},\{\varsigma\}} \right|$ is the energy of the transition of the system from the ground state to the excited one.

Let us consider the following third-order process. The electron transfers from the ligand to the valence shell of the central ion. Then the electron of the valence shell is transferred to one of the higher lying orbitals by the electrostatic field of the hole occurring on the ligand (the electron-hole interaction) and returns back. By using the present approach, for the operator V_2 we obtain:

$$\begin{aligned} V_2 = \sum a_{\xi}^{+} a_{\xi'} \frac{\langle \xi | h_{cr} | \varphi \rangle}{\left| \Delta_{\xi\varsigma} \right|} \Bigg[& \frac{1}{4} \langle \varphi || \varsigma \rangle \langle \theta || \xi' \rangle - \frac{1}{2} \langle \varphi || \varsigma \rangle \overline{\gamma}_{\theta\xi'} + \\ & + \frac{1}{2} \overline{\gamma}_{\varphi\varsigma} \langle \theta || \xi' \rangle - \left(1 + \frac{\left| \Delta_{\xi\varsigma} \right|}{\left| \Delta_{\varphi\theta} \right|} \right) \overline{\gamma}_{\varphi\varsigma} \overline{\gamma}_{\theta\xi'} \Bigg] \langle \varsigma | v | \theta \rangle + h.c. \end{aligned} \qquad (6)$$

where ξ, ξ' are the quantum numbers of the valence shell orbitals, φ are the quantum numbers of the orbitals of the higher-lying empty shells, θ, ζ are the quantum numbers of the ligand orbitals, h_{cr} is the operator of the electron-hole interaction.

Let us consider the following process (Далее рассмотрим следующий). The electron form the ligand goes to the higher empty shell of the central ion. As a result of the Coulomb exchange interaction, contributions to the hyperfine field on the ligand from transitions of the electron with spin up differ from those with down. The operator V_3 taking into account contributions from such processes to the superhyperfine constant in the framework of the semi-empirical approach is given in [17]. By using the present approach, for V_3 we obtain

$$V_3 = \sum a_{\xi}^{+} a_{\xi'} \frac{\langle \xi\varphi | g(1-P) | \xi'\varphi' \rangle}{\left| \Delta_{\varphi\varsigma} \right|} \left[\overline{\gamma}_{\varphi'\varsigma} \overline{\gamma}_{\theta\varphi} - \frac{1}{4} \langle \varphi' || \varsigma \rangle \langle \theta || \varphi \rangle \right] \langle \varsigma | v | \theta \rangle + h.c.$$

where ξ, ξ' are quantum numbers of the valence shell orbitals, φ, φ' are quantum numbers of higher empty shell orbitals, θ, ς are quantum numbers of the ligand orbitals, g is the operator of the Coulomb interaction of electrons.

Finally, let us consider another third-order process. The electron goes from the ligand to the valence shell of the central ion. Then the electron-hole interaction transfers the hole on the ligand to the other orbital and electron returns back. This process can be considered as the ligand polarization. By using the present approach, we obtain for the operator V_4

$$V_4 = \sum a_{\xi}^{+} a_{\xi'} \left[\frac{1}{4} \langle \xi \| \varsigma \rangle \langle \theta \| \xi' \rangle - \frac{1}{2} \langle \xi \| \varsigma \rangle \overline{\gamma}_{\theta\xi'} - \frac{1}{2} \overline{\gamma}_{\xi\varsigma} \langle \theta \| \xi' \rangle + \overline{\gamma}_{\xi\varsigma} \overline{\gamma}_{\theta\xi'} \right] \frac{\langle \varsigma | h_{eh} | \lambda \rangle}{|\Delta_{\xi\lambda}|} \langle \lambda | v | \theta \rangle + h.c.$$

where ξ, ξ' are quantum numbers of the valence shell orbitals, θ, ζ, λ are quantum numbers of ligand orbitals. h_{eh} is the operator of the electron-hole interaction. It is obvious that the operator V_4 is the next-order correction to the operator V_1. Unlike V_2, two cases should be considered for V_4. If the valency of the admixture ion is a unit larger than that of the ion of the host crystal, then at the electron transition from the ligand to the central ion the charge symmetry of the ligand environment is restored and the transitions at the ligand forbidden for the host crystal will be forbidden in the considered excited configuration as well, at least in the approximation of the electrostatic field. In the case of the isovalent substitution the charge symmetry of the ligand environment is violated and the transitioins forbidden for the ground configuration may be allowed for the excited one.

We used the basis of 5s-, 5p-, 4f-, 5d-,6s orbitals of the central ion and 2s-, 2p-ligans orbitals.

Contributions to the THFI A_s and A_p parameters (in MHz) for the fluorine ions of the first coordination coordination sphere [12,13]

Crystal		A_d	V_1	V_2	V_3	V_4	V_5	Sum	Exp.
$CsCaF_3$	A_s	0	9.88	4.34	0.68	0	5.18	20.08	20.577
Cs_2NaYF_6						0.9		20.98	22.111
$CsCaF_3$	A_p	- 9.0	2.89	1.38	- 0.95	0	0.62	- 5.06	- 5.963
Cs_2NaYF_6						- 0.8		- 5.86	-6.208

References

[1] B.A. Фок . ZSf **61**, 126 (1930).

[2] Ch. Froese. Canad. J. Phys. **45**, 7 (1967).

[3] A.B. Kunz. Phys. Rev. B **2**, 2224 (1970).

[4] M. Moshinsky, T. H. Seligman, Annals of Phys. **66,** 311 (1971).

[5] E. Artacho, L.M. Bosch, Phys. Rev. A **43,** 5770 (1991).

[6] M. V. Eremin, A. M. Leushin, Physics of the Solid State **16,** 1917 (1974).

[7] M. V. Eremin, A. A. Kornienko, Physics of the Solid State **19,** 3024 (1977).

[8] B. R. Judd, *Second Quantization and Atomic Spectroscopy* (The Johns Hopkins Press Baltimore, 1967), p. 210.

[9] O. A. Anikeenok, M. V. Eremin, M.L. Falin, V. P. Meiklyar, J. Phys. C: Solid State Phys. **15,** 1557 (1982).

[10] O. A. Anikeenok, M. V. Eremin, M.L. Falin, A.L. Konkin, V.P. Meiklyar, J. Phys. C: Solid State Phys. **17,** 2813 (1984).

[11] O. A. Anikeenok, Physics of the Solid State **45,** 854 (2003).

[12] M.L. Falin, O.A. Anikeenok, V.A. Latypov, N.M. Khaidukov, F. Callens, H. Vrielinck, A. Hoefstaetter. Phys. Rev. B **80**, 174110 (2009)

[13] O. A. Anikeenok, Physics of the Solid State **53,** 2326 (2011).

NMR of ^{3}He in porous media

A.V. Klochkov[1], E.M. Alakshin[1], R.R. Gazizulin[1], V.V. Kuzmin[1], K.R. Safiullin[1], M.S. Tagirov[1], A.N. Yudin[2]

[1]Kazan (Volga region) Federal University, 420008, Kremlevskaja 18, Kazan, Russia

[2]Kapitza Institute, 2, ul. Kosygina, Moscow, 119334, Russia

e-mail: klochkov@gmail.com

Nuclear magnetic resonance of ^{3}He in porous media is a fruitful method of obtaining new information about properties of the porous substrates. It was found in [1] that the magnetic relaxation of the nuclear spins of liquid ^{3}He in confined geometry acquires substantially new features as compared to the relaxation in a bulk liquid and new mechanism of magnetic relaxation has been proposed by Naletov et al.

The NMR properties of normal liquid ^{3}He strongly depend on size of volume where ^{3}He is located. The main reason for that is highly effective spin diffusion, which allows seeing space restriction starting from several mm sizes. The nuclear magnetic relaxation of liquid ^{3}He (both T_1 and T_2) takes place by means of fast spin diffusion from liquid ^{3}He to adsorbed ^{3}He and further effective surface relaxation in adsorbed layer of ^{3}He [2-5]. Thus, the longitudinal relaxation time T_1, the transverse relaxation time T_2 and the spectral line width are strongly dependable on size of geometry filled by liquid ^{3}He.

Additionally, the study of spin kinetics of ^{3}He in porous media at low temperatures is in the matter of interest due to direct magnetic coupling between ^{3}He and solid state substrate at a substrate surface. Magnetic dipole interaction between the nuclear spins of liquid ^{3}He and the nuclear spins of a solid substrate was discovered in 1981 between ^{3}He ($\gamma/2\pi$ = 3243 Hz/Oe) and ^{19}F ($\gamma/2\pi$ = 4007 Hz/Oe) nuclei in the adsorbed ^{3}He–polytetrafluoroethylene DLX-6000 system by L.J. Friedman et al [2]. Later, direct magnetic energy transfer trough the ^{3}He - solid state boundary was discovered in several systems, including van Vleck paramagnets TmES and PrF_3 [6, 7].

The main subject of the present work is the study of spin kinetics of ^{3}He in contact with different types of silica aerogels, charcoals, clay minerals and nanosized crystal powders of Van Vleck paramagnet PrF_3.

The spin kinetics of ^{3}He atoms in the silica aerogel was studied above the Fermi temperature of liquid ^{3}He. The magnetic relaxation times T_1 and T_2 for adsorbed, gaseous, and liquid ^{3}He in the 95%-porosity aerogel at a temperature of 1.5 K were obtained by means of pulse nuclear magnetic resonance techniques. It was found that T_1 in all three cases is proportional to the frequency, whereas T_2 is frequency independent. It is shown that the longitudinal relaxation proceeds due to the exchange motion in the solid adsorbed ^{3}He film. The intrinsic relaxation mechanisms in the liquid and gas phases are much weaker than the relaxation through the adsorbed surface layer. Also, the influence on the magnetic relaxation of thermalization processes in the system "^{3}He – aerogel" has been studied [4, 8].

In the case of clay minerals, new method of determination of integral porosity of porous sample by the means of ^{3}He NMR was proposed and tested. Also, using inverse Laplace transform algorithm, the distribution of nuclear magnetic relaxation times of ^{3}He was obtained [9], which can be converted into pore size distribution, using specific models of relaxation.

As a continuation of our works of studying cross-relaxation effects in the system "^{3}He-PrF_3" nanosized crystal powders of PrF_3 were synthesized. Spin kinetics of ^{3}He in the system "PrF_3-^{3}He" was investigated. The model of longitudinal magnetization relaxation of ^{3}He nuclei was proposed. According to this model the longitudinal relaxation of ^{3}He is carried out both by the ^{3}He adsorbed film on the surface and due to the modulation of dipole-dipole interaction in strongly inhomogeneous magnetic field, caused by nanosized PrF_3 particles [10].

The pictures of studied porous samples are on fig.1.

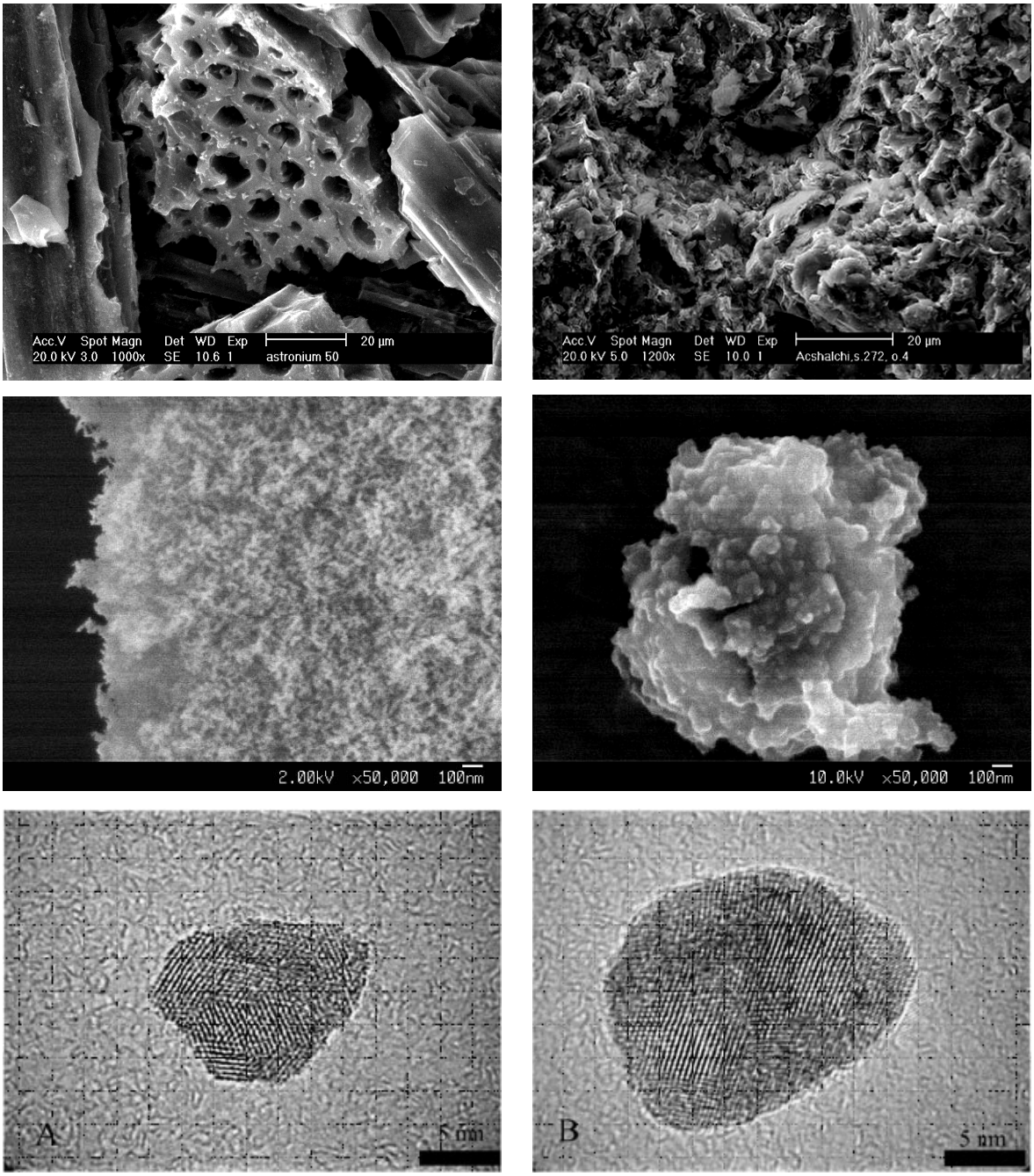

Fig.1. HRTEM images of charcoal "Astronium"(upper left), clay sample (upper right), strand-like silica aerogel (middle left), "powder" aerogel (middle right), nano particles of PrF_3 (bottom left and right).

This work is partially supported by Russian Fund for Basic Research № "12-02-97048-p_povolzhje_a ".

References

[1] Naletov V.V., Tagirov M.S., Tayurskii D.A., Teplov M.A. JETP. **81**, 311 (1995).

[2] L.J. Friedman, P.J. Millet, R.C. Richardson. Phys. Rev. Lett. **47**, 1078 (1981).

[3] L.J. Friedman, T.J. Gramila, R.C. Richardson. J. Low Temp.Phys. **55**, 83 (1984).

[4] A.V. Klochkov, V.V. Kuzmin, K.R. Safiullin, M.S. Tagirov, D.A. Tayurskii, N. Mulders. Pis'ma v ZhETF. **88**, 944 (2008).

[5] Brian P. Cowan. J. Low Temp.Phys. **50**, 135 (1983).

[6] A.V. Egorov et al., JETP Lett. **39**, 584 (1984).

[7] A.V. Egorov et al., JETP Lett., **86**, 416 (2007).

[8] E.M. Alakshin et al., JETP Lett., **93**, 223 (2011).

[9] R.R. Gazizulin et al., Appl. Magn. Resonance., **38**, 271 (2010).

[10] M.S. Tagirov et al., J. Low. Temp. Phys., **162**, 645 (2011).

The use of NMR methods for investigation of new phases in superfluid ^{3}He

V.V. Dmitriev, D.A. Krasnikhin, A.A. Senin, A.N. Yudin

Kapitza Institute, 119334, ul. Kosygina 2, Moscow, Russia

e-mail: alexey-yudin@yandex.ru

The superfluid phases of ^{3}He were studied widely since their discovery in 1972. Remarkable part of these studies was achieved with use of different NMR methods. Since superfluidity of ^{3}He is associated with Cooper pairing of helium atoms into state with orbital moment L=1 and spin moment S=1, it has complex order parameter and rather rich phase diagram at different conditions. Another feature of superfluid ^{3}He is the presence of relatively weak dipole-dipole interaction of the nuclear magnetic moments in a Cooper pair. The influence of this interaction appears as additional rotational torque acting on the magnetization. This influence is reflected in the NMR spectrum, which provides information on the structure of the order parameter. For example in bulk A phase the cw NMR frequency is shifted by $\Delta\omega = \Omega^2_A/(2\omega_L)$ from Larmor frequency ω_L (Ω_A is a characteristic parameter called Leggett frequency of A phase).

An asymmetry of a volume filled by superfluid ^{3}He can influence on resulting pairing states. For example, in the case of a restricted geometry, boundaries of the container can suppress some components of the superfluid order parameter [1]. Theory predicts, that restricted geometry may stabilize superfluid phases which do not occur in bulk liquid ^{3}He [2, 3]. In superfluid ^{3}He inside a narrow gap (or in ^{3}He film) a planar type distortion is expected for the B phase in agreement with results of recent experiments [4].

A spatially inhomogeneous order parameter with polar core may be realized in a narrow channel or in ^{3}He confined in a globally anisotropic aerogel. It is known that the high porosity silica aerogel does not completely suppress the superfluidity of ^{3}He [5, 6]. It is also established that superfluid phases of ^{3}He in aerogel (A-like and B-like phases) are similar to superfluid phases of bulk ^{3}He (A and B phases respectively) if the anisotropy of the aerogel is weak or if it corresponds to the squeezing deformation [7, 8]. In this case the anisotropy of the aerogel influences only on the orientation of the ^{3}He superfluid order parameter and on its spatial structure [9-11]. However, recent theoretical investigations [12] show that the stretching anisotropy of the aerogel should result in a polar distortion of the A-like phase of superfluid ^{3}He in aerogel.

To investigate polar distortion of superfluid ^{3}He “ordered” aerogel is more convenient. This new type of aerogel consists of Al_2O_3 strands which are nearly parallel to each other [13]. The theory predicts that if the anisotropy is large enough then, in some range of temperatures just below the superfluid transition temperature, the pure polar phase may be more favorable than the A phase.

In experiments with superfluid ^{3}He in “ordered” aerogel [14] we observed two superfluid phases: low temperature phase and high temperature phase. NMR properties of the low temperature phase correspond to Balian-Werthamer order parameter which is characterized by temperature dependence of magnetic susceptibility. The origin of the high temperature phase is not yet clear. Spin susceptibility measurements show that this phase belongs to the family of equal spin pairing states. NMR properties of the low temperature phase qualitatively well correspond to both A phase in Larkin-Imry-Ma state and to polar phase: the theory predicts that angular and temperature dependencies of NMR frequency shift are similar for both phases and only absolute values of shift differ. However, the absolute

value of the frequency shift is less than it is expected for the pure polar phase, but greater than it should be for the A phase. It is possible that we observe the polar-like phase with the order parameter suppressed near the aerogel strands.

To detect polar phase of superfluid ^{3}He further experiments with additionally squeezed "ordered" aerogel were carried out. The squeezing leads to changes in Larkin-Imry-Ma state which should have direction of anisotropy in such conditions and its NMR properties change. So A-like phase and polar phase could be separated in such geometry because their NMR properties differ.

Acknowledgments

This work was partly supported by the Grant of the President of Russia (contract 16.120.11.3532-MK) and RFBR (grant 11-02-12069).

References

[1] V. Ambegaokar, P. G. de Gennes, and D. Reiner, Phys. Rev. A **9**, 2676 (1974).
[2] G. Barton and M.A. Moore, J. of Low Temp. Phys. **21**, 75 (1975).
[3] Y. H. Li and T. N. Ho, Phys. Rev. B **38**, 2362 (1988).
[4] L. V. Levitin, R. C. Benett, A. J. Casey et al., J. of Low Temp. Phys. **158**, 159 (2010).
[5] J. V. Porto and J. M. Parpia, Phys. Rev. Lett. **74**, 4667 (1995).
[6] D. T. Sprague, T. M. Haard, J. B. Kycia et al., Phys. Rev. Lett. **75**, 661 (1995).
[7] B. I. Barker, Y. Lee, L. Polukhina et al., Phys. Rev. Lett. **85**, 2148 (2000).
[8] J. Pollanen, J. I. A. Li, C. A. Collett et al., Phys. Rev. Lett. **107**, 195301 (2011).
[9] T. Kunimatsu, T. Sato, K. Izumina et al., JETP Lett. **86**, 216 (2007).
[10] V. V. Dmitriev, D. A. Krasnikhin, N. Mulders et al., JETP Lett. **91**, 599 (2010).
[11] G. E. Volovik, J. of Low Temp. Phys. **150**, 453 (2008).
[12] K. Aoyama and R. Ikeda, Phys. Rev. B **73**, 060504 (2006).
[13] R. Sh. Askhadullin, P. N. Martynov, P. A. Yudintsev et al., J. Phys.: Conf. Ser. **98**, 072012 (2008).
[14] R. Sh. Askhadullin, V. V. Dmitriev, D. A. Krasnikhin et al., JETP Lett. **95**, 326 (2012).

Investigation of cholesterol+model of biological membrane complex by NMR spectroscopy

L.F. Galiullina, D.S. Blokhin, A.V. Aganov, V.V. Klochkov

Kazan (Volga region) Federal University, 420008, Kremlevskaya st., 18, Kazan, Russia.

e-mail: Lejsan.Galiullina@ksu.ru

Introduction

Cholesterol is one of the basic components in cell membranes. It regulates membrane permeability and membrane enzymes activity. Cholesterol is also responsible for cell survival and new cells formation in their division process. Thus cholesterol plays a crucial role in cells biosynthesis and metabolism [1], and generally in organism vital functions.

The capabilities of modern NMR spectroscopy techniques to study the structure and intermolecular interactions in phospholipid membranes are still very limited. NMR technique using nuclear Overhauser effect is the most effective method for such investigations. However, there is a problem in using this technique for phospholipid membrane studies because proton relaxation time of phospholipid aggregates is short relative to NMR time-scale. In addition, cholesterol is poorly soluble in water, and most of phospholipids are not soluble in organic solvents. Therefore, the actual problem is finding the appropriate model systems for investigation by high-resolution NMR spectroscopy.

In contrast to phospholipids, which form bilayers and multilayers in aqueous solutions, sodium dodecyl sulfate molecules can form micelles in solution. Micelles are relatively small spherical aggregates distributed throughout the solution. Hence, SDS is a suitable model system for studying interactions between the various components of cell membranes, particularly cholesterol, and phospholipid membranes [2, 3].

The purpose of this work is to investigate the structure and properties of cholesterol - sodium dodecyl sulfate intermolecular complex in solution using high-resolution NMR spectroscopy modern techniques.

Materials and methods

^{1}H NMR (500,13 MHz) and ^{13}C NMR (125,758 MHz) spectra were recorded on an "Avance II-500" spectrometer (Bruker). The spectrometer operates in the internal ^{2}H resonance stabilization. All spectra were acquired in a 5-mm inverse probe head in 5-mm tubes at temperature 298 (±0.1) K. Sample volume was 500 µl. Chemical shifts (ppm) were internally referenced to the signal of DMSO methoxyl groups (δ ^{1}H 2,5 ppm, δ ^{13}C 39,5 ppm) in all cases. Complete assignments of the ^{1}H and ^{13}C NMR spectra of the title compounds were accomplished by 2D COSY, HSQC and HMBC experiments. Accuracy of ^{1}H and ^{13}C NMR chemical shifts measurement was ±0,01 ppm and ±0,1 ppm respectively. Nuclear Overhauser effect measurements were carried out by selective 1D NOESY experiments [4]. Mixing time values, τ_m, were 0.05, 0.1, 0.15, 0.2, 0.4, 0.6 and 0.8 s.

Results and Discussion

Sodium dodecyl sulfate micelle formation in DMSO+H_2O solution by NMR NOESY spectroscopy data

The initial step of this study was the recording and analysing ^{1}H NMR spectra of SDS in DMSO+H_2O solution at concentrations below (2 g/l) (fig.1) and above (80 g/l) (fig.2) critical micelle concentration.

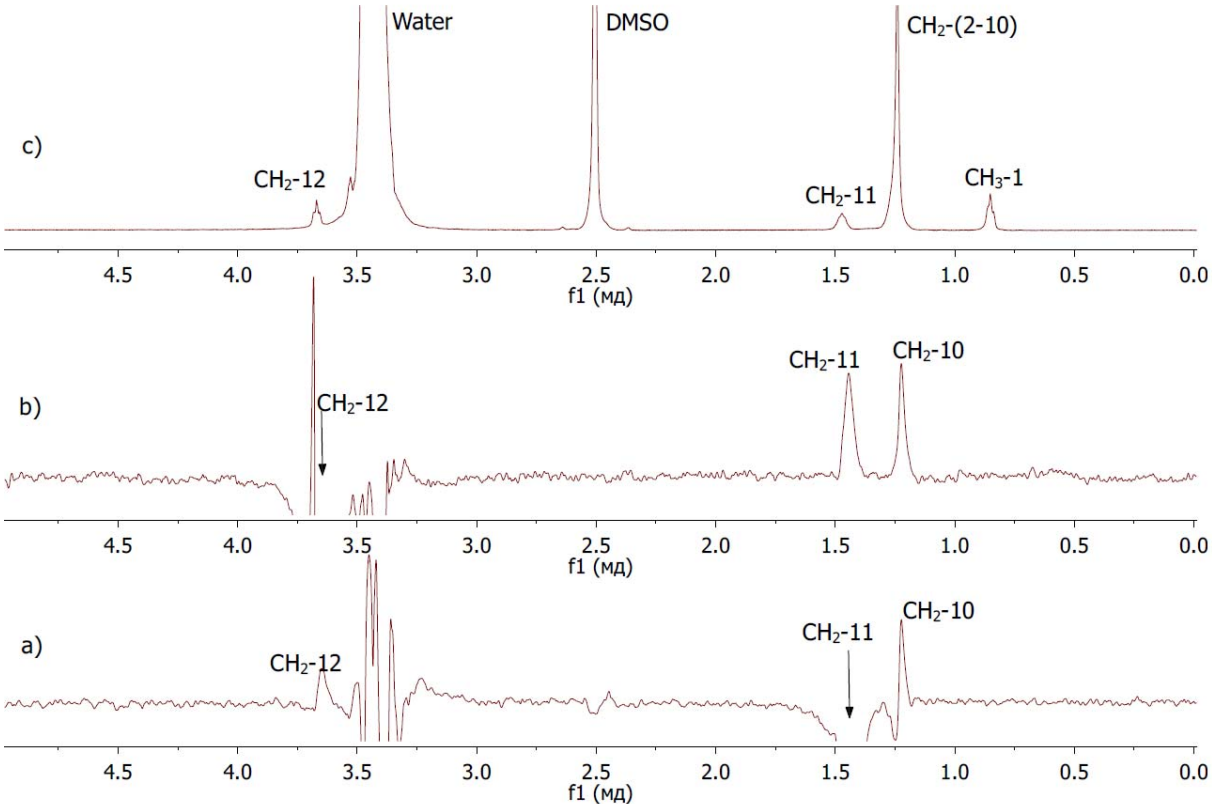

Fig.1. ^{1}H NMR (500,13 MHz) spectrum (c) and selective 1D NOESY spectra (a,b) of SDS in DMSO+H_2O solution at T=298 K (concentration 2 g/l). The arrow shows the signal with the frequency of applied selective RF pulse. Mixing time is τ_M = 400 ms.

The signals of the methyl group CH_3-1, methylene groups CH_2-12 and CH_2-11 are resolved in ^{1}H NMR spectra of SDS(fig.1c and fig.2c). The signals of other functional groups of SDS (CH_2-(2-10)) are represented in the spectrum as one intensive broad signal in 1.2-1.25 ppm region. It can be seen that the chemical shifts of the signals in the spectrum with a higher concentration (80 g/l, fig.2c) differ from the chemical shifts of the signals in solution with a lower concentration (2 g/l, fig.1c). In particular, with concentration increasing low-field shift of CH_2-12 signal is observed (+0.7 ppm). At the same time the signals of CH_2-(2-10) and CH_3-1 are slightly high-field shifted (–0.1 ppm). Such changes in chemical shifts indicate the appearance of intermolecular complexes, which are SDS micelles.

NOESY method is an effective technique to study formation of different intermolecular complexes. It is known that the maximum of observed Overhauser effect depends on the correlation time of molecular motion which is related to the size of molecules [5,6]. Thereby, expected Overhauser effect for the monomeric form of SDS should be positive, and for the micellar form – negative.

At low concentrations of SDS (2 g/l) (fig.1) in NMR selective 1D NOESY spectra of sample irradiated at signal frequency of CH_2-12 group is observed Overhauser effects for the atomic groups CH_2-11 and one of the groups that contribute to the intense signal of CH_2-(2-10). Most likely this is the group CH_2-10, which is closest to the irradiated CH_2-12 group. In 1D NOESY NMR spectrum of the sample irradiated on CH_2-11 signal frequency Overhauser

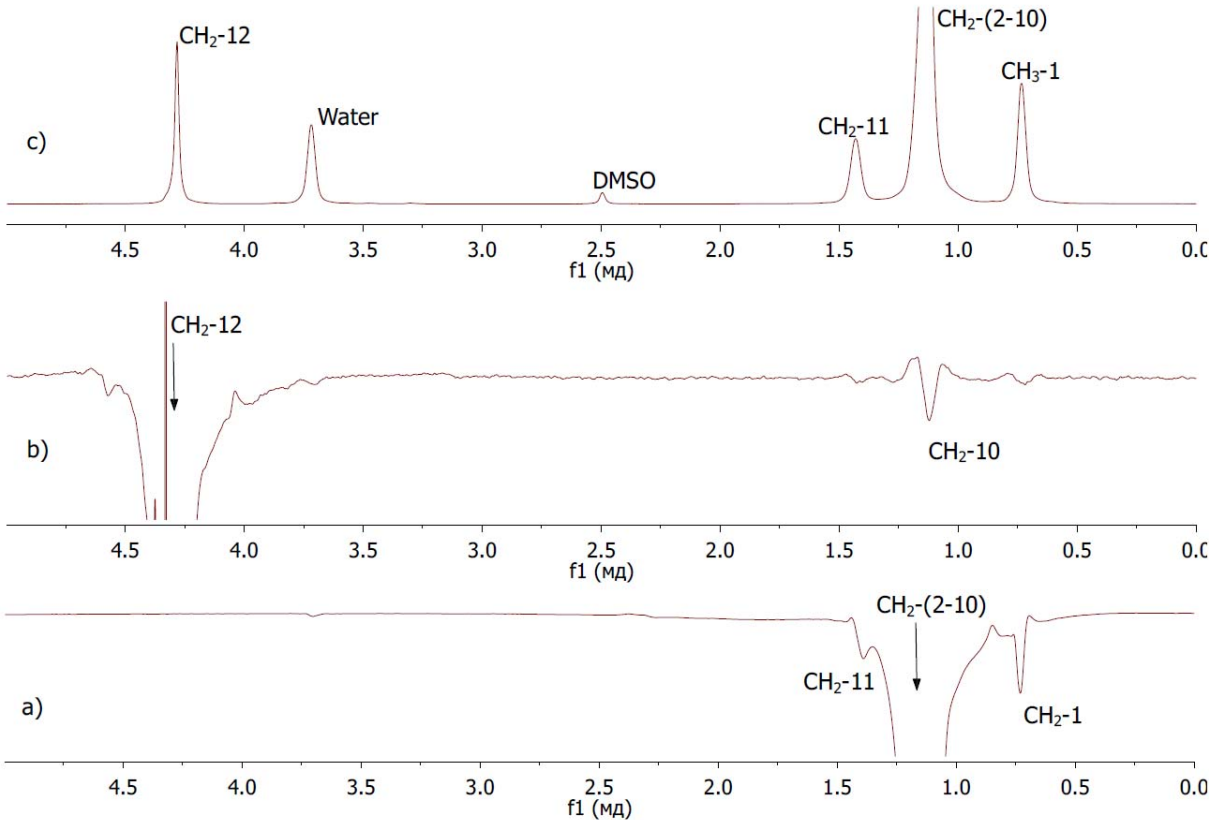

Fig.2. ^{1}H NMR (500,13 MHz) spectrum (c) and selective 1D NOESY spectra (a,b) of SDS in DMSO+H_2O solution at T=298 K (concentration 80 g/l). The arrow shows the signal with the frequency of applied selective RF pulse. Mixing time is $\tau_м$ = 50 ms.

effect is observed for CH_2-10 and CH_2-12 signals. All of the observed Overhauser effects are positive, and thus correspond to small molecules. It means that SDS at this concentration is in a monomeric form. At high concentrations of SDS (80 g/l) (fig.2) in 1D selective NOESY NMR spectra of the sample irradiated on frequency of CH_2-12 group Overhauser effect is observed for CH_2-10 signal. If the sample irradiated on the frequency of intensive signal from CH_2-(2-10) groups, negative Overhauser effect is observed for CH_3-1 and CH_2-11 groups. Negative Overhauser effect is typical for large molecules. Therefore, SDS in solution is presented in micellar form. Dimethylsulfoxide (DMSO) is an aprotic organic solvent. Hence, SDS molecules can form reverse type micelles in DMSO solution [7].

Cholesterol – sodium dodecyl sulfate complex formation in DMSO+H_2O solution by NMR spectroscopy data

The presence of a molecular complex between cholesterol and SDS micelles was established using one-dimensional selective NOESY experiments (fig.3) [4].

In 1D NOESY NMR spectrum of the sample irradiated on OH-group of cholesterol signal frequency Overhauser effect is observed for signals of water, CH_3-1 group of SDS and for the one of aliphatic chain CH_2 groups of SDS molecule. Most likely, it is a signal from the CH_2-2 group of SDS, which is the nearest to the methyl group CH_3-1 of SDS. It means that dipole-dipole interaction between OH-group of cholesterol and «tail» groups of SDS hydrophobic part (fig.3). This indicates spatial proximity of these molecules and the presence of a complex between cholesterol and SDS micelles. Schematic presentation of the complex is shown on fig.4.

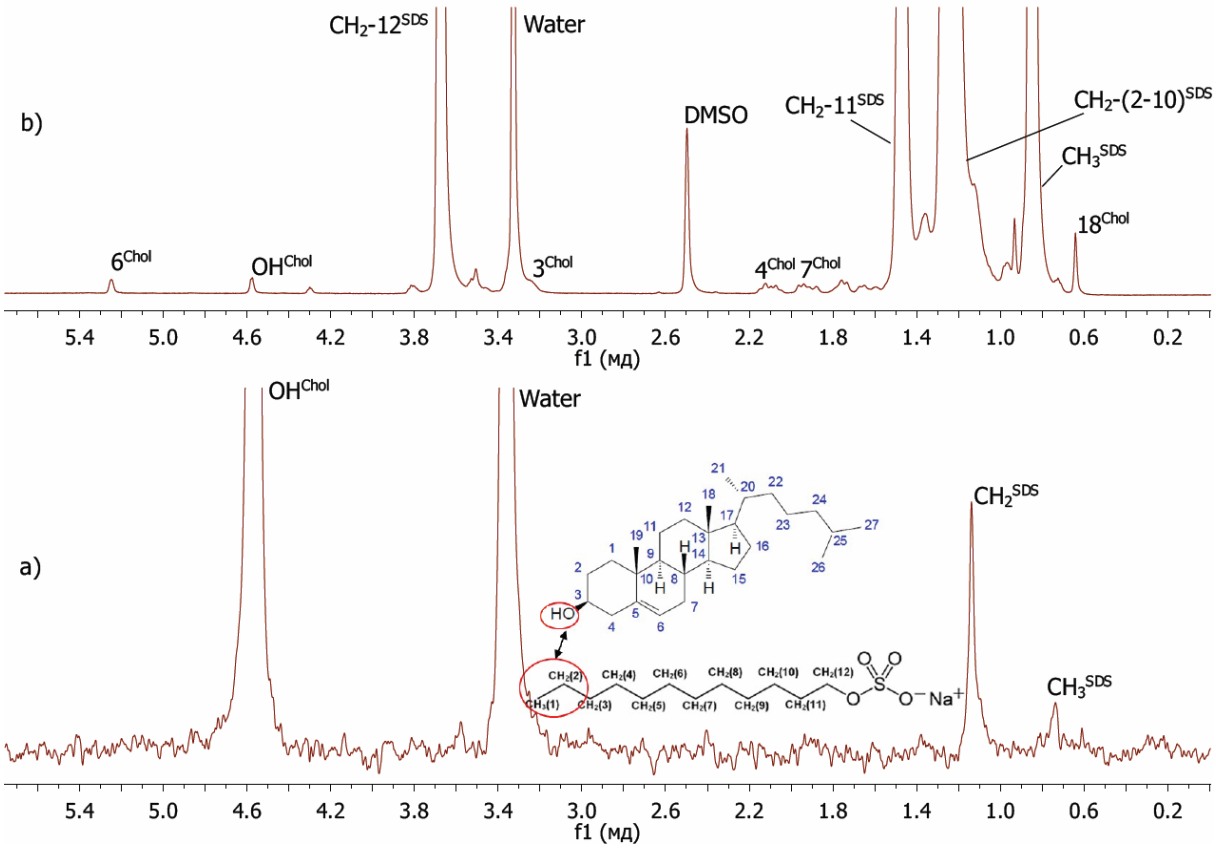

Fig.3. Selective 1D NOESY spectrum (a) and ^{1}H NMR (500,13 MHz) spectrum (b) of cholesterol+SDS mixture in DMSO+H_2O solution at T=298 K. Mixing time is τ_M = 50 ms. Chemical structures of cholesterol and SDS molecules with atom numeration are also shown on the figure. The arrow shows the atoms for which Overhauser effect is observed.

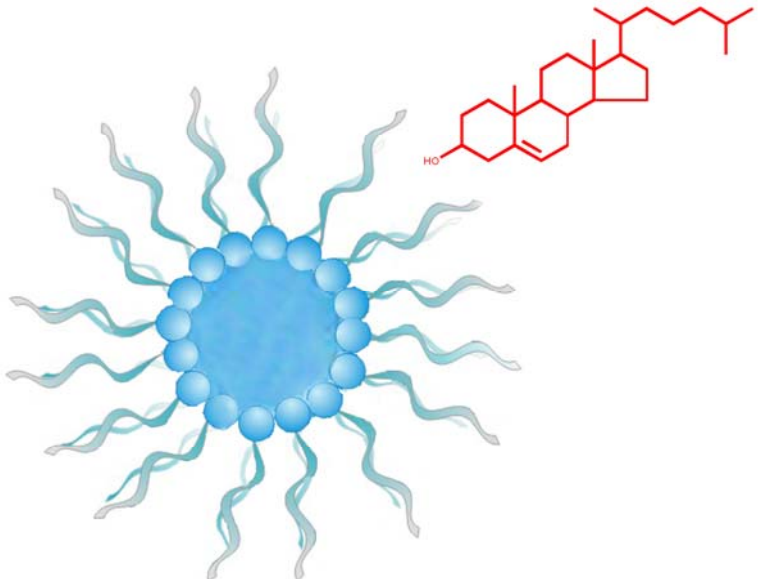

Fig.4. Schematic presentation of the complex between cholesterol and SDS micelles.

This observation is in agreement with the real molecular systems. In the interaction of cholesterol with phospholipid membranes, it penetrates into the space between the hydrophobic "tails" of phospholipid bilayers [8,9]. Thus, the proximity of cholesterol OH-group and “tail” aliphatic groups of SDS is similar to proximity of the same groups of atoms

of cholesterol and aliphatic chains of phospholipid molecules. The only difference is that in phospholipid membranes cholesterol penetrates "deeper" into the space between the hydrophobic "tails" of the phospholipid molecules, but in the model system cholesterol interacts almost exclusively with the surface of the micelles SDS.

Conclusion

The results of NMR experiments showed that sodium dodecyl sulfate aggregates into reversed micelles in DMSO+H_2O solution at concentrations higher than critical micelle concentration. Cholesterol molecules form intermolecular complex with sodium dodecyl sulfate micelles by interaction of the OH group of cholesterol with CH_3-1 and CH_2-2 “tail” aliphatic groups of sodium dodecyl sulfate molecule. This interaction is similar to cholesterol behavior in phospholipid bilayer membranes, where cholesterol penetrates with its cyclic part into space between the hydrophobic "tails" of the phospholipid molecules oriented mostly orthogonal to bilayers.

The work was supported by Federal Program of the Ministry of Education and Science of the Russian Federation (state contract no. 16.552.11.7083) and by Academy of Science of the Republic of Tatarstan (project no. 12-03-97040).

References

[1] Yeagle P.L. Biochim. Biophys. Acta. 1985; 822: 267-87.

[2] Blokhin D.S., Efimov S.V., Klochkov A.V., et al. Appl. Magn. Reson. 2011; 41(2): 267-82.

[3] Henry G.D., Sykes B.D. Methods in Enzymology. 1994; 239: 515-35.

[4] Stonehouse J., Adell P., Keeler J., Shaka A.J. J. Am. Chem. Soc. 1994; 116: 6037-8.

[5] Ernst R.R., Bodenhausen B., Wokaun A. Principles of Nuclear Magnetic Resonance in One and Two Dimensions. Oxford: Oxford University Press; 1987. p. 610.

[6] Gadiev T.A., Khairutdinov B.I., Antipin I.S., Klochkov V.V. Appl. Magn. Reson. 2006; 30(2): 65-73.

[7] Elles Ch.G., Levinger N.E. Chemical Physics Letters. 2000; 317: 624–30.

[8] Robinson A.J.; Richards W.G., Thomas P.J., Hann M.M. Biophysical Journal. 1995; 68: 164-70.

[9] Tiburu E.K., Dave P.C., Lorigan G.A. Magn. Reson. Chem. 2004; 42: 132–8.

The magnon Bose-Einstein condensation in single crystal $CsMnF_3$

E.M. Alakshin[1], Yu.M. Bunkov[1,2], R.R. Gazizulin[1], A.V. Klochkov[1], K.R. Safiullin[1], V.V. Kuzmin[1], R.M. Rakhmatullin[1], A.M. Sabitova[1], T.R. Safin[1], M.S. Tagirov[1]

[1]Kazan Federal University, 420008, Kremlevskya st. 18, Kazan, Russia

[2]Institut Neel, CNRS et Universite Joseph Fourier, F-38042, Grenoble, France

e-mail: g-rasul@yandex.ru

Introduction

The Bose-Einstein condensation (BEC) corresponds to the formation of a collective quantum state in which macroscopic number of particles is governed by a single wave function. The formation of this state was predicted by Einstein in 1925 [1].

The BEC of magnons was discovered experimentally in superfluid phase of ^{3}He-B [2]. Then 6 different states of superfluid ^{3}He with BEC formation were discovered. The review of different experiments on the BEC observation can be found in [3, 4]. In all cases BEC forms on excited non-equilibrium magnons. To excite it the pulse or continuous pumping at nuclear magnetic resonance (NMR) frequency was used.

In [5] it was assumed that the BEC formation is also possible in solid antiferromagnets $CsMnF_3$ and $MnCO_3$. In these antiferromagnets the hyperfine interaction of manganese atoms leads to strong polarization of ^{55}Mn nuclei, so its precession frequency is order of 600 MHz. This frequency is comparable with low frequency mode of antiferromagnetic resonance (AFMR) in low external magnetic field. As a result, there is the coupled nuclear-electron precession with the dynamical frequency shift (pulling). From experiments carried out with ^{3}He it is clear that the magnon BEC formation is the consequence of analogous frequency shift, that is why the attempt to observe the magnons BEC formation in antiferromagnets $CsMnF_3$ and $MnCO_3$ was a prospective task.

We report here the experimental confirmation of magnon BEC in easy-plain antiferromagnet $CsMnF_3$.

Resonator

For NMR studying at frequencies 500 – 600 MHz the traditionally used in resonators radio-frequency (RF) solenoidal coils cannot provide the necessary Q-factor and the sufficient filling factor. That is why it was offered to use the split-ring (loop-gap) resonator [6, 7].

The samples were placed in the split-ring resonator (fig.1) to the maximum of the magnetic field. The experimentally determined quality factor of the resonator was $Q \approx 150$ at the temperature 1.5 K. Irradiation of the resonator and signal detection were performed using ring antennas, matched with the cavity for 50 Ohm. The matching was achieved by adjusting the optimal antennas radius and the optimal distance between antennas and the resonator.

The samples volume was a few mm^3, the resonator volume was $V \approx 308$ mm^3. The antennas diameter was about 5 mm, the distance between antenna and resonator was about 4.5 mm.

The magnetic component of the RF field, created by ring antenna, was polarized along the resonator axis. The amplitude of the magnetic component is described well by

$$H_1^2 \approx \frac{8\pi QP}{fV}, \qquad (1)$$

where P — supplied RF power, f — frequency of the resonator, V — volume of the resonator ($V \approx 308$ mm^3), Q — quality factor of the resonator. In our experiments the supplied RF power was 40 mW, as a result, at resonant frequency 566 MHz the RF field amplitude was about 3 Oe which corresponds to the 300 kHz in frequency units.

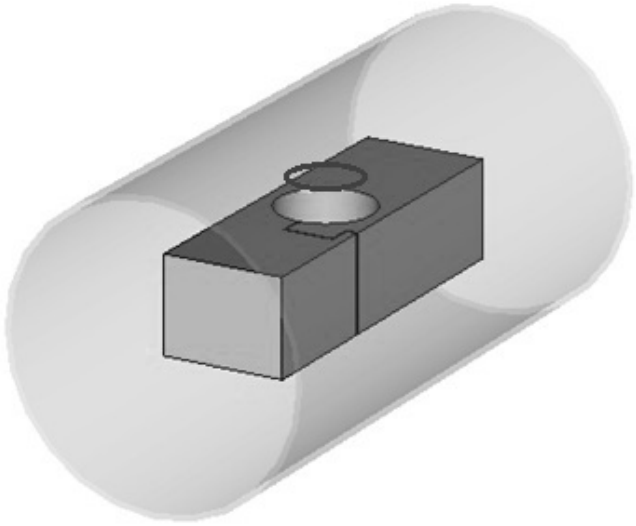

Fig.1. The split-ring resonator

The accurate calculations of the electromagnetic fields were done by using CST Microwave Studio. The Transient Solver in standard settings was used for finding the resonance, the parameters of the scattering matrix S_{11} and the structures of the electromagnetic fields. The condition of the critical link was determined by changing the values of S_{11} and Arg(S_{11}) as a function of the distance between antenna and resonator. The losses in resonator walls and dielectric material in the gap was considered in calculations. The electric properties of the materials were taken from the library in CST Microwave Studio. The material of the resonator is cooper, the dielectric material in the gap is the pyrex glass with the specially selected value of the loss tangent. It was assumed that the electrostatic shield was the ideal conductor without losses because the change the screen material to the copper with losses considering did not lead to the significant changing of the results.

The frequency range in the calculations was from 300 MHz to 1500 MHz. The calculated value of the resonant frequency was 559.2 MHz which is in good agreement with measured value of 560 MHz. The calculated quality factor 173 is also in good agreement with measured value of 150. If the input generator power was 100 mW then the magnetic field amplitude in the rotating frame was 0.5 Oe which agrees well with calculations by (1).

Results and discussion

The magnon BEC was observed under continuous wave NMR conditions in $CsMnF_3$ single crystal [8, 9]. On the analogy of earlier experiments with liquid ^{3}He-A [10] it was also necessary to investigate the free induction decay (FID) for the strong confirmation of the magnons BEC in our substrates. For this reason the modified equipment (fig.2) was built up.

The experiments were carried out at the temperature of 1.5 K. The external magnetic field was about 450 mT. The RF signal from the generator Rohde&Schwarz SML01 was applied to input A of the multiplier AD834. Programmed by PC the Pulse Blaster PB16-32k, SpinCore Technologies Inc., was connected to the input B. As a result, in output C of the multiplier we had the video pulses the filling frequency of which was adjusted by the generator Rohde&Schwarz SML01. After amplifying by the Rohde&Schwarz BBA100-C125

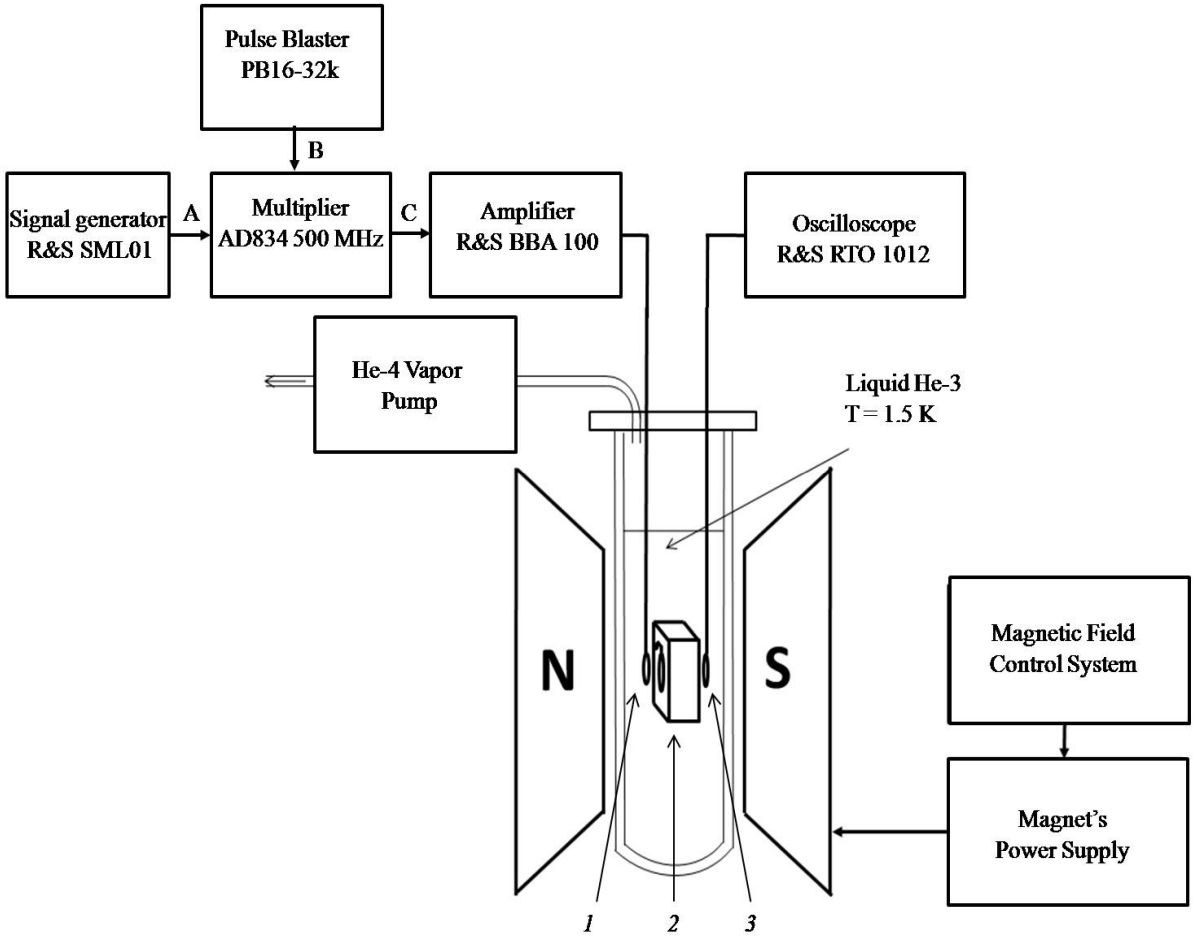

Fig.2. The scheme of spectrometer for NMR measuring by pulse radiation (*1*, *3* – ring antennas, *2* – resonator)

amplifier the video pulse was applied to the loop antenna and excited the spin system. The response of the spin system was observed on the digital oscilloscope Rohde&Schwarz RTO1012 at the NMR frequency.

In fig.3 the amplitude of FID after a long 10 s pulse is shown as a function of magnetic field. A larger initial frequency difference enlarges the FID, whose amplitude corresponded

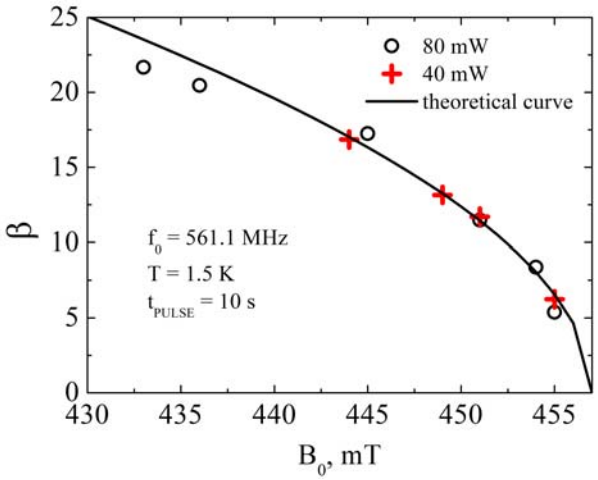

Fig.3. The amplitude of FID after a 10 s pulse as a function of the external magnetic field for two different rf field energies. The solid line shows the theoretical curve which corresponds to the conditions of BEC formation.

well to the angel β for the conditions of BEC formation on a given frequency and field [11].

The samples are inhomogeneous. The characteristic inhomogeneity frequency is about 2 MHz, which is much smaller than the pulling frequency. In this case, the nuclear spins should precess coherently only on a scale of the approximate interaction radius. The effective intensity of the rf field was only about 300 kHz and cannot suppress the inhomogeneity on a long distance. Nevertheless, we observed the FID signal whose amplitude corresponds to a homogeneous precession of full magnetization, deflected on the angle β in complete agreement with the theory of magnon BEC (fig.3).

Acknowledgements

We are grateful to Rene Tschaggellar (ETH, Zurich) for calculations of the electromagnetic fields in resonator. This work is partly supported by the Ministry of Education and Science of the Russian Federation (project no. 13.G25.31.0025).

References

[1] S. Giorgini, L.P. Pitaevskii, and S. Stringari, Rev. Mod. Phys., **80**, 1215 (2008).

[2] A.S. Borovik-Romanov, et al., JETP Letters, **40**, 1033 (1984).

[3] Yu.M. Bunkov and G.Volovik, J. Phys: Condens. Matter, **22**, 164210 (2010).

[4] Yu.M. Bunkov, Progress of Low Temperature Physics, **14**, 68, ed. by W.P. Halperin, Elsevier Science B.V., Amsterdam (1995).

[5] Yu.M. Bunkov, Phys. Usp., **180**, 884 (2010).

[6] B.S. Dumesh, Prib.Tekh. Eksp. **1**, 135 (1986).

[7] W.N. Hardy and L.A. Whitehead, Rev. Sci. Instrum., **52**, 213 (1981).

[8] Yu.M. Bunkov, E.M. Alakshin, R.R. Gazizulin, et al., JETP Letters, **94**, 68 (2011).

[9] Yu.M. Bunkov, E.M. Alakshin, R.R. Gazizulin, et al., J. Phys: Conf. Series, **324**, 012006 (2011).

[10] P. Hunger, Yu.M. Bunkov, E. Collin, H. Godfrin. J. of Low Temp. Phys., **158**, 129 (2010).

[11] Yu.M. Bunkov, E.M. Alakshin, R.R. Gazizulin, et al., Phys. Rev. Lett., **108**, 177002 (2012)

Methods to control formation of micellar systems of sodium dodecyl sulfate in solution

D.S. Blokhin, V.V. Klochkov

Kazan (Volga region) Federal University, 420008, Kremlevskaya st., 18, Kazan, Russia.

e-mail: dblohin@ksu.ru

Introduction

Proteins play a critical role in nature. The unique conformation of a protein's spatial structure determines its properties, particularly, its biological activity. In some cases, the spatial structure and features of a protein can be studied efficiently by using short protein fragments, or oligopeptides. Understanding the spatial structure of oligopeptides in solution is of great value. However, most biochemical processes occur on membrane cell surfaces, so describing and comparing oligopeptide spatial structures in solution and in a protein–membrane surface complex are important to understand fundamentally the biochemical processes occurring on the cell surface [1 – 4].

In studies of protein complexes with membrane surface, micelles of surfactants or small phospholipid vesicles serve as model membranes [5, 6].

Medium, which most closely matches the native lipid bilayer, is composed of phospholipid vesicles, the minimum particle size of 250-300 Å in diameter. Particles of this size have a large rotational correlation time, which leads to a short value transverse relaxation times T_2 and decrease the quality of informative 2D NMR experiments (TOCSY, HSQC, HMBC, NOESY), which are required to assign the resonance signals and to determine the spatial structure of proteins in complex [7 – 9].

It is known that a good model of the membrane surface suitable for structural studies by NMR spectroscopy is micelles or micellar system [10 – 12]. Micellar systems of sodium dodecyl sulfate (SDS) are formed in water at a minimum concentration of 8.1 mM [5]. The majority of proteins associate with SDS micelles in a weight ratio (1.4 g SDS and 1g protein) [8]. SDS micelles can be used to model the behavior of proteins in biological membranes by using small hydrophobic proteins forming complexes directly with the SDS micelle. Note that synthetic SDS micelles, as many biological membranes, possess a negative surface charge. The magnitude of the charge depends on the critical micelle concentration of. The presence of salt (NaCl for SDS systems) in solution can facilitate forming micelles at lower concentrations of SDS [5].

Changing conditions for the sample (temperature, concentration of the solution components) during the 2D NOESY NMR experiments for determination of interproton distances in oligopeptides in a protein–micelle complex requires constant monitoring of the existence of sodium dodecyl sulfate in the form of micelles. This paper described the original methods to control formation of micellar systems of sodium dodecyl sulfate in solution by 1D and 2D NMR spectroscopy.

Experimental

^{1}H NMR (500 MHz) spectra of SDS in water solution were recorded on an AVANCE II-500 spectrometer (Bruker). The spectrometer operates with the internal ^{2}H resonance stabilization. ^{1}H NMR spectra were recorded using 90° pulses and a delay between pulses of 2 s, with a spectral width of SW=9.40 ppm, and the number of scans ≥10.

The repetition time between subsequent runs of the NOESY sequence was at least three times longer than the mean SDS proton T_1. The spectra were recorded in a phase-sensitive mode with 1,024 points in the F2 direction and 256 points in the F1 direction. Exponential filtration was applied in both directions. Mixing time values, τ_m, were 0.15 and 0.30 s.

Results and Discussion

An adequate description of the formation of micellar systems based on surfactants in solution by various physical and chemical methods, including NMR spectroscopy, even today remains an actual problem [13]. Authors of [13] carried out research and analyzed the relationship between the concentration of sodium dodecyl sulfate (fig.1) in water and changes in proton chemical shifts of the surfactant.

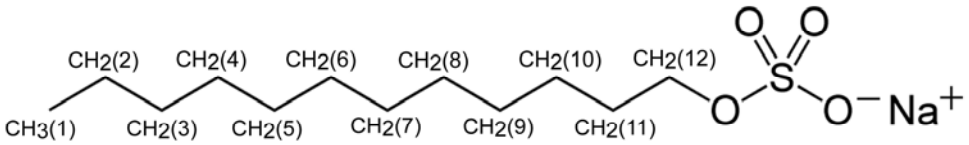

Fig.1. Structural formula of sodium dodecyl sulfate

Controlling formation of micellar systems of sodium dodecyl sulfate in solution by ^1H NMR spectroscopy.

It is well known that change in the concentration of sodium dodecyl sulfate (fig.1) in water leads to a change in chemical shifts of the surfactant protons. Unlike the authors of [13], we considered change in the difference (Δδ, ppm) between proton chemical shifts of the methylene group CH_2 (12) and the methyl group CH_3 (1) in the ^1H NMR spectra (fig.2) as a function of SDS concentration in water, which allowed us to register these changes more accurately.

Fig.2 shows the ^1H NMR spectra of sodium dodecyl sulfate at different concentrations in water solution (NMR signal assignment of the respective groups of protons was made based on the shape and intensity of the signals). As follows from fig.2, ^1H NMR signals shift with changing SDS concentration; this can be explained from the point of view of rapid

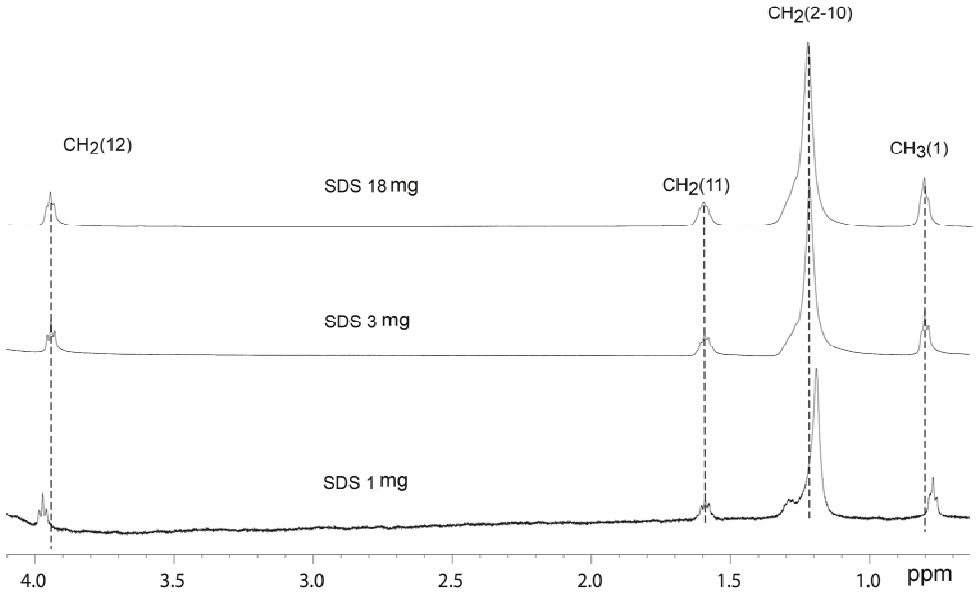

Fig.2. ^1H NMR (500 MHz) spectra of SDS in water solution (0.700 ml H_2O+D_2O (90%+10%)) with different content of SDS. T 298 K

chemical exchange between monomers and micellar form of SDS. Consider in more detail dependence of the difference (Δδ, ppm) between proton chemical shifts of the methylene group CH_2 (12) (fig.2) and the methyl group CH_3 (1) on the concentration of SDS in water solution, which is presented in fig.3. Basing on fig.3, one can say that when SDS concentration in the solution is less than 1.4 g/l, sodium dodecyl sulfate exists in monomeric form; in the concentration range from 1.4 to 4.3 g/l, solution contains both monomeric and micellar forms; and at SDS concentrations exceeding 4.3 g/l, only micellar form exists in the solution, which statement is proved by the invariability of the difference between proton chemical shifts of the considered methylene and methyl groups. Thus, the difference between

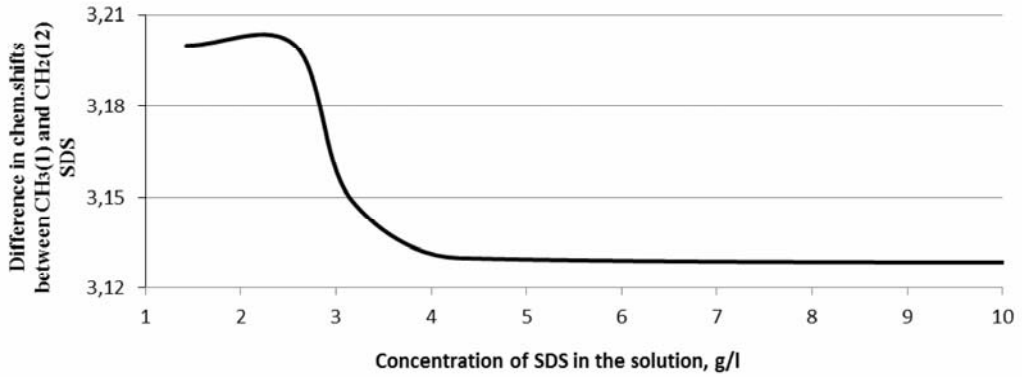

Fig.3. The dependence of the difference between the chemical shifts of CH_3 (1) and CH_2 (12) groups of sodium dodecyl sulfate on SDS concentration in water.

the chemical shifts of the protons of the methylene group CH_2 (12) and the methyl group CH_3 (Δδ, ppm), which equals 3.20 ppm, indicates that SDS exists in monomeric form; whereas Δδ = 3.13 ppm indicates that the solution contains only micellar form of SDS.

Controlling formation of sodium dodecyl sulfate micelles in solution by 2D NOESY NMR spectroscopy.

This method of determination is based on the difference in the intensity and signs of cross-peaks in 2D NOESY NMR spectra of sodium dodecyl sulfate in monomeric and micellar forms. As was already noted, relatively small molecules have weak-intensity cross-peaks in the NOESY NMR spectra, and integral intensities of cross-peaks are negative relative to the intensity of diagonal peaks, which is confirmed in the fig.4a.

Increasing the concentration of SDS in water solution leads to the formation of micellar systems, which are in rapid exchange with the monomeric structures. The critical micelle concentration of surfactants is the concentration of surfactant in the solution, at which the system forms stable micelles. In water solution, the micelles behave as globular proteins. They contain 60 monomer molecules, the particles of this size have a relatively small rotational correlation time ($\tau_c \sim 5\times10^{-8}$ seconds) [5]. The latter leads to intensive cross-peaks of the same sign as the signals of diagonal peaks in the NOESY NMR spectra of SDS in micellar form (fig.4b).

Thus, two NMR methods to control the existence of sodium dodecyl sulfate in the form of micelles may be implemented when performing 2D NOESY NMR experiments for determination of interproton distances in oligopeptides in a peptide–micelle complex.

The work was supported by the Federal Program of the Ministry of Education and Science of the Russian Federation (state contract no. 16.552.11.7083) and by the Academy of Science of the Republic of Tatarstan (project no. 12-03-97040).

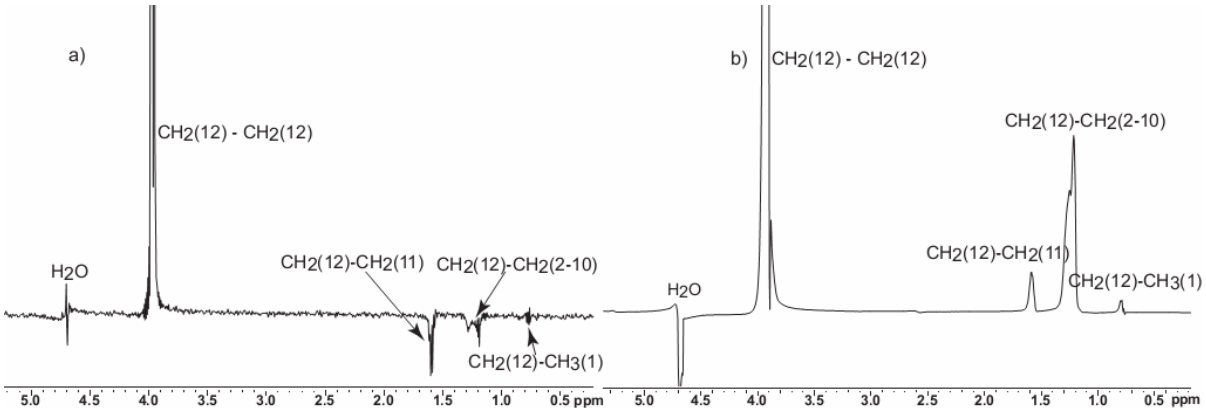

Fig.4. Projection of 2D NOESY NMR spectra of sodium dodecyl sulfate along the frequency corresponding to δ = 3.93 ppm (chemical shift of the methylene protons of CH_2 (12)) in water solution: a) the concentration of SDS in water solution is 2.2 g/l; b) the concentration of SDS in water solution is 7.5 g/l.

References

[1] Boman H.G. Annu. Rev. Immunol., 1995;13: 61-92.

[2] Zasloff M. Nature, 2002; 415: 389–395.

[3] Wang, Z., Wang G. Nucleic Acids Res**.,** 2004; 32: 590–592.

[4] Epand R.M., Vogel H.J. Biochim. Biophys. Acta, 1999; 1462**:** 11–28.

[5] Henry G.D., Sykes B.D. Methods in Enzymology, 1994; 239: 515-535.

[6] Wang G., Keifer P., Peterkofsky A. Protein Science, 2003; 12: 1087–1096.

[7] Ernst R.R., Bodenhausen B., Wokaun A. Principles of Nuclear Magnetic Resonance in One and Two Dimensions. – Oxford : Clarendon Press, 1987., 610 p.

[8] Van de Ven F.J.M., Frank J.M. Multidimensional NMR in liquids: basic principles andexperimental methods. – N.-Y.; Toronto: Wiley-VCH, 1995, 399 p.

[9] Berger S., Braun S. 200 and More NMR Experiments. – Weinheim: Wiley-VCH, 2004, 810 p.

[10] Lee K.H., Fitton J.E., Wüthrich K. Biochimica et Biophysica Acta, 1987; 911: 144-153.

[11] Inagaki F., Shimada I., Kawaguchi K., Hirano M., Teresawa I., Ikura T., and Go N. Biochemistry, 1989; 28: 5985-5991.

[12] Malikayil J.A., Edwards J.V. and McLean L.R**.** Biochemistry, 1992; 31: 7043-7049.

[13] Al-Soufi W., Pineiro L., Novo M. Journal of Colloid and Interface Science, 2012; 370: 102-110.

Superparamagnetic properties in hole doped manganites

K.R. Sharipov, R.M. Eremina, L.V. Mingalieva

[1]E.K. Zavoisky Physical-Technical Institute, 420029 Kazan, Russia

e-mail: Kamil.Sharipov@ksu.ru

Hole doped manganites of the general composition $Ln_{1-x}A_xMnO_3$, where Ln denotes a trivalent rare-earth ion and A a divalent alkaline earth metal like Ca, Sr or Ba, exhibit complex phase diagrams due to competing spin, orbital, charge, and lattice degrees of freedom. Besides orbital order, charge order, and complex magnetic structures, the colossal magneto resistance effect [1, 2] and the existence of electronic phase separation [3, 4] are the most intensely investigated phenomena in this class of materials. This transition from a paramagnetic insulating to a ferromagnetic metallic state basically results from the competition of antiferromagnetic superexchange and ferromagnetic double-exchange interactions [5 – 7].

The issue of phase separation in magnetic semiconductors is the subject of many theoretical and experimental works. Already 40 years ago, Nagaev [8] studied the inhomogeneous ferro-antiferromagnetic state in magnetic semiconductors and introduced the concept of " ferron" - a magnetic polaron, which is a ferromagnetic droplet with a size of about 1-2 nm, arising in an antiferromagnetic semiconductor due to localization of charge carriers introduced by doping the semiconductor. At the same time Krivoglaz suggested the possible formation of ferromagnetically correlated regions in the paramagnetic phase of magnetic semiconductors, when an electron is captured by a ferromagnetic fluctuation of local spins [9]. He called such a quasiparticle consisting of an electron, polarizing the surrounding local core spins as magnetic fluctuon. Later on, Kagan and Kugel [10] termed such quasi particles as "high temperature" ferrons.

Kugel *et al*. [11] explain the transport and magnetic properties of manganites of various compositions assuming the existence of ferromagnetically correlated regions in the paramagnetic phase. According to their estimates, the size of ferromagnetically correlated regions (FM droplets) is about 30 Å. In a recent study of magnetic and transport properties of $Nd_{0.52}Sr_{0.48}MnO_3$ films of different thicknesses, it was found that the films are phase-separated and are composed of magnetic clusters (droplets) in an electrically insulating paramagnetic (at $T > T_N$), or antiferromagnetic (at $T < T_N$) matrix [12]. In the same paper it has been suggested that the ferromagnetic clusters in a magnetic field of 1 T and above can decay into smaller areas, consisting of magnetic polarons of small radius of the order of 1 – 2 nm.

Electron spin resonance turned out to be very sensitive to the formation of ferromagnetic regions in the paramagnetic phase, as has been reported e.g. for $La_{1-x}Sr_xMnO_3$ in the regime $0.075 < x < 0.175$, where weak, strongly anisotropic ferromagnetic resonance (FMR) lines appear besides the paramagnetic resonance line at $g \approx 2$ already below 270 K far above the magnetic ordering temperature [3]. The nature of these ferromagnetic resonances can be explained in terms of a Griffiths phase arising due to the presence of correlated quenched disorder in the orthorhombic cooperative Jahn-Teller phase. As soon as the cooperative Jahn-Teller effect is suppressed, the quenched disorder is lifted and the FMR lines disappear.

We assume that ferromagnetically correlated regions in the paramagnetic phase should have a similar effect on the paramagnetic resonance spectrum like superparamagnetic

particles [13, 14]. We investigated the zinc-doped lanthanum-strontium manganites. Substitution of manganese divalent cations Zn^{2+} leads to an in crease in the content of Mn^{4+} and simultaneously to decrease the concentration of Mn^{3+}. Ions Zn^{2+}, with electronic configuration $3d^{10}$, do not participate in the exchange interaction [15], resulting in an increasing tendency to charge localization and reduced mobility of the carriers. Substitution with zinc ions in the studied manganites can form single-domain ferromagnetic correlated region, the magnetic properties of which can be studied by electron magnetic resonance.

The ESR measurements were performed on a Bruker ER 200 SRC (EMX/plus) spectrometer at X-band frequency. The temperature was controlled in the temperature range from 100 K to 340 K using a Bruker nitrogen- evaporation cryostat. We investigated $La_{1-x}Sr_xMn_{1-y}Zn_yO_3$ ($0.045 \le x \le 0.165$; $0.025 \le y \le 0.125$) and $La_{1-x}Ba_xMn_{1-y}Zn_yO_3$ ($0.045 \le x \le 0.145$; $0.025 \le y \le 0.125$) samples. For the microwave field with a frequency of 9 GHz the skin depth is comparable to the size of the samples 1 mm) in the experimental temperature range. To eliminate the influence of the skin effect on the shape of the ESR, the ceramic samples were powdered and mixed with NaCl.

For all samples the ESR spectrum consists of an exchange-narrowed Lorentzian line in the temperature range under consideration. Fig.1 illustrates the temperature dependence of integral intensity in inverse representation for $La_{0.835}Sr_{0.165}Mn_{0.975}Zn_{0.025}O_3$. Fig.2 illustrates the temperature dependence of the magnetic resonance field H_{RES} for $La_{0.835}Sr_{0.165}Mn_{0.975}Zn_{0.025}O_3$. By linear extrapolation of the high-temperature inverse of the

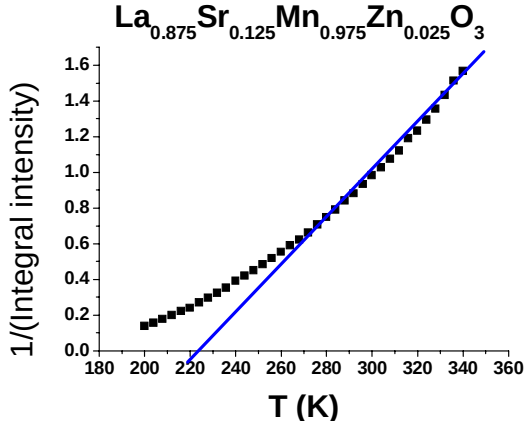

Fig.1. Temperature dependence of the inverse ESR intensity in $La_{0.835}Sr_{0.165}Mn_{0.975}Zn_{0.025}O_3$

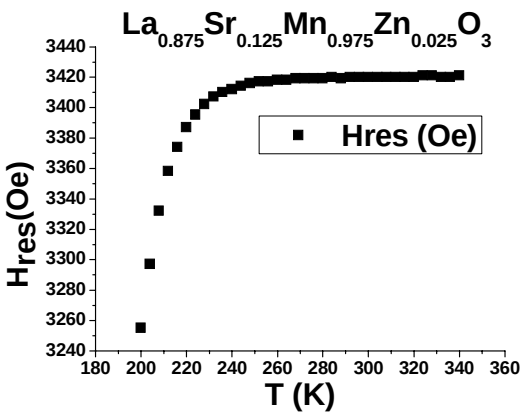

Fig.2. Temperature dependence of the resonance field in $La_{0.835}Sr_{0.165}Mn_{0.975}Zn_{0.025}O_3$

integrated intensity of 1/I(T) to zero (fig.1), we can evaluate the Curie-Weiss temperature. Above 270 K the intensity follows a Curie-Weiss law with a Curie-Weiss temperature of Θ_{cw} ~ 220 K. For all samples, the resonance magnetic fields are independent of temperature in the range from 350 down to 230 K, and the value of the effective g-factor is $g \approx 1.98$. Temperature dependence of the magnetic resonance linewidths in $La_{1-x}Sr_xMn_{1-y}Zn_yO_3$ ($0.045 \le x \le 0.165$; $0.025 \le y \le 0.125$) are shown in fig.3. We believe that the temperature dependence of the resonance fields and linewidths of the electronic magnetic resonance in $La_{1-x}Sr_xMn_{0.925}Zn_{0.075}O_3$ are similar behavior for superparamagnetic particles which were described in [13, 14]. For superparamagnetic particles two mechanisms of the absorption line broadening exist, both induced by fluctuational motion of the partical magnetic moments, but with different temperature behaviors. The nonhomogenious mechanism, associated with the spread of directions of anisotropy axes, saturates at high temperature, where the orientational fluctuations of the magnetic moment of ferromagnetically correlated regions dominates (fig.3,

fig.4). To approximate the temperature dependence of the linewidth the theory of J.L. Raikher

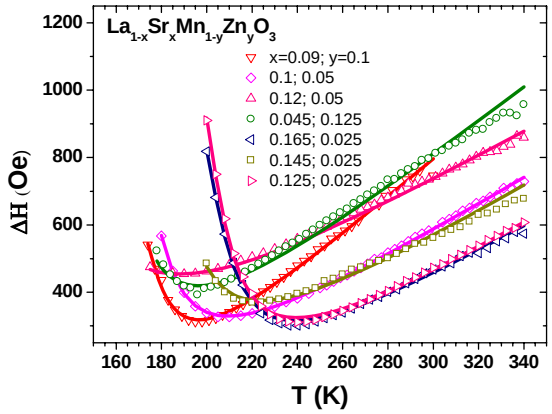

Fig.3. Temperature dependence of the linewidth in $La_{1-x}Sr_xMn_{1-y}Zn_yO_3$ compound

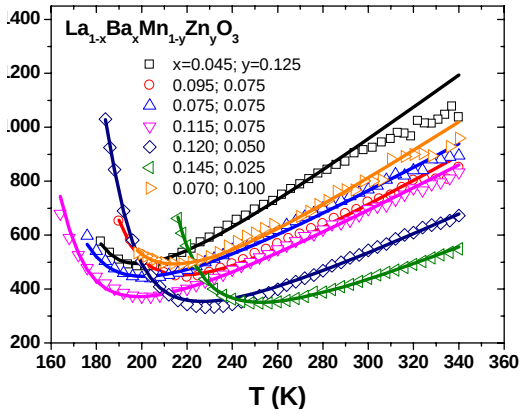

Fig.4. Temperature dependence of the linewidth in $La_{1-x}Ba_xMn_{1-y}Zn_yO_3$ compound

and V.I. Stepanov was used, published in a series of papers, eg [13, 14], in which theoretical expressions are obtained for the temperature dependence of the magnetic resonance linewidth of an ensemble of superparamagnetic particles with uniaxial anisotropy:

$$\Delta H = \Delta H_S + \Delta H_U , \tag{1}$$

$$\Delta H_S = \frac{2\alpha}{\sqrt{3}} H_0 \frac{\xi_0 - L_1}{\xi_0 L_1}, \quad \text{with} \quad \xi_0 = \frac{MH_0}{k_B T} \tag{2}$$

$$\Delta H_U = 3\sigma H_0 \frac{\xi_0 - 3L_1}{\xi_0^2 L_1}, \quad \text{with} \quad \sigma = \frac{W_A}{k_B T} \tag{3}$$

with external magnetic field H_0, magnetic moment of the superparamagnetic particles M, Langevin function $L_1 = \coth \xi_0 - 1/\xi_0$, damping parameter α and anisotropy energy of the superparamagnetic particles W_A.

We take into account the magnetic ordering temperature T_m, by changing $T \to T - T_m$ [12].

The analysis of the temperature dependence of the magnetic resonance linewidths, based on theory of Raikher and Stepanov [13, 14] for superparamagnetic particles, allowed to estimate size of ferromagnetically correlated regions and the value of the magnetic anisotropy. From fitting we found that magnetic moments of the ferromagnetic correlated region of all samples practically are equal $\mu = (175\pm4)\ \mu_B$; anisotropy energy $W_a = 3 \pm 1$ K; the dissipation coefficient $\alpha = 0.025\pm0.004$; ordering temperature depending for samples, for example, $T^* = 141$ K, 138 K, 145 K for x = 0.075, 0.095, 0.115 in $La_{1-x}Sr_xMn_{0.925}Zn_{0.075}O_3$ respectively.

Taking into account that the magnetic moment of the Mn^{3+} ion in perovskites is about 3.5 μ_B [16], ferromagnetically correlated regions contains about 50 of the manganese ions. If we consider that the lattice constant is about 5 Å [17], whereas the size of ferromagnetically correlated regions is about 1-2 nm.

Conclusions

For all samples $La_{1-x}A_xMn_{1-y}Zn_yO_3$ (A = Sr, Ba) the ESR spectrum consists of an exchange – narrowed Lorentzian line in X- band. We assume that ferromagnetically

correlated regions in the paramagnetic phase should have a similar effect on the paramagnetic resonance spectrum like superparamagnetic particles. Temperature dependencies of magnetic resonance linewidth in $La_{1-x}A_xMn_{1-y}Zn_yO_3$ (A = Sr, Ba) are connected with (1) the thermofluctuational effects (superparamagnetism) and (2) the orientational distribution of their anisotropy axis under the influence of the applied field. It is received that the size of ferromagnetic correlated region in ceramics $La1_{-x}A_xMn_{1-y}Zn_yO_3$ (A = Sr, Ba) is about 1-2 nm and value of the magnetic anisotropy is about 2-4K.

The authors are grateful to A.G. Badelin of the Astrakhan State University for the samples preparation.

References

[1] R.M. Kusters, D.A. Singleton, R. Mcgreevy, and W. Hayes, Physica B **155,** 362 (1989)

[2] R. von Helmolt, J. Wecker, B. Holzapfel, L. Schultz, and K. Samwer, Phys. Rev. Lett. **71,** 2331 (1993)

[3] J. Deisenhofer, D. Braak, H.-A. Krug von Nidda, J. Hem- berger, R.M. Eremina, V.A. Ivanshin, A.M. Balbashov, G. Jug, A. Loidl, T. Kimura, and Y. Tokura, Phys. Rev. Lett. **95,** 257202 (2005)

[4] M. Kadomzeva, Y.F. Popov, G.P. Vorobyov, K.I. Kamilov, A.A. Muhin, V.Y. Ivanov, A.M. Balbashov, PhSS **48**, 2014 (2006)

[5] Zener, Phys. Rev. 82, 403 (1951)

[6] P. W. Anderson and H. Hasegawa, Phys. Rev. **100**, 675 (1955)

[7] P. G. de Gennes, Phys. Rev. **118**, 141 (1960)

[8] E. L. Nagaev JETP Letters **16**, 558 (1972)

[9] M. A. Krivoglaz, Sov. Phys. Usp.**106**, 360 (1972)

[10] M. Yu. Kagan and K. I. Kugel, Sov. Phys. Usp.**171**, 577 (2001)

[11] K.I. Kugel, A.L. Rahmanov, A.O. Sboychakov, M.Yu. Kagan, I.V. Brodskiy, A.V. Klapcov , JETP **125**, 648 (2004)

[12] V.A. Khokhlov, A.Yu. Prohorov, Yu.V. Medvedev, Yu. Nikolayenko, A. Muhin, V.P. Paschenko, G.G. Levchenko, V.G. Prohorov, N.I. Solin, V.L.Svetchnikov, J.S. Park, J.B. Kim, G.Y.P. Lee, Technical Physics **81**, 95 (2011)

[13] Yu. L. Raikher and V. I. Stepanov, Phys. Rev. B. **50,** 6250 (1994)

[14] Yu. L. Raikher and V. I. Stepanov, JETP **101,** 1409 (1992)

[15] E.V. Sotirova-Haralambeva, X.L. Wang, K.H. Liu, T.Silver, K. Konstantinov and J. Horvat, Science and Technology of Advanced Materials **4,** 149 (2003)

[16] O. Troyanchuk, D.A. Efimov, D.D. Halyavin, N.V. Pushkarev, R. Shimchak, PhSS **42**, 81 (2000)

[17] Q. Huang, A. Santoro, J.W. Lynn, R.W. Erwin, J.A. Borchers, J.L. Peng, and R.L. Greene, Phys.Rev. B **55,** 14987 (1997)

Double doping nanoparticles of hydroxyapatite

M.R. Gafurov[1], G.V. Mamin[1], S.B. Orlinskii[1], G.A. Tokarev[1],
E.S. Kovaleva[2], V.I. Putlyaev[2]

[1]Kazan (Volga region) Federal University, Kremlevskaya st. 18, Kazan, 420008, Russia.
[2]Lomonosov Moscow State University, GSP-1, Leninskie Gory, Moscow, 119991, Russia.
e-mail: grigoryat@yandex.ru

Inroduction

Synthetic hydroxyapatite (HAP) $Ca_{10}(PO_4)_6(OH)_2$ – widespread material that used in medicine for treatment of damaged bone tissue due to chemical and stage similarity with inorganic components of bone tissue [1, 2]. For enhancement of efficiency of bioresorbable implants as substitutes of bone tissue it is possible to use a material bases on carbonized hydroxyapatite $Ca_{10-x}Na_x(PO_4)_{6-x}(CO_3)_x(OH)_2$, in which PO_4 group partially replaced by CO_3 group. It is more precisely reproduce the structure of bone in comparison with not modified hydroxyapatite.

The process of synthesis of hydroxyapatite according to the following mechanism [2]:

$$(10\text{-}x)Ca(NO_3)_2 + (6\text{-}x)(NH_4)_2HPO_4 + xNaHCO_3 + 8NH_4OH \rightarrow$$
$$\rightarrow Ca_{10-x}Na_x(PO_4)_{6-x}(CO_3)_x(OH)_2\downarrow + (20\text{-}2x)NH_4NO_3 + 6H_2O.$$

In this case, the nanocrystals are precipitated from a colloidal solution and have a size equal to 30 nm, that is the optimal particle diameter for the process of bioresorption [3]. As we can see, in the synthesis of nitrogen-containing NO_3 and NH_4 groups are used, which can be trapped by falling out particles of hydroxyapatite. These compounds are highly toxic and prevent the use of hydroxyapatite in medicine [3].

There are two different mechanisms to capture nitrogen compounds by hydroxyapatite nanoparticles:

1. NO_3 and NH_4 groups replace PO_4 and OH groups in the crystal lattice of hydroxyapatite.

2. On the surface of hydroxyapatite held a mother solution containing NO_3 and NH_4 groups.

In the first case, it is very difficult to remove nitrogen compounds from the drug. In the second case, there is drug wash with distilled water used, followed by removal of water by annealing the powder of HAP with temperatures over 100 °C. The water evaporates and grab NO_3 and NH_4 groups, thereby reducing their concentration in the final preparation.

Thus, there is need for detecting the presence of nitrogen-containing compounds in the hydroxyapatite, the definition of localization and verification mechanism for the HAP by annealing treatment with EPR method.

Results and discussion

In the experiments, we investigated samples of carbonated hydroxyapatite and HAP doped with manganese. In these samples we can observe the EPR signal of manganese centers. In order to detect the other impurity centers, hydroxyapatite samples were irradiated by X-ray. After the irradiation spectrum was observed (fig.1). It consists of three lines of equal integrated intensity, which suggests that the observed spectrum is determined by the hyperfine interaction of the magnetic moment of the unpaired electron of paramagnetic center

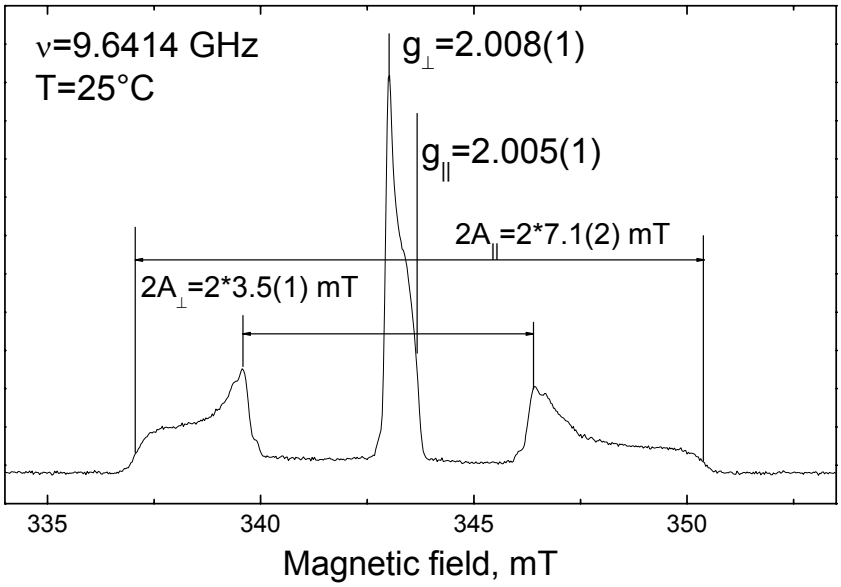

Fig.1. The EPR spectrum of NO_3^{2-} complexes in HAP

with the magnetic moment (I=1) of the nitrogen nucleus ^{14}N. The values of the g-factors and hyperfine constants proves that we have observed the spectrum of NO_3^{2-} complexes.

To check the effect of HAP synthesis technique, we compared the spectrum of the NO_3^{2-} groups in the carbonated HAP and hydroxyapatite doped with manganese (fig.2). The

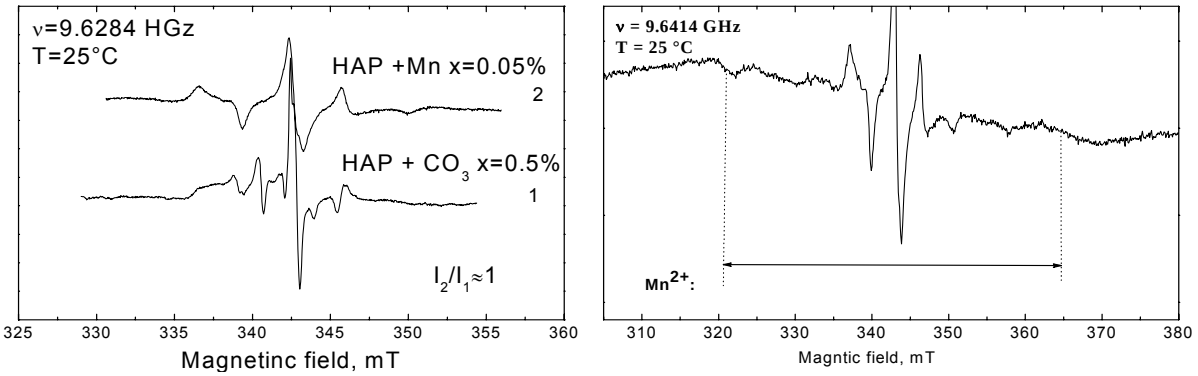

Fig.2. The EPR spectra of NO_3^{2-} complexes in the carbonized hydroxyapatite and HAP doped with manganese

line width of the spectrum for hydroxyapatite doped with manganese is larger than that of carbonated HAP, but the value of the integrated intensity of the EPR spectra are almost equal, which means almost the same concentration of NO_3^{2-} complexes in these samples.

The particles of hydroxyapatite powder might be doped either only manganese ions or CO_3 groups ions or the both. To determine are the particles of HAP co-doped or not, we measured the time of spin-spin relaxation of the NO_3^{2-} groups in the carbonated hydroxyapatite and HAP doped with manganese (fig.3). As we can see, the addition of even very small amount of manganese reduces T_2 to 30 times. Therefore Mn and CO_3 ions co-doped in the particles of powder. But also this prevented the investigations of EPR spectra of NO_3^{2-} groups in HAP doped with manganese by ELDOR methods.

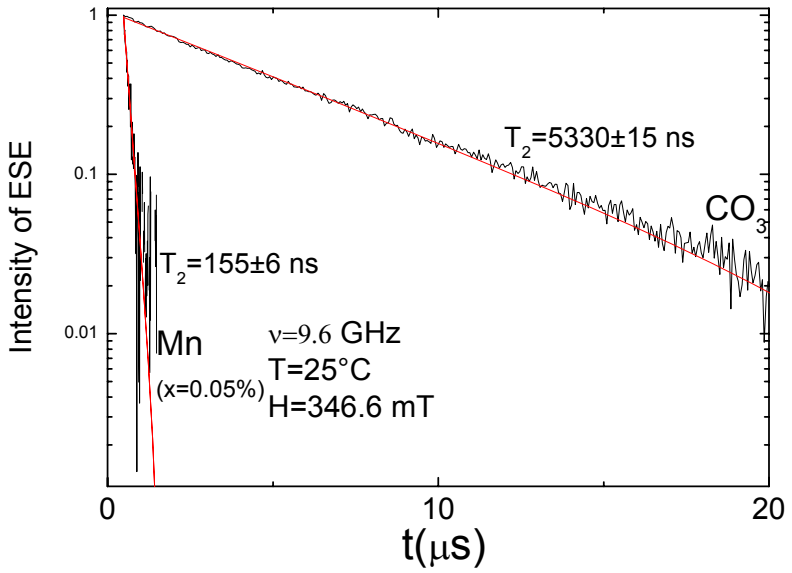

Fig.3. T_2 of NO_3^{2-} complexes in the carbonated HAP and HAP doped with manganese

Conclusion

The CW X-band EPR spectra of carbonized and doped with manganese hydroxyapatite were measured and interpreted, their spectroscopic and relaxation characteristics were obtained.

Measurements showed that the concentration of complexes NO_3^{2-} is equal in the samples of carbonated hydroxyapatite and HAP dopes with manganese. The study of samples of hydroxyapatite doped with manganese ions showed higher probability of complex formation of manganese ions and NO_3 groups within the crystal structure of hydroxyapatite. The results can be useful for the modernization of the synthesis of nanocrystalline hydroxyapatite.

References

[1] Lafon, J. P. Preparation and characteristics of nanosized carbonated apatite by urea addition with coprecipitation method / J. P. Lafon, E. Champion, D. Bernache-Assollant // J. Eur. Cer. Soc. -2008. –V.28. -P.139–147.

[2] LeGeros, R.Z. Properties of osteoconductive biomaterials: calcium phosphates / R.Z. LeGeros // Clin. Orthop. Relat. Res. -2002. –V. 395. –P.81–98.

[3] Kovaleva, E.S. Bioresorbable carbonated hydroxyapatite $Ca_{10-x}Na_x(PO_4)_{6-x}(CO_3)_x(OH)_2$ powders for bioactive materials preparation / E.S. Kovaleva, M.P. Shabanov, V.I. Putlyaev, Y.D. Tretyakov, V.K. Ivanov, N.I. Silkin // Cent. Eur. J. Chem. 2009. –V.7(2). –P. 168

Electron spin polarization of supramolecules based on metalporphyrins

V.S. Iyudin[1], Yu.E. Kandrashkin[1], V.K. Voronkova[1], V.S. Tyurin[2], E.A. Mikhalitsyna[2]

[1]Institution of the Russian Academy of Sciences Kazan E.K. Zavoisky Physical-Technical Institute, Kazan Scientific Center, Russian Academy of Sciences, Kazan, Russian Federation, 420029, Sibirsky tract, 10/7, Kazan, Russian Federation.

[2]A.N. Frumkin Institute of Physical Chemistry and Electrochemistry, 119991, Leninskiy prosp. 31, Moscow, Russian Federation.

e-mail: vasilius@yandex.ru

Self-organizing of porphyrins and metalporphyrins attracts close attention of scientists. Porphyrins ensembles are of interest from the fundamental point of view as a models for studying the process of photosynthesis, in particular, structure of the photosynthetic reactionary center. Multiporphyrin systems can be considered as a biomimetic models which are carrying out various functions, for example catalytic, and to find application as the phototransform devices, transferring materials, molecular wires, molecular switches, photon tubes and molecular elements for information storage in electronics [1].

Formation of supramolecule is based on the phenomenon of molecular recognition and is characteristic for crown-connections. Ability of molecules to self-organizing is provided mainly by "staking" interaction between aromatic rings. Connection of crown- ether groups to porphyrins as lateral deputies leads to additional possibilities to self-organizing at the expense of interaction of cations of alkaline and other metals with crown-ether macrorings. Dimmer or units, depending on a relative positioning of crown-ether rings of the next molecules are thus formed [2].

Materials and Methods

We studied a number of molecules of metalporphyrins with the different deputies, presented on fig.1: meso-porphyrin-Br (H2P-Br), copper-porphyrin-Br (CuP-Br), monomer of aza-crown-zinc-porphyrin ZnPA15C5, monomer of aza-crown-copper-porphyrin CuPA15C5, dimmer of aza-crown-copper-porphyrin CuPA15C5, which is formed at KSCN salt addition. The aza-crown-meso-porphyrin H2PA15C5 molecule, which is similar to ZnPA15C5 and

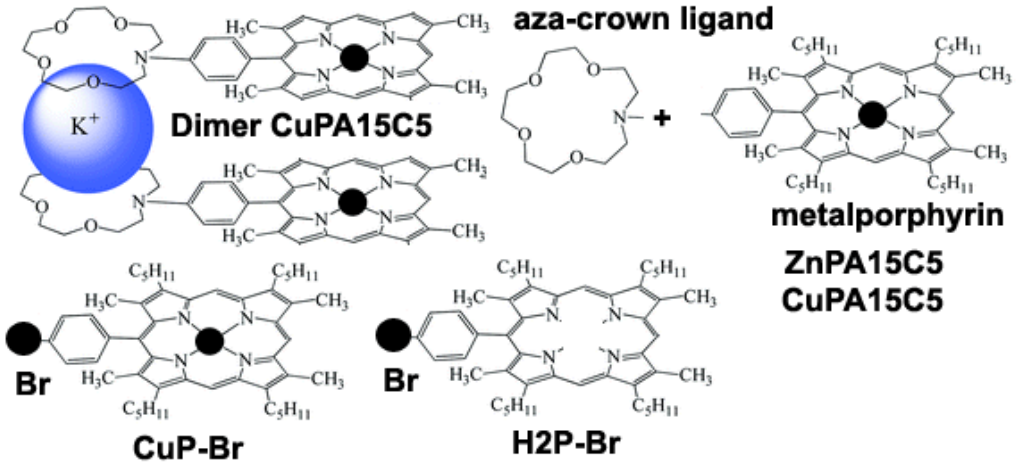

Fig.1. meso-porphyrin-Br (H2P-Br), copper-porphyrin-Br (CuP-Br), monomer of aza-crown-zinc-porphyrin ZnPA15C5, monomer of aza-crown-copper-porphyrin CuPA15C5, dimmer of azacrown-copper-porphyrin CuPA15C5

CuPA15C5, but without a metal ion was investigated also.

Dimerization

As cations of alkaline metals K and Na as a part of NaCl, KCl and KSCN salts were chosen. Addition of salts solution to crown-metalporphyrin solution leads to aggregation of molecules. It is supposed that, the molecules are aggregated in so-called «a sandwich form», from the interaction of cations of alkaline metals with crown-ether macrorings, thereby forming a dimmer of a crown-metalporphyrin (see fig.1.). Concentration of KSCN salt and concentration of crown-metalporphyrin CuPA15C5 was 10-3 M/1.5*10-3 M respectively.

EPR spectroscopy

The of steady-state (CW EPR) and time-resolved EPR (TR EPR) methods were used to study magnetic and spin properties of the supramolecule systems, constructed of metalporphyrins molecules, before and after photoexcitation. The sample was irradiated by the solid-state Nd:YAG laser (Brio) with energy in a bunch of 2,8 mJ. TR EPR measurements were carried out on a Elexsys E580 spectrometer with X microwave range, equipped with the dielectric ER4118X-MD5 resonator. TR EPR spectra were received by summation of data in different time windows directly after laser pulse. CW EPR measurement were carried out on a high-sensitivity Bruker EMXplus spectrometer . The CW EPR method allowed us to establish the fact of dimerization, and also to make the assumption of a relative position of molecules in a dimmer. As a solvent we used a mix of solvents chloroform - toluene in the ratio 1:1 respectively.

Results and discussions

Steady state EPR. In fig.2 the CW EPR spectra from porphyrins complexes at temperature 80K are shown , also in these figures theoretical spectra of these samples are presented. The stationary EPR spectra of porphyrins complexes has a typical line form presented in [3, 4]. The type of spectra, in case of dimerization, has distinct from monomer. In spectra from fig.3B additional resonance lines are shown. The HFI constant in that case decreases in 2 times in relation to porphyrin monomer (A= ~ 100 Gs). As it is known from literature, in case of dimerization, the $\Delta Ms = \pm 2$ transition at g=4 in half fields is shown in EPR spectra also. This statement was also confirmed and shown in fig.3A.

For simulation of spectra we assumed that two magnetic isotopes of copper have identical hyperfine structure and for the model of nitric isotopes the most connected isotope 14N with nuclear spin $I_N=1$ is taken.

Spin Hamiltonian of the system in the main condition includes Zeeman interaction of electrons by a magnetic field and a hyperfine interaction with copper and nitrogen:

$$H = \mu \mathbf{B} \cdot \mathbf{g}_{\mathrm{Cu}} \cdot \mathbf{S}_{\mathrm{Cu}} + \mathbf{S}_{\mathrm{Cu}} \cdot \mathbf{A}^{\mathrm{Cu}} \cdot \mathbf{I}_{\mathrm{Cu}} + \sum_i \mathbf{S}_{\mathrm{Cu}} \cdot \mathbf{A}^{\mathrm{N}} \cdot \mathbf{I}_{\mathrm{N},i} , \quad (1)$$

where, g_{Cu} is a g-tensor of an ion of copper; A_{Cu} and A_N – tensors of a hyperfine interaction (HFI) of noncoupled electron of an copper ion with own nucleus and a nitrogen nucleus. We also assumed that the spin Hamiltonian (1) has axial symmetry and both its g-tensor and A-tensor of hyperfine coupling are collinear. The fitting of experimental data with numerical processing give the following parameters: $g_{xx}=g_{yy}=2.049$, $g_{zz}=2.19$, $A^{Cu}{}_{xx}=A^{Cu}{}_{yy}=0.0021$ cm^{-1}, $A^{Cu}{}_{zz}=0.0204$ cm^{-1}, $A^{N}{}_{xx}=A^{N}{}_{yy}=0.00146$ cm^{-1}, $A^{N}{}_{zz}=0.00166$ cm^{-1}.

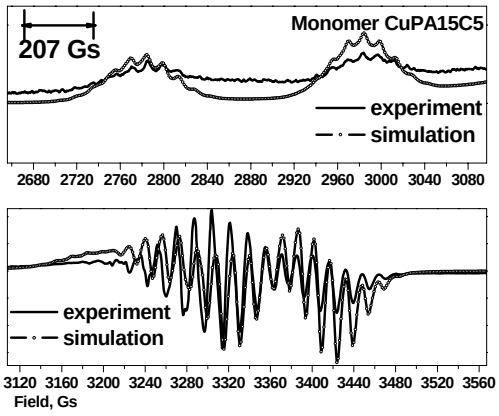

Fig.2. Low field (upper) and high field (lower) region of experimental and theoretical CW EPR spectra from monomer of crown-copper-porphyrin $CuPA1_5C_5$ at 80K. Modeling parameters: $g_{xx} = g_{yy} = 2.049$, $g_{zz} = 2.19$, $A^{Cu}{}_{xx} = A^{Cu}{}_{yy} = 0.0021$ cm^{-1}, $A^{Cu}{}_{zz} = 0.0204$ cm^{-1}, $A^{N}{}_{xx} = A^{N}{}_{yy} = 0.00146$ cm^{-1}, $A^{N}{}_{zz} = 0.00166$ cm^{-1}.

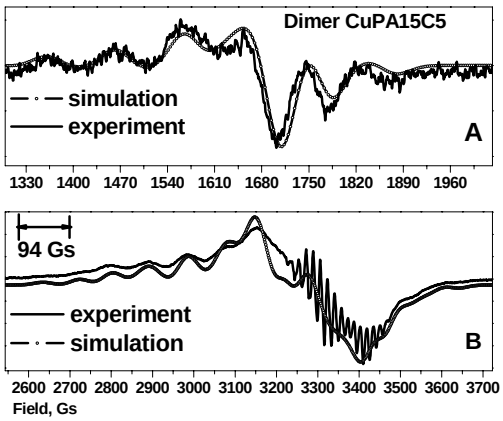

Fig.3. CW EPR spectra of dimmer crown-copper-porphyrin CuPA15C5 at 80K. Comparison of experimental (experiment) and theoretical (simulation) spectra. A) spectra from ΔMs=±2 transition at g=4, B) allowed transitions, main spectra. Modeling parameters: $g_{xx} = g_{yy} = 2.049$, $g_{zz} = 2.19$, $A^{Cu}{}_{xx} = A^{Cu}{}_{yy} = 0.0021$ cm^{-1}, $A^{Cu}{}_{zz} = 0.0204$ cm^{-1}, $A^{N}{}_{xx} = A^{N}{}_{yy} = 0.00146$ cm^{-1}, $A^{N}{}_{zz} = 0.00166$ cm^{-1}, J = 6400 МГц, Cu-Cu distance 5 A, angle θ 40^{o}

It is known that the EPR spectra from a dimmer fragment of a paramagnetic ion, for example, copper, differs from the monomer. Therefore the EPR method can be used for control the dimerization process. CW EPR spectra of crown-copper-porphyrin exhibits properties that is characteristic for dimmer of an copper ion after addition of KSCN salt (fig.3). From comparison of fig.2 and fig.3 it is visible that dimerization of molecules leds to increase the number of lines of HFI, and the HFI constant at dimerization in 2 times is less (A=94Гс) than in monomer of this molecule (A=207Гс). Also in half fields (g = 4) the spectra from ΔMs =±2 transition (fig.3A) was established. This fact also indicates formation of a dimmer of a crown-copper-porphyrin in our case. Spin Hamiltonian of the system includes a dipole - dipolar and isotropic exchange interaction and written as follows:

$$H = \mu_e \sum_{j=1,2} \left(B g_j S_j + S_j A_j I_j \right) + J S_1 S_2 + \mu_e{}^2 r^{-3} \left\{ \left(g_1 S_1 \right) \left(g_2 S_2 \right) - 3 r^{-2} \left(g_1 S_1 r \right) \left(g_2 S_2 r \right) \right\} \qquad (2)$$

Numerical processing of experimental spectra gives the following parameters: $g_{xx} = g_{yy} = 2.049$, $g_{zz} = 2.19$, $A^{Cu}{}_{xx} = A^{Cu}{}_{yy} = 0.0021$ cm^{-1}, $A^{Cu}{}_{zz} = 0.0204$ cm^{-1}, $A^{N}{}_{xx} = A^{N}{}_{yy} = 0.00146$ cm^{-1}, $A^{N}{}_{zz} = 0.00166$ cm^{-1}, J = 6400 МГц, distance between copper ions — 5 A, angle θ = 40^{o}. Good coincidence of theoretical calculation to experimental data shows at fig.2 and fig.3.

Time-resolved EPR of the photoexcited compounds. It is known that after photoexcitation, the porphyrin molecule passes from the nonmagnetic S = 0 state to the exited S = 1 state with nonequilibrium distribution of spin sublevels population. This process is called polarization of electron spins. Spectra typical for such states were observed at photoexcited H2PA15C5 and ZnPA15C5. The situation changes at photoexcitation of copper-porphyrin molecules for which the polarized states are formed by interacting of porphyrin p-systems with paramagnetic copper. The spin states for this case are: the main state with

S = 1/2 and the exited states with S = 1/2 and S = 3/2. More difficult picture is expected at photoexcitation of CuPA15C5 dimmer. TR EPR spectra for monomer and dimmer crown-copper-porphyrin CuPA15C5 are presented on fig.4.

For the photoexited monomer crown-copper-porphyrin the absorption form of signal is observed which corresponds to the main condition from S = 1/2. It is shown from comparison of TR EPR spectra with integrated CW EPR spectra and has the same character shown at [3]. The TR EPR spectra from dimmer have amazing changes in time after photoexcitation.

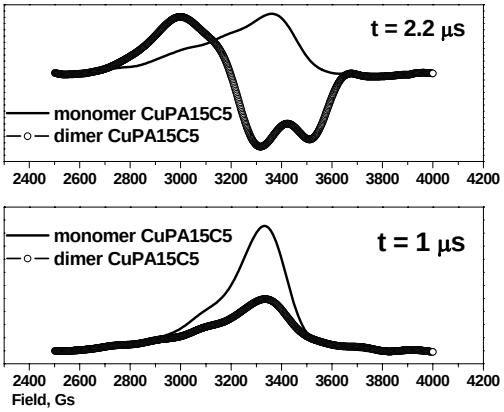

Fig.4. TR EPR spectra of monomer and dimmer of crown-copper-porphyrin CuPA15C5 at 80K, wavelength 532 nm. Time integration after laser pulse 1 and 2.2 μs.

Conclusion

The CW EPR method proved dimerization process of crown-copper-porphyrin adding 1.5 mM solution of the salt KSCN to the solution of crown-copper-porphyrin. Of agreement between the experimental and simulated spectra the parameters of the monomeric fragment is established, estimated the value of the isotropic exchange interaction and the angle between the direction of g_z and Cu–Cu. According to the time-resolved spectroscopy the spin-polarized absorption spectra of ground state after photoexcitation is observed. The excitation of dimmer system leads to the absorption spectra at early times (0.6 ms) and is due to an admixture of monomer fragments. At later times (2.2 ms), in our opinion exhibits the spectrum of spin-polarized state with S = 2, arising from the interaction between the triplet states of copper dimmer and photoexcited triplet state of one of the porphyrin dimmers. Also, there may be the spectrum of S = 1. Mathematical model of photoexcited states of the dimmer complex and description of the data is currently underway.

This work was supported by the Russian Foundation for Basic Research (grants no. 12-03-31294 and 12-03-97078), the grant of the President of the Russian Federation (MK-6407.2012.2).

References

[1] Цивадзе А. Ю. Химия и компьютерное моделирование. Бутлеровские сообщения. 2002. № 9.

[2] Г.М.Мамардашвили, Н.Ж.Мамардашвили, О.И.Койфман. Самоорганизующиеся системы на основе порфиринов. Успехи химии 77 (1) 2008. с. 60-74

[3] V. S. Iyudin, Yu. E. Kandrashkin, V. K. Voronkova, V. S. Tyurin and E. N. Kirichenko Time-Resolved EPR Spectra of Photoexcited Copper Porphyrin, 2009, Applied Magnetic Resonance Volume 40, Number 1, 75-89

[4] V. Rozenshtein, A. Berg, H. Levanon, U. Krueger, D. Stehlik, Y. Kandrashkin, A. van der Est, Israel J Chem. 43, 373-381 (2003)

Mechanochemically-doped Er^{3+} and Yb^{3+} cubic symmetry centers at the surface of fluorite nanoparticles

D.A. Tayurskii, I.A. Irisova, A.A. Rodionov, R.V. Yusupov

Kazan Federal University, 420008, Kremlevskaya 18, Kazan, Russia

e-mail: Irisha-kzn@mail.ru

Introduction

Although nanostructured high-surface area fluorides are of increasing importance for different applications like heterogeneous catalysis, thin films, nanoceramics, bioceramics or glasses, only few papers exist on mechanical activation and mechanochemical reactions of solid fluorides [1]. Mechanochemical doping is an effective way of obtaining the RE-doped fluorides. In the present work we propose a specific self-organization in ensembles of the mechano-doped fluorite (CaF_2) nanoparticles to be responsible for predominant formation of the cubic-symmetry "surface" RE-ion centers. Thereby the base for the development of effective and economically sound methods of the synthesis of powders with predefined properties is created**.**

Materials and methods

Fluorite powders mechanochemically doped with RE ions have been obtained by means of grinding of the mixtures of CaF_2 (CeO_2) and RE fluoride (oxide) high-purity crystalline salts for one hour in an agate mortar in extra-pure isopropyl alcohol. The concentration series of the samples were prepared with a sequential increase of a RE-salt content in the mixture. The ErF_3 concentration dependences in CaF_2 were studied for two sample series. The first series differed from the second only in a preliminary grinding of CaF_2 for 20 minutes. Both series consisted of 6 samples of CaF_2 and 0.1, 0.3, 1.0, 3.0, 10 and 30 wt. % of ErF_3 powders, respectively. The CaF_2 powder doped with Yb^{3+} ions was prepared from the initial mixture of 97 wt. % of CaF_2 and 3 wt. % of YbF_3. Four samples were studied that were prepared by means of grinding of the CeO_2 and 0.3, 1.0, 3.0, 10 wt. % of Er_2O_3 mixture, respectively.

Results and discussion

Four spectra shown in fig.1 contain the component observed at $g \sim 6.75$. This component fits well the properties of the cubic symmetry Er^{3+} ion center in crystalline CaF_2. Grain size dependence $I \propto 1/d$ [2] indicates that these centers are localized at the CaF_2 particle surface. This is hardly compatible with the observed cubic symmetry for a center localized at the surface of an isolated particle. However, the cubic center pattern dominates in the EPR spectrum up to the concentration of 10 wt.% of ErF_3 in the initial mixture. This differs significantly from the situation realized in crystalline CaF_2:RE^{3+}. Already at a RE-ion concentration as low as 0.1 wt. % various axial-symmetry centers appear and even dominate.

EPR spectra up to 10 wt.% of ErF_3 in the mixture are very close the spectrum of CaF_2:Er^{3+} single crystal with 0.8 wt.% of ErF_3 in the initial charge. For illustration fig.3 presents the comparison of the spectra of CaF_2 + 1 wt.% of ErF_3 and the doped Er^{3+} in the CaF_2 single crystal. Obviously, the two spectra essentially reproduce each other, except for the wide structureless background in the spectrum of the mechano-doped sample.

Concentration dependences of the $g \sim 6.75$ feature integral intensity presented in fig.2 can be fit well by the power law $f(\eta)=A\cdot\eta^{\alpha}$. The power index values obtained were $0.79 < \alpha < 0.87$. These values fall in between the two limiting cases:

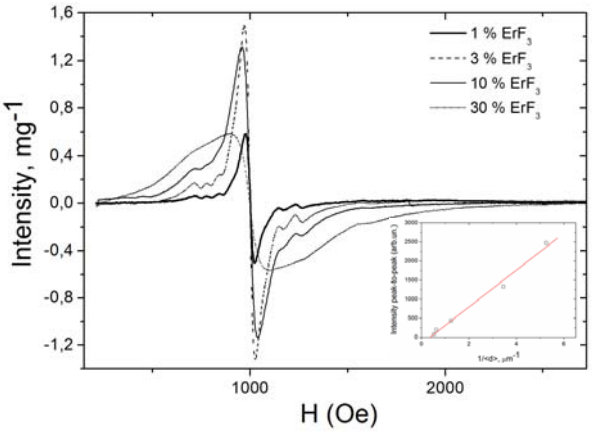

Fig.1. EPR spectra of the CaF_2 powders with different ErF_3 concentrations ground for one hour; $T = 15$ K. Inset: grain size dependence of the signal observed at ~ 1000 Oe [2].

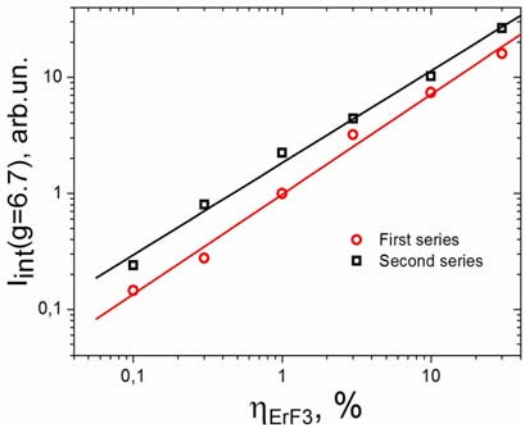

Fig.2. ErF_3 concentration dependences of the EPR lines observed at $g = 6.75$ for the samples in the first series (circle), second series (square) and power law fits (lines) of the dependences.

- "soft" ErF_3 (with respect to CaF_2), for which $I_{int} \sim \eta$ and $\alpha = 1$, and
- "hard" ErF_3, when $I_{int} \sim \eta^{2/3}$ and $\alpha = 0.67$.

Fig.4 depicts the EPR spectrum of CaF_2 nanopowder mechano-doped with Yb^{3+} ions; g-factor value of the signal is $g = 3.43$ as compared to cubic Yb^{3+} centers in the CaF_2 crystal $g = 3.44$ [3]. EPR spectrum of the Er-doped fluorite structure CeO_2 nanopowder doesn't reveal spectra of any well-defined center: only a wide structureless line is found near $g = 6.82$ (986 Oe) (fig.5).

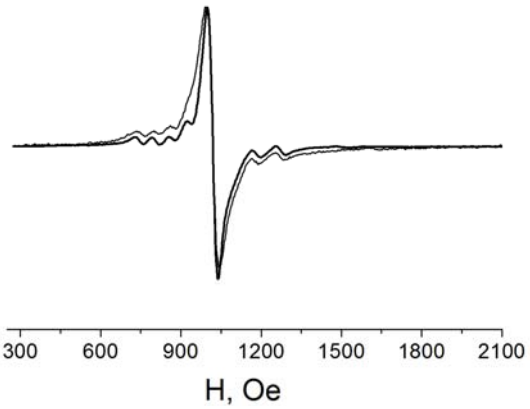

Fig.3. EPR spectra of the CaF_2 nanoparticles with mechanoactivated Er^{3+} centers (1% ErF_3 in initial mixture) and $CaF_2:Er^{3+}$ single crystal with 0.8 wt.% of ErF_3 in initial charge (heavy line); $T = 10$ K. Resonance fields of the two spectra and the peak intensities were adjusted one to the other.

We propose that a specific self-arrangement in CaF_2 nanopowder may be at the origin of the observed situation. Key point here is that CaF_2 cleaves ideally along the (111) crystal plane which is not the case for CeO_2. Then, CaF_2 particles aggregate with cleaved planes sticking to each other. Rare-earth ion, if trapped in between these planes, would possess the symmetry close to cubic, and amount of these centers would be proportional to the particle surface.

Basing on our hypothesis a large difference in the shapes of the EPR spectra of the mechano-doped samples with 10 and 30 wt.% of ErF_3 (Fig.1) can be explained as follows. Up to the concentration of 10 wt.% of ErF_3 the most of the Er^{3+} ions occupy the inter-cleaved-surface near-cubic symmetry positions in the ensemble. At higher concentrations of ErF_3 the spectrum is very similar to that of the mechano-doped $CeO_2:Er^{3+}$ (Fig.5). It looks natural to suppose that these signals originate from the disordered low-symmetry Er^{3+} positions at the exposed surface of the CaF_2 particles.

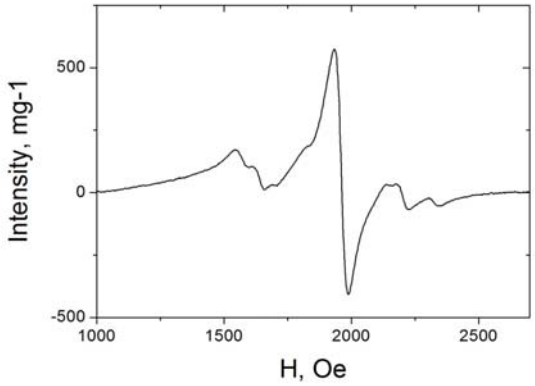

Fig.4. EPR spectrum of the (97 wt. % CaF_2 + 3 wt. % YbF_3) mixture ground for 1 hour; T = 30 K.

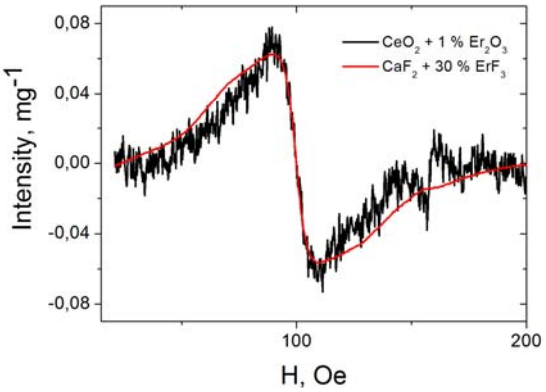

Fig.5. EPR spectra of the CaF_2 (with 30 % ErF_3) and CeO_2 (with 1% Er_2O_3) nanoparticles mechano-doped with Er^{3+} centers. T = 15 K. Resonance fields of the two spectra and the peak intensities were

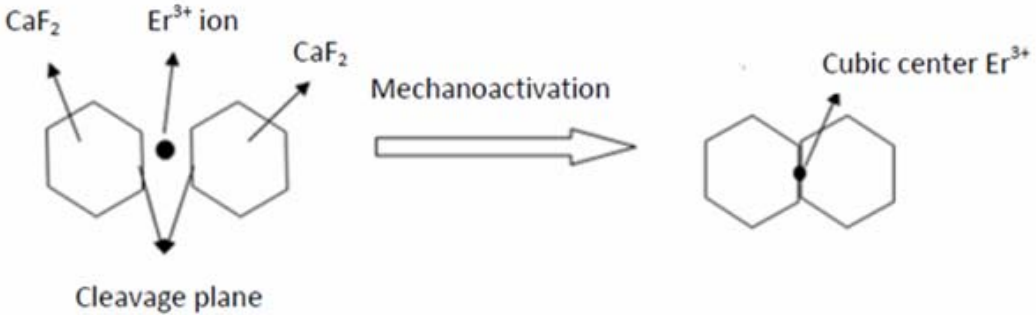

Fig.6. Formation of the surface cubic centers of RE in CaF_2.

Conclusions

- During mechanochemical activation of CaF_2 particles with Er^{3+} и Yb^{3+} ions the cubic symmetry centers are formed with the concentration proportional to the particle surface in the sample
- EPR spectra of rare-earth ions in the obtained samples are represented by superposition of slightly broadened signal which is responsible for cubic symmetry impurity center in the crystal, and the wide structureless absorption band
- Origin of the observed centers is associated with presence of the ideal cleavage plane in the CaF_2 crystal. During the mechanoactivation process as a result of a specific self-organization a considerable fraction of rare-earth ions is trapped between the cleavage planes of the agglomerating particles, thus reproducing the crystal field of the cubic symmetry.

References

[1] G Scholz, D Heidemann et.al., *Journal of Solid State Chemistry* 179, 1119–1128 (2006)

[2] I A Irisova, A A Rodionov et al. *J. Phys.: Conf. Series* 324, 012026 (2011)

[3] U Ranon, J S Hyde, *Phys. Rev* 141 259 (1966)

Preliminary studies of chalcopyrite ($CuFeS_2$) by NMR and Mössbauer effect

R.R. Gainov[1], A.V. Dooglav[1], F.G. Vagizov[1], I.N. Pen'kov[1], V.V. Klekovkina[1], V.A. Golovanevskiy[2], G. Klingelhöfer[3], V. Ksenofontov[3]

[1]Kazan (Volga Region) Federal University, 420008, Kremlevskaya 18, Kazan, Russia

[2]Curtin University of Technology, GPO Box U1987, Kent str. Bentley, Perth, Australia

[3]Johannes Gutenberg-Universität Mainz, D-55099, Staudingerweg 9, Mainz, Germany.

e-mail: Ramil.Gainov@ksu.ru

Nuclear-resonance spectroscopy methods, which include nuclear quadrupole resonance (NQR), nuclear magnetic resonance (NMR), nuclear gamma resonance (NGR or Mössbauer effect), appear to be as the effective microscopic techniques to study, diagnose, and certificate the crystal-chemistry and physical properties of solid-state materials [1]. These methods can be employed in the investigations of both the bulk compounds and the nano-scaled matter (for example, particles and thin films/layers).

This report is devoted to antiferromagnetic semiconductor $CuFeS_2$ (chalcopyrite) with $T_N \approx$ 823 K, which was studied preliminary by combination of ^{63,65}Cu-NMR and ^{57}Fe-Mössbauer spectroscopic methods. Generally, there are strong discussions about the electronic type of $CuFeS_2$: degenerate [2], zero-gap semiconductor [3], Mott insulator [4] or unusual insulator of Haldane–Anderson type [5]. There are also intriguing neutron diffraction [6] and magnetic susceptibility [7] data, showing a certain phase transition at about 50 K, but recent XAS spectroscopic [8] and powder-diffraction [7] reveal no magnetic features for such a behavior. Application of Mössbauer and NMR spectroscopy tools to study chalcopyrite at low temperatures appears to be the best way to examine the behavior of Fe electronic magnetic moments and Cu electronic magnetic moments, if applicable. Indeed, NMR spectroscopy of Cu nuclei provides information about hyperfine and crystal fields as well as their fluctuations felt by the Cu nuclei at different temperatures. Analogous data can be provided by Mossbauer Effect studies of Fe nuclei. Comparison of local (hyperfine) fields at Cu and Fe nuclei provides information about dynamics of hyperfine fields along the polymeric –Cu–S–Fe– chains and details of magnetic ordering.

Preliminary Cu-NMR relaxation and Fe-Mössbauer spectra measurements have been carried out. Actually, an unusual effect is observed near 55 K. Prior analysis points that this phase transition is correlated with the behavior of magnetic moments of Cu ions (spins). The possible nature of phase transition and valence state of Cu and Fe ions are discussed on the base of preliminary data. Further comprehensive Cu-NMR and Fe-Mössbauer spectral measurements and DFT-GGA calculations are very desirable to explain the low-temperature electronic properties of chalcopyrite.

This work is partly supported by RFBR grant under No. 12-02-31282 (mol_a).

References

[1] Bouznik, V.M.: *Nuclear resonance in ionic crystals*. Nauka, Novosibirsk, (1981)
[2] T. Teranishi, J. Phys. Soc. Jpn. 16, 1881 (1961)
[3] Kradinova L.V. et al. Semicond. Sci.Technol. 8, 1616 (1993)
[4] Boekema C. et al. JMMM, 272–276, 559 (2004)
[5] Sato K. et al. Phys. Status Solidi A 206, 1096 (2009)
[6] Woolley J.C. et al. JMMM, L62, 347 (1996)
[7] Knight K.S. Can.Miner., 49, 1015 (2011)
[8] Lovesey S.W. et al. J. Phys.: Condens. Matter 24, 216001(2012).

Investigations of antimony-containing chalcogenides Ag_5SbS_4 and $CuPbSbS_3$ by Sb NQR spectroscopy

A.Yu. Orlova, R.R. Gainov, A.V. Dooglav, I.N. Pen'kov

Kazan Federal University, 420008, Kremlevskaya str.,18, Kazan, Russia.

e-mail: AnnaYuOrlova@gmail.com

Multicomponent silver and copper chalcogenides have received much attention in recent years because of their important technological applications. These compounds offer intriguing optical, electric, and ferroelectric properties; show ionic conduction; etc [1, 2]. In order to understand these properties, an exact knowledge of the crystal structure of the compound is indispensable. NQR spectroscopy is a sensitive tool in studies of solids as it provides detailed information on the static and dynamic properties of the local structure. This method gives information, which is related to local electronic structure, ionic arrangement and phase-structural transformations.

We present the results of recent investigations of two complex sulfides, stephanite Ag_5SbS_4 and bournonite $CuPbSbS_3$ by ^{121,123}Sb NQR. Both of this compounds contain complex composite structure, based on isolated pyramidal groups of SbS_3. Stephanite, Ag_5SbS_4, having the centered orthorhombic unit cell with space group symmetry $Cmc2_1$, contains single Sb atom with a trigonal pyramidal coordination by three S atoms [3]. The SbS_3 pyramids are isolated in stephanite and connected only via Ag atoms. Bournonite, $CuPbSbS_3$, having the unit cell with space group symmetry $Pn2_1m$, contains two different Sb atoms in a unit cell: Sb (A) and Sb (B); each of them has an isolated trigonal pyramidal coordination by three S atoms; SbS_3 pyramids are connected via Cu or Pb atoms [4].

There exist two isotopes of antimony: ^{121}Sb with nuclear spin $I = 5/2$ and ^{123}Sb with spin $I = 7/2$. The ^{121,123}Sb NQR spectrum of Ag_5SbS_4 and $CuPbSbS_3$ is presented in fig.1. The ^{121,123}Sb-NQR spectrum for Ag_5SbS_4 consists of five lines (2 lines for ^{121}Sb transitions $\pm1/2 \leftrightarrow \pm3/2$, $\pm3/2 \leftrightarrow \pm5/2$ and 3 lines for ^{123}Sb transitions $\pm1/2 \leftrightarrow \pm3/2$, $\pm3/2 \leftrightarrow \pm5/2$ and

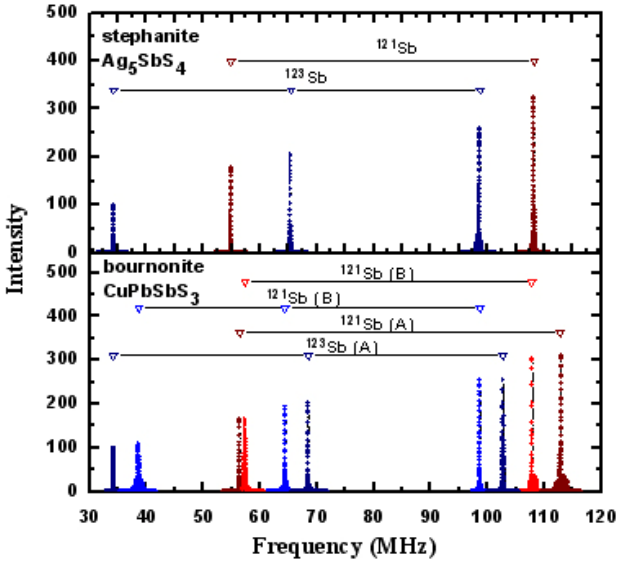

Fig.1. The ^{121,123}Sb NQR spectrum of stephanite Ag_5SbS_4 and bournonite $CuPbSbS_3$. As one can see, Sb atoms occupied one crystallographic position in Ag_5SbS_4 and two positions (A and B) in $CuPbSbS_3$

±5/2 ↔ ±7/2), whereas ^{121,123}Sb-NQR spectrum for $CuPbSbS_3$ contains ten lines. The observed number of Sb NQR lines confirmed that Ag_5SbS_4 has only one crystal-chemical site of antimony, but $CuPbSbS_3$ has two nonequivalent antimony positions.

The temperature dependencies of ^{123}Sb-NQR spectral lines positions and their line-widths for Ag_5SbS_4 and $CuPbSbS_3$ (Sb site A) are shown in fig.2 and fig.3 (transitions ±1/2 ↔ ±3/2). In general, the quadrupole frequencies decrease with increasing temperature

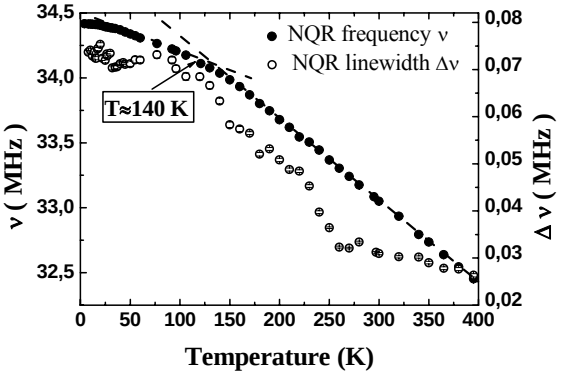

Fig.2. The temperature dependence of ^{123}Sb NQR frequency ν (±1/2↔±3/2) and line-width $\Delta\nu$ in Ag_5SbS_4

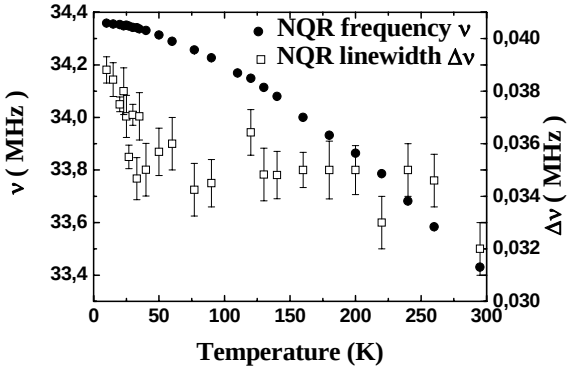

Fig.3. The temperature dependence of ^{123}Sb (A site) NQR frequency ν (±1/2↔±3/2) and line-width $\Delta\nu$ in $CuPbSbS_3$

for both sulfides according to the Bayer model. However, we focus here on weak change of the slope in the temperature dependence of ν for Ag_5SbS_4 at about 140 K. NQR line-widths, $\Delta\nu$, have also similar behavior: these parameters decrease with increasing temperature. At the same time, there are the bends at about 140 K and 250 K for Ag_5SbS_4 and at about 50 K for $CuPbSbS_3$. The values of EFG component V_{xx} and asymmetry parameter η have been calculated for Ag_5SbS_4 (fig.4). The peculiarities in the V_{xx} behavior at 140 K correlate with the bend in $\eta(T)$, $\nu(T)$, $\Delta\nu(T)$ dependencies. Thus all parameters of Sb NQR spectra for Ag_5SbS_4 show anomalous temperature dependence. Presence of such bends on the temperature dependencies is typical to structural changes of the displacement type which change the configuration of the local field but does not change the local symmetry. In Ag_5SbS_4 the anomaly is pronounced at $T = 140$ K. The reason for such anomaly might be the directional volume effect arising from the pronounced inclination of Ag atoms to have a twofold coordination [5]. Deformations arising within the SbS_3 complexes must by-turn lead to the changes in Ag ions mobility. Note that similar structural changes of the displacement type take place in compounds related to stephanite – proustite Ag_3AsS_3 and pyrargirite Ag_3SbS_3, in which they are thought to lead to ferroelectric properties [6, 7].

As it was found for Ag_5SbS_4, the temperature dependence of antimony nuclear spin-lattice relaxation rate T_1^{-1} can be described very well by expression $T_1^{-1}(T) = \alpha T^2 + \beta \cdot e^{-Ea/T}$, where α and β are numerical parameters, E_a is an activation energy. The exponential term in this dependence reflects the presence of internal movements obeying the Arrhenius law with the activation energy $E_a = 0.29$ eV in case of stephanite. These internal movements in Ag_5SbS_4 are actually the Ag ions diffusion through the stephanite crystal structure. Since the ions movement averages the EFG dispersion, the NQR spectral line width should decrease. Indeed, such line narrowing with temperature increasing is observed in stephanite (fig.2). Most likely, such character of the dependence could be explained by different hopping activation energy for Ag ions in different AgS_4 tetrahedra. It is notable that in compounds related to stephanite, such as pyrargyrite Ag_3SbS_3 and proustite Ag_3AsS_3, in which ion

conductivity through silver ions was revealed, activation energy makes up 0.4 and 0.42 eV, respectively [8].

The NQR line-width is a good indicator of the degree of lattice perfection of crystal under study. The NQR line-width is determined by the dispersion of the V_{zz} component of EFG and asymmetry parameter η. For Ag_5SbS_4 at room temperature Sb NQR line-width $\Delta\nu$ is about 30 kHz. This is a relatively small value for a natural mineral pointing at a high degree of the structural ordering. For comparison, for $CuPbSbS_3$ Sb NQR line for site A is 30 kHz wide (transition between m_I = 1/2 and 3/2 levels), whereas that for site B is 250 kHz wide (the same transition). This indicates that antimony atoms at site B do not occupy strict location in respect to their S neighbors in the $Sb(B)S_3$ complex, but their location is rather spread near some average value, and that this spread is larger than for site A antimony.

The temperature dependence of spin-lattice relaxation rate in $CuPbSbS_3$ is $T_1^{-1}(T) = \alpha T^n$, with $n \approx 2.4$, what is typical of the Raman process. This dependence is typical for chalcogenides and indicates the existence of very low-frequency vibrational modes which are strongly coupled to nuclear spins and provide a dominant relaxation mechanism. Note that T_1 for positions A and B are nearly the same ($T_1(^{121}Sb(A) = 0.11$ s, $T_1(^{121}Sb(B) = 0.13$ s at 77 K). It differs from data on the related compound, stibnite Sb_2S_3, which has $T_1(^{121}Sb(A) = 0.004$ s and $T_1(^{121}Sb(B) = 0.013$ s at 77 K [9]. Longer relaxations times in $CuPbSbS_3$ may be due to slowed down lattice dynamics, caused by the presence of Cu and Pb atoms.

Another important experimental result is the behavior of nuclear transverse relaxation in $CuPbSbS_3$. In the whole temperature range studied the beatings in the nuclear echo decay

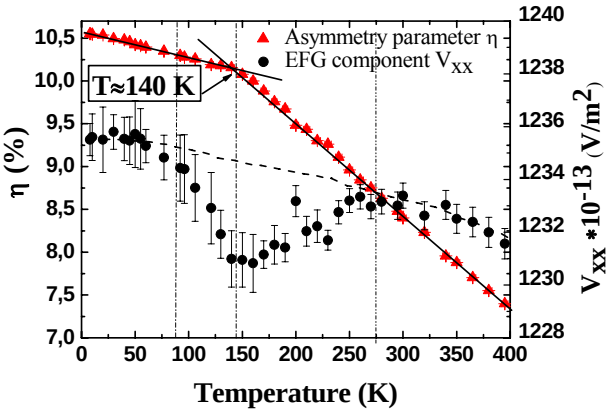

Fig.4. The temperature dependence of asymmetry parameter η and EFG V_{xx} component (^{123}Sb)

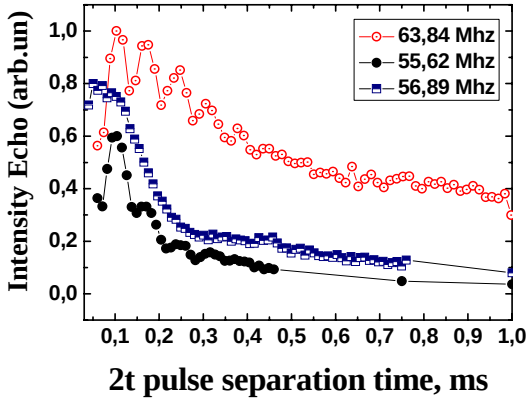

Fig.5. NQR echo decay (T_2) in Ag_5SbS_4. Data were taken at 220 K.

envelope curve were observed (fig.5.). It is known that "slow" beatings appear due to indirect JI_1I_2 spin-spin interactions [10, 11]. The beating frequencies in bournonite are 3, 14 and 30 kHz. In similar compounds (for example, in orpiment As_2S_3, stibnite Sb_2S_3, $Ge_2As_2Se_5$), such phenomena have also been observed and were explained by indirect spin-spin interactions of As atoms via covalent bonds through the bridging S atoms [12, 13].

Acknowledgments

The work was partially implemented in Leipzig University with Financial Support from the Ministry of Education and Science of the Republic of Tatarstan and Deutscher Akademischer Austauschdienst (DAAD).

The work was supported by the grant from the Russian Foundation for Basic Research, project no. Mol_a 12-02-31282.

References

[1] H. Dittich, A. Stadler, D. Topa et al., Phys.Status Solidi A, **206**, 1034 (2009)
[2] L. Bindi, M. Evani, S. Menchetti, Acta. Cryst. B, **62**, 212, (2006)
[3] M Leitl, A Pfitzner, L Bindi, Mineralogical Magazine, **73**, 17 (2009)
[4] A. Edenharter, W. Nowacki, Y. Takeuchi, Z. Kristallogr., **131**, 397, (1970)
[5] A. Yu. Orlova, R.R. Gainov, A. V. Dooglav et al., JETP Letters, **96**, 407 (2012)
[6] D.F. Baisa, A.V. Bondar, A.Ja. Gordon, Ferroelectrics, **20**, 219 (1978)
[7] R.S. Abdullin, I. N. Pen'kov, et al., Phys.Stat. Solid State, **19**, 1632 (1977)
[8] K.A. Schonau, S.T. Redfern, J. Appl. Phys., **92**, 7415 (2002)
[9] I. A. Safin, I. A. Pen'kov, Dok.Akad Nauk SSSR, **147**, 2 (1962)
[10] H. S.Gutowsky, C. Hoffman, R.E. McClure, Phys. Rev, **81**, 305 (1951)
[11] N. F. Ramsey, Phys.Rev., **91**, 303 (1953)
[12] J.Whitaker, E. Ahn, P. Hari et al., J. Chem. Phys, **119**, 8519 (2003)
[13] E. Mammadov, P. C. Taylor, Jpn. J. Appl. Phys. **47**, 8166 (2008)

NMR Studies and Molecular Dynamics Simulation of Cyclosporin in Complex with Detergent Micelles

S.V. Efimov, V.V. Klochkov

Kazan Federal University, 420008, Kremlevskaya str. 18, Kazan, Russia

e-mail: Sergej.Efimov@ksu.ru

Introduction

Cyclosporin A (CsA), cyclo(-Bmt-Abu-Sar-Mle-Val-Mle-Ala-DAla-Mle-Mle-Mva-), is a peptide used in therapeutics as an immunosuppressant. It acts through formation of a complex with the 18-kDa protein cyclophilin (Cyp18). This protein is ubiquitous, and the CsA–Cyp18 complex accumulates in cytoplasm in many types of cells; however, cyclosporin influences selectively T-cells. Apparently, cell recognition occurs, involving receptor proteins on cell membranes [1].

The task of determination of the structure of a molecule bound to a cell membrane is thus of a great importance. Phospholipid vesicles are the best structures representing cell membranes *in vitro*; however, NMR-based structure determination for molecules bound to heavy vesicles is hampered due to short transverse relaxation times. Fortunately, useful information can be obtained if relatively small supramolecular structures, detergent micelles, are employed [2].

Experimental

Cyclosporin A (≥98.5%) was purchased from Sigma-Aldrich, Inc. and used without further purification. Sodium dodecyl sulphate in concentration exceeding the CMC was used as the model-mimicking compound. Spectra were recorded on a Bruker Avance II spectrometer operating at the proton frequency of 500 MHz; heteronuclear measurements and some of the NOESY experiments were performed on a Bruker Avance at 700 MHz (Leipzig University). For the sake of signal assignment, heteronuclear correlation spectra were acquired: HSQC, HMBC, and band-selective HMBC. Geometric restraints, extracted from the NMR data, were then employed as input data in molecular dynamics (MD). Ensembles of structures were built in XPLOR-NIH 2.29 [3]. One hundred structures were generated in the simulated annealing protocol (6000 iterations at the initial temperature of 800 K, then cooling during 14000 iterations down to 100 K).

Results and Discussion

One-dimensional ^{1}H NMR spectrum of cyclosporin is shown in fig.1. Evidently, four resonances are dominant in the amide region (6.5–8.5 ppm); seven lines of NCH_3-groups are notable in the region 2.4–3.4 ppm. Signals of amide protons are absent in the spectrum recorded in D_2O due to intermolecular exchange with deuterium; signals of α-protons are suppressed in the H_2O/D_2O sample together with the solvent resonance. One conformation is thus dominant, and we can assign the signals using two-dimensional correlation experiments TOCSY, (^{13}C,^{1}H)-HSQC, (^{13}C,^{1}H)-HMBC, and NOESY.

Increase in temperature causes small changes in the amide resonances. The signal of Abu^{2} shifts significantly to the higher field (0.018 ppm/K in the range from 10 to 35°C), what is interpreted usually as an evidence of outward NH bond, preventing the formation of an intramolecular hydrogen bond [4]. Alanine NH signal has the temperature gradient of 0.005; the other two protons (D-Ala^{8} and Val^{5}) show $\Delta\delta/\Delta T < 0.003$ ppm/K, which may be an

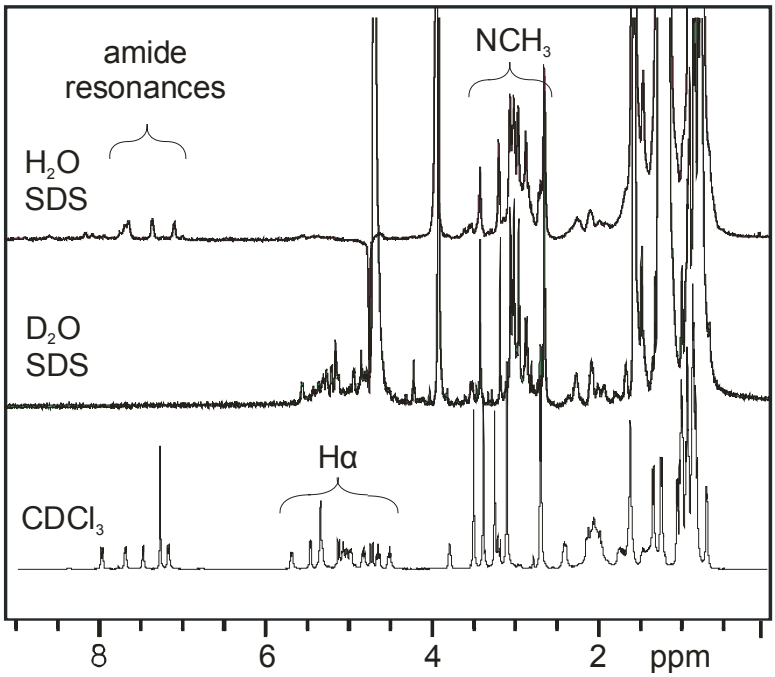

Fig.1. ^{1}H NMR spectra of cyclosporin at 20°C. From top: the CsA–SDS micelles system, spectrum with water suppression; micellar solution based on D_2O; chloroform.

evidence of intramolecular hydrogen bonds involving the latter two protons. The minor signals also move to the higher field in a similar manner. Their intensity remains the same.

Some information on the spatial structure of a molecule is contained in chemical shifts. Systematic deviations in signals of backbone protons to the higher or lower field mean that corresponding backbone region is a part of an α- or β-structure, respectively [5]. Comparison of ^{1}H and ^{13}C spectra can give an evidence of similarity or dissimilarity of molecular conformations in different solvents. Proton spectra are sensitive to local environments (including solvent effects), while ^{13}C resonances depend mainly on local conformations. In general, ^{13}C NMR spectra of CsA in apolar solvents and in micellar solution are similar (fig.2). The sequence of the C^{α} signals in all three media is this: residue 1 (formally also 12) is the leftmost, then we observe 11 and 10; closely located three signals 4, 5, and 6; after an

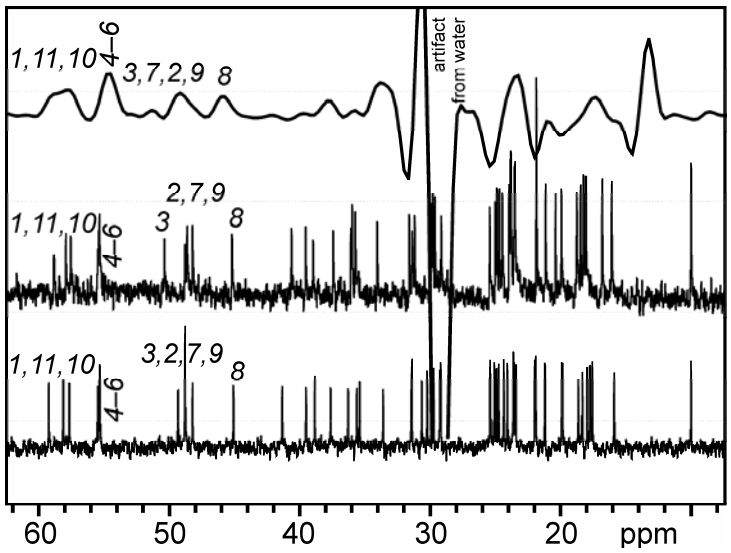

Fig.2. Comparison of ^{13}C spectra of CsA in three media: top, complex with SDS micelles (projection from an HSQC spectrum); middle, chloroform; bottom, benzene.

empty interval of ~5 ppm stand signals of residues 3, 2, 7, 9, and 8. Proton spectra, despite their narrow frequency range and relatively big variations in chemical shifts, can also be identified. For instance, the α-proton of Mle^{9} resonates always in the lowest field, while that of Ala^{7}, in the highest field. We can thus expect that local conformations of each amino acid residue undergo subtle changes when going from one apolar medium to another.

Two-dimensional NOE spectroscopy provides information for constructing a model structure of cyclosporin. Analysis of NOESY spectra was made following [6, 7]. Intensity of a cross-peak of the nuclei a and b is normalized by intensities of corresponding diagonal peaks (standing in the cross-section with the same indirect frequency F1). After that, dependencies of intensities on the mixing time $I(F_{1a},F_{2b})/I(F_{1a},F_{1a})=f(\tau_m)$ are built. Atom pair $Ala^{7}(H^{\alpha}\text{-}H_3^{\beta})$ was chosen for calibration. Corresponding distance is 2.8 Å, according to the jump model of averaging [8]; simpler averaging models yield lesser values (by 0.1–0.2 Å). For the NCH_3-groups, averaging $R=(\langle R_{ij}^{-3}\rangle)^{-1/3}$ was used (see [9]).

One hundred structures were generated in the simulated annealing protocol; ten of them, having minimal energies, were selected. They are moderately close to each other; RMSDs between the lowest-energy structure and remaining nine molecules in positions of backbone atoms lie from 3.1 to 4.8 Å. Some violations were observed: $Mle^{10}(H^{\alpha})$–$Mva(H^{\beta})$, $Mle^{10}(NCH_3)$–$Mle^{9}(H^{\alpha})$ (after averaging the distances to the methyl protons), $Mle^{6}(NCH_3)$–$Ala(H^{\alpha})$, and $Sar(NCH_3)$–$Bmt(H^{\alpha})$ were all longer that the NOE-based values. Analysis of NOEs underestimates the distances due to spin diffusion, when the coherence is transferred between atoms a and b via one or several intermediate atoms; the apparent cross-relaxation rate has no clear correlation with the distance r_{ab} in this case. We repeated the simulation, having omitted the incorrect distances. The new ten structures with minimal energies showed backbone RMSDs from 2.6 to 4.6 Å. Fig.3 presents one of them (with the lowest energy) compared with the structure of cyclosporin in chloroform, modelled allowing for hydrogen bonds.

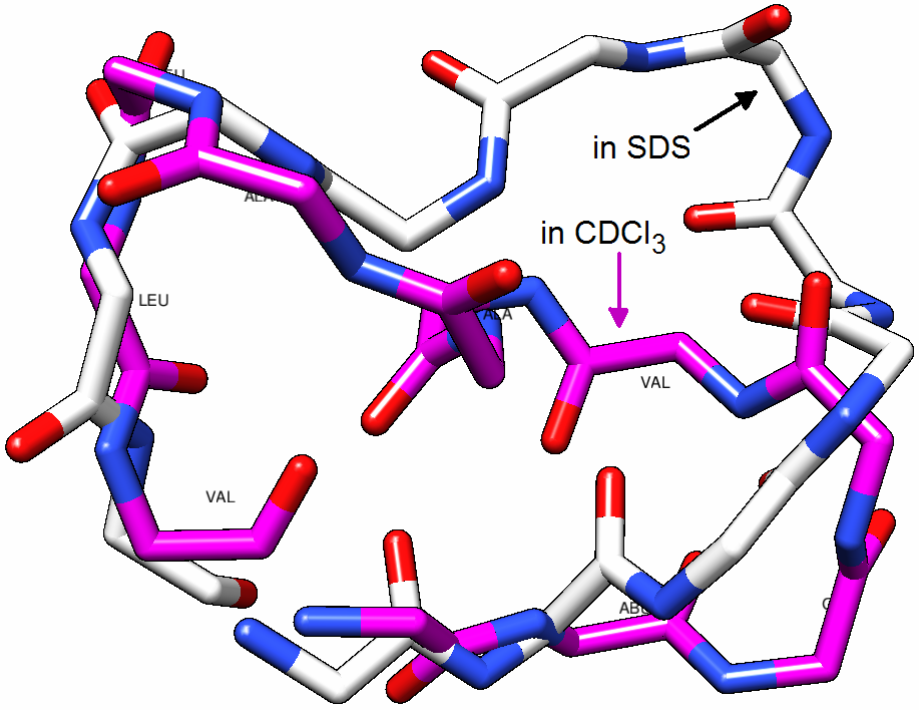

Fig.3. Comparison of the CsA structures based on NOE data obtained in chloroform and in complex with SDS micelles. Illustration was prepared in the Chimera programme [10].

Conclusions

Several conformers of cyclosporin coexist in micellar solution based in SDS. Structure of the main conformer was determined with the aid of the NOESY method. The peptide ring is nearly planar; some differences compared to its structure in apolar organic solvents were found. Close contacts of Bmt H^{α} with α-protons of Mle^{6} and Ala^{7} are absent. The ring of cyclosporin becomes less oblate; chain regions with residues 9–11,1 and 4–6, which in chloroform are close to each other and resemble β-structure, move off from each other in the complex. This change may be due to steric interaction with SDS molecules which prevents formation of intramolecular hydrogen bonds. Note also that H^{α} chemical shifts in the micellar solution are, in general, smaller that in organic solvents. It gives an evidence of additional shielding of the peptide by surrounding detergent molecules.

Acknowledgements

Certain part of the work was performed in Leipzig University under the auspices of the "Evgenii Zavoiskii" grant of the Ministry of Science and Education of the Republic of Tatarstan and Deutscher Akademischer Austauschdienst.

References

[1] Evidence for a functional receptor for cyclosporin A on the surface of lymphocytes / N.A. Cacalano [et al.] // Proc. Natl. Acad. Sci. USA. – 1992. – Vol. 89. – P. 4353-4357.

[2] Henry, G.D. Methods to Study Membrane Protein Structure in Solution / G.D. Henry, B.D. Sykes // Meth. Enzymol. – 1994. – Vol. 239. – P. 515-535.

[3] The Xplor-NIH NMR molecular structure determination package / C.D. Schwieters [et al.] // J. Magn. Reson. – 2003. – Vol. 160. – P. 65-73.

[4] Kessler, H. Conformation and biological activity of cyclic peptides / H. Kessler // Angew. Chem. Int. Ed. – 1982. – Vol. 21. – P. 512-523.

[5] Wishart, D.S. The Chemical Shift Index: A Fast and Simple Method for the Assignment of Protein Secondary Structure through NMR Spectroscopy / D.S. Wishart, B.D. Sykes, and F.M. Richards // Biochemistry. – 1992. – Vol. 31. – P. 1647-1651.

[6] Macura, S. An improved method for the determination of cross-relaxation rates from NOE data / S. Macura, B.T. Farmer II, and L.R. Brown // J. Magn. Reson. – 1986. – Vol. 70. – P. 493-499.

[7] Hu, H. Revisiting the initial rate approximation in kinetic NOE measurements / H. Hu, K. Krishnamurthy // J. Magn. Reson. – 2006. – Vol. 182. – P. 173-177.

[8] Treatment of NOE constraints involving equivalent or nonstereoassigned protons in calculations of biomacromolecular structures / C.M. Fletcher [et al.] // J. Biomol. NMR – 1996. – Vol. 8. – P. 292-310.

[9] Brünger, A.T. XPLOR (Version 3.1). A System for X-ray Crystallography and NMR / A.T. Brünger. – New Haven : Yale University, 1992. – XVIII, 418 p.

[10] UCSF Chimera – a visualization system for exploratory research and analysis / E.F. Pettersen [et al.] // J. Comput. Chem. – 2004. – Vol. 25. – P. 1605-1612.

Structural and dynamic properties of a channel protein transmembrane segment studied using solid-state NMR

A.V. Khaliullina[1], S.L. Grage[2], S. Afonin[2], P. Wadhwani[2], A.S. Ulrich[2,3]

[1]Kazan Federal University, Kremlevskaya 16a, 420008, Kazan, Russian Federation.

[2]Karlsruhe Institute of Technology, Institute of Biological Interfaces (IBG-2), P.O. Box 3640, D-76021 Karlsruhe, Germany

[3]Karlsruhe Institute of Technology, Institute of Organic Chemistry, Fritz-Haber-Weg 6, D-76131 Karlsruhe, Germany.

e-mail: aliyakhaliullina@gmail.com

The bacterial Mechanosensitive channel of Large Conductance (MscL) is a membrane protein that acts as "safety valve", opening a water-filled pore across the membrane in response to mechanical stress (fig.1a) [1]. MscL consists of five subunits which form an aperture-like transmembrane pore lined by five "M1" helices. It has been shown that even without the loops connecting M1 to the residual protein components, MscL possesses a mechanosensitive gating property [2, 3]. Hence the M1 segment seems to play an important role in mechanosensitivity. In this study, we have examined the isolated M1 segment as a simplified model of the channel protein, to gain insight into the possible mechanism of pore opening and closing of MscL, and into the general design principles of helix oligomerization in membranes. To this aim the isolated M1 segments were ^{2}H-labeled with Ala-d_3 in four amino acid positions to probe the local helix orientation and dynamical properties in membranes using solid-state ^{2}H-NMR. To obtain orientational information, quadrupolar splittings were measured in mechanically oriented bilayer samples.

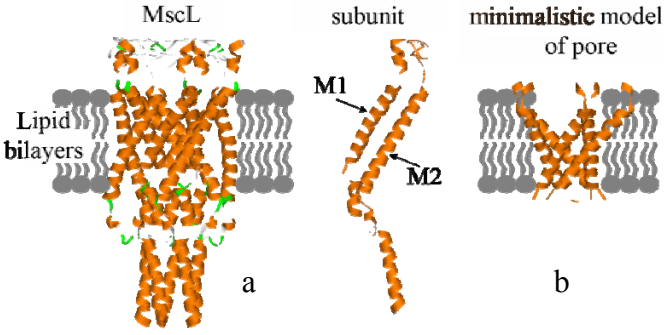

Fig.1. (a) Structure of the *E. coli* MscL homo-pentamer in the closed state (H. Robert Guy [4]). Each MscL subunit contributes two transmembrane helical segments, M1 and M2. (b) Model of a minimalistic pore lined by five M1 segments.

By analyzing the deuterium quadrupolar coupling of the four labeled positions, we found that in liquid-crystalline lipid bilayers the pore-forming transmembrane segment M1 of MscL adopts a tilted state with a tilt angle $\psi \approx 28°$ between the helix axis and the membrane normal (fig.2). This alignment is in good agreement with the respective tilt angle ψ for the M1 helix in the context of the full-length MscL protein, which is 30° [1]. This result indicates that the individual M1 segment is oriented in the same way as when part of the pore forming helix bundle of the full-length MscL protein.

To obtain information about dynamical behaviour of M1, the rotational correlation time τ_c of the membrane-bound molecule was determined by measuring ^{2}H transverse relaxation times. According to the value of $\tau_c \approx 18$ μs extracted from the T_2 relaxation time analysis, M1 segments

possess a low molecular mobility, which is compatible with the formation of oligomeric structures in membrane.

In summary, using solid-state ^{2}H-NMR, we determined the alignment of the pore-forming segment of MscL in the membrane with an almost upright tilt angle of 28° and a rotational correlation time of 18 μs. The isolated transmembrane helical M1 segment thus exhibits structural and dynamical properties that fit well with a pore forming helix bundle, just like M1 in full-length MscL. The oblique tilt together with the slow motional time scale appears to be compatible with the formation of oligomeric peptide bundles in membrane. This could imply an important role of the M1 segment for the self-assembled of the homo-pentameric pore of MscL. The details of this study will be published in full length elsewhere.

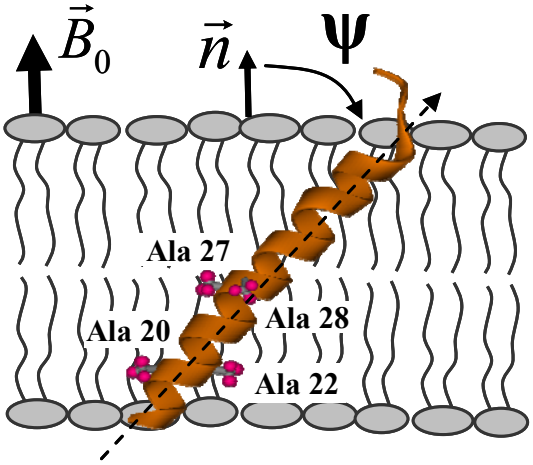

Fig.2. Representation of the alignment of the M1 segment in lipid bilayers. The tilt angle ψ is defined as the angle between the membrane normal $\vec{n}$ and the helix axis. B_0 is the applied magnetic field direction.

Acknowledgments

This work has been supported by the Center for Functional Nanostructures (CFN, TP E1.2 and E3.4) and the Helmholtz Association.

References

[1] Perozo E. Gating prokaryotic mechanosensitive channels / E. Perozo. // Nature reviews| Molecular cell biology – 2006. – V. 7. – P. 109–119.

[2] Ajouz B. Contributions of the Different Extramembranous Domains of the Mechanosensitive Ion Channel MscL to its response to membrane tension / B. Ajouz, C. Berrier, M. Besnard, et al. // J. Biol. Chem. – 2000. – V. 275. – P. 1015-1022.

[3] Park K.-H. Purification and functional reconstitution of N- and C-halves of the MscL channel. / K.-H. Park, C. Berrier, B. Martinac, et al. // Biophysical J. – 2004. – V. 86. – P. 2129–2136.

[4] Sukharev S. Structural Models of the MscL Gating Mechanism / S. Sukharev, S.R. Durell, H.R.Guy. // Biophysical J. – 2001. – V. 81. – P. 917–936.

Preliminary NQR studies of Cu_3SbS_3

I.A. Evlampiev, R.R. Gainov, A.V. Dooglav, I.N. Pen'kov

Kazan (Volga Region) Federal University, 420008, Kremlevskaya 18, Kazan, Russia

e-mail: Ilya.Evlampiev@ksu.ru

$Cu_xSb_yS_z$ system is a potential absorber material for thin film solar cells. In this report we present NQR study of Cu_3SbS_3, skinnerite at temperatures 4.2 – 77 K. The Cu_3SbS_3 compound has polymorphs, below 263 K it has wittichenite structure (Ws), and between 263 K and 395 K it has skinnerite structure (Sk) [1]. The NQR study for Cu_3SbS_3 Sk structure was performed by Abdullin et al [2], thus revealing three non-equivalent Cu sites. The Cu_3SbS_3 Ws exhibits only two sites with non-equivalent copper sites below 77 K, that is in accordance with NQR data on wittichenite proper (Cu_3BiS_3)[3].

The temperature dependence of Sb NQR reveals that a kind of structural transition can be observed at the temperature about 15 K. This structural transition manifest itself via changing in slope of NQR frequencies and asymmetry parameter, thus resembling a structural transition that occurs in copper sulfides below the liquid nitrogen temperature [4, 5].

This work is partly supported by RFBR grant under No. 12-02-31282 (mol_a).

References

[1] C. Tablero, Solar Energy Materials & Solar Cells. 104, 180 (2012)

[2] R.S. Abdullin et al.,Doklady Akademii Nauk SSSR. 218, 4, 859 (1974)

[3] Pen'kov I.N. et al. Semicond. Izvestiya Akademii Nauk SSSR, Seriya Fizicheskaya. 42, 10, 2105 (1978)

[4] R.R. Gainov et al. Pys. Rev. B, 79, 075115 (2009)

[5] I.A.Evlampiev et al. Actual Problems of Magnetic Resonance and its applications. XII International Youth Scientific School, Kazan 5-9 October, 2009, Proceedings, p. 192-195.

Low-field NMR studies of gadolinium based contrast agents

N.A. Krylatykh, I.A. Nurmamyatov

Zavoisky Physical-Technical Institute (ZPhTI) of the Kazan Scientific Center of the Russian Academy of Sciences, 420029, Kazan, Russian Federation

e-mail: el-a-nur@yandex.ru

In magnetic resonance imaging medical methods, the signal from hydrogen nuclei is registers. In different tissues, hydrogen nuclei has different spin-lattice and spin-spin relaxation times (T1 and T2 times), what allows to differ tissues on MR images by adjusting imaging protocols, i.e. to contrast tissues by relaxation times. In some cases contrast agents (CA) injects into blood. CA are salts and chelates of strong paramagnetic ion (just like gadolinium).

Contrast of images were made with CA in high magnetic and low magnetic fields is very different [1]. This work is focused on different CA contrast in different magnetic fields.

Contrast of images depends on proportion of signals amplitudes from tissues, in spin-echo signal. (fig.1)

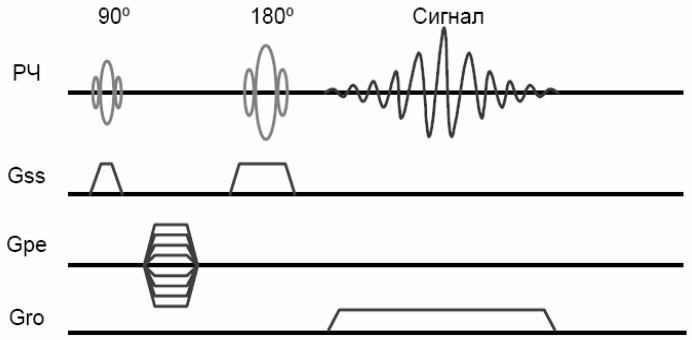

Fig.1. Pulse sequence Spin-Echo.

Proportion of signals amplitudes also depends on relaxation times of hydrogen nuclei. As we know from nuclear magnetic resonance theory, relaxation processes in low fields are occur faster, than in high fields. Contrast agents reduce T1 and T2 relaxation times. [2] As was shown by measurements, water solutions of CA “Gadovist” have the same value of T1 and T2 relaxation times. In this work was made mathematical model by MRI simulator “ODIN” and it shows that contrast in different fields should not be different (fig.2).

Each phantom has two areas with different concentration of solution – 0.2 and 0.6 mmol/l. Structure of phantoms is the same for field 9.4 T and 0.06 T. Modeling was made with repetition time 300 msec and echo time 23.4 msec.

As you can assume from these results, it is possible to make diagnostic images more effectively in low fields by using lower concentrations of CA. Researches shows that we can decrease CA concentration without decreasing of diagnostic information. This effect is due to the fact that when magnetic field strength increases, relaxation times also increase, however as experimental data shows influence of CA on relaxation times is non-linear for magnetic field strength variation.

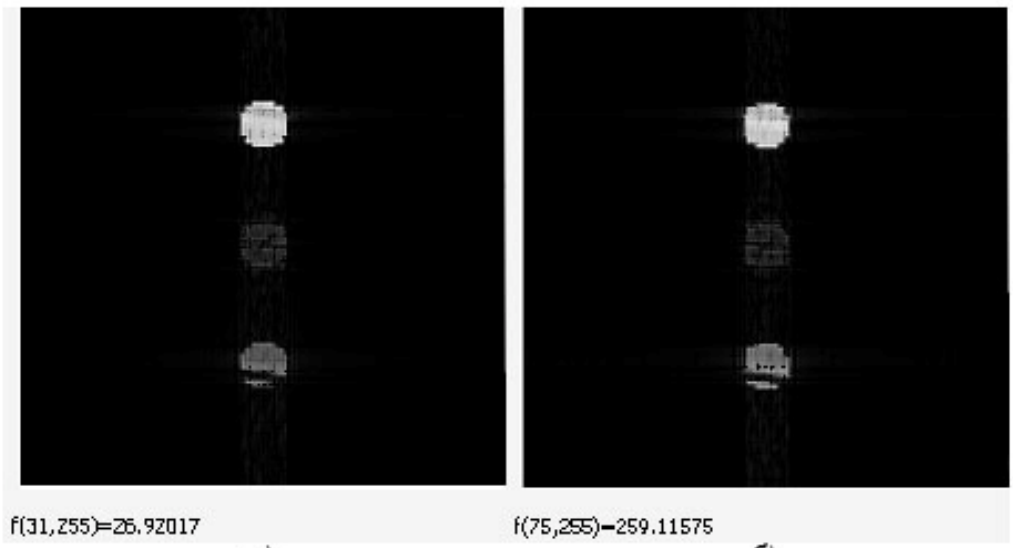

Fig.2. Phantom "ODIN'" in field 9.4 T (a) and in field 0,06 T (b).

General researches were made on ultralow field MR system TMR-KFTI with magnetic field strength 0.06 T and NMR spectrometer of high resolution "AVANCE 400". Results are presented in table 1.

Table 1. Experimental data

Concentration of solution mmol/l	T1 in 9.4 T field (msec)	T1 in 0.06 T field (msec)
0.0	2656	2486
0.1	1100	740
0.2	800	540
0.3	480	280
0.4	340	270
0.6	290	190
1.2	160	104

Also in this work relaxation times of different gadolinium chemicals solutions were measured on mr-system TMR-KFTI with field strength 0.06 T, results of measurements are presented on fig.3 and fig.4.

From all above you can make conclusion that efficient relaxation time decreasing in ultralow fields is coming with concentrations near 0.3-0.4 mmol/l, but producer of CA recommends concentrations 0.6 mmol/l and higher. Another demonstration of this effect is an images of different solutions in different magnetic fields. (fig.5) The pictures were made on MR system GE SIGNA with magnetic field strength 1.5 T and MR system TMR-KFTI with magnetic field strength 0.06 T. Capturing was made at the same pulse sequence parameters.

In ultra low magnetic resonance imaging systems CA influence on tissue contrast is optimal with lower concentrations, than recommended dosage, and more effectively than in MR-systems with high magnetic field strength.

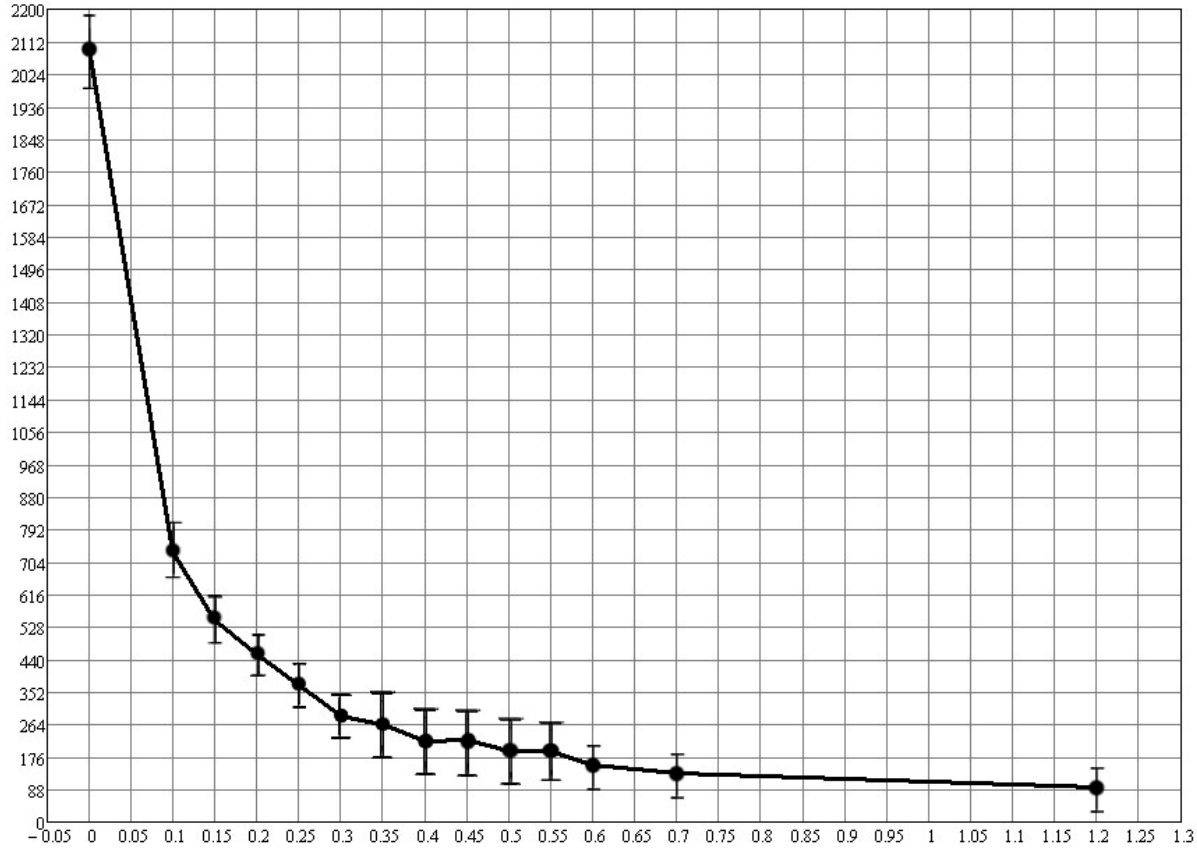

Fig.3. T1 relaxation time dependence on Gd chelates concentration in solution.

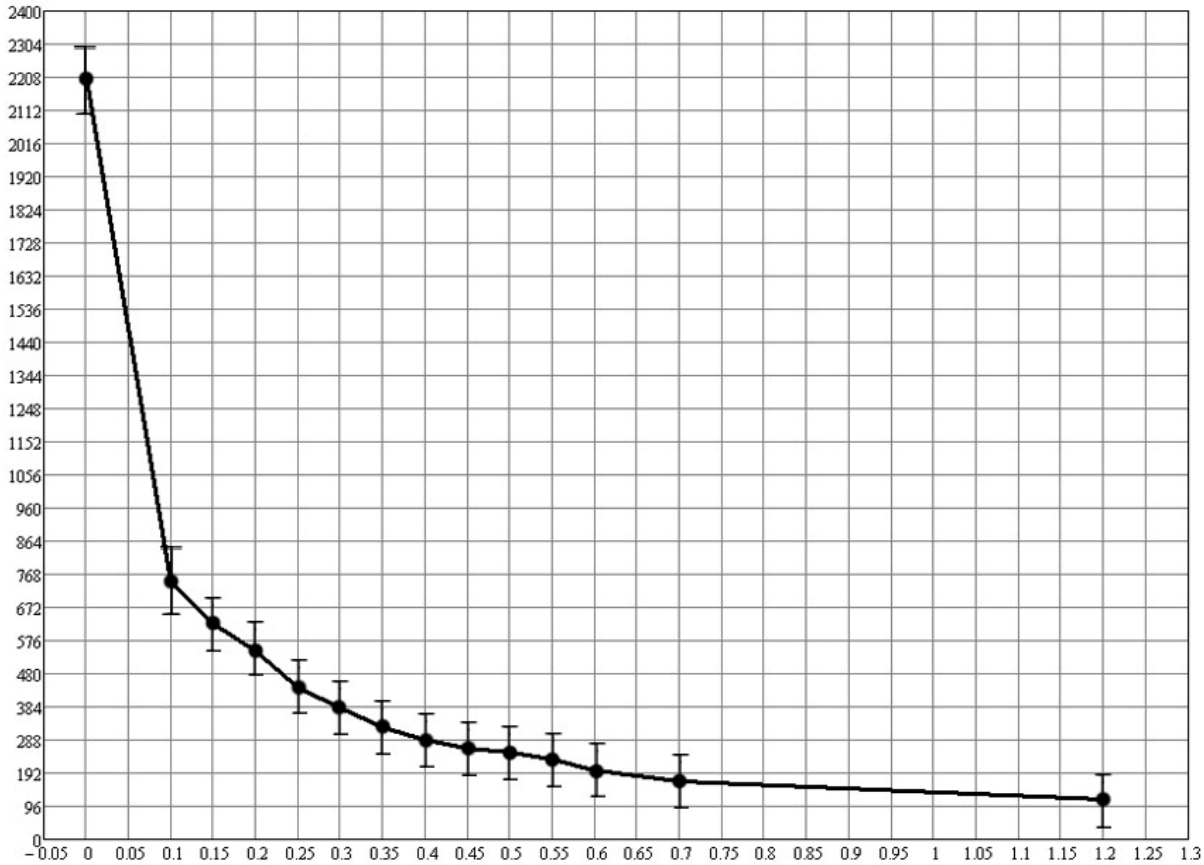

Fig.4. T2 relaxation time dependence on Gd chelates concentration in solution.

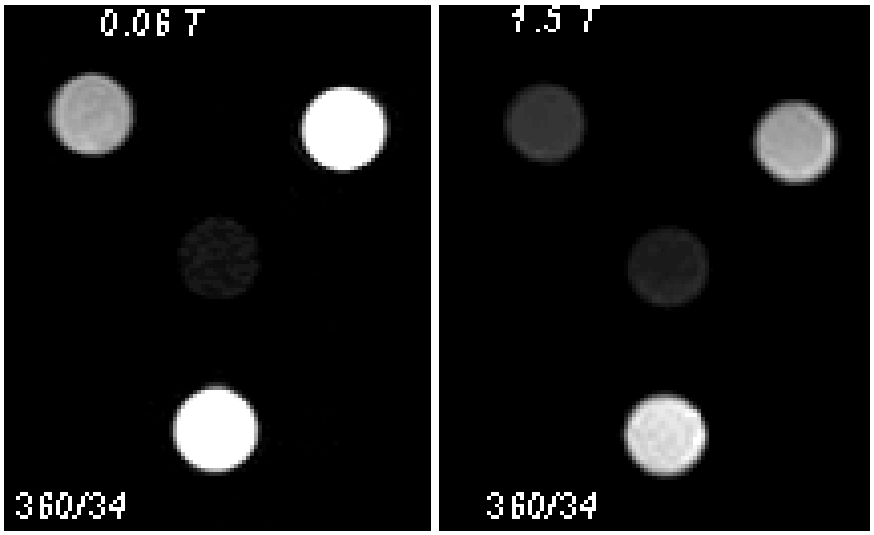

Fig.5. Images of solutions with different concentration of CA. In the centre tube with distilled water, from up-left corner by clock: 0,1 mmol/l, 0,3 mmol/l, 0,6 mmol/l respectively.

References

[1] Балакин В.Е., Биктимиров Э.Ф., Гилязутдинов В.А., Жаворонков А.Е., Салихов К.М., Сахапова Л.Р., Фаттахов Я.В., Хабиров Р.А., Хасанов Р.Ш., Хафизов Р.Т., Юсупова Л.Р. Исследование эффективности визуализации с применением контрастных веществ в низкополевой томографии//Онкохирургия. -2009.-№2.-с.86

[2] Rink P., ed. *Magnetic resonance in medicine* // Oxford. – 1993 – 228c.

Imaging using polarised ^{3}He at low magnetic fields

K.R. Safiullin[1,2], P.-J. Nacher[2]

[1]Institute of Physics, Kazan Federal University, 420008, Kremlevskaya, 18, Kazan, Russia

[2]Laboratoire Kastler Brossel, Ecole Normale Supérieure, 75005, 24 rue Lhomond, Paris, France

e-mail: kajum@inbox.ru

Magnetic resonance imaging (MRI) is a non-invasive technique based on the nuclear magnetic resonance phenomena and used to visualize structure of the objects. Lung MRI using polarised ^{3}He gas provides an information about gas flow in the airways, lung ventilation properties, lung function (by O_2 concentration measurements) and lung microstructure (by diffusion measurements).

Most of the lung MRI studies using ^{3}He gas have been made at 0.1-3 T magnetic fields on standard commercial systems. The use of the polarised gas allows for a high and nearly field-independent signal to noise ratio (SNR) over a broad range of field values. Low magnetic field systems provide several advantages: very long precession times (T_2^*) for NMR signals, low equipment cost, negligible rf-heating of tissues, etc [1, 2]. Only few demonstrations of lung MRI at low fields of order few mT are known [2, 3].

We have build a compact 1:4-scale model of a whole-body imaging to explore the potential of such ultra-low fields. The system includes a resistive magnet, imaging gradient coils, and NMR coils, and operates at magnetic field of 2.7 mT and 85 kHz frequency. Combination of the high detection bandwidth (~10 kHz) requested for imaging and low thermal noise (i.e., high Q-factors) is challenging at this frequency, but was obtained using appropriate detection schemes.

First imaging tests have been made using cylindrical sealed ^{3}He cells (5 cmx5 cm and 1.8 cmx12 cm), polarised in situ by MEOP (metastability exchange optical pumping). Due to low pressures (50-400 mbar), fast diffusion limited the resolution of the images. Further investigations were made on improved samples, sets of two and five refillable interconnected glass tubes (5 cm long, 0.7 cm and 1.1 cm inner diameter). The ^{3}He gas was polarised using the compact MEOP polariser next door and cells were filled using compressor. This allowed to fill the samples under desirable pressure with the highly polarised gas, and consequently this led to higher signal values. Typical values of the avhieved ^{3}He gas nuclear polarisation were 1-4% for low pressure sealed cells and 30-40% for refillable ones.

The imaging abilities of our ultra-low field MRI setup were demonstrated using refillable ^{3}He cells and preserved lungs of a small mammalian. Series of 2D and 3D imaging experiments on lung phantoms were performed and will be reported.

References

[1] Bidinosti C.P. et al., *J.Magn.Reson.*, **162**, 122 (2003).

[2] Tsai L.L. et al., *Academic Radiology*, **15**, 728 (2008).

[3] Bidinosti C.P. et al., *Magn. Reson. Mater. Phy.*, **16**, 255 (2004).

EPR study of the spatial modulation of magnetization in $La_{2-x}Sr_xCuO_4$

V.O. Sahin[1], Yu.I. Talanov[2]

[1]Kazan Federal University, 420008, Kremlevskaya str. 18, Kazan, Russia

[2]Zavoisky Physical-Technical Institute, 420029, Sibirsky tract, Kazan, Russia

e-mail: sakhin.vasily@gmail.com

Introduction

Since it's discovering in 1986, high-temperature superconductivity wasn't explained with a conventional theory. But the fact that some properties, usually observed in superconductor state, remained above T_c [1, 2, 3] makes the description of the magnetic state of superconductor above T_c being very important for understanding high-temperature superconductivity. Previously, the inhomogeneity of distribution of local magnetic fields has been found [4], but the results did not conclusively agree with one of the theoretical models. So the aim of the work was to research the spatial characteristics of inhomogeneities of local magnetic fields in HTSC above T_c and try to correlate results with one of the models of magnetic state. The idea of the work is to use Electron Paramagnetic Resonance (EPR), due to its powerful abilities to study the local magnetic field distribution of any origin.

An object of our research were three single crystals of $La_{2-x}Sr_xCuO_4$ (LSCO) with x=0.077, x=0.116 and x=0.160. In the context of this study important fact is that at low temperatures LSCO undergoes a phase transition from the tetragonal symmetry of oxygen environment of the Cu atom and to orthorhombic one [5]. This leads to formation of domains with different orientation of the anisotropy of the lattice.

Experimental results and discussion

To characterize samples we measured temperature dependence of magnetic AC susceptibility (fig.1). Critical temperature (T_c), corresponding to the middle of the transition from normal to superconducting state, and the full width of the superconducting transition (ΔT_c) were determined from this dependence.

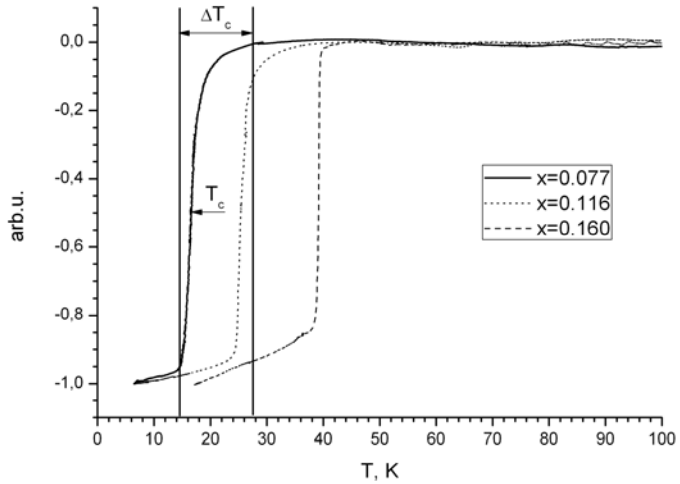

Fig.1. Temperature dependence of magnetic AC susceptibility in $La_{2-x}Sr_xCuO_4$ with different doping concentrations

Width of the EPR signal of LSCO with embedded magnetic centers is over 400 Oe [6] and it is difficult to obtain the effects caused by magnetic state above T_c (which prospective

value is 1-2 Oe). So we used paramagnetic probes with a narrow EPR signal. In this study 2,2-diphenyl-1-picrylhydrazyl (DPPH) applied. Magnetic state of superconductor causes the inhomogeneties of local magnetic fields on the surface of sample. So we used method of vacuum deposition to place DPPH probe on the surface of LSCO crystal. To determine the spatial scale of the irregularities layer of paraffin was applied between the DPPH layer and the surface of the superconductor. By changing the thickness of the paraffin layer, we can determine the maximum distance at which the probe still feel inhomogeneity of a field. Paraffin used in the experiments is chemically pure and has no EPR signal. For a more accurate determination of the resonance field value the LiF crystal with the Li dendrites is used for obtaining the reference signal. EPR signal of lithium and signal from DPPH can be easily separated.

To take account of effects caused by DPPH itself we also deposited layer of paramagnetic on the quartz substrate. We must take into account the demagnetization field of paramagnetic layer, which can make a contribution in the magnitude of resonance field. Fig.2 shows the temperature dependence of resonance field of the EPR signal of DPPH deposited on the quartz substrate.

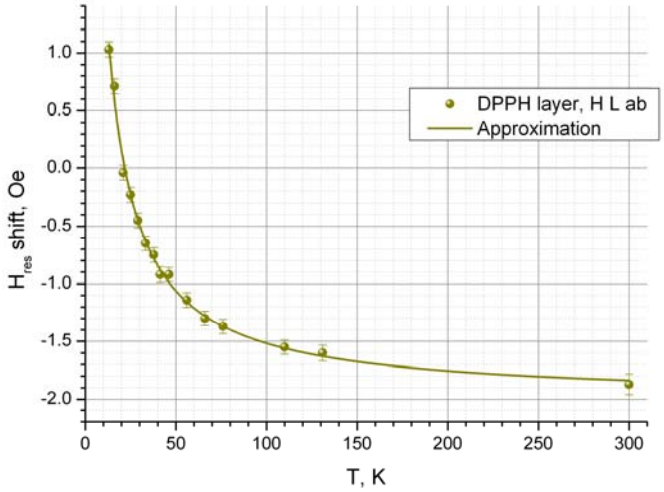

Fig.2. Temperature dependence of the resonance field of the EPR signal of DPPH deposited on glass substrate and approximation by a theoretical function

In the following dependencies of the resonance signal shift with respect to the position of the resonance field of the EPR signal of lithium and contribution of the demagnetizing field of a thin layer of DPPH were subtracted, so the features of dependencies due to the magnetic state of a superconductor only remained. Fig.3 shows the temperature dependence of the line width of the EPR signal of different DPPH layers deposited on a superconductor.

Above T_c the width of the line is approximately the same for both samples. Below T_c the line is broadened. It is due to the superconducting transition and the Abrikosov vortex formation. There is no observable broadening of the line above T_c in both cases (the probe layer on the sample surface and on the distance of 2 mkm from it). So we can propose that the paramagnetic probe is in a uniform magnetic field.

Below T_c the broadening of the signal of probe, placed far from a plane of a sample is greater, than of probe placed on the surface directly. The dispersion of the local magnetic field results in that the different areas of the probe are in a local magnetic field of different magnitude, and the EPR line of the whole probe layer is the sum of lines from different parts of the probe. We can assume that in the case of a probe located on the surface of the superconductor the part of these lines is broadened so that we no longer observe it. Away

from the surface the field becomes more homogeneous, components of the EPR line become narrower, and we can see them. This is confirmed by the normalized temperature dependence of the integral intensity of the EPR signal (fig.4). When removing the probe from the surface the signal intensity increases, as it includes lines not visible at the location of the probe on the surface.

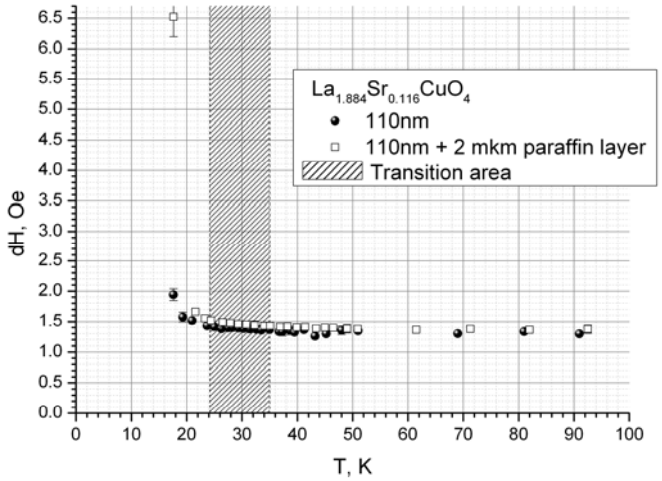

Fig.3. Temperature dependence of the line width of the EPR signal of different DPPH probes for samples with x=0.116

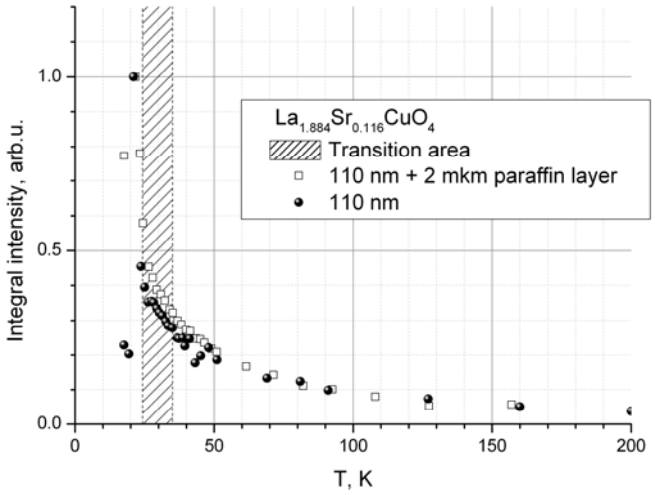

Fig.4. Temperature dependence of the normalized integral intensity of the EPR signal of different DPPH probes for samples with x=0.116.

Fig.5 shows the temperature dependence of the EPR signal shift for DPPH deposited on a superconductor.

The shift of the resonance signal towards the low-field region clearly indicates that the local magnetic field at the surface of a superconductor at temperatures above T_c is greater than the external magnetic field, as the peculiar field of a superconductor is added to the external field. Further, even at a distance of 2 mkm from the sample surface the shift of the resonance field does not change, that means the spatial scale of the magnetization modulation at the surface of a superconductor being at least more than 2 microns.

We can conclude that the vortex model does not correspond to the experimental data, since the observed shift occurs towards the lower fields, and the expected shift in the case of vortices should be toward the higher fields, as it occurs in case of vortex state of the

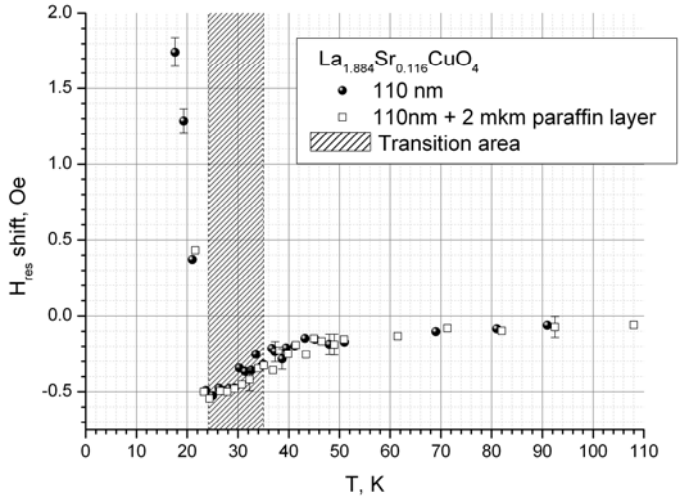

Fig.5. Temperature dependence of the EPR signal shift of different DPPH probes for samples with x=0.116

superconductor at temperatures below the T_c. The model of stripes can be applied in the case of a twinned structure, with the accumulation of the stripes on the domain boundaries, the size of which is about 10 microns. The behavior of the line width with the temperature variation suggests another possibility of the magnetic state of a superconductor at temperatures near the onset temperature of the superconducting transition: the entire sample may have a uniform magnetization. For the final assessment of the scale of the spatial modulation of magnetization it is necessary to continue the study. It will allow us to make the more confident selection of model of the magnetic state of a superconductor at temperatures above the T_c.

References

[1] Patrick A. Lee, Naoto Nagaosa, Xiao-Gang Wen, Reviews of modern physics (2006), vol.78, 17-85

[2] Kenjiro K. Gomes, Abhay N. Pasupathy, Aakash Pushp, Shimpei Ono, Yoichi Ando & Ali Yazdani, Nature B(2007) Vol. 47 569-572.

[3] Y. Wang, L. Li, N. Ong, Phys. Rev. B.73, 024510 (2006).

[4] V. Sahin, L. Salakhutdinov, Yu. Talanov, "ESR Research of High-temperature Superconductor Bi2Sr2Ca1-xYxCu2O8", "Actual problems of magnetic resonance and its application" Program Proceedings (2011) 38-42

[5] Arnold R. Moodenbaugh Superconductivity and structure in $La_{2-x}M_xCuO_4$, M=Ba,Sr and (Nd,Sr), Studies of High Temperature Superconductors (2000), V.33, 157-181

[6] B.I. Kochelaev, G.B. Teitel'baum, Nanoscale properties of the superconducting cuprates probed by the Electron Paramagnetic Resonance, Superconductivity in Complex Systems(2005) V.114 205-266

Magnetic resonance of $GdMnO_3$

J.V. Mamedov[1], I.V. Yatsyk[2], R.M. Eremina[2], T.P. Gavrilova[2], Ya.M. Mukovskii[3], H.-A. Krug von Nidda[4]

[1]Kazan (Volga Region) Federal University, 420008, Kremlyovskaya st., Kazan, Russia

[2]E. K. Zavoisky Physical-Technical Institute RAS, 420029, Sibirsky tract, Kazan, Russia

[3]Moscow Institute of Steel and Alloys, 119049, Leninskii pr., Moscow, Russia

[4]Experimentalphysik V, Elektronische Korrelationen und Magnetismus, Universität Augsburg, 86135 Universitätsstr. 1, Augsburg, Germany

e-mail: javi-m@yandex.ru

Recently there has been an increasingly growing interest in the substances, where the magnetic and electric degrees of freedom are linked (multiferroics). This is due not only to new physical properties of these substances, but also the ability to control their condition with the help of external magnetic or electric fields, which opens up good prospects for the creation of new functional materials and devices based on them. The literature discusses several models to explain the coexistence of magnetic and ferroelectric orderings. One of them is a change of symmetry. Distortion in the substance of spatial inversion leads to the formation of modulated spin structures, but it is possible the opposite effect: spatial modulation of spin can lead to the disappearance of the center of symmetry among the elements of crystal symmetry and the appearance of electric polarization. Such a mechanism is believed to be determines the appearance of electric polarization in orthorhombic manganites [1] and explains the control the electric polarization by a magnetic field [2].

We investigated the temperature and angular dependencies of the ESR spectra of $GdMnO_3$ single crystals and $GdMnO_3/LaAlO_3$ thin films in the X- and Q-bands. The ESR spectrum of $GdMnO_3/LaAlO_3$ thin film consists of a group of lines with a strong angular anisotropy (fig.1a).

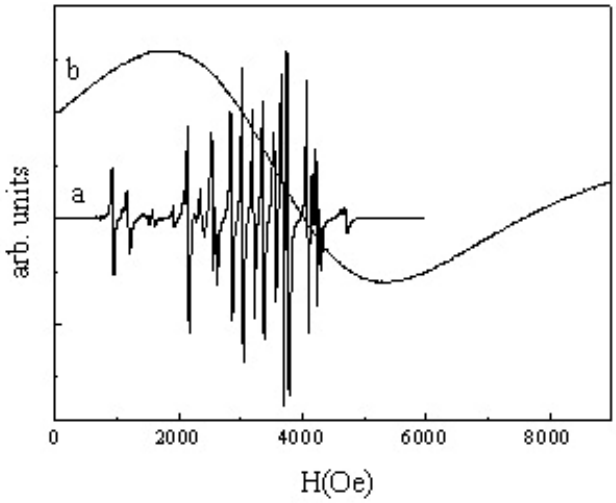

Fig.1. ESR spectra of: a — $GdMnO_3$ monocrystal, b — $GdMnO_3/LaAlO_3$ thin film

We assume that this group of lines refers to the paramagnetic centers Gd^{3+} with $4f^7$ configuration. The angular dependences of this group of lines in X- and Q-bands are presented in fig.2 and can be described in the frame of the following spin Hamiltonian:

$$H = g\mu_B BS + \frac{1}{3}\sum_m (b_2^m O_2^m + c_2^m \Omega_2^m) + \frac{1}{60}\sum_m (b_4^m O_4^m + c_4^m \Omega_4^m) + \frac{1}{1260}\sum_m (b_6^m O_6^m + c_6^m \Omega_6^m),$$

where μ_B – Bohr magneton, b_n^m, c_n^m – fine-structure parameters, O_n^m, Ω_n^m – Stevens spin operators.

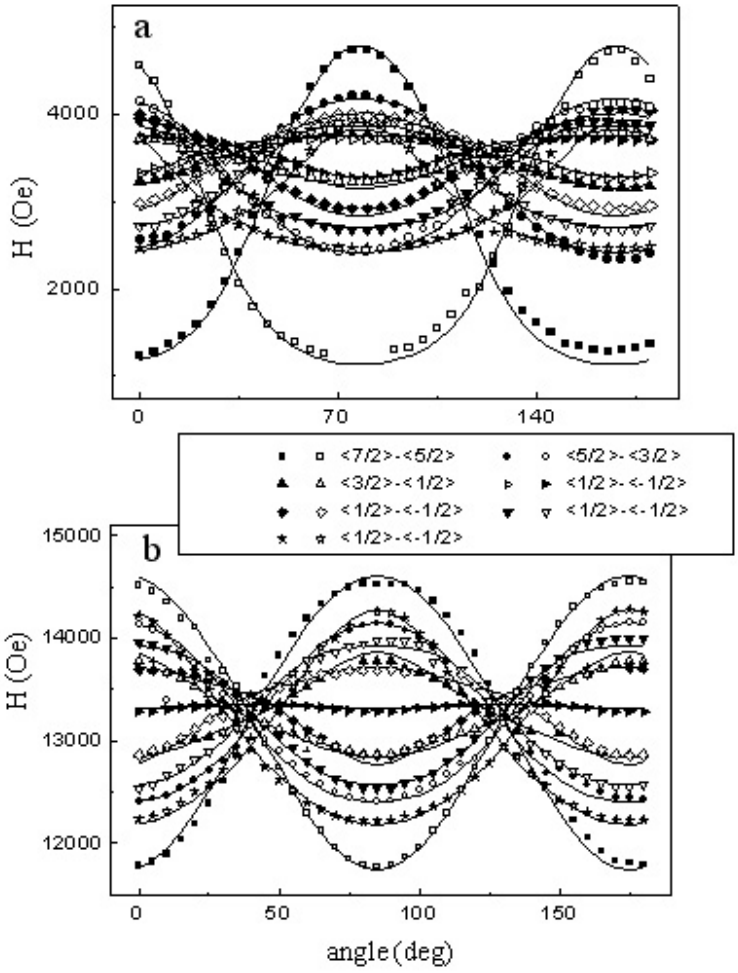

Fig.2. Angular dependencies of the positions of the ESR lines in $GdMnO_3/LaAlO_3$ thin film: a X-band, b - Q-band. Symbols - experimental data, lines - theoretical calculations.

The analysis showed that the experimental angular dependences of the position of the ESR lines in X- and Q-bands are described well by the following parameters (10^{-4} cm^{-1}): b_2^0=192±1; b_2^2=62±1; c_2^2= -179±1; b_4^0= –4±1; b_4^2= –4±1; b_4^4=8±1; b_6^0=5.6±0.5; g_y = 1.995; g_z=1.965 [3]. We took into account that there are two types of paramagnetic centers, which are rotated relative to each other in the plane (ab) by 90º, and the third paramagnetic center, which is rotated relative to the first by 85º.

The temperature dependence of the ESR spectrum of $GdMnO_3/LaAlO_3$ thin film at 4.2 K to 250 K is presented in fig.3. It should be noted, that the positions of resonance lines are moved at the temperature range 50-250 K and they do not move below 50 K. It is interesting that there is the phase transition at the temperature 40 K in monocrystal $GdMnO_3$. And this transition can possibly influence to the temperature behavior of Gd^{3+} ions in $GdMnO_3/LaAlO_3$ thin film.

The ESR spectrum of $GdMnO_3$ monocrystal consists of one exchange narrowed line (fig.1b). The temperature dependence of the ESR linewidth in $GdMnO_3$ is presented in fig.4.

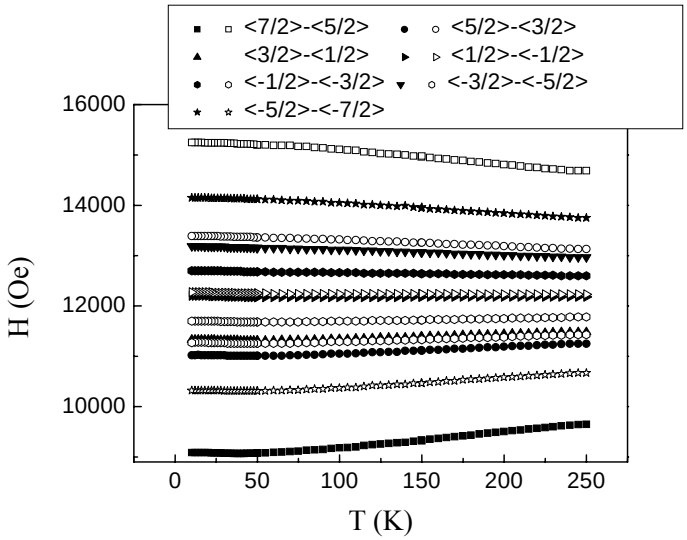

Fig.3. Temperature dependence of the ESR spectrum of $GdMnO_3/LaAlO_3$ thin film in Q-band.

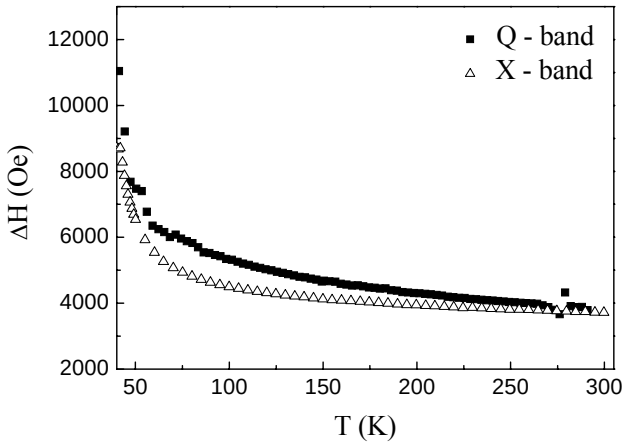

Fig.4. Temperature dependence of the ESR in $GdMnO_3$ monocrystals linewidth in X- and Q-bands.

The ESR linewidth decreases monotonically in range from 40 K up to room temperature. We can't tell about absolute value of the ESR linewidth for temperature below 40 K, because it is comparative with the value of resonance magnetic field in X-band. The difference of the ESR linewidth between X-band and Q-band decreases with increasing temperature. Position of the ESR line for single crystal doesn't dependent on of temperature for region above 40 K. Effective g-factor is about 1.92.

In summary, we investigate the temperature and angular dependencies of the ESR spectra of $GdMnO_3$ single crystals and $GdMnO_3/LaAlO_3$ thin films in the X- and Q-bands and also determine spin Hamiltonian parameters for triclinic paramagnetic centre Gd^{3+} ion in $GdMnO_3/LaAlO_3$ system. We suppose that total contribution in the ESR spectra of $GdMnO_3/LaAlO_3$ thin film is due to Gd^{3+} ions which are localized on film-bulk boundary.

References

[1] Kadomtseva A.M., Popov Yu.F., Vorob'ev G.P., et al. JETP Letters, **82**, 590-593 (2005)

[2] Kimura T., Goto T., Shintani H., et all. Nature, **426**, 55-58 (2003).

[3] Yatsyk I.V., Mamedov J.V.,Fazlizhanov I. I., et all. JETP Letters, **96,** 455-459 (2012)

Hydration properties of organic molecules functional groups as studied by NMR-relaxation and quantum chemical calculations

S.O. Rabdano, A.V. Donets

Saint-Petersburg State University, 198504, Ulianovskaya St. 3, Saint-Petersburg, Russia

e-mail: sevastyan@rabdano.ru

Introduction

A clear understanding of interaction of amino-acid functional groups with different environment allows us to understand the formation of the spatial structure of proteins in complicated biological solution and live tissues. This is the subject of this work.

Experiment: NMR-relaxation

Investigated systems are aqueous amino-acids solutions. Water structure in the solution with amino-acids can be described as the superposition of different substructures: hydration shells of functional groups of β-alanine or glycine molecule (methylene, amino and carboxyl) and pure solvent. Relaxation rate should be calculated as a sum of contributions of each substructure. In the case of fast exchange of the water molecules between all substructures, the spin-lattice relaxation of the solvent nuclei in the investigated system is given by expression:

$$R_1(m) = \frac{1}{T_1} = \frac{1}{T_{10}}\left(1 - \sum_{i=1}^{N-1} p_i(m)\right) + \sum_{i=1}^{N-1} \frac{p_i(m)}{T_{1i}} \qquad (1)$$

where m — is amino acid concentration, p_i — relative concentration of i-th substructure, N — number of substructures. The first sum corresponds to pure water and second to hydration shells of amino acid molecule.

The expression (1) predicts the linear concentration dependence of R_1, but experimentally distinct deviations from linearity have been observed. The deviations can be explained by disappearance of some substructures in the solution. At low amino-acid concentration (m) all these substructures of the solution exist. With increase of concentration the amount of pure water decreases. Position of the first bend corresponds to concentration, when all hydration shells become completely filled and the pure water disappears. It can be estimated the number of water molecules in the hydration shells of organic molecule. The examples of the experimental data are presented in fig.2. The hydration shells of β-alanine and glycine consist of 32 and 25 water molecules respectively.

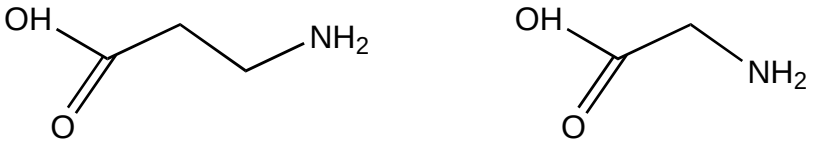

Fig.1. β-alanine (left) and glycine (right) molecules.

The molecules of β-alanine and glycine differ in one methylene group (fig.1). So the difference in the values of deuteron relaxation rates in aqueous solution of these amino acids is determined by water molecules in the hydration shell of this group. As result, the relaxation rate of water deuterons in the substructure near CH_2 group can be obtained. The n_{CH_2} is number of D_2O molecules in hydration shell of the methylene group. Glycine and β-alanine hydration shells consist of 25 and 32 water molecules (fig.2). The difference in the

coordination numbers of these organic molecules is the coordination number of CH_2 group, so $n_{CH_2} = 7$.

$$R_1^{CH_2} = \frac{1}{T^{CH_2}} = \left(\frac{1}{T_{10}} + \frac{R_1^{Alanine} - R_1^{Clycine}}{p_{CH_2}} \right)\Bigg|_{T=2^\circ C} = 7.798\ s^{-1} \qquad (2)$$

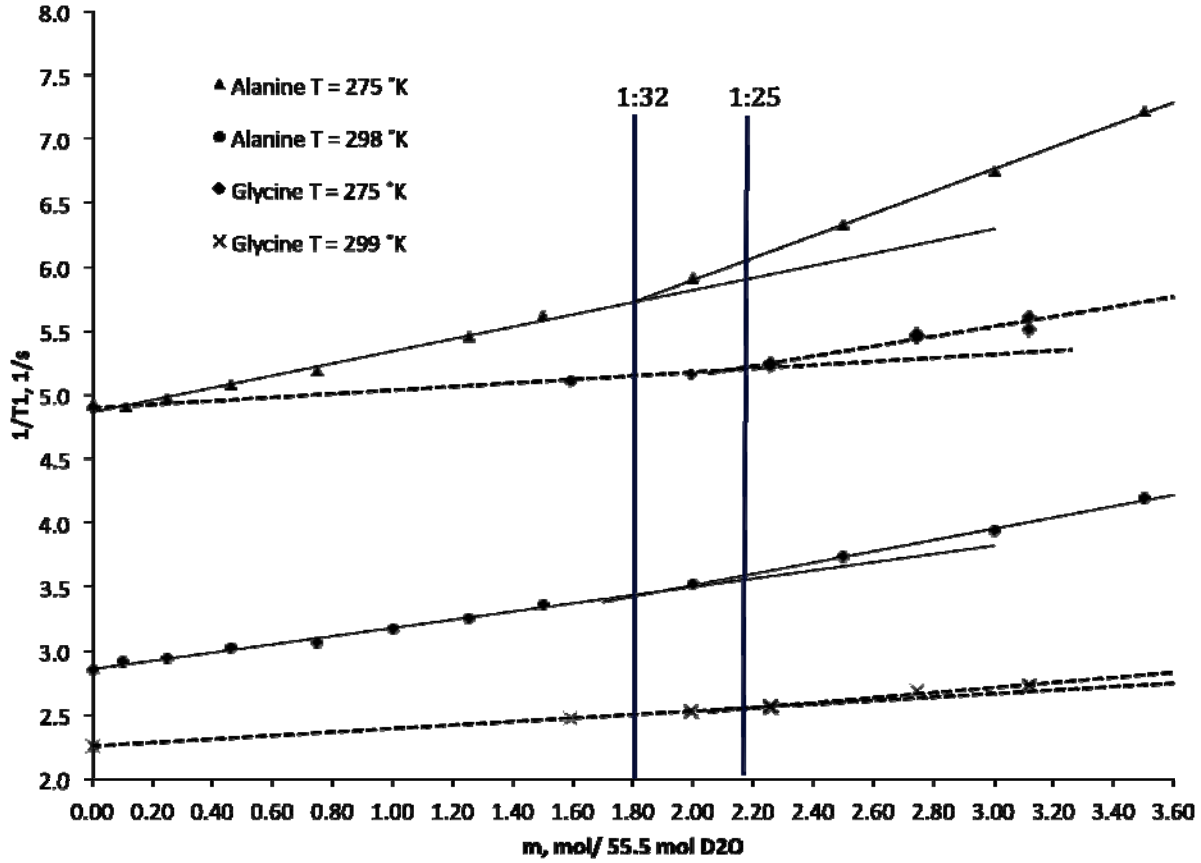

Fig.2. Concentration dependences of deuteron spin-lattice relaxation rates in water solutions with beta-alanine and glycine at different temperatures.

Quantum chemical calculations

The detailed study of the microstructure of the β-alanine hydration shells was performed by quantum chemical calculations. Firstly, to find the system with the lowest energy, the single amino acid molecule was optimized with ROHF 6-31G level of theory, then water were added by 2 - 3 water molecules, and the calculations of the optimal geometry were carried out. These processes were repeated and the complete structure of the alanine environment consists of 39 H_2O.

The cluster [β-alanine + $(H_2O)_{39}$] was optimized with density functional theory calculations, using 6-311++G** basis set. The parameters of the cluster microstructure were calculated. Some results of geometry optimization are presented in fig.3.

The coordination numbers, obtained on the basis of quantum-chemical calculations (Table 1), is in a very good agreement with those obtained experimentally. Values of quadrupole coupling constants of the water deuterons located near particular functional groups of the amino acid molecules are presented in Table 2.

Table 1. The coordination number of functional groups of amino acids, obtained by quantum chemical calculations.

Substance	**–COO^-**	**–CH_3**	**–CH_2–**	**–NH_3^+**
β-alanine	4-6	-	7	3
Glycine	4-6	-	7	3

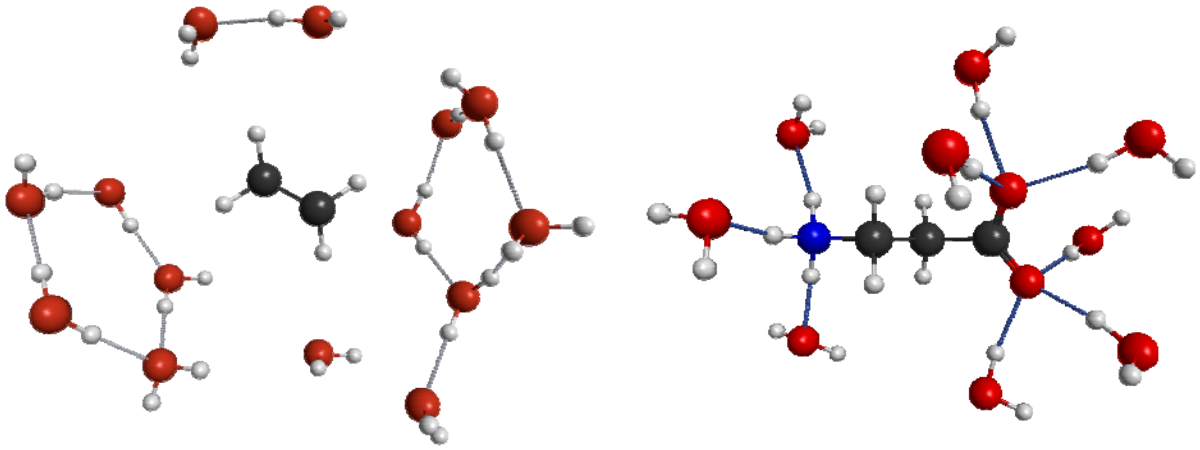

Fig.3. Hydration shells of functional groups of β-alanine (methylene groups — left, amino and carboxyl groups — right). System: β-alanine + $(H_2O)_{39}$. Level of theory: DFT/B3LYP 6-311++G**.

The calculated values of the quadrupole coupling constants of deuterons of "free" water molecule are in agreement with the experiment (255 and 258.6 kHz [3]). The values of the dipole moment of the β-alanine zwitterion form are also satisfactory (19.4 D from [4] and 17.8 D calculated).

Table 2. Absolute and relative deuteron quadrupole coupling constant (χ) of water in the hydration shells of the functional groups of the organic molecules.

Substance	**–COO^-**	**–CH_3**	**–CH_2–**	**–NH_3^+**
χ[β-alanine], kHz	221	-	248	198
χ[β-alanine]/ χ_0	0,90	-	1,01	0,80
χ[glycine]/ χ_0	0,92	-	1,03	0,81

References

[1] Chizhik V.I. Molec. Phys. (1997). 90(4), 653.

[2] Vovk M.A., Pavlova M.S. Chizhik V.I. et al. Rus. J. Phys. Chem. (2011). 85(9), 1715.

[3] Hindman J.C., Zielen A.J., Svirmick A., Wood M. (1971). J. Chem. Phys., 54(2), 621.

[4] Donoian, H. C., Kegeles, G. (1961). J. Am. Chem. Soc., 83(2), 1–5.

Determination of Tris(dibenzylideneacetone)dipalladium Structure and Purity in Solution by Modern NMR Techniques

S.S. Zalesskiy, V.P. Ananikov

N.D. Zelinsky Institute of Organic Chemistry, Russian Academy of Sciences, Leninsky Prospect 47, Moscow, 119991, Russia;

e-mail: s.zalesskiy@ioc.ac.ru

Tris(dibenzylideneacetone)dipalladium(0) is a canonical precursor widely used to generate catalytically active palladium species for diverse applications. For example, these include various coupling reactions such as Suzuki [1] and Negishi [2] cross-coupling reactions, Heck reaction [3]. Ubiquitous utilization of Pd_2dba_3 in transition metal catalysis on one hand was governed by simple preparation from readily available Pd(II) salts [4], on the other hand by relative stability in air and convenient generation of desired PdL_n species.

In contrast with widespread use, a little is known about the structure of the complex in solution. The question is of special importance in view of current studies of cross-coupling, Heck and other catalytic reactions, where determination of the nature of the catalyst (homogeneous catalysis *vs*. heterogeneous catalysis *vs.* leaching) is a challenging problem [5].

It is well known that ^{1}H NMR spectrum of Pd_2dba_3 in solution is rather complex and contains more than 20 resonances (see top projection on fig.1). Signal assignment in the spectrum of such sample using conventional technique would be a difficult and time consuming task. The application of DOSY NMR allowed discrimination of the ^{1}H spectrum of the mixture into principal components (fig.1). Particularly, the signals corresponding to free dba were aligned on horizontal line at log(D) = -9.19 ± 0.05. Other two sets of resonances, distinguished by different intensities, were recorded aligned on the same horizontal line of the DOSY spectrum at log(D) = -9.42 ± 0.13. These signals correspond to the compounds of the same size and according to the diffusion coefficient can be assigned to

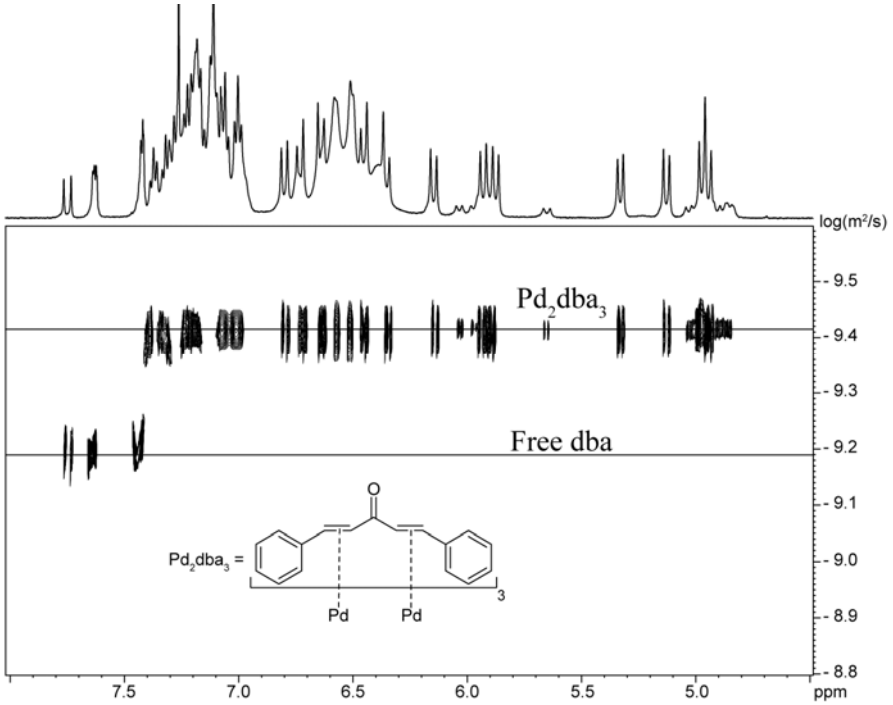

Fig.1. ^{1}H DOSY spectrum of Pd_2dba_3 in $CDCl_3$ solution at 260 K, 600 MHz.

major and minor isomers of Pd_2dba_3 in solution.

Further analysis was performed using 2D COSY experiment in order to identify H-C=C-H olefinic fragments in the complex molecule. The 2D spectrum allowed us to split twelve separate peaks into 6 groups, each representing a HC=CH fragment of coordinated dba molecule. A typical values of $^3J(H_\alpha\text{-}H_\beta)$ = 12.8 Hz suggested preferable E-geometry of the double bonds. The interconnections between these groups were determined by performing LR-COSY experiment optimized for observation of long-range (LR) proton-proton coupling constants (fig.2). Three cross-peaks shown in different colors have aroused due to $^4J(H_\alpha{}^1\text{-}H_\alpha{}^2)$ coupling constant, that binds together two parts of dba molecule across the carbonyl group. This data was further confirmed with $^1H\text{-}^{13}C$ HMBC NMR spectroscopy.

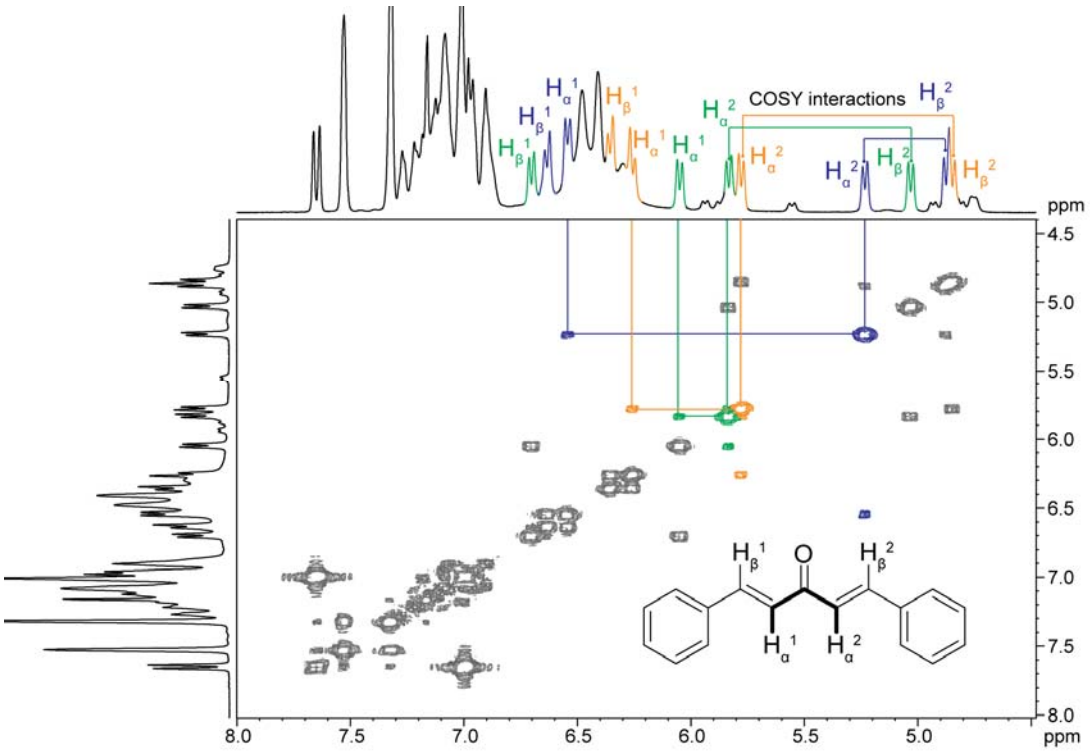

Fig.2. Olefinic part of the LR-COSY correlation of Pd_2dba_3 in $CDCl_3$ at 600 MHz; the key long-range cross-peaks are marked by colors for three different dba molecules in complex. Relevant COSY interactions helpful to bind two HC=CH systems together are shown on the top projection.

Thus, we have assigned each of twelve peaks to corresponding olefinic protons in Pd_2dba_3 molecule. Long range correlation allowed us to identify each of three molecules individually. On the second step we had to determine the relative conformation of the dba molecules in the complex. Consequently, we have employed a 2D nuclear Overhauser effect spectroscopy to map the conformations of the dba units in Pd_2dba_3 (fig.3). The recorded 2D NOESY spectrum clearly showed three well-resolved positive NOE cross-peaks corresponding to H-H interactions in the molecules of dba (blue circles). On the basis of proton spectrum assignment, all three peaks were found to represent $H_\alpha{}^1\text{<->}H_\alpha{}^2$ NOE contacts, which indicated that each of the ligands of the complex exists in solution in s-cis,s-cis conformation. Remaining NOE peaks (magenta marks) represent NOE contacts between olefinic H_β and o-protons of aromatic rings. The rest of the peaks (negative) demonstrated chemical exchange between different dba moieties. It is important to emphasize, that some of the exchange cross-peaks (marked with dotted circles) appear between the major olefinic resonances and low-intensity ones, which serves as a direct evidence of the fact that the latter

indeed correspond to the minor form of Pd_2dba_3 complex (as detected above in the DOSY study).

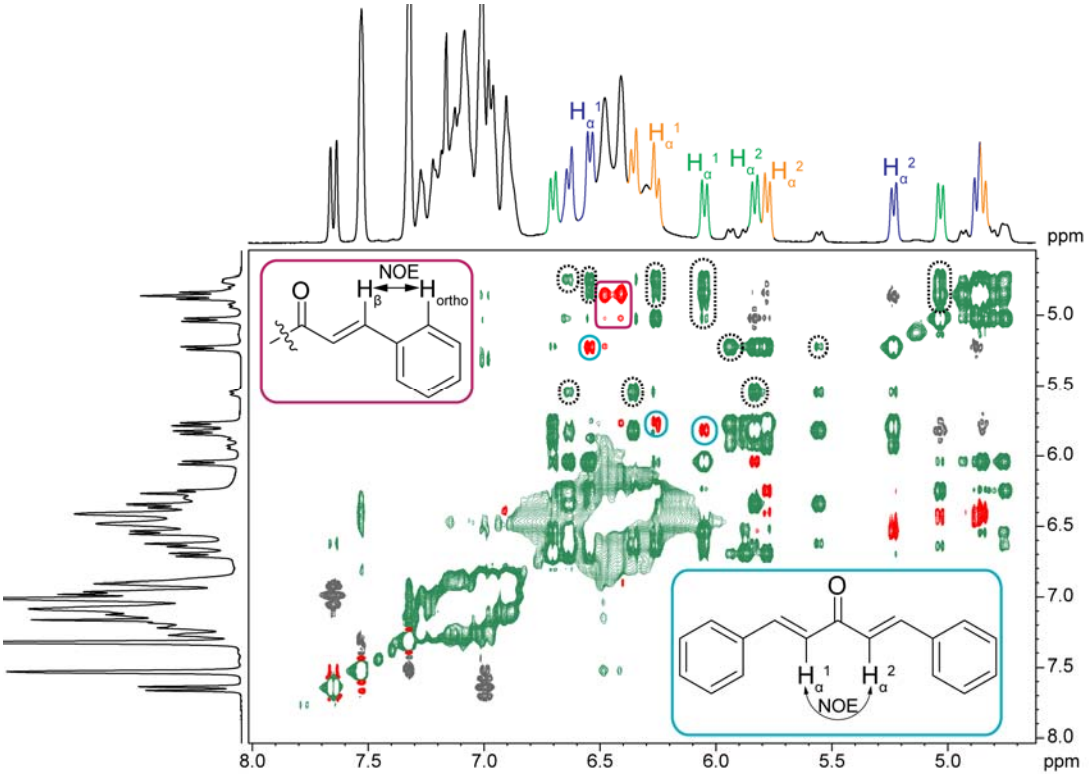

Fig.3. 2D NOESY spectrum of Pd_2dba_3 in $CDCl_3$ at 600 MHz (0.3 s mixing time); NOE peaks are shown as positive out-of-phase with diagonal peaks (red color), whereas exchange peaks are shown as negative in-phase with diagonal peaks (green color).

Based on the full assignment in the ^1H NMR spectrum a simple way to calculate Pd_2dba_3 purity from the integral ratio can be proposed [6].

It was of much interest to characterize the purity of Pd_2dba_3 used in everyday laboratory practice. The measurements carried out for Pd_2dba_3 received from commercial sources showed large variations in the ratio of the complex and free ligand (Table 1).

Pd black formed in the decomposition of Pd_2dba_3 was isolated as insoluble dark powder. Analysis by ICP-MS confirmed formation of a pure palladium material. The isolated material was studied by field-emission scanning electron microscopy (FE-SEM). It was found that the isolated material formed in the decomposition of Pd_2dba_3 consist of metal particles in the broad range of sizes of 60 – 200 nm and contained a minor amount of small nanoparticles of ca 10 – 20 nm of size. Most of the particles were round shaped or rectangular shaped with round corners. Some of the particles were agglomerated into microstructures, where the boundaries between the individual subunits were kept visible.

Up to date in far most reports resulted from widespread application of Pd_2dba_3 in modern chemistry, including various catalytic reactions, this palladium complex was obtained from commercial sources and used as received. The present study has clearly shown that it is an unacceptable practice. The content of catalytically active species may significantly vary, thus leading to estimation of incorrect values of mol %, TON and TOF actually employed in the reaction.

In spite of widespread use, there was no systematic study on the complex structure. In the solid state $Pd_2(dba)_3$ was characterized by means of elemental analysis, X-ray diffraction and IR spectroscopy. Only a little was known about the structure of the complex in solution.

Low solubility of the complex resulting in poor signal-to-noise ratio further complicated the NMR studies.

Table 1. Analysis of purity of Pd_2dba_3 obtained form different sources and stability of the complex in solution and in the solid state.

Entry	Description	Pd_2dba_3 : dba ratio	Purity of Pd_2dba_3, %
1	Commercial source 1, as received	1 : 0.30	77
2	Commercial source 2, as received	1 : 0.09	92
3	Commercial source 3, as received	1 : 0.56	64
4	Freshly synthesized	1 : 0.01	99
5	Freshly synthesized, stored for 1 week in the solid state at r.t.	1 : 0.05	95
6	Freshly synthesized, stored for 1 month in the solid state at r.t.	1 : 0.05	95
7	Freshly synthesized, stored for 6 months in solid state at r.t.	1 : 0.41	71
8	Freshly synthesized, stored for 1 hour in solution under air at r.t.	1 : 0.14	88
9	Freshly synthesized, stored for 1 day in solution under air at r.t.	1 : 0.39	72
10	Freshly synthesized, heated for 1h at 50°C in $CDCl_3$ under air	1 : 0.30	77
11	Freshly synthesized, heated for 1h at 50°C in $CDCl_3$ under Ar	1 : 0.28	78

In this work for the first time a detailed examination of the complex structure in solution was conducted. We utilized modern liquid-state NMR methods to elucidate both the molecular composition of the complex solution and the structure of the $Pd_{2(}dba)_3$ molecule itself. A careful study revealed the existence of several rotameric forms of the complex in solution, all of which were found to be active towards catalytic reactions. A sequential combination of 2D NMR experiments allowed us to make full assignment of the crowded ^{1}H NMR spectrum of the complex. Results of 2D NOESY studies propose the most plausible geometry of the ligands arrangement around binuclear metal core.

In addition we have developed a simple procedure to determine the purity of $Pd_2(dba)_3$ based on ^{1}H NMR. The procedure developed can be used for quick evaluation of quality and nature of the catalyst precursor just before use in the catalytic reaction.

References

[1] Grasa, G.A.; Viciu, M.S.; Huang, J.; Zhang, C.; Trudell, M.L.; Nolan, S.P. *Organometallics* **2002**, *21*, 2866.

[2] Zhou, J.; Fu, G.C. *J. Am. Chem. Soc.* **2003**, *125*, 12527.

[3] Beletskaya, I.P.; Cheprakov, A.V. *Chem. Rev.* **2000**, *100*, 3009.

[4] Ukai, T.; Kawazura, H.; Ishii, Y.; Bonnet, J. J.; Ibers, J. A. *J. Organomet. Chem.* **1974**, *65*, 253.

[5] Ananikov, V. P.; Beletskaya, I. P. *Organometallics* **2012**, 31, 1595.

[6] Zalesskiy S. S., Ananikov V. P., *Organometallics*, **2012**, *31*, 2302.

ESR study of antiferromagnetic zigzag chain system β-$TeVO_4$

Yu. Savina, A. Bludov, V. Pashchenko, S. Gnatchenko

B.I. Verkin Institute for Low Temperature Physics and Engineering NASU, 61103, Lenin ave., 47, Kharkiv, Ukraine

e-mail: savina@ilt.kharkov.ua

The properties of various one-dimensional (1D) quantum spin systems have been explored intensively both experimentally and theoretically. The physical realizations of 1D spin systems are compounds in which the exchange interaction J along one direction is significantly stronger than the J' exchange along to other direction ($J \gg J'$ or $J'/J \ll 1$). Although in 1D systems a classical Neel ordered state isn't expected, but the existence of a small non-vanishing interchain coupling often lead to the realization of a 3D long-range magnetically ordered state at low temperatures. The typical feature of uniform 1D spin system is the presence of a broad maximum $\chi_{\max} = 0.146926 \cdot Ng^2\mu_B^2 / |J_{1D}|$ at $T_{\max} = 0.64J / k_B$ [1] on temperature dependence of magnetic susceptibility.

The vanadium oxides containing VO_5 square pyramids in the structure demonstrate a large variety of the different 1D quantum spin systems such as: linear (α'-NaV_2O_5 [2]) and alternating exchange chain (α-$TeVO_4$ [3]), zigzag chain ($CdVO_3$ [4]), two-leg ladder (β–SrV_6O_{15} [5]) etc.

In present work we report the results of the ESR measurements on a high-quality single crystal of β-$TeVO_4$. The structure of this compound contains of zigzag chains parallel to the c axis formed by slightly distorted square pyramids VO_5 sharing corners. There are two identical zigzag chains, in which all apices of square pyramids are pointing alternatively below and above the bc plane [6]. Magnetic susceptibility and magnetization of a single crystal β-$TeVO_4$ were reported in work [7]. Magnetic data show an axial anisotropy of magnetic properties with respect to the b axis, which can be due to a small anisotropy of the g-tensor for the V^{4+} ions ($S = ½$). This compound behaves as an $S = ½$ one-dimensional Heisenberg antiferromagnet with single intrachain exchange $J/k_B = 21.4 \pm 0.2$ K. Below 5K, a series of phase transition are observed that indicates the presence of non-vanishing interchain exchange couplings.

Electron paramagnetic resonance is a powerful tool for probing the low-energy magnetic excitations with unique sensitivity and resolution. The ESR measurements (The temperature and angular dependences) were performed by using a Bruker X-band spectrometer at frequency 9.4 GHz in the temperature range 4.7 K $\leq T \leq$ 300 K and magnetic fields from 0 to 1.2×10^4 Oe. The etalon sample of DPPH with $g = 2.0032$ was used.

Fig.1 shows the temperature evolution of the ESR spectra of β-$TeVO_4$ at 9.4 GHz for orientation of the applied magnetic field perpendicular to the b axis ($H \perp b$). Each ESR spectrum consists of two lines: the narrow line (ΔH~800 Oe, denoted as I) and broad one (ΔH~20000 Oe, marked as II). The third line at H=3440 Oe is the etalon signal of the DPPH. As one can see in fig.1 the line I situate near the DPPH position. The resonance position of line II is shifted to higher field. The linewidth of line II shows the significant temperature dependence from 300 K to ~15 K (roughly this dependence is shown as a dash line). At ~ 30 K the linewidth of line II reaches its minimum value $\Delta H \approx$ 13000 Oe. In contrast of the line I the line II is not observable at $T <$ 15 K. Below 15 K the additional small signal is detected at $H = ½H_{res}$ (marked as a vertical dash line).

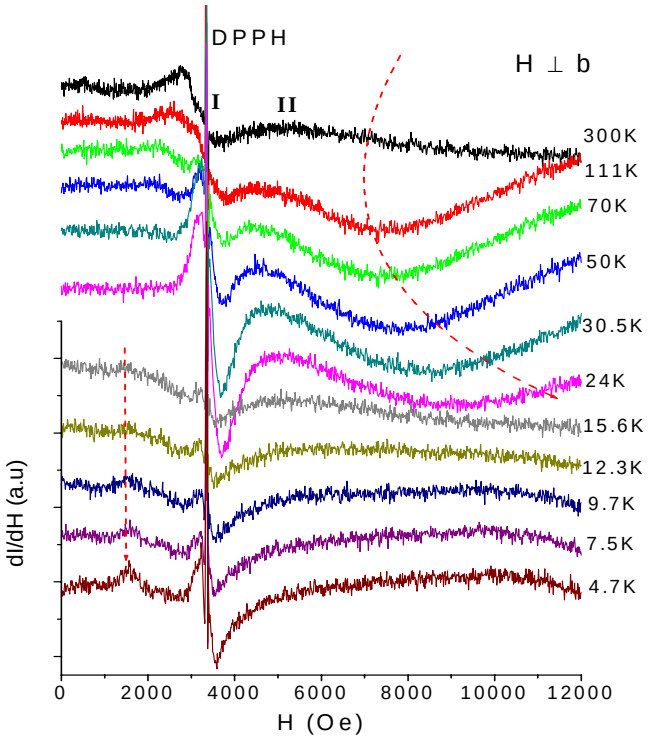

Fig.1. The temperature dependence of the ESR spectra of β-$TeVO_4$ for $H \perp b$.

In order to study the anisotropy of two lines the angular dependence of the ESR spectra of β-$TeVO_4$ for the rotation of magnetic field from $H \perp b$ to $H \| b$ at $T = 31.4$ K was measured, which are shown in fig.2. As one can see in fig.2 the broad line is almost non-detectable for $H \| b$ (its linewidth becomes extremely large). At the same time the linewidth of narrow line is weak angular dependent.

For obtaining the parameters of the resonance absorptions such as the spin susceptibility χ_{ESR}, linewidth ΔH and resonance position H_{res} we have used a simple model containing of two different lines with a Lorentzian line shape. The results of analysis of angular and temperature dependences of single crystal β-$TeVO_4$ are summarized in fig.4 and fig.5, respectively. As an example, the experimental data (open ($H \| b$) and close ($H \perp b$) circles) and

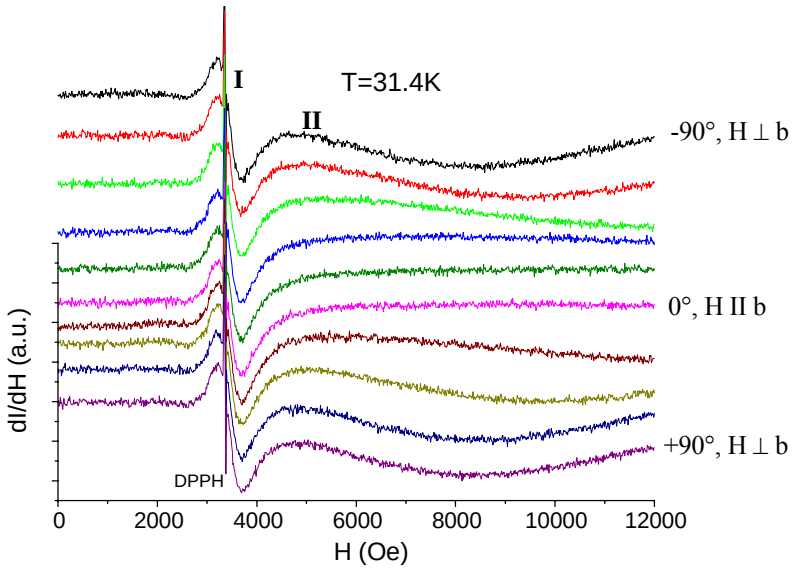

Fig.2. The angular dependence of the ESR spectra of β-$TeVO_4$ at $T = 31.4$ K.

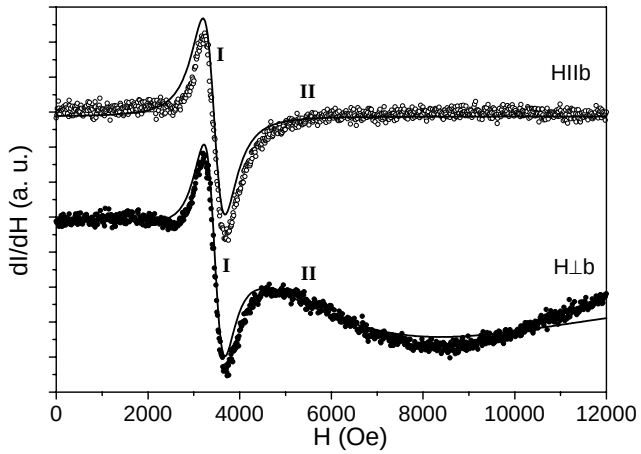

Fig.3. Single crystal ESR spectra of β-$TeVO_4$ for orientations $H||b$ (open circles) and $H\perp b$ (solid circles) at $T = 31.4$ K. The solid lines were calculated by using the best fit parameters.

the best fit (solid line) at $T = 31.4$ K are shown in fig.3. The quality of the description of each spectra is quite satisfactory.

The angular dependencies of the resonance position H_{res} and line-width ΔH of two resonance lines at $T = 31.4$ K are presented in fig.4. As one can see in fig.4 the both lines exhibit a 180° symmetry, as expected from the crystal structure. The angular dependence $H_{res}(\varphi)$ for line I is quite weak: H_{res} changes from 3440 Oe to 3450 Oe, that corresponds to the changing of g-factor from 1.99 to 2.00. The obtained values may be explained by two hypotheses: first, a presence of some impurities in the crystal; the second, a realization of only one expected value of g-factor (g_{max}~1.99) for a square-pyramidal environment of V^{4+} ions ($S = ½$) [8]. The observed behavior of line I (angular and temperature dependences) is in a favor of the first case. The field position $H_{res}(\varphi)$ for line II is larger than for line I: it changes from 4500 Oe up to 9000 Oe (corresponds to g-factor from 0.8 to 1.6 with the average value $\langle g \rangle = 1.2$). Such behavior is not typical for V^{4+} magnetic centers. It should be noted for $H||b$ the resonance field H_{res} of the line I is minimal, and the resonance field H_{res} of the line II has a maximum.

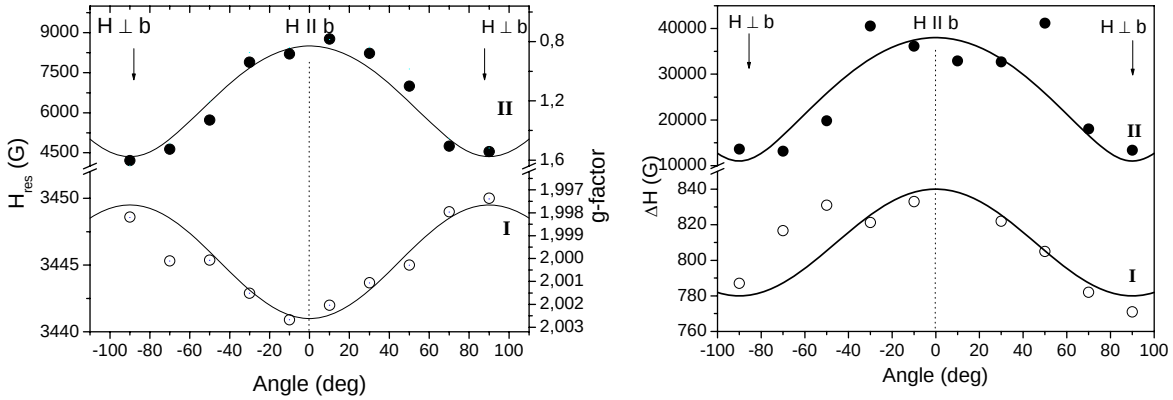

Fig.4. The angular dependencies of the position $H_{res}(\varphi)$ (left) and linewidth $\Delta H(\varphi)$ (right) of two lines of β-$TeVO_4$ at T = 31.4 K. Date for line I is open circles; data for the line II - solid circles.

The obtained temperature dependences of spin susceptibility $\chi_{ESR}(T)$ (circle), linewidth ΔH (square) and resonance field H_{res} (triangle) of the two lines in single crystal β-$TeVO_4$ are shown in fig.5. Spin susceptibility χ_{ESR} of the both lines are diverged at low temperatures. By using expression $\chi_{ESR} = C/(T-T^*)$ we have estimated a critical temperature as $T^* \sim 5 \div 9$ K, that is closed to temperature of magnetic ordering $T_N = 4.65$ K. With the temperature decreasing from 300 K down to ~ 60 K the linewidth ΔH of the both lines reduce; at 60 K ΔH has a minimum and then ΔH undergo a rapidly go up. Low temperature divergence of ΔH

correlates well with the value of T_N too. The light shifts of the resonance fields of the both lines with decreasing temperature are detected (see low parts of fig.5).

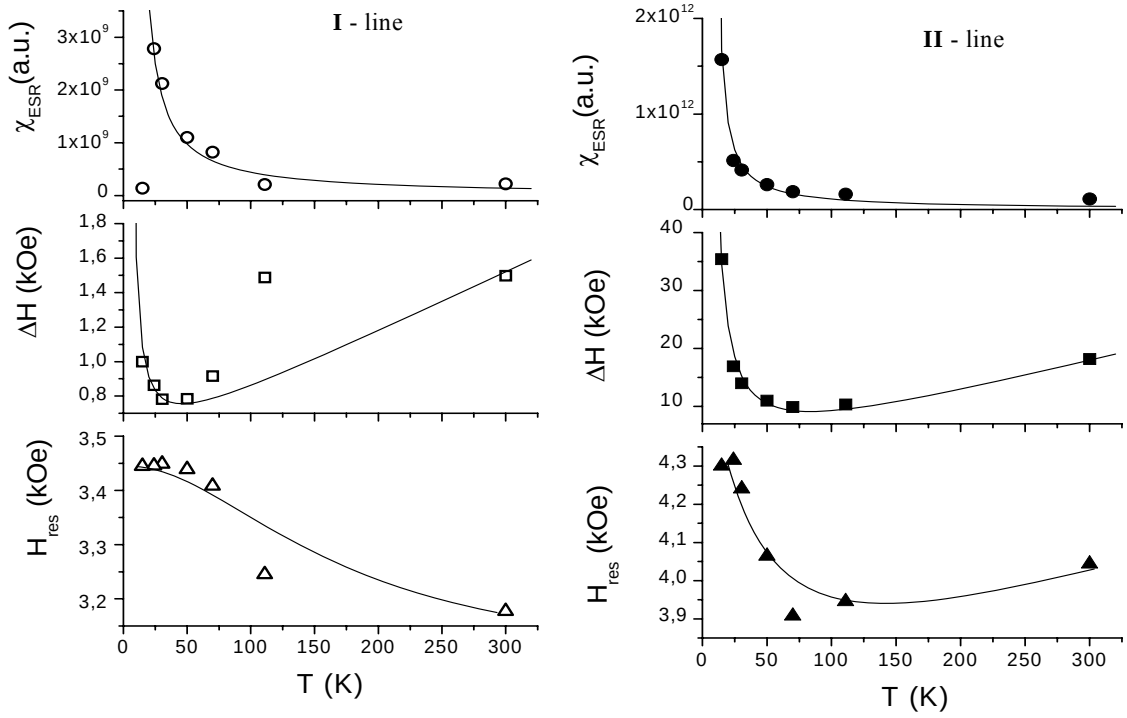

Fig.5. Temperature dependences of the spin susceptibility $\chi_{ESR}(T)$ (circle), linewidth ΔH (square) and resonance field H_{res} (triangle) of the derivatives ESR lines of β-$TeVO_4$ for measuring geometry $H||b$. Date for line I is open circles; data for the line II - solid circles.

In summary, we have studied the angular and temperature dependences of the ESR spectra in the quasi-1D spin-½ AF zigzag chain system β-$TeVO_4$. Two resonance absorption lines have been detected. The nature of these lines are still unknown. The narrow line might be due to impurity, the characteristics of broad absorption don't fit with a picture of the typical behavior of the V^{4+} ions with square-pyramidal environment. It was found that the observed low-temperature critical divergence of the spin susceptibility and linewidth of absorption lines can be due to the realization of a three-dimensional order at $T_N = 4.65$ K in the single crystal β-$TeVO_4$.

References

[1] D.C. Johnston, R.K. Kremer, M. Troyer, X. Wang, A. Klümper, S.L. Bud'ko, A.F. Panchula and P.C. Canfield, Phys. Rev. B **61**, 9558 (2000).

[2] M.Isobe, Y.Ueda, J. Phys. Soc. Jap. **65**, 1178 (1996).

[3] V. Gnezdilov, P. Lemmens, A.A. Zvyagin, V.O. Cheranovskii, K. Lamonova, Yu.G. Pashkevich, R.K. Kremer and H. Berger, Phys. Rev. B **78**, 184407 (2008).

[4] M. Onoda, N. Nishiguchi, J. Phys.: Condens. Matter **11**, 749 (1999).

[5] M.-L. Doublet, M.-B. Lepetit, Phys. Rev. B **72**, 075119 (2005).

[6] G. Meunier, J. Darriet, J. Galy, J. Sol. Stat. Chem. **6**, 67-73 (1973).

[7] Yu. Savina, O. Bludov, V. Pashchenko, S. Gnatchenko, P. Lemmens, H. Berger, Phys. Rev. B **84**, 104447 (2011).

[8] A. Abraham, B. Bleaney, *Electron Paramagnetic Resonance of Transition Ions*, Clarendon press, Oxford, (1970).

Versatile coordination sphere dynamics in o-semiquinonic pincer nickel complexes: an EPR study and mechanistic aspects

K.A. Kozhanov, M.P. Bubnov, V.K. Cherkasov, G.A. Abakumov

G.A. Razuvaev Institute of Organometallic Chemistry of RAS, 603950, 49 Tropinina Str., Nizhniy Novgorod, Russia.

e-mail: kostik@iomc.ras.ru

Pincer complexes of transition metals are of a great interest last decades. Being fine catalysts for wide scale of reactions they have an excelent chemical stability [1]. From the other hand, the *o*-semiquinonato ligands can be successfully used for the study of the composition of the transition complexes, their geometry and dynamical properties in their coordination sphere as well [2].

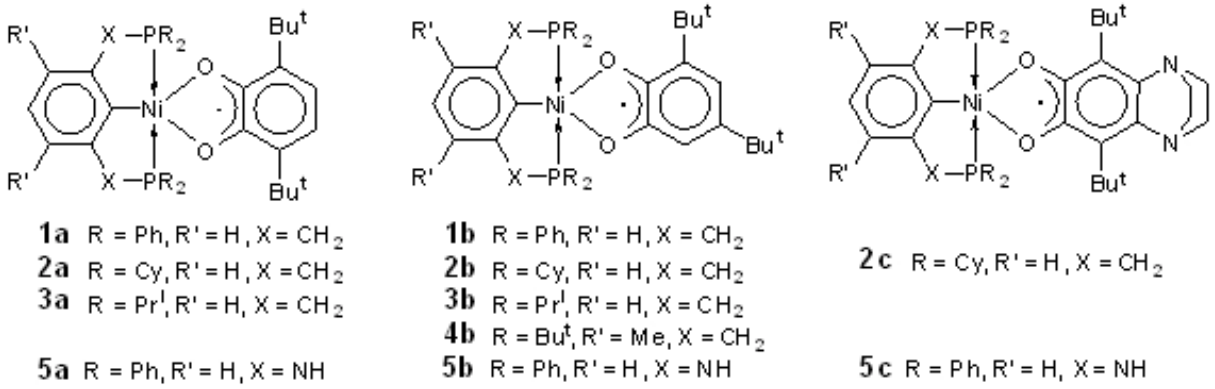

Scheme 1. Notation of *o*-semiquininic pincer nickel complexes.

In present study we have obtained some pincer nickel complexes containing different substituents at phosphorus atoms and *o*-semiquinonic ligands with different symmetry and sterical properties in *ortho*- and *para*-positions to oxygene atoms (Scheme 1).

EPR spectrum of **1a** at 200K (Table 1) is triplet 1:2:1 of doublets of doublets resulting from the hyperfine splitting on two equivalent phosphorus nuclei and two non-equivalent protons of *o*-semiquinonic ring. The asymmetry of the spin density distribution inside the *o*-semiquinone follows from the difference of the bonds lengths (fig.1) in the chains Ni1-O1-C1 and Ni1-O2-C2. The chelate cycle of each complex can be presented as a sum of the resonance structures A and B which are responsible for appearing of spin density on the protons H4 and H5. The excess of spin density on the O2 means that the resonance structure **B** predominates over the structure **A** (Scheme 2).

The temperature rising results in averaging of protonic HFC constants (fig.1, Table 1) via fast (in EPR timescale) "swing" oscillations (Scheme 3) [3]. It must be noted that the phosphorus constants are kept equivalent with temperature variations.

For complex **1b** at low temperature the superposition of two spectra is observed (Table 1). These spectra can be attributed to different structure isomers (Scheme 3). Temperature rising leads to average the spectrum (Table 1) which is a result of fast isomers interconversion via "swing"

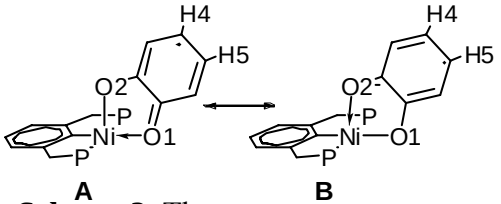

Scheme 2. The resonance structures responsible for protonic HFC splitting

oscillations (Scheme 3).

Table 1. Parameters of EPR spectra for investigated complexes

Complex	T, K	g_i	^{31}P HFC constants, G	SQ HFC constants, G
1a	290	2.0060	$a_{P1}=a_{P2}=24.2$	$a_{H1}=a_{H2}=2.8$
	180	2.0056	$a_{P1}=a_{P2}=25.6$	$a_{H1}=3.4$, $a_{H2}=2.2$
1b	330	2.0052	$a_{P1}=a_{P2}=20.3$	$a_H=2.6$
	200, isomer 1	2.0064	$a_{P1}=a_{P2}=18.4$	$a_H=2.4$
	200, isomer 2	2.0041	$a_{P1}=a_{P2}=24.4$	$a_H=3.4$
2a	340	2.0071	$a_{P1}=a_{P2}=21.7$	— [a]
	260	2.0071	$a_{P1}=26.7$, $a_{P2}=15.5$	$a_{H1}=3.6$, $a_{H2}=2.2$
	220	2.0071	$a_{P1}=27.8$, $a_{P2}=14.7$	$a_{H1}=3.6$, $a_{H2}=2.2$
2b	320	2.0054	$a_{P1}=a_{P2}=17.9$	— [a]
	220	2.0054	$a_{P1}=22.7$, $a_{P2}=13.4$	$a_H=2.5$
2c	320	2.0055	$a_{P1}=a_{P2}=21.2$	— [a]
	220	2.0055	$a_{P1}=28.0$, $a_{P2}=14.5$	— [a]
3a	300	2.0055	$a_{P1}=a_{P2}=19.8$	$a_{H1}=a_{H2}=2.8$
	190	2.0054	$a_{P1}=25.3$, $a_{P2}=15.7$	$a_{H1}=3.8$, $a_{H2}=2.2$
3b	290	2.0054	$a_{P1}=a_{P2}=16.6$	$a_H=2.7$
	200, isomer 1	2.0043	$a_{P1}=a_{P2}=14.4$	$a_H=2.2$
	200, isomer 2	2.0054	$a_{P1}=22.2$, $a_{P2}=14.2$	$a_H=2.5$
4b	290	2.0062	$a_{P1}=a_{P2}=14.1$	$a_H=2.5$
	170	2.0062	$a_{P1}=a_{P2}=17.0$	$a_H=2.5$
5a	290	2.0036	$a_{P1}=a_{P2}=19.4$	$a_{H1}=a_{H2}=3.0$
	170	2.0036	$a_{P1}=a_{P2}=19.9$	$a_{H1}=4.1$, $a_{H2}=1.9$
5b	290, signal 1	2.0044	$a_{P1}=a_{P2}=16.7$	$a_H=2.55$
	290, signal 2	2.0105	$a_P=3.1$	$a_H=2.9$
5c	300	2.0036	$a_P=3.1$	— [a]
	160	2.0036	$a_{P1}=a_{P2}=16.7$	— [a]

[a] Unobserved due to broad lines.

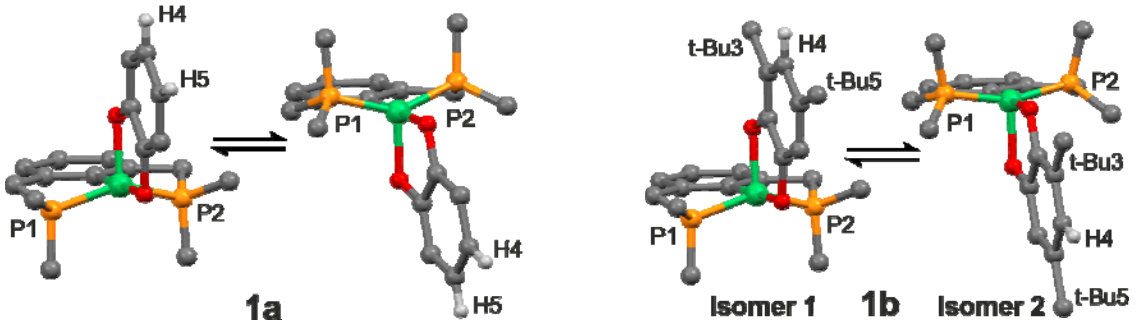

Scheme 3. "Swing" oscillations in **1a** and **1b** (without non-relevant atoms).

Complexes **2a-c** demonstrates another scheme of dynamics which we called "fan" oscillations (Scheme 4) [3]. The temperature dependence of EPR spectra of all three complexes is similar (Table 1). So, at low temperature the splitting on two non-equivalent phosphoruses is observed. Such unequivalence is a result of "sloped" configuration of chelate fragments in molecule (fig.1).

In general, HFC constant on the magnetic nuclear of ligand (^{31}P) bonded to the metal-*o*-semiquinone fragment can appear due to two mechanisms [4]: spin polarization of σ-bonds O-Ni-P and direct interaction of group Ni-P orbital with π* orbital of semiquinone containing unpaired electron. The second path is quite more effective and in the case of pincer-*o*-

semiquinonato-nickel complexes it determines the phosphorus splitting constants. As the consequence this value is very sensitive to geometrical features and particularly to the angle between Ni-P axis and o-semiquinonic plane [4] (particularly to the normal to this plane). Phosphorus HFC constant is larger when this angle is close to 90° [4]. Examination of inner coordination core (fig.1) describes that the angles P1-Ni1-O2 in the complexes **2a** and **2b** are close to right angle (89.39° in **2a** and 87.86° in **2b**) comparing with the P2-Ni1-O2 (124.54° in **2a** and 111.03° in **2b**) whereas in **1a** both angles are closer one to another (115.70° and 101.58°). It is the reason of the larger difference between phosphorus HFC constants a_{P1}/a_{P2} for **2a** and **2b** comparing with the same value for **1a** (a_{P1}/a_{P2}= 27.8/14.7 G in **2a**, 25.3/15.7 G in **2b** and 25.6/25.6 G in **1a**). The angles P1-Ni1-O2 and P2-Ni1-O2 (both relative to O2) are especially preferred in examination of phosphorus HFC constants because O2 has an excess of spin

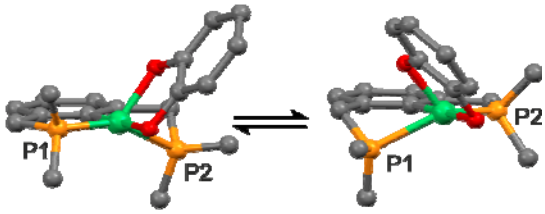

Scheme 4. "Fan" oscillations in **2a-c** (hydrogens and substituents are omitted for clarity).

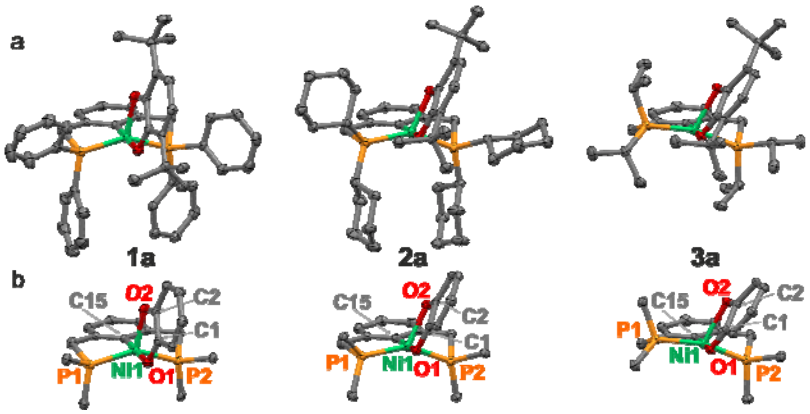

Complex	1a	2a	3a
Ni1-O1	1.9238	1.9306	1.9377
Ni1-O2	2.0595	2.0664	2.2165
C1-O1	1.2975	1.3076	1.3006
C2-O2	1.2890	1.2922	1.2763
P1-Ni1-O1	98.30	101.98	99.21
P1-Ni1-O2	115.70	89.39	87.86
P2-Ni1-O1	95.47	92.65	94.35
P2-Ni1-O2	101.58	124.54	111.03
Ar-Ar[a]	75.64	60.87	50.79

[a]The angle between the plane of the aromatic ring of the pincer ligand and the plane of the pseudo-aromatic ring of the *o*-semiquinone

Fig.1 Structure of **1a-3a** (a – full, b – core only), selected bonds (Å) and angles (°).

density comparing with O1 (vide supra).

Heating averages these constants (Table 1). It should be noted that for **2a** protonic HFC constants are kept unequivalent at least below 260K. Moreover, no isomers interconversion is observed for **2b** (in contrast with **1b**). These facts are the direct evidence of the absence of "swing" oscillations for these complexes.

In the case of **3a** and **3b** the coordination sphere dynamics is more complicated. For these complexes both kinds of oscillations are observed simultaneously. So, for **3a** at low temperature in EPR spectrum the hyperfine splitting on two nonequivalent phoshoruses and two nonequivalent protons is observed (Table 1). With the temperature rising the averaging of the phosporous constants in observed (like for **2a**), but the same process is observed for protonic constants too (like for **1a**). It means that both "swing" and "fan" oscillations take place simultaneously (Scheme 5). For **3b** the similar transformation of EPR spectrum is observed (Table 1). The superposition of two signals at low temperature transforms into averaged spectrum with the heating. So, the structural isomers interconversion via "swing" oscillations (as for **1b**) is observed as well as "fan" oscillations (Scheme 5). It must be noted that only one of isomers (Isomer 2 at Scheme 5) has different phosphorus constants and correspondingly demonstrates the "fan" oscillations (like for **2b**). It means that the presence of bulky *t*-Bu group in *ortho*-position to basal oxygen is relevant for "fan" oscillations appearance.

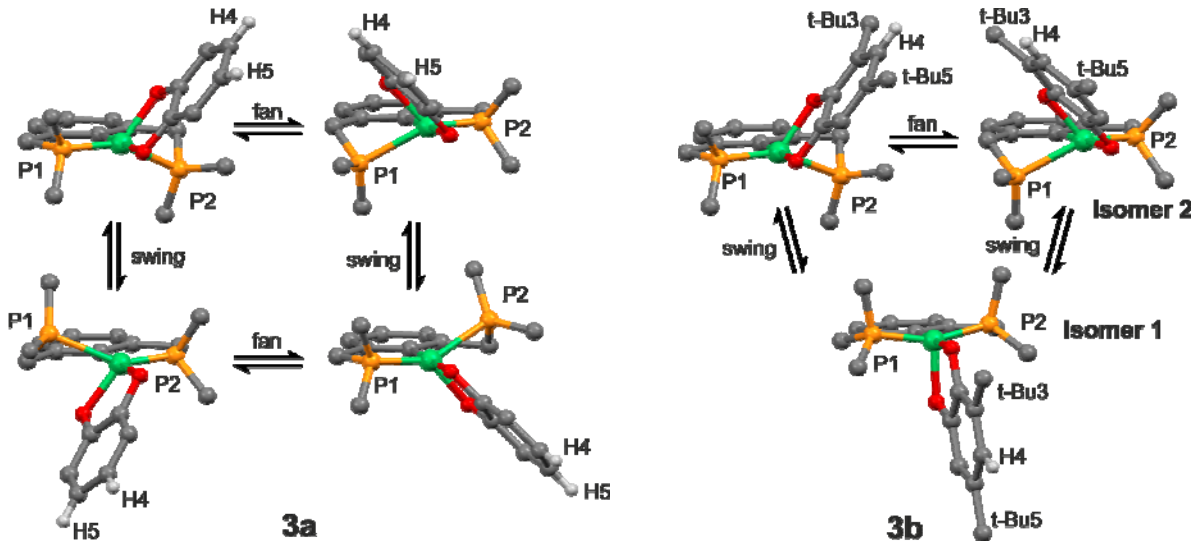

Scheme 5. Simultaneous "fan" ans "swing" oscillations in **3a** and **3b**.

For **4b** neither "fan" nor "swing" oscillations were observed [3]. So, it can be concluded that "swing" oscillations are driven by sterical properties of the phosphorus substituents of the pincer fragment. For "fan" oscillations the driving force is not so clear. Most probably, the mechanism of these oscillations is related with the absence of axial symmetry along P-C axis in Cy and *i*-Pr substituents.

EPR spectrum of **5a** (Table 1) is similar with **1a** analog as well as its temperature dependence. So, the "swing" oscillations are observed for this compound as well as for **1a**.

Surprisingly, in the case of **5b** the EPR spectrum is drastically differ (Table 1). It looks as superposition of two signals: one with two phosphorus constants with large value ($a_{P1}=a_{P2}=16.7$G) and another with only one phosphorus constant with small value ($a_P=3.1$G). Such low values of HFC contants on phosphorus nuclei (a_P~0–3G) are typical for four-coordinated square-plane and related complexes [4]. So, in our case we proposed the decoordination of one of phosphine group of pincer fragment forming corresponding four-coordinated product (Scheme 6).

Most probably the reason of this decoordination is a presence of bulky t-Bu group in *para*-position to *o*-semiquinonic oxygens together with rigid –NH– linker in pincer fragment. This proposal is confirmed in the case of **5c**. In its EPR spectrum (Table 1) at ambient temperature only one signal with only one phosphorus constant with small value ($a_P=4.1$G) is observed, which can be attributed to four-coordinated product (Scheme 6). With temperature decreasing this signal desappears, and another one with two larger phosphorus constants ($a_{P1}=a_{P2}=16.4$G) appears. So, low-temperature signal can be attributed to five-coordinated product (Scheme 6).

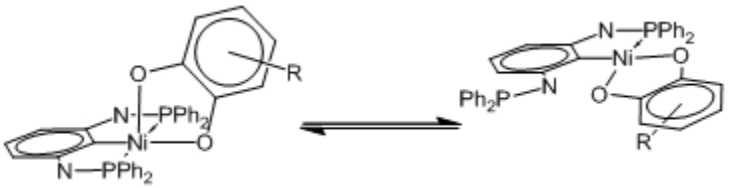

Scheme 6. Isomerization of **5a** and **5b**.

Acknowledgements

The work was supported by Russian President (grants NSh-1113.2012.3 and MK-474.2011.3), Russian Foundation for Basic Research (grants 10-03-00788-a and 12-03-31087-mol) and FSP "Scientific and scientific-pedagogical cadres of innovation Russia" for 2009-2013 years (GK-P839 from 25.05.2010).

References.

[1] M. Albrecht and G. van Koten, *Angew. Chem., Int. Ed. Engl.*, 2001, **40**, 3750

[2] G. A. Abakumov, V. K. Cherkasov, V. I. Nevodchikov and V. A. Garnov, *Bull. Acad. Sci. USSR, Div. Chem. Sci. (Engl. Transl.)*, 1991, **40**(9), 1754–1759.

[3] K.A. Kozhanov, M.P. Bubnov, V. K. Cherkasov, N.N. Vavilina, L.Yu. Efremova, O.I. Artyushin, I.L. Odinets, G.A. Abakumov, *Dalton Trans.*, 2008, 2849.

[4] G.A. Razuvaev, V.K. Cherkasov, G.A. Abakumov, *J. Organomet. Chem.*, 1978, **160**, 361.

EPR Study of Dynamics of Triplet Fullerenes in Glassy and Polymer Matrices

M.N. Uvarov, L.V. Kulik, S.A. Dzuba

Institute of Chemical Kinetics and Combustion, Siberian Branch of Russian Academy of Sciences, Institutskaya, 3, 630090, Novosibirsk, Russia

e-mail: uvarov@kinetics.nsc.ru

X-band electron spin echo (ESE) method was applied to investigate the correlation between spin and orientation dynamics of triplet fullerenes $^3C_{60}$ and $^3C_{70}$ as spin probes with nanometer scale in disordered matrices.

Two-pulse echo-detected (ED) electron paramagnetic resonance (EPR) spectra of $^3C_{60}$ in glassy *o*-terphenyl (fig.1, thin lines) were obtained using photoexcitation by laser pulse with wavelength 532 nm (*laser flash - π/2 - 120 ns - π - ESE*). The temperature narrowing of ED EPR spectra was simulated within the model of fast anisotropic pseudorotations of $^3C_{60}$ molecules due to dynamic Jahn-Teller effect. The model for the numerical simulation implied the exchange of EPR lines due to rotation of $^3C_{60}$ dipolar tensor in the local potential $U = -V\cos(\alpha)$, where α is angle between Z-axis of $^3C_{60}$ molecule and a local direction of glassy media. The simulations are presented at fig. 1 (thick curves). Only V value was varied from 39 meV for 85 K to 52 meV for 245 K. The characteristic time of pseudorotations, $\tau_c \sim 10^{-12}$ s, was estimated using the Redfield theory [1].

In contrast, no temperature narrowing was revealed in ED EPR spectra of $^3C_{70}$, which has temperature independent width about 105 G (data not shown).

To measure phase memory times of triplet fullerenes $^3C_{60}$ and $^3C_{70}$ in disordered matrices ESE decays were obtained in maxima of ED EPR spectra (fig. 2). The signal decays were fitted fairly well by exponential functions. The decays were interpreted as arising from $^3C_{60}$ and $^3C_{70}$ molecular dynamics.

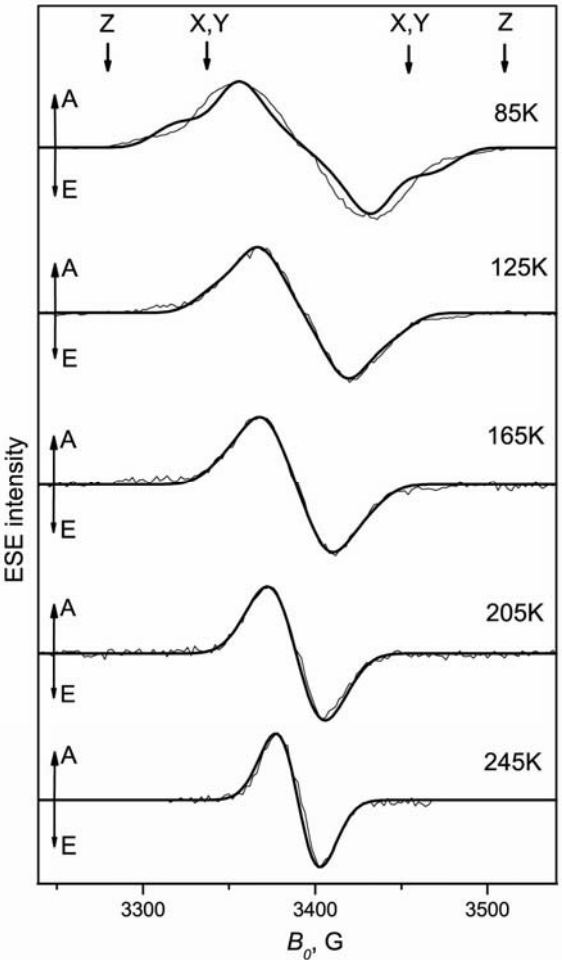

Fig.1. ED EPR spectra of $^3C_{60}$ in glassy o-terphenyl at different temperatires (thin lines), and their numerical simulation (thick lines). “A” is absorption, “E” is emission.

Continuous wave (CW) X-band EPR spectra of fullerene C_{70} molecules excited to a triplet state by continuous light illumination were measured for C_{70} in molecular glasses of *o*-terphenyl and *cis/trans*-decaline (fig. 3, thin lines) and in the glassy polymers polymethylmethacrylate (PMMA) and polystyrene (PS) (data not shown). Above ~ 100 K, a distinct narrowing of EPR lineshape of the triplet was observed, which was very similar for

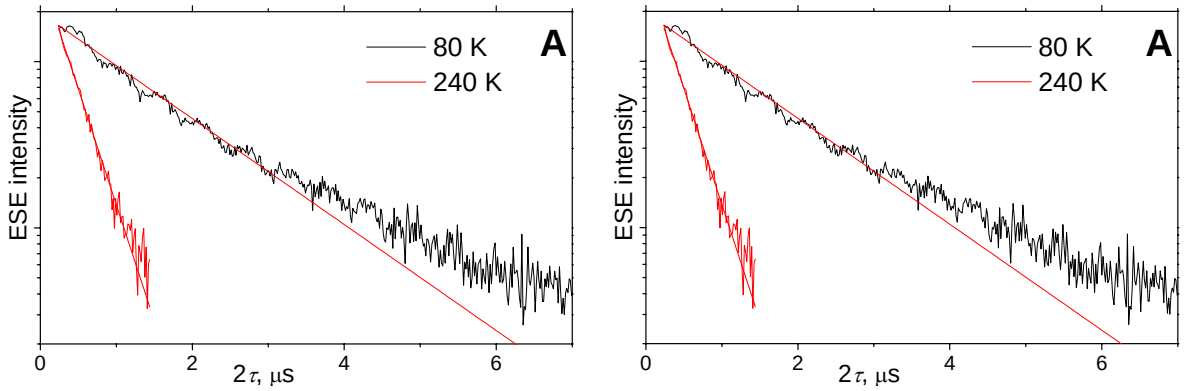

Fig.2. ESE decays of $^3C_{60}$ (A) and $^3C_{70}$ (B) obtained with pulse pattern *laser flash - π/2 – τ – π - ESE* at different temperatures (solid noisy curves), and their fitting by exponential or biexponential decays (dashed lines).

all systems studied. At 77 K EPR lineshape was simulated reasonably well using model of distribution of zero-field splitting parameters within triplet $^3C_{70}$ ensemble [2]. To simulate EPR lineshape for temperatures above 100 K a framework of a simple model of random jumps was used. It implies that the C_{70} molecule performs isotropic orientational motion by sudden jumps of arbitrary angles (fig. 3, thick lines). In the simulations, a single correlation time τ_c was used, varying in the range of 10^{-7} - 10^{-8} s [3].

Correlation times τ_c obtained from simulation of the EPR spectra in the slow-motion limit (τ_c close to 10^{-7} s) turned out to be in good agreement with the phase memory times of the ESE decay, which additionally supports the employed simple model. That fact is illustrated in fig. 4, where at temperatures about 100 K transversal relaxation rates, T_2^{-1}, of

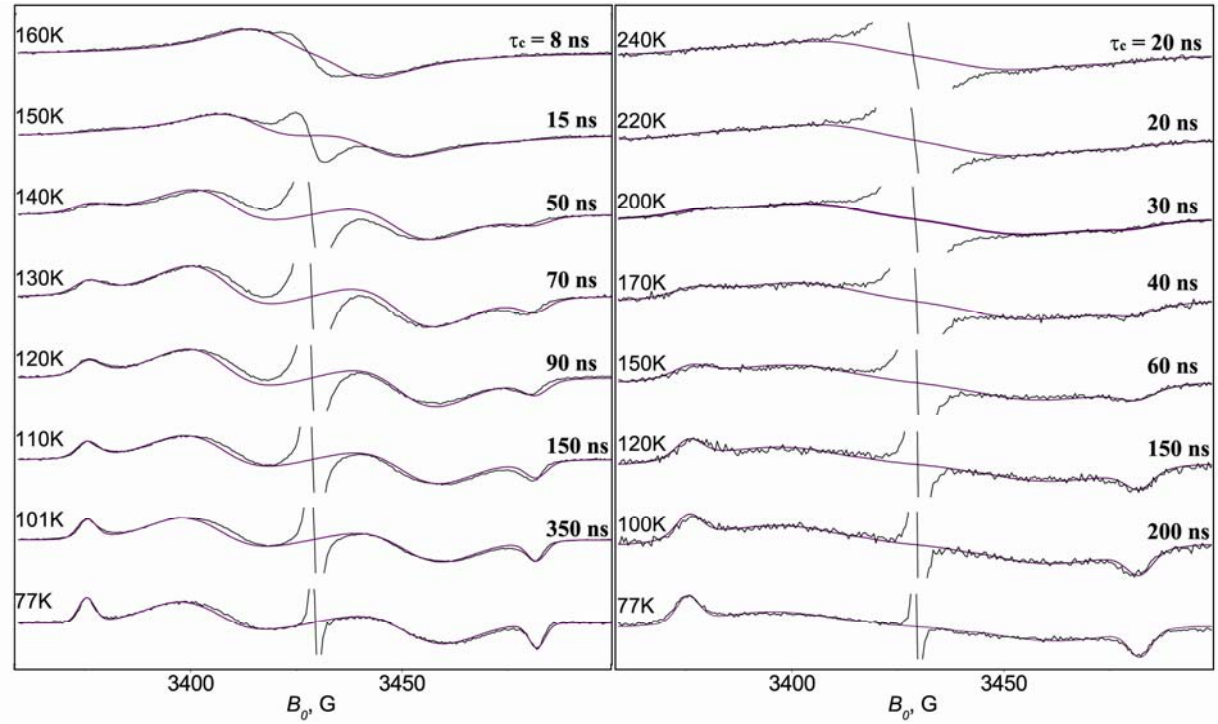

Fig.3. CW EPR spectra of C_{70} in glassy decaline (A) and o-terphenyl (B) obtained under continuous light illumination at different temperatures (thin lines). The numerical simulations of the experimental CW EPR spectra were performed as static averaging of randomly oriented $^3C_{70}$ molecules for 77K. For other temperatures the model of random exchange between EPR lines with certain τ_c value was implied (thick lines).

$^3C_{70}$ has the same value as reorientation rate τ_c^{-1} of C_{70} molecule. The observed rapid isotropic rotations of a large asymmetric C_{70} molecule provides evidence that the nanostructure of solid glassy media of different origins becomes soft well below the glass transition temperature.

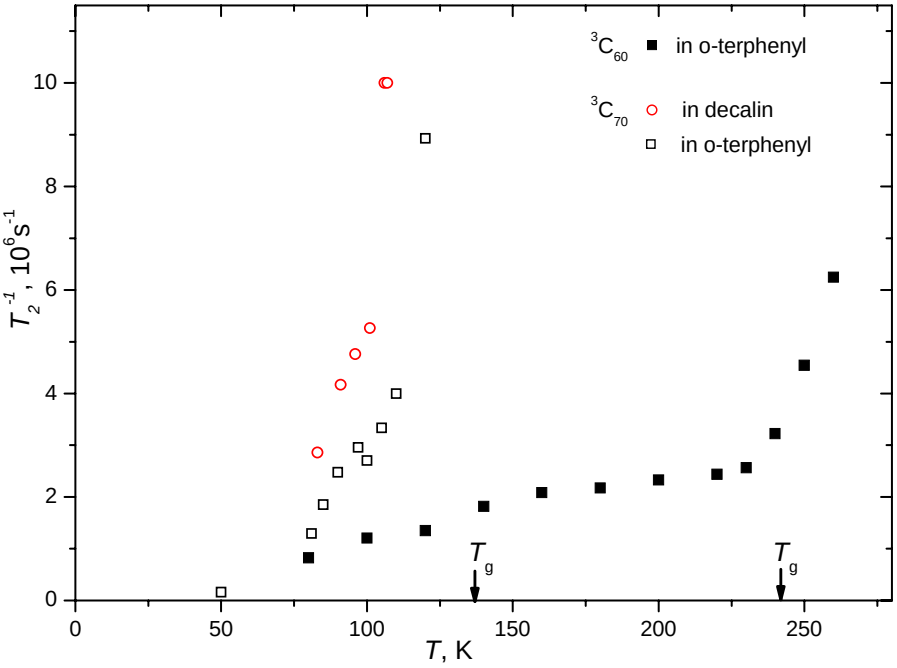

Fig.4. Transversal spin relaxation rates of $^3C_{60}$ and $^3C_{70}$ in glassy o-terphenyl and decaline at different temperatures. "T_g" stands for glass transition temperatures of decaline (138K) and o-terphenyl (243 K).

The strong difference of the temperature dependence of T_2^{-1} of $^3C_{60}$ and $^3C_{70}$ in o-terphenyl appear. The effect for $^3C_{60}$ appears at temperatures near glass transition temperature T_g. The strong difference was explained by fast exchange between lines of EPR spectrum due to pseudorotations of $^3C_{60}$ molecules, whereas reorientations of $^3C_{70}$ molecules provide slow or intermediate exchange.

In this work the strong divergence between temperature dependences of $^3C_{60}$ and $^3C_{70}$ phase memory times was explained by difference types and characteristic times of $^3C_{60}$ and $^3C_{70}$ molecular dynamics.

At the present time the researches of organic photovoltaics are very popular. Fullerene-based materials are perspective as acceptor materials in active layers of organic solar cells. The triplet signal was not revealed for the photoexcited blend of [6,6]-phenyl C_{61} butyric acid methyl ester and poly(3-hexylthiophene) (P3HT:PCBM). In contrast, the characteristic EPR signal of $P3HT^+$:$PCBM^-$ spin-correlated radical pair was observed [4].

Acknowledgements

The work was supported by RFBR grant №12-03-31190-mol-a and the Program of Russian Ministry of Science and Education (Grant №8175).

References

[1] Uvarov M.N., Kulik L.V., Bizin M.A., et. al. J. Phys. Chem. A, 112, 2519 -2525 (2008).

[2] Uvarov M.N., Kulik L.V., and Dzuba S.A. Appl. Magn. Res., 40, 489 (2011).

[3] Uvarov M.N., Kulik L.V., Doktorov A.B., and Dzuba S.A. J. Chem. Phys., 135, 054507 (2011).

[4] Uvarov M.N., and Kulik L.V. Appl. Magn. Res., in press.

EPR study of kinetics and mechanism of phototransformations of tetraalkylammonuim tetrachlorocuprates in low-temperature matrices

E.M. Zubanova[1], E.N. Golubeva[1], G.M. Zhidomirov[1,2]

[1]Chemistry Department, Lomonosov Moscow State University, 119991, Leninskie Gory 1-3, Moscow, Russia

[2]Boreskov Institute of Catalysis (BIC), SO RAN, 630090, Novosibirsk, Russia

e-mail: kate_zub@mail.ru

Copper (II) chloride complexes are of research interest as catalysts and model objects, e.g. for photochemical and theoretical studies. It was shown earlier that copper chlorocomplexes in frozen solutions transform by exposure of light with formation of organic radicals, copper (I) chloride complexes and new labile copper-containing intermediates [1, 2]. According to spectroscopic data and quantum-chemical calculations these intermediates were supposed to be Cu (II) complexes including, besides chlorine atoms, organic fragments in copper coordination sphere [3].

Photoreduction of copper (II) chloride complexes was considered to be the main direction of their phototransformationss, and three mechanisms of phototransformations of tetrachlorocuprates in low-temperature matrices were proposed. The first assumes the inner-sphere electron transfer $Cl^{-}\rightarrow Cu^{2+}$, that leads to formation of chlorine atom and copper (I) chloride complex [4]. The second mechanism is based on the outer-sphere electron transfer from molecule of donor solvent to excited copper (II) complex [1]. The products of this process are organic radicals formed from the solvent molecules and monovalent copper chlorides. But there are some experimental facts such as lack of products of chlorine atom interaction with solvent molecules and other components of the reaction system and occurrence of the reaction in donor solvents absence, which indicates the realization of these mechanisms to be unlikely. The third mechanism proposed by Golubeva et al assumes concerted breaking of Cu-Cl bond in the excited complex and C-H bond in organic fragments of counter ion [5]. This leads to formation of alkyl copper(II) complexes in primary photoprocess.

The aim of this work was determination of the mechanism details of photochemical transformations and secondary thermal reactions by obtaining and analysing of dose and concentration dependencies of the phototransformations of quaternary ammonium tetrachlorocuprates using EPR-spectroscopy and theoretical modeling of some thermal processes using methods of molecular dynamics.

Experimental and calculation details

The reagents and some of the products of the photolysis are paramagnetic compounds, that is why the method of electronic paramagnetic resonance spectroscopy could be applied to study such systems. The solutions of tetrahexylammonium tetrachlorocuprates in 2-chlorobutane and chlorobenzene with different initial concentrates were chosen as objects of research. The photolysis was performed at 77 K and 293 K by light with 405 nm wave length, that is close to the absorption maximum of $Cl^{-}\rightarrow Cu^{2+}$ charge transfer band.

Calculations of equilibrium geometric configurations and following calculations of fundamental frequencies were performed in the framework of density functional theory using exchange-correlation functional PBE and 6-311G^{++}(3df,3pd) basis set. Computation of classical trajectories was performed in the scope of Born-Oppenheimer molecular dynamics

(BOMD). Calculation of electronic structure in the each point of trajectory was also perfomed using PBE functional and 6-31G^{++}(d,p) and LANL2DZ basis sets.

Results and discussion

During the photolysis at room temperature only decreasing of tetrachlorocuprate absorption was observed in EPR spectra, and no new signals were found. The dose dependencies in this case were linear and quantum yield doesn't depend upon the initial concentration. Different results were obtained during the photolysis in 2-chlorobutane at 77 K. Besides the intensity decrease of tetrachlorocuprate signal, the appearing of a new absorption corresponding to the superposition of several bands of paramagnetic products was observed (fig.1). The new absorption is the EPR signal of a mixture of alkyl radicals and components of new copper complexes. Alkyl radicals in this system could be formed only as a result of hydrogen atom detachment from alkyl fragments of quaternary ammonium cation. Recently it was shown that as a result of the photolysis two new complexes formed (components I and II) [6]. After annealing to 100 K the alkyl radicals vanish and one copper complex (component II) transform to another (component I). After further heating this complex also disappears. The spectrum of the complex recorded after annealing to 100 K was described earlier and according to the literature data could correspond to the copper(II) alkyl complex [2].

The analysis of EPR spectra registered at different times of the photolysis for samples with different initial tetrachlorocuprate concentrations showed that in studied concentration

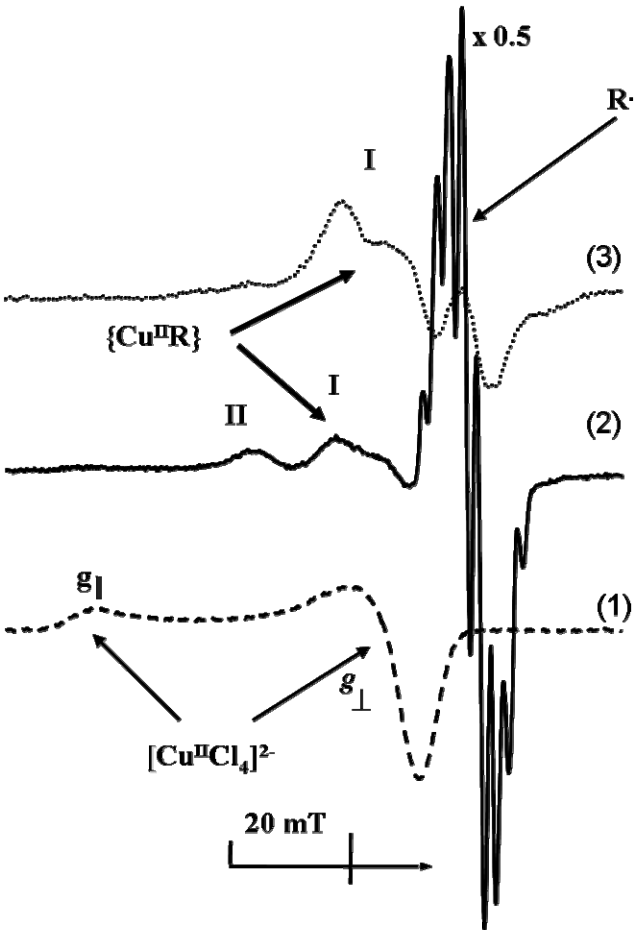

Fig.1. EPR spectra $[(C_6H_{13})_4N^+]_2[CuCl_4]^{2-}$ in 2-chlorobutane at 77 K: (1) – before photolysis, (2) – after photolysis, (3) – after heating (2) to 100 K.

range the qualitative composition of products does not change, while the quantitative composition depend on initial concentration. Dose dependencies of $CuCl_4^{2-}$ consumption and accumulation of photolysis products were plotted to find the quantum yields. All the dependencies are linear only at the beginning of the photolysis. The observed distortion of dose dependencies from linearity may be concerned with kinetic non-equivalence, e.g. dependence of the photochemical reaction speed on the particles environment. The concentration of more reactive particles drops during the photolysis, that's why the effective quantum yield decreases.

The obtained results are in agreement with the scheme of phototransformations of tetraalkylammonium tetrachlorocuprates in frozen solutions based on the concerted process. This mechanism assumes the formation both alkyl copper(II) complexes and alkyl radicals with monovalent copper complexes from excited complex $[(C_6H_{13})_4N^+]_2[CuCl_4]^{2-}$ (fig.2). The decreasing of quantum yield during the photolysis evidences the existence of complexes distribution by photochemical activity. Apparently, the distribution of relative disposition of alkyl substituent of quaternary ammonium cation and tetrachlorocuprate anion appears by freezing the solutions. By the way more favorable disposition of these fragments is necessary for organocuprates formation, otherwise the reaction will occur by the second way with formation of radicals and copper(I) chlorocomplexes. Thus, in solutions with lower initial concentration of $CuCl_4^{2-}$ formation of alkyl radicals was observed in greater extent, and the probability of occurring of the reaction with formation of radicals and chloride copper (I) complexes is higher. We suppose that at 77 K the reactions of radicals decay may take place. After heating to 100 K the probability of the secondary thermal processes increases. We also suppose that organic radicals may vanish in reactions with tetrachlorocuprates and new copper (II) complexes.

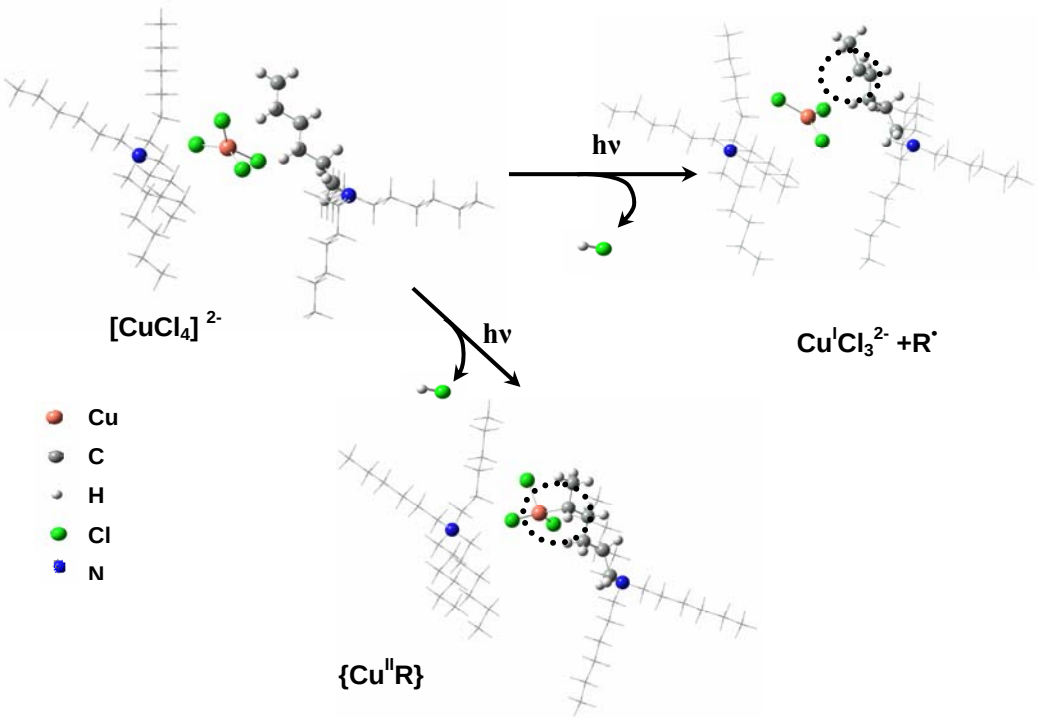

Fig.2. The scheme of dehydrochlorination reaction of excited complex $[(C_6H_{13})_4N^+]_2[CuCl_4]^{2-}$

After annealing to 110 K vanishing of copper (II) alkyl complexes occurs. The mechanism of the destruction of these complexes isn't still established. Two possible mechanisms are the monomolecular decay with carbon-copper bond breaking [7] and

bimolecular destruction [8]. Earlier quantum chemical calculations of potential energy surfaces for model alkyl complexes showed that bimolecular decay of these complexes occurred with large energy effect and barrierless [9]. In this paper the method of molecular dynamics was used to study the processes of organocuprates decay. The systems of two molecules of complexes $CuClCH_3$ and $[(CH_3)_4N^+]\,[CuCl_2CH_3]^-$ were chosen as simplest models. The BOMD simulations demonstrate spontaneous formation of the products – ethane and copper (I) chlorides in both cases. Therefore, the results of *ab initio* molecular dynamics calculations indicate the possibility of the fast bimolecular destruction of copper (II)-alkyl complexes even at low temperatures. The reaction is likely to be controlled by diffusion and could be inhibited by fixation in inflexible matrices or on the surfaces of different supports.

Conclusions

The mechanism of phototransformations of quaternary ammonium tetrachlorocuprates in low-temperature matrixes including both photoprocesses and secondary thermal reactions of the photolysis products at 77 – 110 K was proposed basing at the analysis of EPR data. Molecular dynamics calculations confirmed the suggestion that the destruction of products of phototransformations of quaternary ammonium tetrachlorocuprates - alkyl complexes of copper (II) at low temperatures can occur via bimolecular reaction.

Acknowledgements

The research is partially supported by RFBR Grant 10-03-00603a. We gratefully acknowledge Prof. Andrey Kh. Vorobiev for providing the computer programs for treatment and modeling of EPR spectra.

References

[1] V.F. Plyusnin, N.M. Bazhin, O.B. Kiseleva, *Zh. Khim. Fiz.* 1980, **54**, 672 (in Russian)

[2] E.N. Golubeva, A.V. Lobanov, V.I. Pergushov, N.A. Chumakova, A.I. Kokorin, *Dokl. Chem.*, 2008, **421**, 171.

[3] E.N. Golubeva, O.I. Gromov, G. M.Zhidomirov, J. *Phys. Chem. A*, 2011, **115**, 8147

[4] Kochi J.K. , J. Am. Chem. Soc., 1962, **84**, 2121.

[5] E. N. Golubeva, A. V. Lobanov, A. I. Kokorin, *Khim. Fiz.*, 2009, **28**, 9 (*Russ. J. Phys. Chem. B*., 2009, **3**, 179).

[6] A.V. Lobanov, E.N. Golubeva, M.Ya. Mel'nikov, Mendeleev. Commun., 2010, **20**, 343.

[7] I.V. Khmelinskii,, V.F. Plyusnin, N.P. Gritsan, N.M. Bazhin, Khim. Fiz., 1985, **4**, 12, 1666 (in Russian).

[8] H.Cohen, D. Meyerstein, Inorg. Chem., 1986, **25**, 1505.

[9] E. N. Golubeva, G. M. Zhidomirov, A. I. Kokorin, *Doklady Chemistry*, 2009, **426**, 6, 143.

Determination of the translational order of spin probe in smectic liquid crystal

D.A. Pomogailo, N.A. Chumakova, A.Kh. Vorobiev

Department of Chemistry, Lomonosov Moscow State University, 119991, Leninskiye gory, 1/3, Moscow, Russian Federation

e-mail: texafirin@ya.ru

Elucidation of structural organization of liquid crystal materials is an urgent task of modern material science. Orientational alignment of liquid crystals can be determined by optical methods and X-ray dispersion as well as nuclear and electron magnetic resonance. But at present time there is no reliable method for determination of translational alignment –that is, the alignment of mass centers of the molecules.

The goal of this work is to determine translational order of matrix molecules using electron paramagnetic resonance by means of spin probe technique. The main idea of our approach is as follows. It is widely accepted that liquid crystal possessing translational alignment consists of molecular layers. We introduce spin probe in liquid crystal media and expect that the probe molecules will be accumulated in the layers. Thus, local probe concentration in the layer will exceed the average concentration in the sample. Such concentration heterogeneity must manifest itself in the angular dependence of dipole-dipole broadening of the EPR spectrum lines.

It is known that dipole-dipole interaction of radicals depends on the distance between the paramagnetic particles as well as the angle between the line connecting two spins and the direction of external magnetic field. In fig.1a the angular dependence of the line broadening is presented which was calculated with two assumptions. Firstly, only dipole-dipole interaction of the probes located in one layer of liquid crystal was taken into account. Secondly, the paired distribution of the radicals at fixed distances was considered.

In fig.1b the experimental angular dependence recorded for spin probe possessing liquid crystal properties in smectic liquid crystal 8CB is shown. One can see that this dependence corresponds to the theoretical prediction.

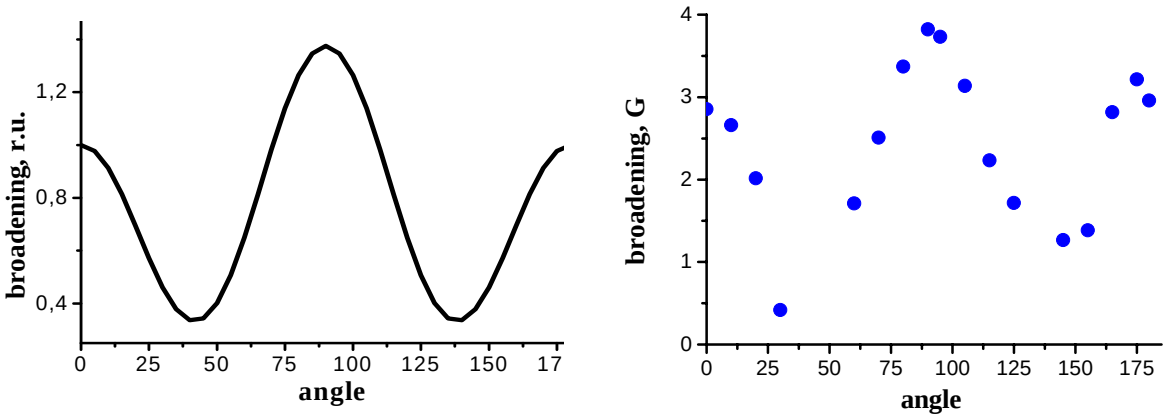

Fig.1. Theoretical (a) and experimental (b) angular dependence of dipole-dipole broadening of the EPR spectrum line.

This work was supported by Russian Foundation for Basic Research, grants No. MOL_A_2012 № 12-03-31114. The authors thank Prof. R.Tamura for provision of paramagnetic probe.

Charge ordering in $Nd_{2/3}Ca_{1/3}MnO_3$: evidence for ferromagnetic correlations

O. Kravchyna[1], E. Fertman[1], S. Dolya[1], V. Desnenko[1], N. Pascher[2], H.-A. Krug von Nidda[2], M. Hemmida[2], S. Schaile[2], A. Loidl[2], A. Anders[3], M. Kajňaková[4], A. Feher[4]

[1]B. Verkin Institute for Low Temp. Physics & Eng., 61103, 47 Lenin Ave., Kharkov, Ukraine

[2]Experimental Physics V, Center for Electronic Correlations and Magnetism, University of Augsburg, 86135 Augsburg, Germany

[3]V.N. Karazin Kharkiv National University, 61022, Svobody Sq. 4, Kharkiv, Ukraine

[4]P. J. Šafárik University in Košice, Faculty of Science, 04154, Park Angelinum 9, Košice, Slovakia

e-mail: kravcina@mail.ru

Below room temperature the physical properties of most colossal magnetoresistant (CMR) manganites are governed by phase separation phenomena, which means a coexistence of different phases in a wide temperature region [1]. In the case of CMR compound $Nd_{2/3}Ca_{1/3}MnO_3$, self-organized phase separation occurs in the vicinity of the charge ordering at $T_{CO} \sim 212$ K due to its first order martensite nature [2]. Below T_{CO} the compound represents a mixture of alternating nano-sized charge ordered (CO) and charge disordered (CD) regions, which on further cooling become antiferromagnetic (AFM) and ferromagnetic (FM) ones, respectively [3]. In the present study we report resistivity, magnetization and electron spin resonance (ESR) measurements on $Nd_{2/3}Ca_{1/3}MnO_3$ manganite across the charge-ordering transformation at T_{CO} down to the antiferromagnetic transition temperature $T_N \sim 130$ K.

A ceramic $Nd_{2/3}Ca_{1/3}MnO_3$ sample was prepared by a standard solid-state reaction technique from stoichiometric amounts of proper powders. X-ray crystal-structure analysis and neutron-diffraction study indicated a single-phased material at room temperature. Magnetic measurements were made using the Quantum Design Magnetic Properties Measurement System (MPMS) and a noncommercial superconducting quantum interference device (SQUID) magnetometer in 4 – 300 K temperature range. The ESR measurements were performed on a Bruker ELEXSYS E500-CW spectrometer at *X*-band (9.4 GHz) frequency, equipped with a continuous He-gas flow cryostat (Oxford instruments) working in the temperature range 4.2 – 300 K.

The $Nd_{2/3}Ca_{1/3}MnO_3$ compound is a mixed-valence one, containing two types of manganese ions, Mn^{3+} and Mn^{4+}. Charge ordering refers to the real space ordering of the Mn^{3+} and Mn^{4+} ions which occurs on cooling below a certain temperature T_{CO}. The CO state becomes stable when the Coulomb energy is dominant over the kinetic energy. The compound $Nd_{2/3}Ca_{1/3}MnO_3$ is insulating at all temperatures in zero magnetic field (fig.1). Above T_{CO} the compound is a paramagnetic insulator. Its resistivity changes by about three orders of magnitude from 300 K to 150 K. There is a change in slope of the temperature dependent resistivity curve at T_{CO}, the anomaly is brightly seen in the insert, fig.1.

The charge carriers play an important role in the exchange coupling in the mixed-valence manganites [4]. The charge ordering phase transition is seen as anomaly on the dc magnetization curves $M(T)$ at all external magnetic fields studied: a pronounced shoulder is observed in the $M(T)$ curves at T_{CO} (fig.2). Similar anomalies of the temperature dependent dc magnetization, which are more or less pronounced, are usually seen in the vicinity of the charge ordering in mixed-valence manganites [5, 6]. There exists a strong competition between the double-exchange interaction which favours ferromagnetism and the CO state

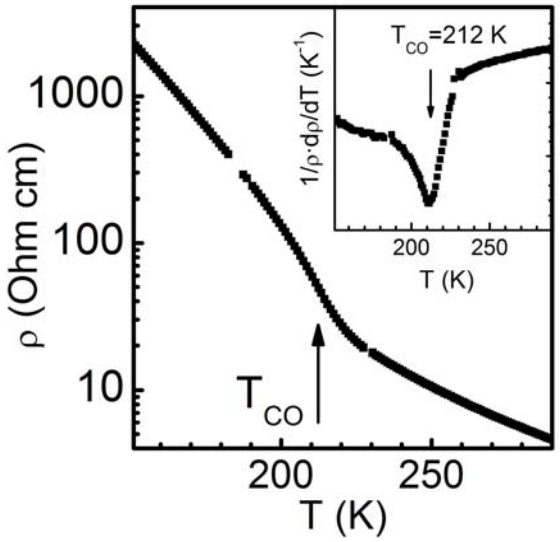

Fig.1. Temperature dependence of the resistivity of $Nd_{2/3}Ca_{1/3}MnO_3$ measured at a frequency of 30 Hz. Inset: the temperature dependence of the derivative of resistivity around T_{CO}

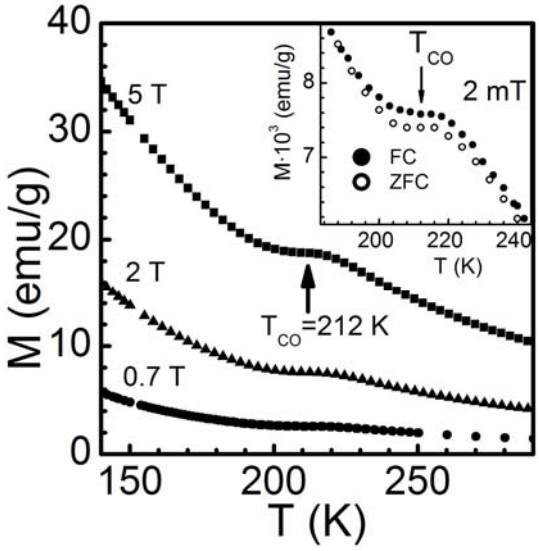

Fig.2. Temperature dependence of dc magnetization for $Nd_{2/3}Ca_{1/3}MnO_3$ in different magnetic fields. Inset: ZFC and FC dc magnetization in the low external magnetic field.

which favours antiferromagnetism. The anomaly of the dc magnetization observed at T_{CO} is usually attributed to the competition of ferromagnetic and antiferromagnetic exchange interaction and weakening of the double exchange due to the localization of the charge carriers below T_{CO}, resulting in a drop of the susceptibility [7]. But the magnetic state of the compound in the temperature range between T_{CO} and T_N (T_N <T< T_{CO}) is still not quite clear.

Electron paramagnetic resonance is a powerful method which gives information on the static and dynamic correlations on a microscopic level and helps to clarify the complex magnetic states of manganites. The ESR spectra, (*dP/dH*) vs *H*, where *P* is the microwave power absorbed and *H* is the magnetic field, from room temperature down to T_N, showed a symmetric line shape (fig.3, the insert). We have found an anomalous temperature dependence of ESR linewidth ΔH on crossing T_{CO}, which reflects the transition from itinerant to localized electrons in the system: above T_{CO} it may be well described by the Korringa law [8], below T_{CO} it was described by the Huber et al.'s approach [9]. Note that ΔH exhibits a continuous decrease below T_{CO} down to the antiferromagnetic transition at $T_N \sim 130$ K (fig.3), whereas the most of other CO compounds exhibit a continuous increase in a such case [10, 11, 12].

At the temperature range $T > T_{CO}$ the linear dependence of ΔH seems to be associated with Korringa-type relaxation of localized moments via itinerant charge carriers (eq.1). The line shape is Lorentzian, its linewidth defines the spin-lattice relaxation time, and it can be described by the well-known Korringa expression [8]

$$\Delta H = \Delta H_0 + b \cdot T \ . \qquad (1)$$

The relaxation process is considered in the model of the isotropic exchange Hamiltonian $\mathcal{H} = J\vec{S}\vec{s}$, where *S* is the spin of the localized moment and *s* is the spin density of the conduction electrons in the *S* site. Therefore, the coefficient *b* (eq.1) is proportional to the

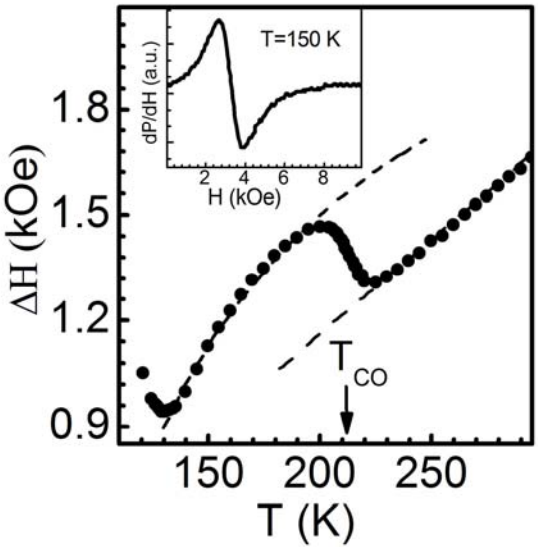

Fig.3. Temperature dependence of the ESR linewidth ΔH in $Nd_{2/3}Ca_{1/3}MnO_3$. Inset: ESR absorption spectrum at T = 150 K. Lines are the approximations by the Korringa law for $T > T_{CO}$ and by the Huber law for $T < T_{CO}$.

square of the density of states of the conduction electrons at the Fermi level $\rho^2(E_F)$ and the exchange integral $J^2(q)$, averaged over the Fermi surface.

$\Delta H(T)$ below T_{CO} was analyzed using Huber et al's law

$$\Delta H(T) = \frac{T-\Theta}{T}\Delta H_\infty, \qquad (2)$$

where ΔH_∞ is the high-T asymptote due to spin-spin relaxation mechanism in a system of localized spins; Θ is the Curie-Weiss (CW) temperature. Such an approach assumes strong exchange coupling providing a bottleneck regime of resonating spins from atomic to nanometer scale.

Earlier we have shown that the parameters of the low-field temperature dependent dc susceptibility are evident of the appearance of FM correlations in the paramagnetic state of $Nd_{2/3}Ca_{1/3}MnO_3$ compound and of the formation of ferromagnetic nano-clusters in the system, which increase in size with decreasing temperature down to T_N [2]. The CW temperature value obtained from the fitting procedure of the low-field dc magnetization in the temperature interval $T_N < T < T_{CO}$ is $\Theta = 89$ K. The CW temperature value obtained from the fitting of $\Delta H(T)$ data (fig.3) in the same temperature interval in the present work is $\Theta = 85$ K. The CW temperatures obtained from dc magnetization and ESR data are in a good agreement. From eq.2 it is clear that a positive Θ value determines a continuous decrease of ΔH below T_{CO} on cooling the sample. So, it may be concluded that the anomalous behavior of the ESR linewidth in $Nd_{2/3}Ca_{1/3}MnO_3$ compound, compared with the other charge ordered manganites, originates from the presence of ferromagnetic correlations in the paramagnetic state, well above its Néel temperature. This may be connected with a phase segregated state of the studied compound. Note, that charge-ordered manganite $Ca_{0.9}Ce_{0.1}MnO_3$, in which the similar anomalous behavior $\Delta H(T)$ were earlier found [10], is phase segregated as well.

This work was supported by Slovak Grant Agency VEGA-1/0159/09, the Grant of NAS of Ukraine (No.1/07-N)) and by the DFG within TRR80 (Augsburg/Munich).

References

[1] E. Dagotto, Nanoscale Phase Sepatation and Colossal Magnetoresistance, Springer Series in Solid State Physics, Springer-Verlag, Berlin (2003).

[2] A.B. Beznosov, E.L. Fertman, V.A. Desnenko, Fiz. Nizk. Temp. **34** 790 (2008) [Low Temp. Phys. **34** 624 (2008)].

[3] A.B. Beznosov, V.V. Eremenko, E.L. Fertman, V.A. Desnenko, D.D. Khalyavin, Fiz. Nizk. Temp. **28** 1065 (2002) [Low Temp. Phys. **28** 762 (2002)].

[4] E. Granado, N. O. Moreno, H. Martinho, A. García, J.A. Sanjurjo, I. Torriani, C. Rettori, J. J. Neumeier, S. B. Oseroff, Phys. Rev. Lett. **86** 5385 (2001).

[5] F. Dupont, F. Millange, S.de Brion, A. Janossy, G. Chouteau, Phys. Rev. B **64,** 220403 (2001).

[6] S. Jandl, A.A. Mukhin, V.Yu. Ivanov, A.M. Balbashov, J. Phys.: Condens. Matter **18** 1667 (2006).

[7] R. Gupta, J.P Joshi, S.V. Bhat, A.K. Sood, C.N.R. Rao, J. Phys.: Condens. Matter **12** 1919 (2000).

[8] J. Korringa, Physica **16** 601 (1950).

[9] D.L. Huber, G. Alejandro, A. Caneiro, M.T. Causa, F. Prado, M. Tovar S.B. Oseroff, Phys. Rev. B **60** 12155 (1999).

[10] A. Sharma, S. Sarangi, S.V. Bhat, Phys. Rev. B **73** 035129 (2006).

[11] D. V. Zakharov, J. Deisenhofer, H.-A. Krug von Nidda, A. Loidl, T. Nakajima, and Y. Ueda, Phys. Rev. B **78** 235105 (2008).

[12] S. Schaile, H.-A. Krug von Nidda, J. Deisenhofer, A. Loidl, T. Nakajima, and Y. Ueda, Phys. Rev. B **85** 205121 (2012).

Spatial structure of felodipine in DMSO-d6 solution by 1-D NOE and 2-D NOESY NMR spectroscopy

I.A. Khodov[1], M.Y. Nikiforov[1], G.A. Alper[1], D.S. Blokhin[2], S.V. Efimov[2], V.V. Klochkov[2], N. Georgi[3]

[1]G.A. Krestov Institute of Solution Chemistry of RAS, 153045, Akademicheskaya St., 1, Ivanovo, Russia.

[2]Kazan (Volga region) Federal University, 420008, Kremlyovskaya St., 18. Kazan, Russia.

[3]Max-Planck-Institute for mathematics in the sciences, 04103, Inselstraße St. 22, Leipzig, Germany.

e-mail: iakh@isc-ras.ru

Intriduction

The accurate determination of interproton distance in relatively small, flexible molecules by 1D and 2D NOE NMR spectroscopy is the subject of increasing interest in recent years [1–3] The results of such investigations can be applied to establishing conformational details for biologically active molecules in solutions. It is well known that polymorphism of drug compounds affect the biological activity and plays an important role in the production of pharmaceuticals. In turn, the properties of polymorphs due to the moleculare structure of compounds and their ability to exist in different conformational forms in the solvent form which recrystallization occurs. Therefore, the search for new polymorphic forms of drug closely associated with the study of the conformational state of biological active molecules in solutions.

Felodipine is a calcium channel blocker and widely used in the treatment of hypertension. Conformational flexibility of felodipine is determined by two dihedral angles (c3-c4-c1'-c2') defines the rotation of 2,4 dichlorophenyl group around c1'-c4 bond and the second(c3a-O-c3b-c3c) the rotation of ethyl group around O-3b (fig.1). Teberikidis and Sigalas in 2007 published the result of a theoretical study of felodipine using a hybrid density functional method B3LYP [4]. They located six conformers with very close energies (within 4,2 kJ / mol), starting from number 1(the global minimum) up to number 6 (with a maximum energy). It is important for the purposes of further discussion, that in the conformers 1,2,5 chlorine atoms lying towards dihydropyridine, whereas in the conformers 3,4,6 in the opposite direction.

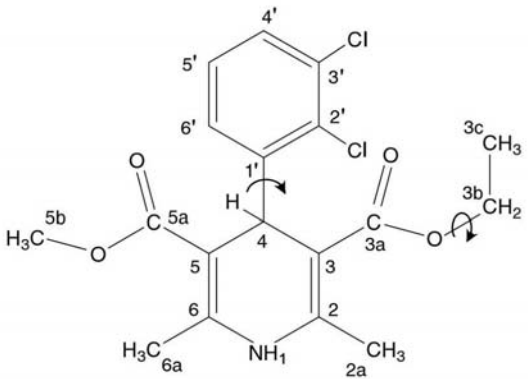

Fig.1. Structure and nomenclature of felodipine

Theory

NOE spectroscopy is a powerful tool of studying the spatial structure and conformations of molecules in solutions. The method of estimating internuclear distances for various pairs of protons in a molecule is based on the existence of a strong dependence of the cross-relaxation rate constant σ_{ij} on the distance r_{ij} between the interacting nuclear spins. Normally, such a dependence is easily approximated by the formula $\sigma_{ij} \sim 1/r_{ij}^6$ and then internuclear distances are obtained according to the formula:

$$r_{ij} = r_0 \left(\frac{\sigma_0}{\sigma_{ij}} \right)^{\frac{1}{6}}, \quad (1)$$

where the quantities r_0, σ_0 refer to a pair of protons chosen for calibration the distance r_0 is supposed to be known from some independent source (e.g. quantum chemical calculations). However, for small, conformationally flexible molecules, of great importance is the problem of more accurate determination of internuclear distances in order to obtain information of relative population of various conformers. This goal may be obtained both by a more accurate interpretation of the 2D NOESY experiment and by taking account of the anisotropic molecular rotation.

Experimental

All NMR experiments were performed on a "Bruker Avance II-500" NMR spectrometer equipped with a 5 mm probe using standart the Bruker TOPSPIN Software. Temperature control was performed using a Bruker variable temperature (BVT-2000) unit in combination with a Bruker cooling unit (BCU-05) to provide chilled air. Experiments were performed at 298 K without spinning. ^{1}H NMR(500 MHz) spectra were recorded using 90° pulses and relaxation delay of 1 s, with a spectral width of 12.02 ppm, 128 scans. 13C NMR spectra were recorded using 45° pulse sequence with power-gated decoupling for suppression of the NOE effect.

The ^{13}C NMR spectra were acquired with relaxation delay 1s, 236 ppm spectral width, 1024 scans. Total correlation spectroscopy (TOCSY), one dimension gradient homonuclear selective total correlation spectroscopy (1D ge-TOCSY), heteronuclear multiple-bond correlation (HMBC)[5] and gradient heteronuclear single-quantum coherence (ge-HSQC), have been used to assign the complex ^{1}H and ^{13}C NMR spectra**.**

Two-dimensional nuclear Overhauser effect spectroscopy (2D ge-NOESY) experiments were performed with pulsed filtered gradient techniques. The spectra were recorded in a phase-sensitive mode with 2048 points in the F2-direction and 512 points in the F1-direction. Mixing time values, were 0.30, 0.50, 0.70 and 0.90 s.The spectra were acquired with 24 scans and 2 s relaxation delay.

Selective One-dimensional nuclear Overhauser effect spectroscopy (ge-1D NOESY) experiments were carried out by using the double-pulse field gradient spin-echo NOE (1D-DPFGSENOE) NOE pulse sequence. The 1D NOESY spectra were acquired with 64 k data points, 160 scans, 12 ppm spectral width, 2 s relaxation delay, acquisition time of 5.45 s, mixing times of 0.3, 0.5, 0.7 and 0.9 s. The pulse programs for all NMR experiments were taken from the Bruker software library.

The list of atomic coordinates for the various conformations of felodipine from supplementary data [4] has enable us to calculate the effective distances required for comparison with experiment (calculated distances in tables 1-4. Effective distances show in tables as a calibration distance, chosen as such because of their equality for all conformations of felodipine. It should be noted that the distance between aromatic protons can not be taken for the calibration because of artifacts observed in the NOE intensities [2].

Results of 2D NOE experiments are presented in table 1. It is obvious that the calculated values of the distances for a conformation 1,2,5 are very close match to experimental data, while for the conformations 3,4,6 agreement with experiment is very poor. The experimental value of rij for the pair of protons 4-6' lies within interval 2.12 Å (conformations 1,2,5) – 3,73 Å (conformations 3,4,6), while the difference between 2.21 A

and 2.12 A goes beyond the experimental error (~ 3%). Really 2D NOE experiments show that at the concentration investigated conformations 1,2,5 prevail although there are of some conformations 3,4,6.

In favor of the existence of a significant amount conformations of 3,4,6 show the result of 1D NOE experiment: the closeness of experimental and calculated values of r_{ij} for protons NH-6'(Table 2).

Table 1. 2D NOESY

Atomic group	Experimental distance Å	Calculated distances Å					
		Conf 1	Conf 2	Conf 3	Conf 4	Conf 5	Conf 6
3b-3c	calibration	2,69	2,69	2,69	2,69	2,69	2,69
4-6'	2,21	2,12	2,12	3,73	3,73	2,12	3,73

Table 2. 1D NOE NH proton selective

Atomic group	Experimental distance Å	Calculated distances Å					
		Conf 1	Conf 2	Conf 3	Conf 4	Conf 5	Conf 6
NH-2a	calibration	2.48	2.48	2.48	2.48	2.48	2.48
NH-6a	2.50 ±0.08	2.48	2.48	2.48	2.48	2.48	2.48
NH-6'	3.44±0.06	-	-	3.50	3.48	-	3.37

Recently Butts et al [6] gave a convincing example of the fundamental possibility of quantitative determination of conformations of flexible molecules by NOE. This success is due to the presence in a molecule arugosin C just five short interproton distances (<3 Å), which can be determined with high accuray. Unfortunately, in our case, for each of conformations we have only one distance less 4 Å (if not take into account 3,92 Å for conf. 2 in table 4). It is well known that errors in measuring distances by NOE in this range (>4 Å) are greatly increased, mainly due to spin diffusion. Therefore the problem of the suppression of spin diffusion in NOE-measurements of interproton distances for small molecules remains very important.

Thus, the result of 1D and 2D NOE studies of felodipine in DMSO solution 0,08 g/l show the dominant presence of felodipine conformations in which chlorine atoms lying towards dihydropyridine. However, the existence of a of some amount of conformations in which chlorine atoms lying in the opposite direction clearly reveals. We were not able to make quantitative evaluation of populations of the felodipine conformations in DMSO because of insufficient accuracy in the range of relativity large distances (~4 Å). In such circumstances, we see two ways to improve the accuracy of interproton distance determination of interproton distances, concerted T-ROESY/NOESY experiments or suppression of spin diffusion. Well try to use both approaches and analyze their capabilities in our next work.

Acknowledgements

This work was performed in the Marie Curie International Research Staff Exchange Scheme PIRSES-GA-2009-247500. The reported study was partially supported by RFBR, research project No. 12-03-31001 a.

References

[1] Butts, C. P. Jones, C. R. Towers, E. C. Flynn, J. L. Appleby, L. Barron, N. J. Org. Biomol. Chem. 2011, 9, 177–184.

[2] Jones, C. R. Butts, C. P. Harvey, J. N. Beilstein J. Org. Chem. 2011, 7, 145–150.

[3] Chini, M. G. Jones, C. R. Zampella, A. Auria, M. V. D. Renga, B. Fiorucci, S. Butts, C. P. Bifulco, G. Clinica, M. Perugia, U. Facolta, N. Gerardo, V. Andrea, D. S. J. Org. Chem. 2012, 77, 1489–1496.

[4] Teberekidis, V. I. Sigalas, M. P. J. Mol. Struct.: THEOCHEM 2007, 803, 29–38.

[5] Bax, A. Summers, M. F. J. Am. Chem. Soc. 1986, 108, 2093–2094.

[6] Butts, C. P. Jones, C. R. Song, Z. Simpson, T. J. Chem. Commun. 2012, 48, 9023–9025.

Hydration properties of the Na^+ in aqueous solutions studied by NMR relaxation and quantum chemical calculations

S.E. Kurnikov, A.V. Donets

198504, St. Petersburg State University, St. Petersburg, Petrodvorets, ul. Ulyanovsk, 1

e-mail: serkurnikov@gmail.com

Introduction

Investigation of microstructure of aqueous electrolyte solutions attracts great interest due to their important role in various physical, chemical, technological and biological processes. The method developed in the Department of Quantum Magnetic Phenomena [1] makes it possible to determine important parameters of the microstructure of electrolyte solutions. The study of the microstructure of the hydration shell of sodium cation was carried out by independent and complementary methods: NMR-relaxation and quantum chemical calculations.

Nuclear magnetic relaxation in aqueous electrolyte solutions

Relaxation processes are governed by the interaction of the nuclei with fluctuating magnetic or inhomogeneous electric fields in the media, which depend on the molecular thermal motion. When several relaxation mechanisms act simultaneously the total relaxation rate is calculated as follows, under the condition of the independence of relaxation processes, that is often realized:

$$\frac{1}{T_1} = \sum_k \frac{1}{T_{1k}}, \tag{1}$$

$$\frac{1}{T_{1k}} = \sum_i \frac{p_i}{T_{1k,i}}, \quad \sum_i p_i = 1, \tag{2}$$

where T_{1k} is the relaxation time of the *k-th* mechanism. In the case of electrolyte solutions, the each term in the relation (1) can be written in the form (2). Where p_i are the relative concentrations of the *i-th* substructure of the solvent nuclei, $T_{1k,i}$ is the spin-lattice relaxation time of the *k-th* relaxation mechanism in the *i-th* substructure of the solvent nuclei. Usually, one relaxation mechanism predominates in aqueous electrolyte solutions. If the exchange of solvent nuclei between all substructures is fast, the spin-lattice relaxation rate is given by the expression:

$$\frac{1}{T_1} = \frac{1}{T_{10}} + \sum_{i=1}^{N-1} \frac{m n_i L_{\pm}}{M} \left[\frac{1}{T_{1i}} - \frac{1}{T_{10}} \right], \tag{3}$$

where m is the molality of the solution; T_{1i} and T_{10} are the relaxation times of the nuclei in the *i*-th substructure of the solution and in the pure solvent, respectively; n_i is the number of water molecules in the *i*-th substructure; M is the number of moles in 1000 g of the solvent (for water, M=55.5 mol kg^{-1}); $\alpha^{\pm}$ is the number of positive and negative ions in the solute molecule; N is the number of substructures in the solution including the undisturbed water structure. Relation (3) predicts a linear concentration dependence of the relaxation rates; however, experimentally distinct deviations from linearity have been observed. The deviations can be explained by disappearance of some substructures in the solution [2].

For liquids, the expression of quadrupole spin-lattice relaxation may be written as

$$\frac{1}{T_{1,2}} = \frac{3}{40}\frac{2I+3}{I^2(2I-1)}\left(1-\frac{\eta^2}{3}\right)\left(\frac{e^2q_iQ}{\hbar}\right)^2\tau_i, \qquad (4)$$

where I is the spin of the quadrupole nucleus, q_i is the largest component of EFG tensor at the nuclear place in the *i-th* substructure; eQ is the nuclear quadrupole moment; and $e^2q_iQ/\hbar$ is the quadrupole coupling constant.

^{23}Na NMR-relaxation

The fig.1 shows the concentration dependence of the spin-lattice relaxation time ^{23}Na in $NaNO_3$ aqueous solution. The slope of the experimental curve changes at concentration m = 2,3 mol ([$NaNO_3$]:[D_2O] = 1:24). The main reason is the disappearance of zone of free solvent in the solution. The first hydration shell of the sodium consists of 6 water molecules, second shell – 12. The NO_3^- ion coordinates 6 molecules.

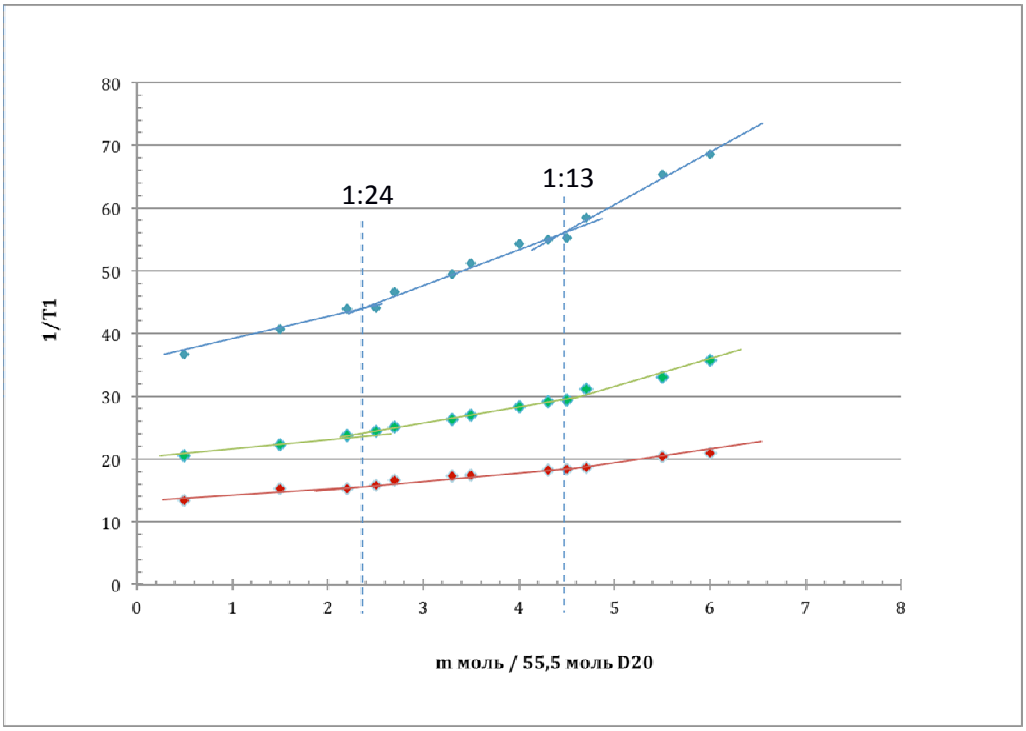

Fig.1. Concentration dependence of the ^{23}Na spin-lattice relaxation in aqueous solutions $NaNO_3$ at 5°C, 28°C and 54°C

The bend at concentration m = 4,6 mol ([$NaNO_3$]:[D_2O] = 1:12) indicates complete disappearance of the second layer of the hydration shell of the ion Na+. With further increase in concentration does not exclude the formation of contact ion pairs. The experimental results are in good agreement with data previously obtained on the basis of relaxation of the solvent nuclei.

Quantum-chemical calculation

Quantum-chemical calculation water clusters around the sodium cation were carried out. Several structures are characterized by the most stable configurations with minimal values of the energy. It was shown that the hydration shells of the sodium cation consist of the 6 water molecules in the first layer and 12 in the second. (Basic symmetry group obtained clusters: D2d, C2, Th. fig.2). The quadrupole coupling constants of the deuterons and sodium were calculated by quantum-chemical calculations. Mobility of sodium was determined by

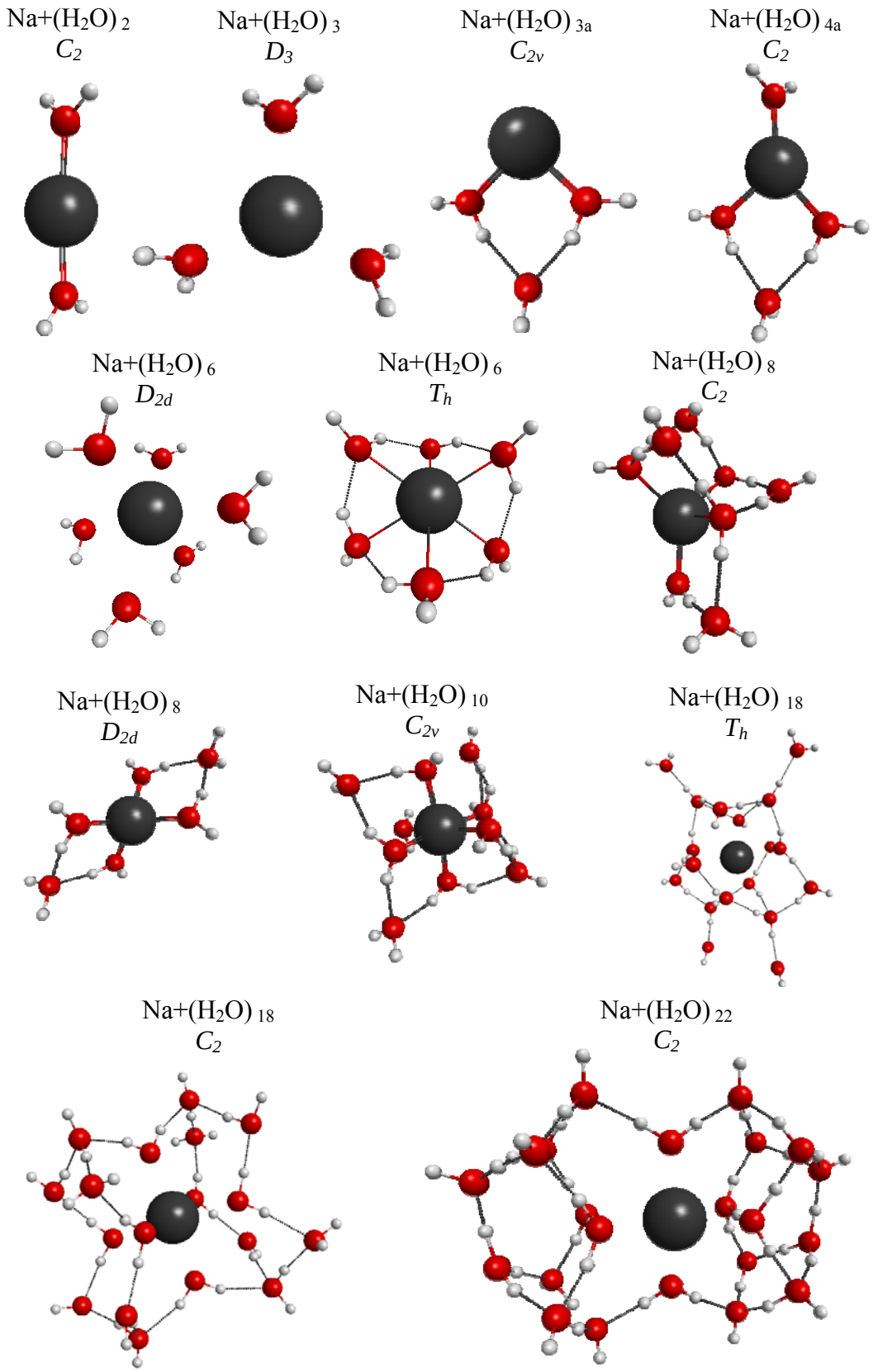

Fig.2. Structures of $Na^{+}(H_2O)_n$ clusters (n = 2-6, 8, 10, 18, 22) with the corresponding type of symmetry. The method: DFT B3LYB, basis the 6-31G (3df, 3pd)

molecular dynamics. The calculated relaxation time of the ^{23}Na was compared with experimental results.

The structures of the molecular clusters $Na^+(H_2O)_n$ (n = 6, 8, 10, 18) used in this work are shown in fig.2. As the initial approximation, the $Na^+(D_2O)_6$ clusters containing water molecules only in the first hydration shell were considered. It was followed by analysis of the variation of the sodium QCC following gradual filling of the second hydration shell. The calculated QCC of the sodium with the first and second hydration shells are given in Table 1. Quantum chemical calculations were performed using the 6-31G-basis set for Na^+ ion.

Table 1. Results of DFT quantum chemical calculations of the molecular clusters $Na^+(H_2O)_n$ (n = 2 – 6, 8, 10, 18, 22) with the B3LYP functional (for the ^{23}Na)

Cluster	Symmetry	Total energy	Distance O–Na (r) *A* first shell	$\sqrt{1+\frac{\eta^2}{3}}\frac{e^2qQ}{\hbar}$	$\frac{1}{T_{1,2}}$, c^{-1}
$Na+(H_2O)_2$	C_2	-314.849	2.290	1.928 MHz	3.68
$Na+(H_2O)_{3a}$	D_3 , C_{2v}	-391.360	2.322	5.159 MHz	26.34
$Na+(H_2O)_{4a, 4b}$	C_2 , S_4	-467.786	2.355	4.937 MHz	24.13
$Na+(H_2O)_{5b, 5c}$	C_1 , C_2	-544.199	2.414	5.162 MHz	26.37
$Na+(H_2O)_{6a, 6f}$	T_h , D_{2d} ,C_s	-620.655	2.452	1.015 MHz	1.01
$Na+(H_2O)_8$	C_2 , C_{2v}	-762.406	2.393	2.127 MHz	4.47
$Na+(H_2O)_{10}$	D_2	-926.266	2.145	1.007 MHz	1.00
$Na+(H_2O)_{18}$	D_2 , T_h	-1537.659	2.618	5.398 MHz	28.84
$Na+(H_2O)_{22}$	C_2	-1816.052	3.121	4.831 MHz	23,15

Conclusion

The quantum chemical study of clusters comprising the Na^+ ion surrounded by water molecules, which model the structure of the hydration shells of the ion in solution, were carried out. Using the density functional approach with the B3LYP hybrid functional and the 6-31G basis set, two equilibrium structures of the $Na^+(D_2O)_{18}$ complex with two completely filled hydration shells of the ion were obtained. The calculations confirm experimental results. Thus, we were able to get fundamental results using two complementary and independent methods.

References

[1] Chizhik V.I., Molec. Phys., 1997. V.90, 653.

[2] Donets A. V., Chizhik V.I., Structural Chemistry, 2011. V. 22, № 2. 465-470

New mixed-valence tellurates $Li_{1-x}Mn_{2+x}TeO_6$ and $LiMn_{2-x}Fe_xTeO_6$: magnetization and EPR studies

E.A. Samohvalov[1], E.A. Zvereva[1], O.A. Savelieva[1], V.B. Nalbandyan[2], O.S. Volkova[1], E.L. Vavilova[3], A.N. Vasiliev[1]

[1]Faculty of Physics, Moscow State University, 119991 Moscow, Russia
[2]Chemistry Faculty, Southern Federal University, 344090 Rostov-on-Don, Russia
[3]Zavoisky Physical - Technical Institute, 420029 Kazan, Russia

e-mail: samokhvalov@physics.msu.ru

Introduction

In the last decades metal oxides, containing manganese in the mixed valence attract the special interest of the scientists, since their potential prospects for the practical applications. Some of these compounds, for example, $LiMn_2O_4$, are promising materials for the manufacture of electrodes in lithium-ion batteries [1]. Others, in particular $R^{3+}_{1-x}A^{2+}_xMnO_3$ (where R is rare earth element, and A is alkaline earth group II metals), show the effect of a colossal magnetoresistance [2]. In the compounds mentioned above, the average manganese oxidation is between 3+ and 4+, while oxides with mixed Mn^{2+} and Mn^{3+} ions are relatively rare. In the present work we report on static and dynamic magnetic properties of new tellurate systems $Li_{1-x}Mn_{2+x}TeO_6$ and $LiMn_{2-x}Fe_xTeO_6$, in which the manganese is in the mixed-valence state Mn^{2+} - Mn^{3+}. They represent a new triclinic structure type (space group P1) derived from orthorhombic Li_2TiTeO_6 [3].

Experiment

The ceramic samples $Li_{1-x}Mn_{2+x}TeO_6$ (x=0÷0.04) and $LiMn_{2-y}Fe_yTeO_6$ (y=0÷0.10) have been prepared by conventional solid-state reaction. Temperature dependencies of the magnetic susceptibility and magnetic field dependencies of the magnetization have been measured by SQUID magnetometer in the range T=2-300 K, $B\leq$7 T, electron paramagnetic resonance (EPR) studies have been carried out using X-band spectrometer ($f\approx$9.4 GHz, $B\leq$0.7 T, T=6-470 K).

Results and discussion

It was found that all samples $Li_{1-x}Mn_{2+x}TeO_6$ of various compositions demonstrate the common features in the magnetic properties. Temperature dependence of the magnetic susceptibility has a complicated character and reveals the presence of two distinct anomalies at low temperatures: the first one at T_1=12 K and the second at T_2=20 K. The presence of both anomalies is also evident in the NMR spectra at low temperatures. We assume that the maximum at T_2 = 20 K corresponds to the transition to antiferromagnetic (AFM) phase at low temperatures. Upon an increase of manganese content amplitude of the first anomaly monotonously increases, while the magnitude of the second one remains practically unchanged (fig.1). At temperatures higher T_2 the magnetic susceptibility follows the Curie-Weiss law $\chi = \chi_0 + C/(T-\Theta)$. Curie-Weiss temperature weakly depends on the composition and is on average $\Theta\approx$-90-95 K, indicating antiferromagnetic interaction between Mn ions. Effective magnetic moment estimated from the Curie constant values C was found to be 7.6-8.0 μ_B. These values agree satisfactorily with theoretical estimations for given concentration of manganese if assume that half of Mn ions per formula unit is in high-spin Mn^{2+} (S=5/2) state and another half is in high-spin Mn^{3+} (S=2) state.

EPR spectra of samples studied show inhomogeneously broaden absorption line probably originated from Mn^{3+} ions in weakly distorted octahedral coordination. Thorough analysis of the line shape indicates that absorption line is a superposition of two spectral components (broad 1 and narrow 2 ones) with rather different effective g-factors: at T=300 K - g_1=1.52±0.01 and g_2=2.15±0.01. This is likely to correspond to the presence of four crystallographically non-equivalent Mn sites in the structure [3]. With decreasing temperature down to helium temperature the EPR line essentially broadens by analogy with behavior of other antiferromagnetic and spin-glass systems due to slowing down of the spins in the vicinity of the Neel temperature.

The magnetic properties of iron-doped system $LiMn_{2-y}Fe_yTeO_6$ qualitatively differ from the system described above. The temperature dependence of the magnetic susceptibility χ(T) has complex character, which changes visibly under variation of the compound composition (fig.2). When the concentration of Fe is low the presence of both anomalies, which we

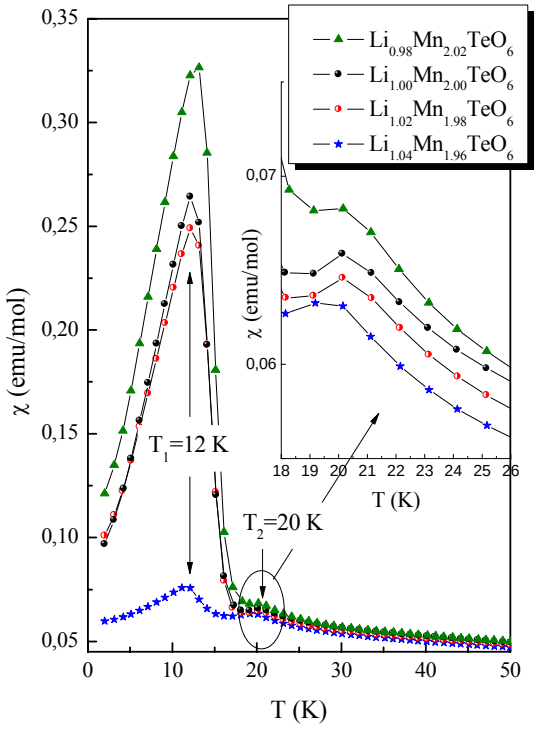

Fig.1. Temperature dependence of the magnetic susceptibility for $Li_{1-x}Mn_{2+x}TeO_6$ of various composition at B = 0.1 T.

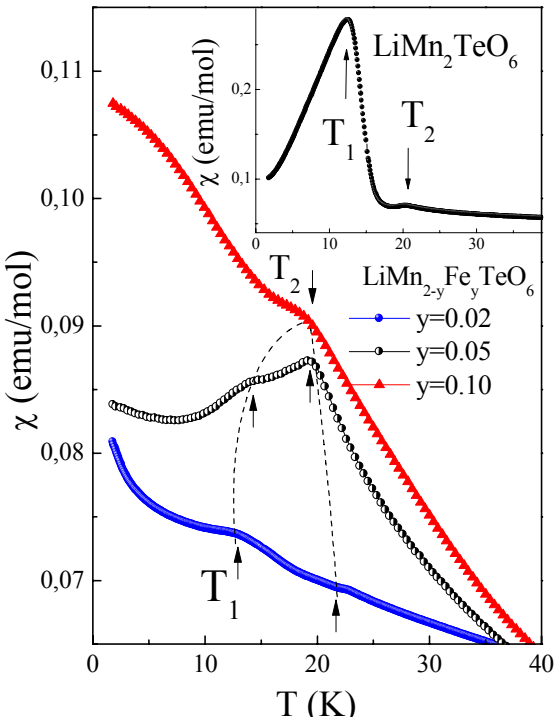

Fig.2. Temperature dependence of the magnetic susceptibility for $LiMn_{2-y}Fe_yTeO_6$ at B = 0.1 T.

revealed for $LiMn_2TeO_6$ at T_1 = 12 K and T_2 = 20 K, is also evident on χ(T). With increase of the Fe concentration the position of $T_2 = T_N$ maximum remains practically unchanged, while the low-temperature anomaly at T_1 rapidly weakens and is shifted to higher temperatures, and becomes almost undetectable at y ≥ 0.10. In the high-temperature range the behavior of χ(T) is well described by the Curie-Weiss law. The Weiss temperature remains negative, but it markedly decreases from -90 K for y = 0 to -70 K for y = 0.10 with increasing of the iron content. Field dependence of the magnetization is also qualitatively changed with the introduction of iron: for all the samples with y > 0 there is a narrow but clear hysteresis, and residual magnetization increases with increasing Fe content. This probably indicates of appearance of the additional ferromagnetic interactions, competing with the basic AFM ones, which in particular leads to reducing of the Weiss temperature with increasing of y.

In the EPR spectra of $LiMn_{2-y}Fe_yTeO_6$ there are at least two resonance modes for all samples with $y > 0$, apparently corresponding to the presence of two magnetic ions (Mn and Fe) in the system (fig.3). The width of both lines significantly increases when the sample is cooled, implying an extended range of the magnetic short-range correlations essentially higher than long-range ordering temperature. At $T > 150$ K two main resonance modes are characterized by the effective g-factors $g_1 \approx 1.5$, which varies only slightly with temperature, and $g_2 \approx 2$, which sharply increases below 150 K. At temperatures below ~ 30 K, the degradation of the absorption line indicating a set of long-range magnetic order in the system, and as a result, the opening of the gap for resonance excitations.

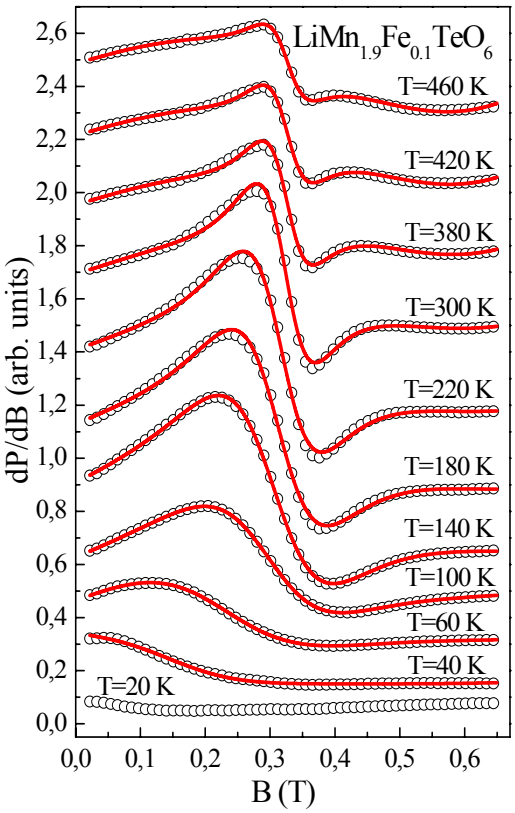

Fig.3. Evolution of the EPR spectra for $LiMn_{1.9}Fe_{0.1}TeO_6$ with temperature. The points are experimental data, solid lines - approximation by sum of two Lorenzians.

Conclusion

In conclusion, we have studied the static and dynamic magnetic properties of two new tellurate systems $Li_{1-x}Mn_{2+x}TeO_6$ and $LiMn_{2-y}Fe_yTeO_6$ with mixed-valence of transition metal (2+ - 3+). Two anomalies on $\chi(T)$ at low temperatures were revealed. The higher one at $T_2=20$ K was attributed to the transition to antiferromagnetic phase. The precise origin of the second anomaly at $T_1=12$ K, which observed also in NMR spectra is still unclear. Doping with iron leads to qualitative changes of the $\chi(T)$, M(B) dependencies and EPR spectra, that were interpreted assuming an appearance of ferromagnetic contribution to the magnetic correlations in the system, which partially suppresses the dominating antiferromagnetic interaction.

The work was supported by the Russian Foundation for Basic Research (grant 11-03-01101).

References

[1] M.S. Whittigham, *Chem. Rev.* **104**, 4271 (2004)

[2] B. Raveau, A. Maignan, C. Martin, and M. Hervieu, *Chem. Mater.* **10**, 2641(1998)

[3] A.A. Pospelov, V.B. Nalbandyan, E.I. Serikova, B.S. Medvedev, M.A. Evstigneeva, E.V. Ni, V.V. Lukov, *Sol. State Sci.* **13**, 1931 (2011)

Spin crossover in cobalt(II) tris-dioximate complexes by EPR and NMR spectroscopy

A.A. Pavlov, Y.Z. Voloshin, V.V. Novikov

Nesmeyanov Institute of Organoelement Compounds, Vavilova Str. 28, Moscow, Russia

e-mail: alex90pavlov@mail.ru

Compounds that display the spin crossover behavior, i.e. the changes in the spin state of a metal ion under external factors, are of great practical interest because of their potential use as molecular electronic and information storing devices. The investigations of these spin crossover compounds now are mainly focused on the iron(II) and iron(III) complexes [1].

In our study, however, we analyzed tris-dioximate cobalt(II) complexes (clathrochelates). In these compounds, a metal ion is fully encapsulated by three-dimensional macrobycyclic framework and is thus isolated from the influence of the environment. Clathrochelates are chemically, photochemicaly and thermally stable. Moreover, they can be obtained selectively under rather mild conditions from readily available precursors [2].

Recently, the spin crossover behavior was also observed for clathrochelates. Here we report the structural details for some of these complexes in two spin states of the metal ion by EPR and NMR spectroscopy. Those in the low spin (LS) state were studied by the EPR spectroscopy. Values of the g-tensor and the tensor of hyperfine interactions were estimated by simulating the EPR spectra of their solutions using the EasySpin toolbox (fig.1). The values obtained show a large anisotropy of the tensors.

The simulation of the EPR spectra of a single crystal was complicated by the LS-state of these complexes having a very low symmetry. In total, we analyzed 36 spectra, each one corresponding to a given orientation of the single crystal in the external magnetic field. We simulated all of them using an original script within the EasySpin functionality, allowing us to simulate all these spectra at once. As the directions of the tensors in a molecule are constant, we needed to calculate only 3 parameters (3 Euler angels) to obtain the orientation of each tensor, 6 parameters in total. Unfortunately, we were unable to measure the EPR spectra of the single crystal for which the X-ray structure was available, so we didn't know how the single crystal was oriented in the external field.

As a result, we had to calculate 3 parameters that determine the position of the single crystal in the spectrometer, giving 9 parameters in total. Such a small number of parameters and a respectively big amount of data lead to the non-degeneracy of the solution, so we successfully calculated the orientations of the magnetic tensors' axes in a molecule. The results for one of the simulations are shown in fig.2. We have also calculated the energies of the cobalt ion's orbitals within the crystal field theory. Those showed that the unpaired electron is localized on d_{xy}-orbital (fig.3), which is in line with the DFT calculations [3].

At the same time, we observed no signals in the EPR spectra that corresponded to the HS-complex, so the latter was studied by the NMR spectroscopy. In the temperature range of 200 – 360°C, the value of the magnetic moment in a solution estimated by the Evans method [4] is close to that for a pure HS state complex (μ_{eff} = 3.78 M.B.). Unfortunately, this method does not give very accurate estimates of the magnetic moment, as it is solvent-dependent; so we did not observed a clear trend in the position of the points on the graph. Fig.4, however, shows that the spin crossover occurs faster in a solution, slower in the crystal (powdered sample) and is the slowest in the case of the single crystal. So the smaller is the size of a crystal domain, the faster the spin crossover occurs. This is a very rare example of such a behavior of spin crossover compounds, as in the most cases the inverse relation is observed (the positive cooperative effect).

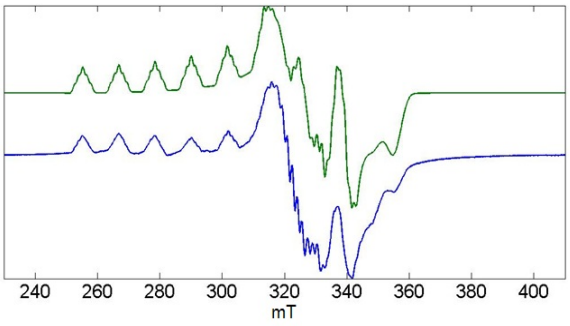

Fig.1. Simulation of the solution spectra

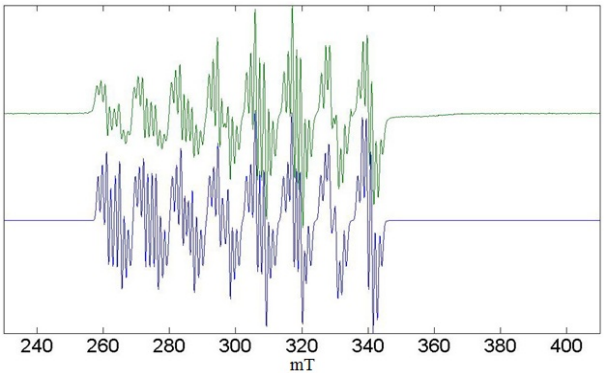

Fig.2. Simulation of the single crystal spectra

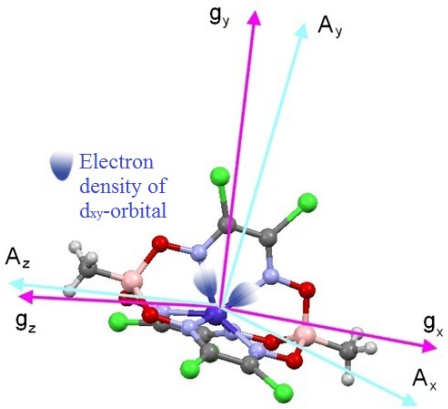

Fig.3. Orientations of the tensors' vectors

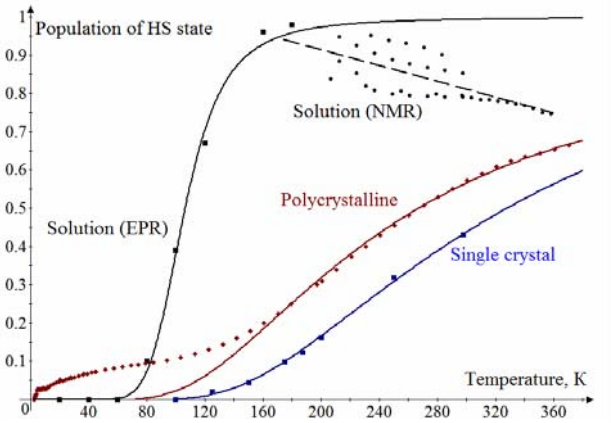

Fig.4. Fitting the data for different phase states

Usually, the spin states equilibrium (LS↔HS) is described by the equation: $\Delta G_{HL} = \Delta H^0_{HL} - T\Delta S^0_{HL} - 2\Gamma\left(\gamma_{HS} - 1/2\right) = -k_B T \ln\left(\frac{\gamma_{HS}}{1-\gamma_{HS}}\right)$, where Γ is the constant describing the interactions between the spin-changing complexes. In the case of the positive cooperative effects, Γ is positive too.

However, fitting the data for two phase states (fig.4) gave us the values of Γ that are negative for the crystal and equal to zero for the solution. Therefore, we are dealing with the complexes with a negative cooperative effect. To get deeper insight into the reasons of this effect, further studies are needed.

References

[1] Gutlich, P. Spin crossover phenomena in Fe(II) complexes// Chemical Society Reviews. 2000. T. 29. - C. 419-427.

[2] Ya.Z. Voloshin, N.A. Kostromina and R. Krämer, Clathrochelates: synthesis, structure and properties, Elsevier, Amsterdam, 2002

[3] Nguyen, M.T.D. Structural, Electronic, and Theoretical Description of a Series of Cobalt Clathrochelate Complexes in the Co(III), Co(II) and Co(I) Oxidation States// J. Phys. Chem. 2010. T. 115. № 5. - C. 911–922.

[4] Evans, D.F. The Determination of the Pararnagnetic Susceptibility of Substances in Solution by Nuclear Magnetic Resonance// Proc. Chem. Soc. 1959.

Static and dynamic magnetic properties of $Eu_{1-x}Ca_xCoO_{3-\delta}$

G.V. Rodchenkov, T.M. Vasilchikova, T.G. Kuzmova, Ya.D. Titov, E.A. Zvereva, A.N. Vasiliev

M.V. Lomonosov Moscow State University, 119991 Moscow, Russia

e-mail: g.rodchenkov@gmail.com

Introduction

Among the transition metal oxides the cobalt-based ones exhibit the richest variety of valence and spin states. The system $Eu_{1-x}Ca_xCoO_{3-\delta}$ provides a rather peculiar way to study the spin-state transition in cobalt-based complex oxides since partial substitution of Eu^{3+} ions by Ca^{2+} ions does not increase the main valence state of Co but is accompanied by appearance of oxygen vacancies in the ratio $\delta \sim x/2$. The magnetization in $Eu_{1-x}Ca_xCoO_{3-\delta}$ were studied in order to reveal the associated effects on the magnetic properties at low temperatures and to evaluate trends in the spin-state transitions upon doping at high temperatures. Electron spin resonance was used as a local probe of spin-state of cobalt ions to study the magnetic correlations on a microscopic level and to clarify the complex magnetic properties.

Experimental

The temperature dependences of the magnetization in the $Eu_{1-x}Ca_xCoO_{3-\delta}$ family of compounds were measured by means of a VSM-SQUID magnetometer (Quantum Design) in the temperature range 2 – 390 K. Electron spin resonance (ESR) studies have been carried out using X-band spectrometer (f≈9.4 GHz, B≤0.7 T, T=6-270 K).

Results and discussion

The magnetic response of the undoped material $EuCoO_3$ is in a good qualitative agreement to previous studies on single- and polycrystalline materials [1]. Below about T = 250 K, the magnetization is nearly perfectly described by the Van Vleck magnetism of the Eu^{3+} ions and a Curie-Weiss-like divergence of the magnetic susceptibility. Temperature independent diamagnetic and Co^{3+} Van Vleck contributions are very small in comparison. The Curie-Weiss-like contribution implies a negligible number of paramagnetic sites in the material, i.e. of either high-spin (HS) or (intermediate-spin) IS Co-ions or Eu^{2+} ions, cf. with tiny Schottky-type anomaly found in the specific heat of the nominally pure parent compound $EuCoO_3$. At higher temperature there is an additional contribution to the magnetization which we ascribe to the temperature-induced evolution of Co^{3+} ions in the HS or IS state.

Upon Ca-doping, several effects show up in the data in fig.1: (i) there is a strong increase of the Curie-Weiss-like low-temperature response; (ii) the pronounced shoulder at intermediate temperature which signals a dominant Eu^{3+} Van Vleck contribution to the susceptibility in this temperature range is suppressed; (iii) the susceptibility at high temperatures increases. Qualitatively, these features suggest the increase of paramagnetic sites at low-temperatures, the decreasing relevance of the Eu^{3+} Van Vleck magnetism and the decrease of the magnetic excitation gap associated with the Co^{3+} HS- or IS-state formation. In the parent compound $EuCoO_3$, the low spin (LS) – high spin (HS) transition takes place at temperatures so high that the chemical decomposition prevents its direct observation. The substitution of Eu^{3+} for Ca^{2+} in this system shifts the LS-HS transition to lower temperatures. The energy gap Δ associated with this transition in octahedrally-coordinated

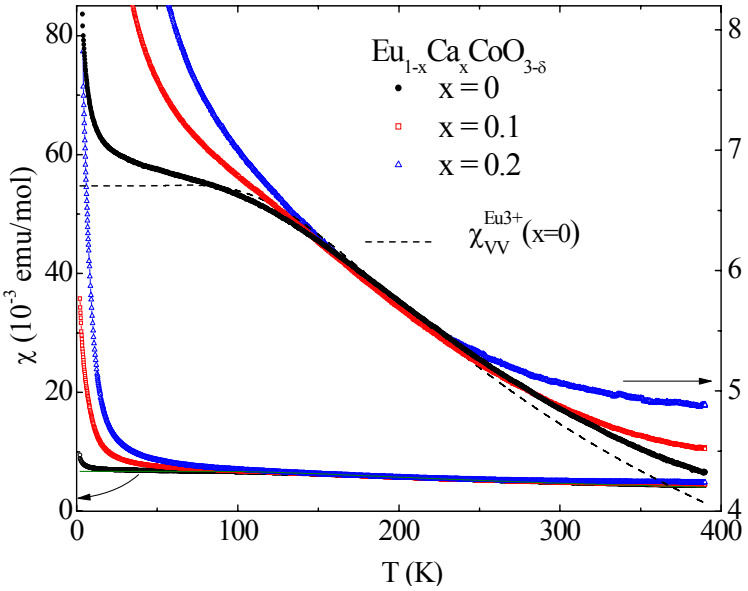

Fig.1. Temperature dependence of the magnetic susceptibility χ of $Eu_{1-x}Ca_xCoO_{3-\delta}$. The dashed line represents the Eu^{3+} Van Vleck contribution for the parent compound $EuCoO_3$.

Co^{3+} ions changes from 1940 K in $EuCoO_3$ to 1540 K in $Eu_{0.9}Ca_{0.1}CoO_{2.95}$ and 1050 K in $Eu_{0.8}Ca_{0.2}CoO_{2.9}$. Besides, each O^{2-} vacancy reduces the local coordination of two neighboring Co^{3+} ions from octahedral to pyramidal thereby locally creating magnetically active sites which couple into dimers. These dimers at low temperatures form another gapped magnetic system with very different energy scale, D ~ 3 K, on the background of intrinsically non-magnetic lattice of octahedrally-coordinated low-spin Co^{3+} ions. Our data hence show that the energy gap Δ between the low-spin and intermediate-spin state strongly decreases upon doping. This behavior agrees to what is expected for changing the chemical pressure in $EuCoO_3$ by partial substitution of Eu ions (the ionic radius of Eu^{3+} is 120 pm) for larger calcium ions (the ionic radius of Ca^{3+} is 126 pm). A similar tendency is observed when Eu is replaced by smaller La as well as in hydrostatic external pressure experiments on $LaCoO_3$ [2].

The EPR spectra were measured for six samples with different contents of calcium (x = 0.05 – 0.4) in the solid solution $Eu_{1-x}Ca_xCoO_{3-\delta}$. ESR signal was revealed only below 50 K. Representative examples are given in fig.2. The absorption line has complex anisotropic shape, its intensity increases rapidly with decreasing temperature. It was found that the character of the ESR spectrum monotonically changes with variation of alloy composition (fig.3). For the samples with calcium content x≥0.25 the line is strongly anisotropic and characterized by almost temperature-independent effective g-factor $g=1/3(g_\perp + g_\parallel) = 3.2 \pm 0.1$. Upon diluting magnetic subsystem (for x <0.25) the spectrum qualitatively changes revealing a superposition of hyperfine (hf) multiplets (fig.3).

It is assumed from static magnetization measurements, that the doping with calcium leads to the emergence of the magnetically active cobalt ions Co^{3+} (S = 1) in pyramidal environment. The concentration of these ions increases with increasing calcium content in the system $Eu_{1-x}Ca_xCoO_{3-\delta}$. Therefore, it is natural to associate the experimentally observed low-temperature EPR signal with an appearance of the magnetic ions Co^{3+} (S = 1). For the sample with minimal content of calcium (x = 0.05), which corresponds to the minimal concentration of paramagnetic centers, a multiplet structure is well-resolved. The presence of two sets of 8 equidistant lines can be identified. It is known that there is one stable isotope ^{59}Co (natural abundance 100%) with non-zero nuclear magnetic moment I = 7/2. Thus one can expect 8 lines in the EPR spectrum due to interaction between the electron magnetic moment of

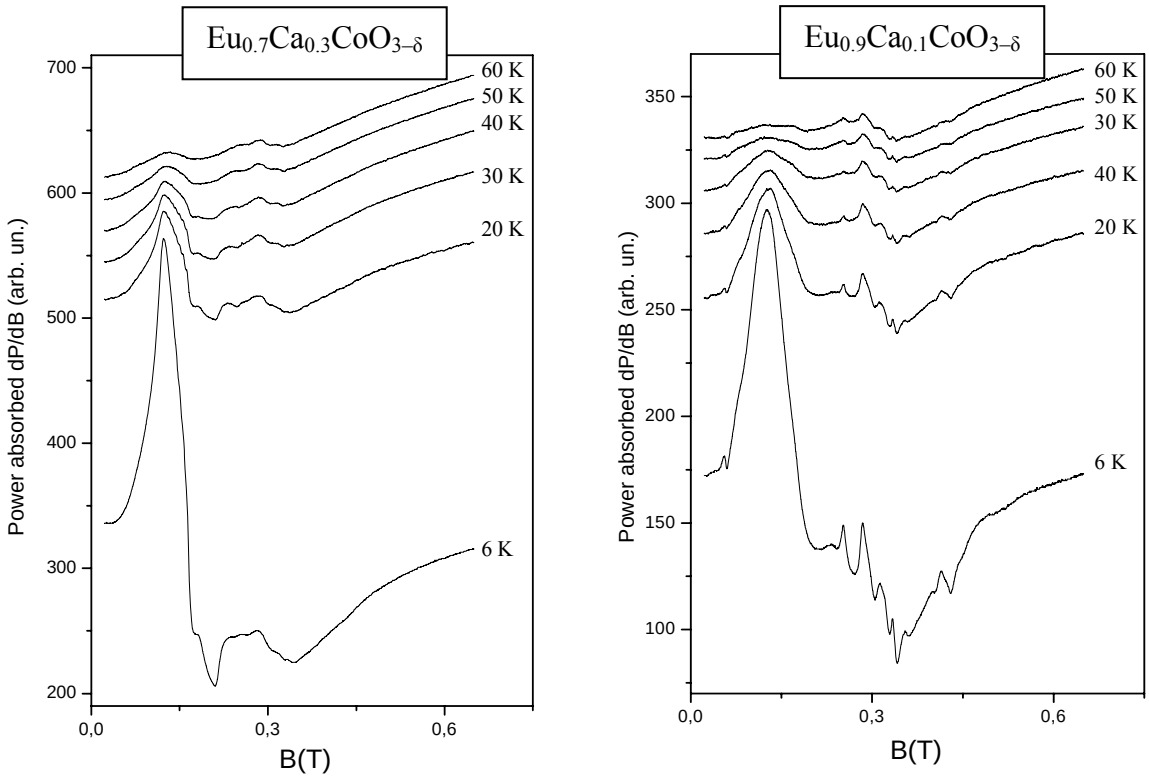

Fig.2. Typical ESR spectra in the solid solution $Eu_{1-x}Ca_xCoO_{3-\delta}$.

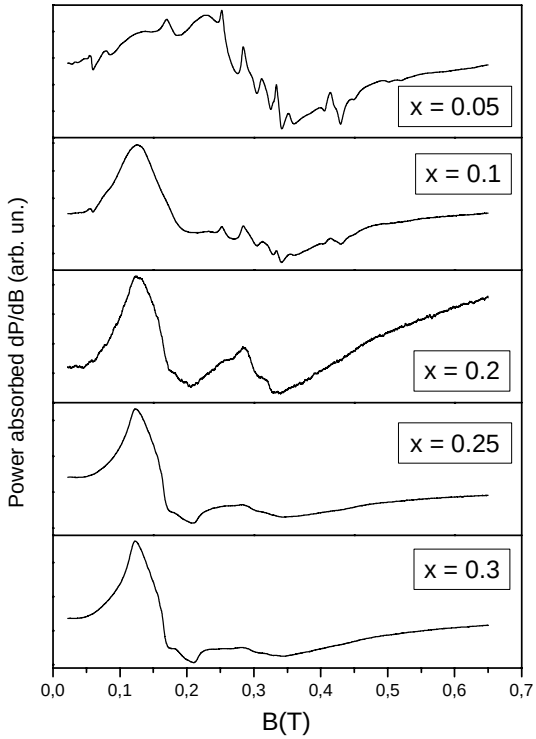

Fig.3. Evolution of the ESR spectra at 6 K under variation of calcium content in $Eu_{1-x}Ca_xCoO_{3-\delta}$

unfilled 3*d* electron shell of Co^{3+} ions and nuclear magnetic moment of ^{59}Co. The presence of two different sets of lines in the hf structure is apparently due to the strong anisotropy in the investigated system, which leads to the appearance of the longitudinal and transverse components of the tensor of the anisotropic hf interaction. The hf splitting constants for the

sample with x=0.05 were estimated as high as $a_{\perp} \approx 500$ Oe and $a_{\parallel} \approx 200$ Oe respectively, which agree with the values for other Co^{3+} compounds. The effective g-factors for the samples with various calcium content x were estimated as:

Calcium content	Effective g-factor
x = 0.05	2.6 ± 0.1 (from hf multiplets)
x = 0.20	2.9 ± 0.1
x = 0.25	3.1 ± 0.1
x = 0.30	3.2 ± 0.1

References

[1] J. Baier, S. Jodlauk, M. Kriener, A. Reichl, C. Zobel, H. Kierspel, A. Freimuth, T. Lorenz, *Phys. Rev. B* **71**, 014443 (2005).

[2] K. Asai, O. Yokokura, M. Suzuki, T. Naka, T. Matsumoto, H. Takahashi, N. Môri, K. Kohn. *J. Phys. Soc. Japan* **66**, 967 (1997).

Structure of the 4-aminononafluorobiphenyl radical anion. Study by optically detected ESR

D.A. Ovchinnikov[1], V.A. Bagryansky[1], S.V. Blinkova[1], L.N. Shchegoleva[2], I.V. Beregovaya[2], Yu.N. Molin[1]

[1]Institute of Chemical Kinetics and Combustion, 630090, Institutskaya st., Novosibirsk, Russia.

[2]N.N. Vorozhtsov Institute of Organic Chemistry, 630090, Lavrentjev Avenue, Novosibirsk, Russia.

e-mail: dima_ovchin@mail.ru

Fluorine containing aminoarenes are of practical interest. Thus, application have found either some monofluoronaphthylamines prepared by traditional methods of fluorine and amino group introduction in an aromatic nucleus and being biologically active substances, or perfluoro-β-naphthylamines and perfluoro-β-naphthylenediamines accessible via aminodefluorination of octafluoronaphthalene; the latter compounds used as building blocks for polyimides meant for manufacturing optical wave conductors. Unlike this, aminonaphthalenes with partially fluorinated skeleton were until recently almost inaccessible for extensive study and application.

At the same time, reductive defluorination of N-acetyl derivatives of the polyfluoroanilines, readily accessible by ammonolysis of base polyfluoroarenes, with use of the simplest reductive system — zinc in aqueous ammonia — was found as an unprecedentedly concise approach to previously difficultly accessible polyfluoroanilines containing 1–3 hydrogen atoms in a benzene ring, in particular in ortho-position to an amino group. Thanks to this, there has been opened for intensive elaboration the area of quinolines and their functional derivatives polyfluorinated on a benzene ring.

This methodology was applied to N-acetyl derivatives of perfluoronaphthylamines for preparing their less fluorinated analogues unsubstituted ortho to an amino group as potential building blocks for polyfluoronaphthoazaheterocycles, some of which also can be highly biologically active (for example, by analogy with mono- and difluorobenzoquinolines).

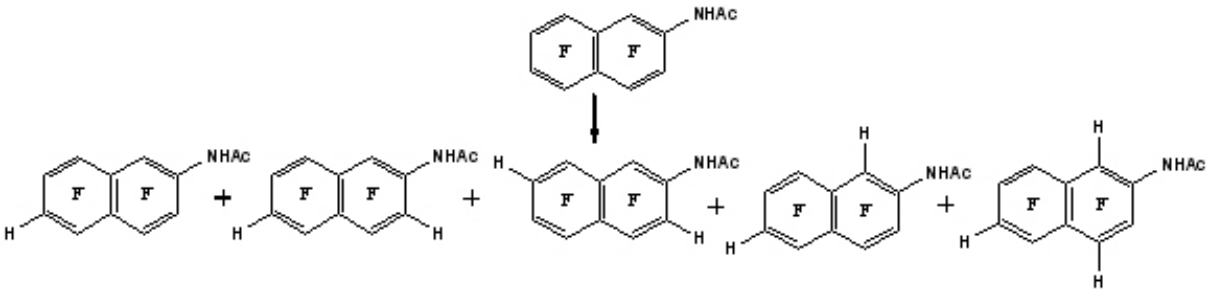

Fig.1. Hydrodefluorination of N-(heptafluoro-2-naphthyl)acetamide.

The key stages in this process are single electron reduction of a substrate and the subsequent fast fragmentation of a derived radical anion (RA) with an elimination of fluoride anion and formation of a polyfluoroaryl radical. The latter is reduced to a polyfluoroaryl anion the protonation of which completes the formation of a hydrodefluorination product [1, 2, 3].

The purpose of this paper is to confirm the formation of 4-aminononafluorobiphenyl RA in analogous reaction and to study it by optically detected ESR (OD ESR).

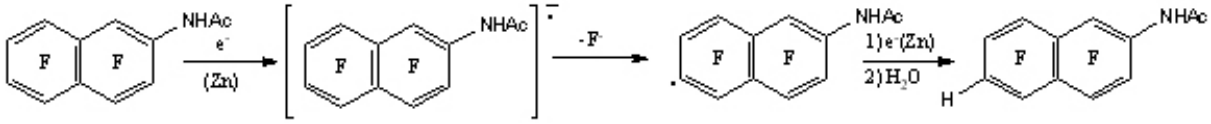

Fig.2. Mechanism of hydrodefluorination of N-(heptafluoro-2-naphthyl)acetamide.

OD ESR method allows registering radical pairs, forming in dilute non-polar solutions under ionizing radiation. Measured value is recombination fluorescence intensity from the permanent magnetic field strength.

The radical cation and the quasifree electron that arise upon ionization of a solvent molecule (S) in non-polar solutions constitute the primary singlet spin-correlated pair held together by Coulomb interaction:

$$(S^{+}\uparrow \ldots\ldots A^{-}\downarrow)$$
$$(D^{+}\uparrow \ldots\ldots e^{-}\downarrow)$$
$$(D^{+}\uparrow \ldots\ldots A^{-}\downarrow)$$

It is crucial that the event of the formation of the radical pair per se has effect neither on the Coulomb interaction nor on the spin correlation between the partners of the pair.

OD ESR method is based on the effect of resonant microwave fields on the recombination fluorescence of radical ion pairs.

Fig.3 depicts the collective spin sublevels of radical ion pair for different situations. In the zero field (a) the hyperfine coupling (hfc) may mix up the singlet pair level with three triplet levels. In high magnetic field of the OD ESR spectrometer (b), only one of triplet sublevels, T_0, is coupled with the singlet level by hfc's and by the g-value difference. Due to Zeeman splitting, T_+ and T_- sublevels remain unpopulated. Under the resonance microwave pumping (c), the ESR-transitions occur between the T_0 and T_+ T_- states of the pair. This leads to the further decrease of population of the singlet state of the pair and, as a consequence, to a drop in fluorescence intensity, thus giving rise to the OD ESR signal. As in conventional ESR spectroscopy, the OD ESR spectra are often recorded as the first derivative of the signal with respect to magnetic field [4, 5].

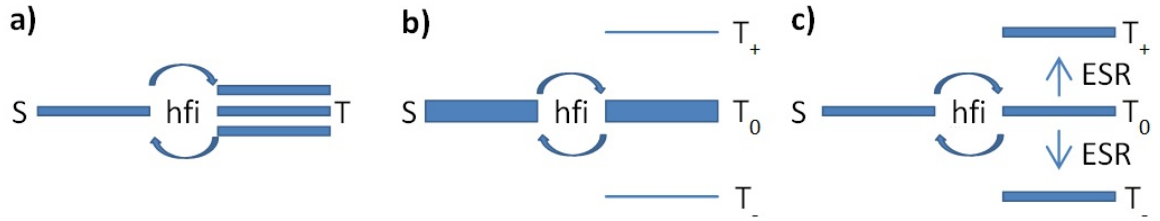

Fig.3. Singlet-triplet transitions in a radical pair due to hyperfine interactions (a) in low magnetic field, (b) in high magnetic field, (c) in high magnetic field plus resonance microwave radiation.

We have obtained the ESR spectrum of 4-aminononafluorobiphenyl RA (Fig.4). The spectrum consists of a narrow central line and a multiplet. The central intense line in the spectrum belongs to radical ions of PTF. The multiplet corresponds to the hyperfine interaction on three groups of fluorine with hfc constants a_1 (2F) = 4.2 mT, a_2 (2F) = 7.6 mT, a_3 (F) = 19.4 mT. This multiplet refers to the 4-aminononafluorobiphenyl RA. Hyperfine coupling constants with the nuclei 1H and 14N in 4-aminononafluorobiphenyl RA are small and contribute to the width of the lines.

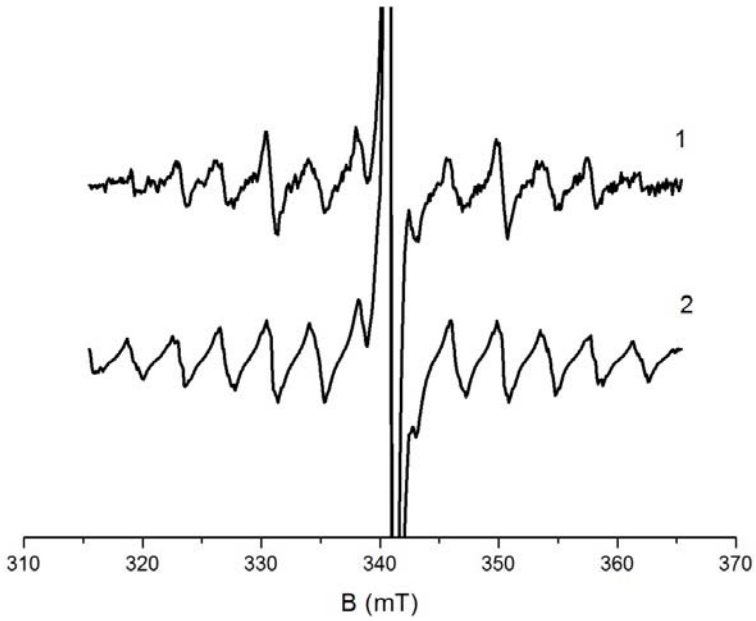

Fig.4. (1) OD ESR spectrum of a solution of 7×10^{-4} M 4-aminononafluorobiphenyl + 1×10^{-3} M PTF in dodecane at room temperature. (2) Simulation of the spectrum with hfc constants of 4-aminononafluorobiphenyl RA a_1 (2F) = 4.2 mT, a_2 (2F) = 7.6 mT, a_3 (F) = 19.4 mT.

Comparison of the hyperfine constants, which were determined by calculations of the potential energy surface (PES), performed by BHHLYP/6-31 + G * [6], with the experimental values shows that taking into account the contribution of structures corresponding to local minima of the PES, in the approximation of fast exchange between them correctly describes the spectrum of 4-aminononafluorobiphenyl RA.

We showed that the RA of 4-aminononafluorobiohenyl forms as a dimer. At a lower temperature (273 K) in the spectrum become significant additional lines. Simulation shows that there is another particle with half the hfc constants and twice the number of equal nuclei. Temperature and concentration dependence in Table 1, confirm the formation of the dimeric form of the RA of 4-aminononafluorobiphenyl, according to [7, 8].

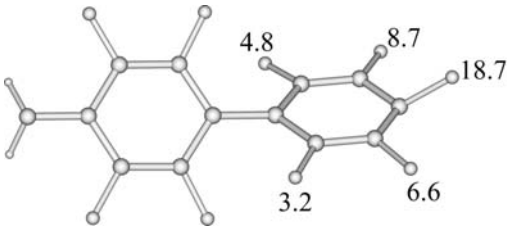

Fig.5. hfc constants of 19F (mT) for $C_{12}F_9NH_2^{\cdot -}$ according to B3LYP/6-31 + G * calculations.

Table 1. Dependence of dimeric form fraction of the concentration and temperature.

concentration of 4-aminononafluorobiphenyl, 10^3 M	temperature, K	hfc constants of monomer, mT			hfc constants of dimer, mT			dimer percentage
		a1 (2F)	a2 (2F)	a3 (1F)	a1 (4F)	a2 (4F)	a3 (2F)	
0.70	300	4.2	7.6	19.4	2.1	3.9	9.6	16
0.70	273	4.1	7.5	19.8	2.2	3.9	9.5	43
0.35	273	4.1	7.6	19.7	2.1	3.6	10.1	26

The formation of dimer of 4-aminononafluorobiphenyl RA is also confirmed by quantum-chemical calculations.

References

[1] Reshetov A.V., Selivanova G.A., Politanskaya L.V. Hydrodefluorination of N-acetylheptafluoro-2-naphthylamine by zinc in aqueous ammonia: synthetic outcomes and mechanistic considerations // Archive for Organic Chemistry. – 2011. Part VIII. P. 242-262.

[2] Selivanova G.A., Reshetov A.V., Beregovaya I.V. Hydrodefluorenation of Polyfluoro-2-naphtylamines by Zn in aqueous NH3: a Correlation of the product Distrybition and the Computationally Predicted Regioselectivity of the Substrate Radical Anion Fragmentation

[3] Laev S.S., Gurskaya L. Yu., Selivanova G.A. N-Acetylation as a Means to Activate Polyfluoroarylamines for Selectiveortho-Hydrodefluorination by Zinc in Aqueous Ammonia: A Concise Route to Polyfluorobenzo Azaheterocycles // European Journal of Organic Chemistry. – 2007. V. 2007, Issue 2, P. 306–316.

[4] Optically Detected Electron Spin Resonance Studies of Electrons and Holes Involved into Geminate Recombination in Non-Polar Solutions / Yu. N. Molin, O. A. Anisimov, V. I. Melekhov, S. N. Smirnov // Faraday Discuss. Chem. Soc. 1984. V. 78. P. 289-301.

[5] Molin Yu.N., Anisimov, O.A., Melekhov V.I., Smirnov S.N.Optically Detected Electron Spin Resonance Studies of Electrons and Holes Involved into Geminate Recombination in Non-Polar Solutions // Faraday Discuss. Chem. Soc. - 1984. - V. 78. - P. 289-301.

[6] L. N. Shchegoleva, I. V. Beregovaya, to be published.

[7] Werst D.W. Solvent effects in nonpolar solvents: radical anion reactions // Chemical physics letters. – 1993. – V.202. – N.1,2. – P. 101-107.

[8] Saik V.O., Anisimov O.A. Fast reactions involving radical-cations during their geminate recombination as studied by the OD ESR method // Z. Naturforsch. – 1985. P. 239-245.

An examination of complexing between copper chloride (II) and 5-aminouracil in aqueous solutions using UV-visible spectrometry and NMR ^{13}C spectroscopy methods

O.V. Zakiryanova, V.Yu. Mishinkin

Institute of Organic Chemistry, 450054, Prospekt oktyabrya, 71, Ufa, Russia

e-mail: murinov@anrb.ru

Uracil and its derivatives, constituents of the genetic materials, play a fundamental role in basic biological processes. 5-Substituted uracils exhibit significant pharmacological activity and they are used as antitumour, antibacterial and antiviral drugs, being therefore the most interesting and studied uracils [[1]-[2]].

Complexes of uracil derivatives with salt of transition metals play an important role in vital activity processes of an organism. However, literature data about interaction between aminouracils with biogenic metals are not numerous [[3],[4]]. The focus of the present paper is complexing between 5-aminouracil (**1**) with the copper (II) ion using spectrophotometric methods and NMR ^{13}C spectroscopy.

The composition of the complex has been identified by molar ratios method under constant concentration of the copper (II) ion. The dependency of the optical density of solutions at the maximum of the copper chloride (II) ion aquacomplex's absorption band (800 nm) on the ratio between concentrations of the copper (II) ion and 5-aminouracil (fig.1) demonstrates that complex between the copper (II) ion and **1** has the composition equals to 1:4.

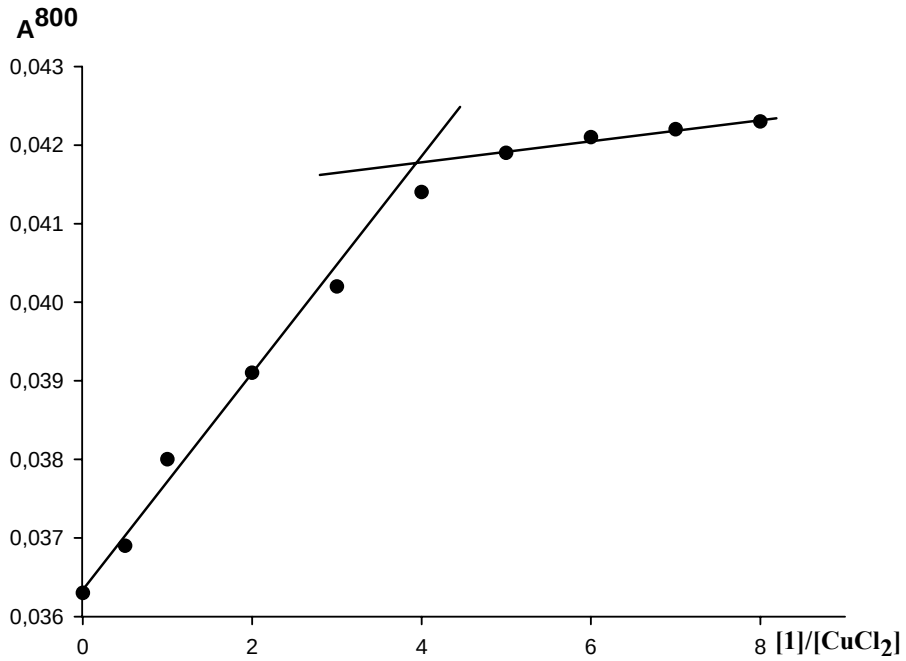

Fig.1. The dependency of solutions' optical density at 800 nm on the ratio between concentrations of the copper (II) ion and 5-aminouracil

However, we should note that in the visible spectral region the second absorption band of low intensity at 430 nm is observed, which is typical for a four-coordination copper (II) ion flat complex. Fig.2 shows the dependency of solutions' optical density at wavelength of

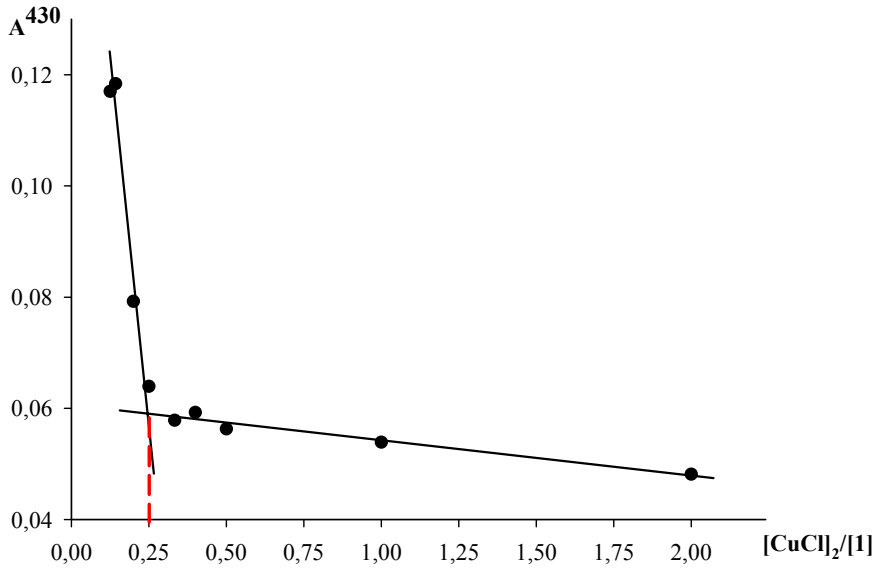

Fig.2. The dependency of solutions' optical density at 430 nm on the ratio between concentrations of the copper (II) ion and 5-aminouracil

430 nm on the ratio between concentrations of the copper (II) ion and 5-aminouracil. As you can see, the composition of the complex between copper (II) ion and **1** at this wavelength is 1:4.

The presence of two absorption bands in the visible spectral region with maximums at 800 and 430 nm indicates the formation of two copper (II) ion complexes – a six-coordination octahedron and a four-coordination flat ones, which are equilibrious:

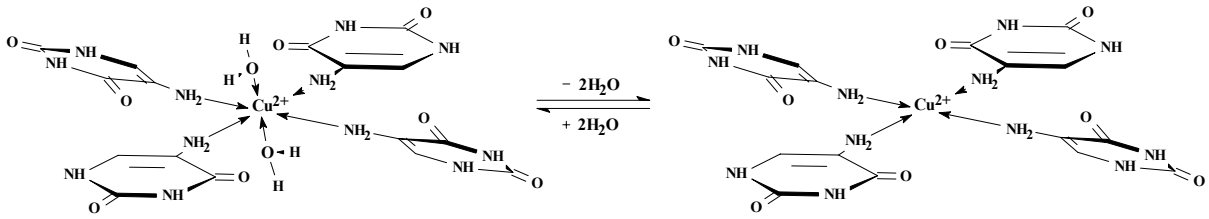

To establish ligand donor centers which participate in formation of donor-acceptor bonds with the copper (II) ion, we have recorded ^{13}C NMR spectra of **1** in presence of $CuCl_2$ with a molar ratio of 4:1 in DMSO-d_6 (table 1). DMSO has been chosen due to the highest solubility of 5-aminouracil.

Table 1. Chemical shift values of carbon atoms (parts by weight) in ^{13}C NMR spectra of 5-aminouracil and its complex with $CuCl_2$ (the solvent is DMSO-d_6)

Compound	δ C(2)	δ C(4)	δ C(5)	δ C(6)
1	149.94	161.81	122.00	116.81
4(**1**)·$CuCl_2$	150.17	161.68	118.87	121.06
Δδ	+0.23	-0.13	**-3.13**	**+4.25**

As table 1 demonstrates, the most significant chemical shifts are observed for signals from carbon C(5) and C(6) atoms, which is conditional on participation of the nitrogen atom of the primary amino group in the formation of the donor-acceptor bond with the copper (II) ion.

As opposed to an aqueous solution, when examining complexing between 5-aminouracil with the copper (II) ion in a nonaqueous aprotic solvent (drained DMSO), in the visible spectral region one absorption band with the maximum of 430 nm is observed, which indicates the flat-square environment of the copper (II) ion. However, when adding even small amounts of water the absorption band at 790 nm is observed, which indicates the formation of a six-coordination octahedron copper (II) ion complex and the decrease in intensity of the absorption band at 430 nm.

Based on experimental data we conclude that complexing between 5-aminouracil and the copper (II) ion in aqueous solutions occurs according to the following equation:

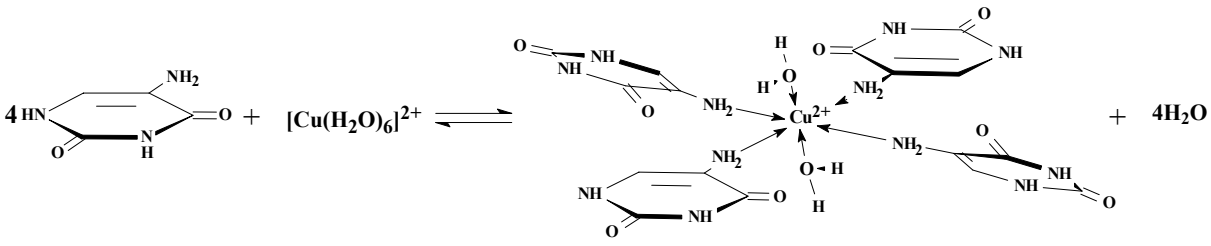

The value of the complexing constant K between copper (II) ions and 5-aminouracil calculated using a spectrophotometric method is equal to $(1.8 \pm 0.6)\cdot 10^{10}$ (mole/l)$^{-4}$.

$$K = \frac{\left[Cu(1)_4\right]}{[1]^4\left[Cu^{2+}\right]}$$

Therefore, the coordination of 5-aminouracil with the copper (II) ion occurs via the primary amino group at the C(5) carbon atom. The complex composition identified using the molar ratios method corresponds to $[Cu^{2+}]$: 5-aminouracil = 1 : 4.

This work was supported by RFBR, research project №12-03-31712.

References

[1] Topal M.D., Fresco J.R. Complementary base pairing and the origin of substitution mutations // Nature. − 1976.− V. 263, №5575. − P. 285-289.

[2] Watson J.D., Crick F.H.C. Genetical implication of the structure of deoxyribonucleic acid // Nature. − 1953.− V. 171, №4361. − P. 964-966.

[3] Palafox M.A., Nielsen O.F., Lang K., Garg P., Rastogi V.K. Geometry and vibrational spectra of 5-substituted uracils // Asian Chemistry Letters. – 2004. – V.8, №1. – P.81-93.

[4] Masoud M.S., Khalil E.A., Hindawy A.M., Ramadan A.M. Structural chemistry of some pyrimidine – transition metal complexes // CJASS. – 2005. – V. 50, №6. – P. 297-310.

[5] Rastogi V.K., Palafox M.A., Kumar V., Mital H.P., Sharma R. Laser raman and IR spectra of complexes of lanthanide (III) with 5-aminouracil // Proceedings of the XIX International Conference on Raman Spectroscopy. – 2004. – P. 150-151.

ESR study of photoorientation in azobenzene-containing liquid-crystalline polymer

A.V. Bogdanov, A.Kh. Vorobiev

Lomonosov Moscow State University, Chemistry Department, 119991, Moscow, Russia

e-mail: bogdanov@kinet.chem.msu.ru

In the present work spin probe technique is used to study photo-induced alignment (process of photo-orientation) of liquid-crystalline polymer material containing azobenzene fragments covalently linked to the polymer chain. The phenomenon of photo-orientation is promising for the development of "smart" light-controlled materials and optical storage devices [1]. Nevertheless, at present time, the understanding of microscopic mechanism of the alignment process is lacking. For the elaboration of such mechanism the knowledge of detailed structural and dynamic characteristics of the material is necessary. These characteristics can be obtained using electron spin resonance technique.

In the present work, photosensitive liquid-crystalline copolymer PAAzo6 [2] is studied. This polymer exhibits high efficiency of photo-orientation, low tendency towards chromophore aggregation and wide temperature range of nematic phase. Stable nitroxyl containing phenyl benzoate moiety [3] was used as a spin probe. The anisometric shape of the probe molecule allows it to embed into the liquid crystalline medium and to efficiently reflect its molecular ordering.

The alignment of the sample is characterized by the orientation distribution function (ODF), defined as the density of number of probe molecules with the given orientation:

$$\rho(\Omega) = \frac{dN(\Omega)}{d\Omega},$$

where Ω is the set of Euler angles, relating reference frames of the probe molecule and the sample. The ODF is determined via joint numerical simulation of a set of ESR spectra recorded at different orientations of the sample in the magnetic field of spectrometer [4]. In fig.1a an example of experimental and theoretical spectra of the angular dependence of ESR spectrum is presented. The axis in the probe molecule, which possesses the highest degree of ordering ("the orientation axis"), is determined in course of simulation. The direction of the orientation axis in g-tensor reference frame is depicted in fig.1b. It is seen that the orientation axis is close to the long inertia axis of the probe molecule. The orientation distribution function of this molecular axis is presented in fig.1c. The polymer in the course of photo-orientation was also characterized with polarized optical spectroscopy and microscopy.

At temperatures above 350K, the studied polymer can be aligned with magnetic field (3300 G). The characteristic time of the alignment process is ca. 35 minutes. The model [5] can be used to relate the characteristic alignment time with the rotation correlation time of mesogenic fragments of the polymer:

$$\tau_{R,\perp} = \frac{\Delta\chi H^2}{k_B T \sqrt{T_c \langle P_2 \rangle / T}\, e^{T_c \langle P_2 \rangle / T}} \tau_H ,$$

Where τ_H is the characteristic time of the sample alignment in the magnetic field with flux density H, $\tau_{R,\perp}$ is the correlation time of rotation of long axes of mesogenic fragments, $\Delta\chi$ is the anisotropy of diamagnetic susceptibility of mesogenic fragments, T_c is the temperature of nematic-to-isotropic transition (for the studied polymer $T_c = 393$ K), $\langle P_2 \rangle$ is the order

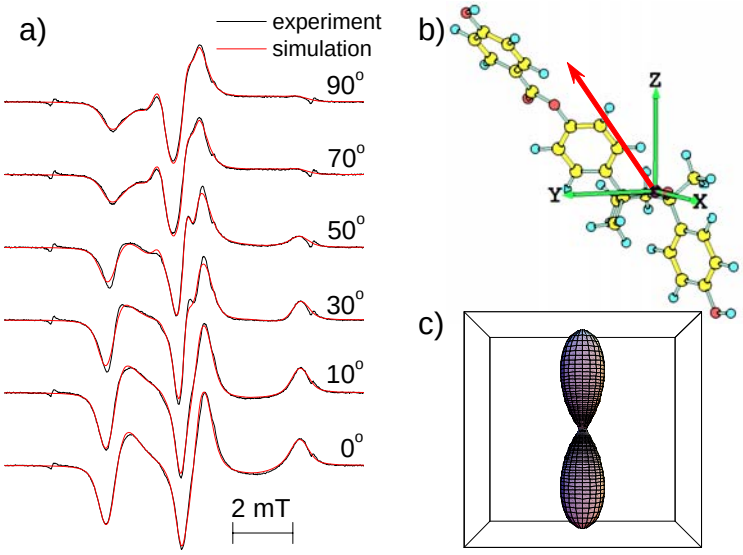

Fig.1. a) Experimental ESR spectra of the spin probe, recorded at different angles between the sample anisotropy axis and the direction of the spectrometer magnetic field (black lines) and the results of numerical simulation of these spectra (red lines); b) the molecular model of the spin probe in g-tensor reference frame and the direction of the orientation axis, determined in the course of the simulation; c) the orientation distribution function of the orientation axes of the probe molecules in the sample, determined in the course of the simulation.

parameter of the material (see below). Using the presented equation one can estimate $\tau_{R,\perp}$ as 10^{-5} s at 350 K.

The irradiation with non-polarized light ($\lambda = 546$ nm, 16 mW·cm^{-2}) at 293 K leads to uniaxial alignment of the polymer with the preferred orientation of LC director along the light propagation direction. The alignment process takes ca. 60 min. In fig.2a the evolution of ODF of the spin probe in the course of photo-orientation is presented. It can be seen that upon irradiation the anisotropy of the orientation distribution increases.

Uniaxial alignment can be quantitatively characterized by order parameters, defined as follows:

$$\left\langle P_j \right\rangle = \int P_j(\cos\theta)\rho(\theta)\sin\theta d\theta, j = 0,2,4,...$$

where θ is the angle between molecule orientation axis and the anisotropy axis of the sample, $P_j(\cos\theta)$ are Legendre polynomials. The kinetics of order parameters growth in the course of orientation is presented in fig.2a. In table 1 the values of order parameters of the polymer PAAzo6, aligned with magnetic field at 360 K, and with the use of photo-orientation are presented. It is seen that order parameters are higher in the latter case. High anisotropy of orientation distribution in the case of photo-orientation enables determination of order parameter values up to 8th rank, and thus detailed information about orientation alignment can be obtained.

The irradiation of sample of PAAzo6, pre-oriented in the direction perpendicular to light propagation direction, leads to photo-reorientation (fig.2b). In the course of this process, the anisotropy of the orientation distribution at first diminishes, up to isotropization, then increases in the new direction.

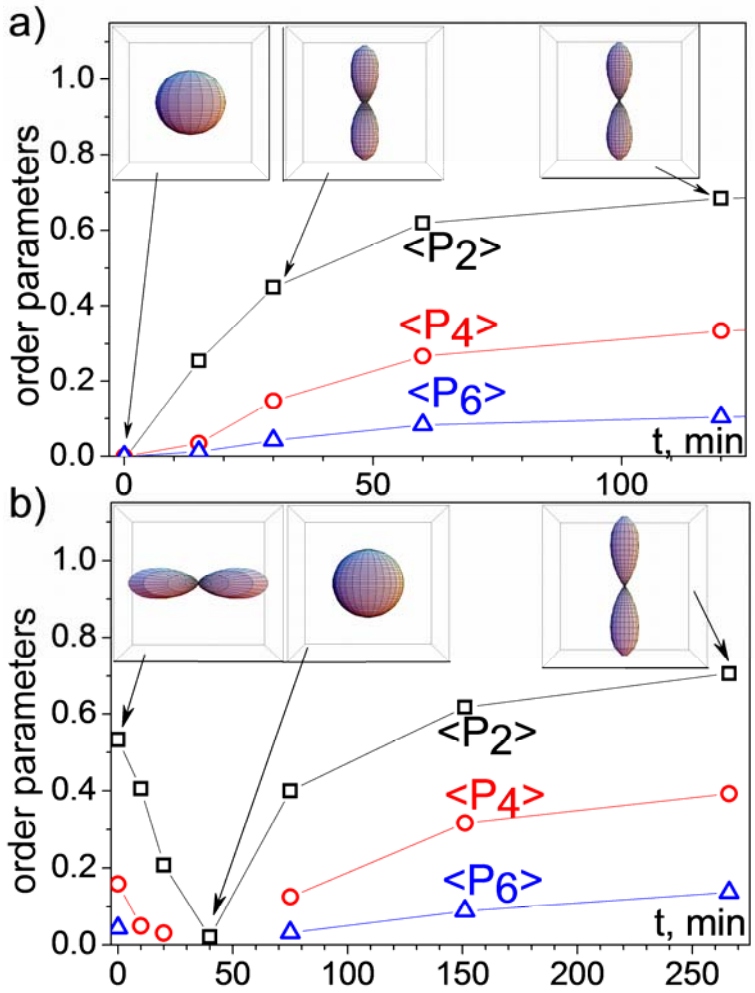

Fig.2. The change of ODF shape and order parameters $<P_2>$, $<P_4>$ and $<P_6>$ in the course of photo-orientation (a) and photo-reorientation (b) in PAAzo6 upon irradiation with non-polarized light (λ=546 nm).

Table 1. Order parameters of the spin probe in the polymer PAAzo6 aligned with different orientation techniques.

	alignment technique	
	magnetic field	photo-orientation
$<P_2>$	0.602±0.004	0.750±0.004
$<P_4>$	0.248±0.005	0.444±0.006
$<P_6>$	0.076±0.003	0.164±0.003
$<P_8>$	–	0.044±0.005

Polarization microscopy indicates that during photo-orientation the change of domain structure of liquid-crystalline material takes place (fig.3). The darkening of the texture originates from the preferential alignment of LC director perpendicular to the sample plane (i. e. along the irradiating light propagation direction). A possible cause of domain rearrangement is that due to anisotropy of light absorption, photostationary concentrations of cis and trans isomers of azobenzene fragments are different in domains with different orientations. The non-mesogenic cis-isomer disrupts the structure of liquid crystalline medium, therefore increasing the free energy of the liquid crystalline phase. The difference in photostationary cis concentrations leads to the difference in free energies of domains with different orientations, which provides the driving force for domain rearrangement.

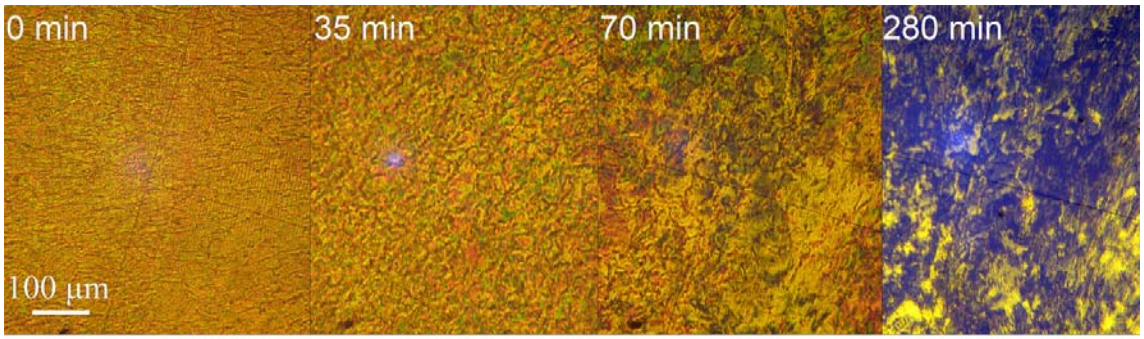

Fig.3. Microphotographs of PAAzo6 sample between crossed polarizers, taken at different irradiation times.

Experimental results obtained in the present work are discussed in the context of this and other existing theoretical models of photo-orientation of azobenzene-containing materials.

The authors are grateful to prof. A. Yu. Bobrovsky for provision of the polymer PAAzo6, and to prof. R. Tamura for provision of the spin probe. The financial support of RFBR (grant. no. mol-a-12-03-31114) is gratefully acknowledged.

References:

[1] K. G. Yager and C. J. Barrett, J. Photochem. Photobiol. A **182**, 250 (2006).

[2] A. Bobrovsky, A. Ryabchun, A. Medvedev, and V. Shibaev, J. Photochem. Photobiol. A **206**, 46 (2009.)

[3] N. Ikuma, R. Tamura et al, Angew. Chem. Intl. Ed. **43**, 3677 (2004).

[4] A. Kh. Vorobiev, N. A. Chumakova, in Nitroxides – Theory, Experiment and Applications, Ed. A. I. Kokorin, InTech, 2012, DOI: 10.5772/2887.

[5] M. A. Osipov, E. M. Terentjev, Phys. Lett. A, **134**, 301 (1989).

Palladium influence on magnetic anisotropy of Ni-Pd nanowire arrays chemically electrodeposited in porous anodized alumina

V.G. Bayev[1], J.A. Fedotova[1], E.A. Streltsov[2], M. Milosavljević[3], I.I. Azarko[2], M.V. Malashchonak[2], A.A. Maximenko[1]

[1]National Scientific and Educational Centre of Particle and High Energy Physics of the Belarusian State University, 220040, 153 M. Bogdanovich Str., Minsk, Republic of Belarus.

[2]Belarusian State University, 220030, Nezavisimosti Av. 4, Minsk, Republic of Belarus.

[3]Vinča Institute of Nuclear Sciences, 11001, Mike Petrovića Alasa 12-14, Belgrade, Serbia.

e-mail: Bayev@hep.by

New technological approaches to fabrication of template-based ordered nanoarrays (nanorods or nanowires) is of great importance not only because of the fundamental new physics involved in such highly correlated system, but also because of a diversity of applications, such as high density storage media, functional nanomaterials exhibiting quantum size effect, highly sensitive chemical sensors, nanoelectronic devices and functional bio-chemical membranes [1, 2].

Nanoarray based structures for creation of nanoelectronic devices are the object of particular interest because modern electronic components are approaching the size limit of standard photolithography techniques. While self-assembled template-assisted nanostructures have the potential to circumvent such limitations and thus could be used as alternative future electronic components. This paper is related to recent achievements in template-assisted electrochemical deposition of nickel-palladium composition nanowires inside porous anodized alumina templates. Structure, electric and magnetic properties investigations of such systems favor the development of manufacturing technique of nano-sized semiconductor-metal junctions on substrates (Si, GaAs, etc.) with perpendicular magnetic anisotropy relatively to substrate that provides an opportunity to create perspective magnetically sensitive MOS structures for magnetoelectric devices of a new type. The important advantages of the proposed heterostructures are their compatibility with silicon planar technology, low production costs as well as reliable reproducible technology processing.

Matrixes of anodized aluminum oxide (AAO) were prepared by the double-anodization method [3]. In order to form alumina layer high purity Al plates (99.99 %) were annealed at temperature 550°C in the air during 5 h and chemically polished in mixture of mineral (H3PO4, HNO3) and acetic (CH3COOH) acids. First anodization was carried out in 0.3 M oxalic acid at 10°C and 40 V during 20 h with following immersing in phosphoric (H_3PO_4, 6 %) and chromic (CrO_3, 1.8 %) acid mixture at 80°C for 30 min. Second anodization was performed for 1 h at temperature 10 °C and 40 V. Formed pores were widened in 0.3 M oxalic acid solution at 35°C during 2.5 h. Nanowire arrays of Ni(1-x)Pd(x) metal composition were synthesized via ac electrochemical deposition of Ni and Pd from nickel chloride ($NiCl_2$) and potassium tetrachloropallidate (K_2PdCl_4) in dimethyl sulfoxide (DMSO) solution into Al/AAO templates with frequency of electric current of 50 Hz and voltage of 12 ± 1 V for 20 min.

Microstructural characterization was performed using a field-emission scanning electron microscope (SEM) LEO1455VP **(**Carl Zeiss) with four-compartment reflected electron detector. More detailed structure investigation was performed by transmission electron microscope (TEM) Philips CM200 with accelerating potential 200 keV. Elemental

composition of Ni(1-*x*)Pd(*x*) nanowires was analyzed by energy-dispersive X-ray spectroscopy (EDX) with Ronteg analyzer. Typical surface and cross section SEM and TEM micrographs of Al/AAO template with Ni(1-*x*)Pd(*x*) nanowire arrays are shown in fig.1. Cross sectional analyses of filled templates reveals a dispersion of wire length value from 1 to 5 μm. According to TEM (fig.1c) nanowires consists of metal nanoparticles of 5 nm in diameter. It should be noted that the minimal wire length was observed for sample Al/AAO/Ni(78)Pd(22). The pore diameter was determined to be $d = 70$ nm and pore center-to-center distance — $r = 120$ nm. Thus assuming the fact that wires conform to pore shape and are relatively uniform along their length the packing factor P for nanowire arrays was defined as $P = (\pi / 2\sqrt{3})(d / r)^2 = 0.3$.

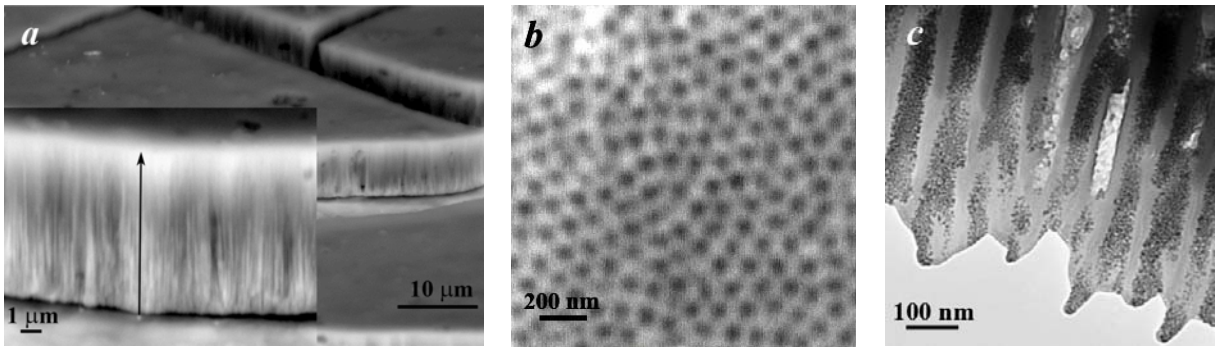

Fig.1. Cross section SEM (*a*) and TEM (*c*) images, surface SEM image (*b*) of Al/AAO template filled with Ni(50)Pd(50) metal composition. The growth direction of nanowires is shown by an arrow on (*a*).

Magnetic properties were investigated by vibrating sample magnetometry (VSM) and magnetic resonance spectrometry at room temperature using a cryogenic high field universal measuring system (Liquid Helium Free High Field Measurement System, Cryogenic Ltd) and continuous wave X-band EPR spectrometer Varian E112, respectively. In order to reveal palladium influence on magnetic anisotropy of Ni(1-*x*)Pd(*x*) nanowires magnetization data *M*(*H*) (fig.2) and magnetic resonance spectra (fig.3) were obtained in perpendicular and parallel orientations of Al/AAO templates towards the induction vector of applied magnetic field. Determined magnetic parameters are presented in table 1. The values of saturation magnetization M_S are normalized on the mass of whole template by the reason of difficult metal content determination in samples.

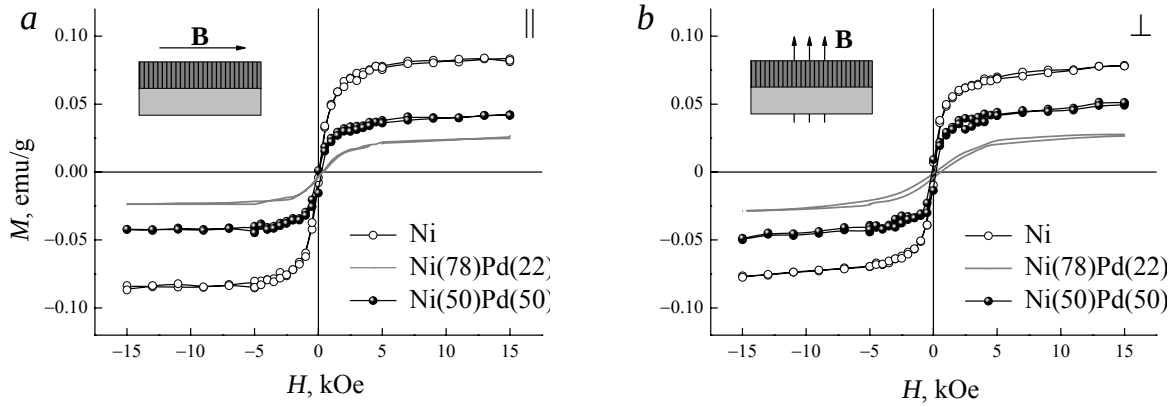

Fig.2. Magnetization loops of anodized alumina templates filled with Ni(1-*x*)Pd(*x*) metal composition in perpendicular (*a*) and parallel (*b*) orientations of template towards the induction vector of applied magnetic field.

Table 1. Magnetic parameters of Al/AAO templates filled with Ni(1-*x*)Pd(*x*) metal compositions.

Sample	H_C, Oe		M_S, emu/g		*g*-factor	B_a, mT	$N_\square$	$N_\parallel$
	∥	⊥	∥	⊥				
Al/AOA/ Ni	20	90	0.084	0.078	2.21	– 28.4	0	0.5
Al/AOA/ Ni(78)Pd(22)	30	240	0.026	0.027	2.21	– 7.3	0.12	0.44
Al/AOA/ Ni(50)Pd(50)	160	180	0.047	0.051	2.10	+ 24.8	0.30	0.35

The shape of hysteresis loops shown on fig.2 and values of coercitivity (table 1) indicate a magnetic anisotropy of "easy axis" type along growth direction of metal nanowires for samples Al/AOA/Ni and Al/AOA/Ni(78)Pd(22). Ratio $H_{C\perp}$ (the applied magnetic field is out of template plane) to $H_{C\parallel}$ (the applied magnetic field is in template plane) for nickel nanowires was determined as 4.5. For Ni(78)Pd(22) the ratio $H_{C\perp}/H_{C\parallel}$ upraises to 8 times while further increase of palladium content reduces this amount to 1.1. Observed perpendicular magnetic anisotropy is caused by stretched form anisotropy of nanowires. The increase of coercitivity can be explained by a formation of multi quasi-layered structure Ni/Pd during the ac electrochemical deposition that reduces cluster size of nickel and as a consequence enlarges coercitivity [4, 5]. Further increment of palladium content in Ni(1-*x*)Pd(*x*) nanowires reduces the magnetic exchange interaction between nickel clusters and suppresses magnetic anisotropy as a result of form anisotropy. This explanation also clarify the rise of $H_{C\parallel}$ with the increment of palladium content in Ni(1-*x*)Pd(*x*) nanowires.

Obtained magnetic resonance spectra of samples (fig.3) denote a ferromagnetic character of resonance microwave absorption and distinctly reveals magnetic anisotropy of "easy axis" type along growth direction of metal nanowires for samples Al/AOA/Ni and Al/AOA/Ni(78)Pd(22) and of "easy plane" for Al/AOA/ Ni(50)Pd(50).

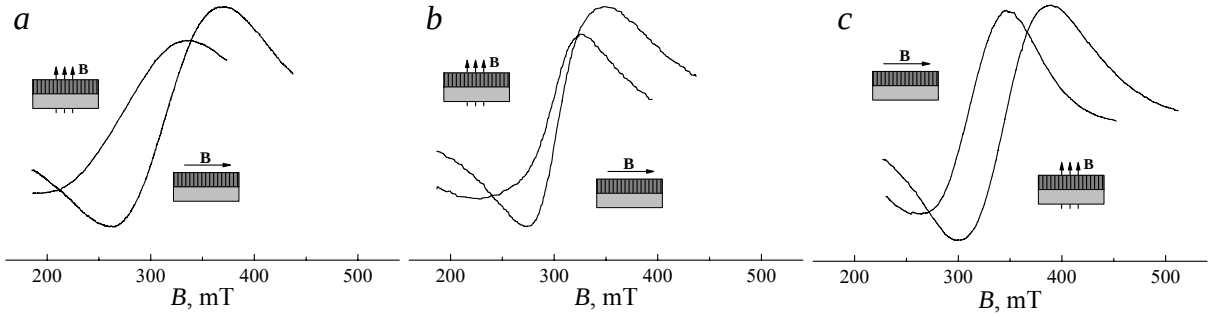

Fig.3. First derivative of magnetic resonance absorption of anodized alumina templates filled with Ni (*a*), Ni(78)Pd(22) (*b*) and Ni(50)Pd(50) (*c*) metal compositions in perpendicular and parallel orientations of nanowires towards the induction vector of applied magnetic field.

The values of g-factor and induction of effective anisotropy magnetic field B_a were determined from following system of equations for magnetic resonance conditions given by the Landau – Lifshitz dynamical equation of motion for magnetization:

$$\begin{aligned} h\nu &= g\mu_B(B_\parallel - B_{an}), \\ (h\nu)^2 &= g\mu_B B_\perp (B_\perp + B_{an}), \end{aligned} \qquad (1)$$

where h — Plank constant, ν — microwave frequency, μ_B — Bohr magneton, $B_{\|}$ and $B_{\perp}$ — induction values of resonance field in case of parallel and perpendicular sample orientation. Positive value of B_a corresponds to "easy plane" magnetic anisotropy type of the whole template filled with metal composition while negative value of B_a — to "easy axis" magnetic anisotropy type. The change of anisotropy type explains the behavior of coercitivity in parallel and perpendicular directions of applied magnetic field observed by VSM.

Calculated values of g-factor are in perfect agreement with those of nickel for samples Al/AOA/Ni and Al/AOA/Ni(78)Pd(22) [6]. On the other hand for Ni(50)Pd(50) nanowires g-factor appears to be lower (g = 2.10) that may be caused by small (less than 10 nm) thickness of nickel quasi-layers in Ni/Pd multi quasi-layered nanostructure [7].

The induction of effective magnetic anisotropy field B_a in assumption of homogeneously nanowire magnetization and the uniform length of nanowires can be represented as:

$$B_{an} = (1-x)\mu_0 M[(1-(1-x)P)(N_{\|} - N_{\perp}) - (1-x)P], \quad (2)$$

where $(1-x)$ — nickel content, μ_0 — vacuum permeability, M — magnetization of $\mathrm{Ni}(1-x)\mathrm{Pd}(x)$ nanowires, P — packing factor, $N_{\|}$ and $N_{\perp}$ — demagnetizing factor of single nanowire in parallel and perpendicular direction towards template plane.

The values of demagnetizing factors were obtained using eq. (2). As one can see from tabl. 1 the increase of palladium content in samples reduces the perpendicular magnetic anisotropy provided by the form anisotropy of Ni(1-x)Pd(x) nanowires in Al/AAO templates. It confirms assumption made previously of multi quasi-layered structure Ni/Pd formation during the ac electrochemical deposition that causes a cluster size decrease of nickel and reduction of form factor role in anisotropy origin.

Thus presented results indicate a possibility of forming magnetic ordered nanostructured arrays with perpendicular magnetic anisotropy relatively to substrate in AAO templates using ac electrochemical deposition of magnetic (Ni) / non-magnetic (Pd) metal composition. Proposed technique can be successfully used in creation of magnetically sensitive metal/oxide/semiconductor (MOS) nanostructures for magnetoelectric devices of a new type.

Acknowledgments

The work was supported by the State Program of Scientific Researches «Functional and engineering materials, nanomaterials» and the State Committee for Science and Technology of the Republic of Belarus (BRFFR project F11SRB-006).

References

[1] N. Lupu. Electrodeposited Nanowires and their Applications (2010). 228 p.

[2] U. Yogeswaran, S.-M. Chen. Sensors (2008) **8**, 290.

[3] H. Masuda, K. Fukuda. Science (1995) **268**, 1466.

[4] S. P. Gubin. Magnetic Nanoparticles (2009). 466 p.

[5] V. M. Fedosyuk. Journal of Advanced Materials (2005) **9**, 416.

[6] B.D. Cullity, C.D. Graham. Introduction to Magnetic Materials (2009). 544 p.

[7] J. P. Nibarger, R. Lopusnik, Z. Celinski, T. J. Silva. Appl. Phys. Lett. (2003) **83**, 93.

Spin dynamics in new layered antimonate Na_4FeSbO_6

T.V. Frantsuzenko[1], E.A. Zvereva[1], O.A. Savelieva[1], V.B. Nalbandyan[2], A.N. Vasiliev[1]

[1]Faculty of Physics, Moscow State University, ul. Leniskie Gory, 119991, Moscow, Russia
[2]Chemistry Faculty, South Federal University, ul. Zorge 7, 344090 Rostov-na-Donu, Russia
e-mail: tvfrantsuzenko@gmail.com

Introduction

Static and dynamic magnetic properties of new sodium-iron-antymoni oxide Na_4FeSbO_6 have investigated. Compound has layered structure with α-$NaFeO_2$ superlattice type ($P3_112$) [1] and large and small cations alteration. Such compound is potentially interesting as material for batteries fabrication as a solid electrolyte.

Experimental

The Na_4FeSbO_6 compound was prepared by conventional solid-state reactions. The magnetic measurements were performed using a Quantum Design MPMS-7 SQUID magnetometer. The temperature dependence of magnetic susceptibility was measured under variation of the magnetic field $B \leq 7$ T in the temperature range 1.8÷400 K. Electron spin resonance (ESR) studies were carried out using an X-band ESR spectrometer CMS 8400 (ADANI) (f≈9.4 GHz, B≤0.7 T) equipped by a low temperature mount, operating in the range T=6-470 K. The effective g-factors of our samples have been calculated with respect to an external reference for the resonance field. We used BDPA (*a,g* - bisdiphenyline-*b*-phenylallyl), g_{et}=2.00359, as a reference material.

Results

The static susceptibility data χ = M/B for the Na_4FeSbO_6 (fig.1) compound demonstrates a broad flatter maximum (cusplike) at T_m=65±2 K, probably indicating either

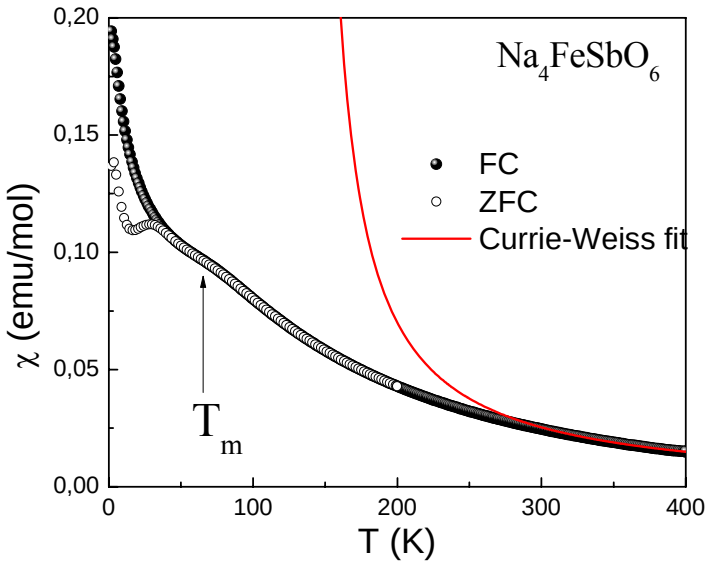

Fig.1. Temperature dependence of the magnetic susceptibility in ZFC (open circles) and FC (filled circles) regimes at B=0.1 T. The solid curves represent an approximation in accordance with the Curie-Weiss law.

spin-glass or low-dimensional character of magnetic correlations in the material. Upon a decrease of the temperature, though, χ continues to increase and below T~40 K we observe the difference in χ(T) curves recorded in zero-field cooling (ZFC) regime and field cooling (FC) one. Approximation of experimental data at T>300 K was carried out in accordance with the Curie-Weiss law indicating extended range of short-range correlations, which is typical of spin-glasslike or low- dimensional magnets.

The effective magnetic moment μ_{eff} has estimated from the Curie-Weiss law and we have obtained μ_{eff} to be 5.92 μ_B/f.u., which satisfactorily agrees with the theoretical value assuming high-spin configuration of Fe^{3+} (S=5/2) ions and with *g*-factor g = 2. The Weiss temperature obtained from the fit of the χ(T) dependence is found to be large positive Θ ~ 140 K. It is consistent with the predominance of strong ferromagnetic coupling in this compound and hysteresis with the residual magnetization as high as M_r = 110 emu/mol at T=1.8 K.

The ESR spectra has comlicated structure and we have used one or two Lorenzians to fit the experimental data at high temperatures (T>140 K) and at low temperatures correspondingly (fig.2). One line L_1 remains virtually unchanged with temperature variation,

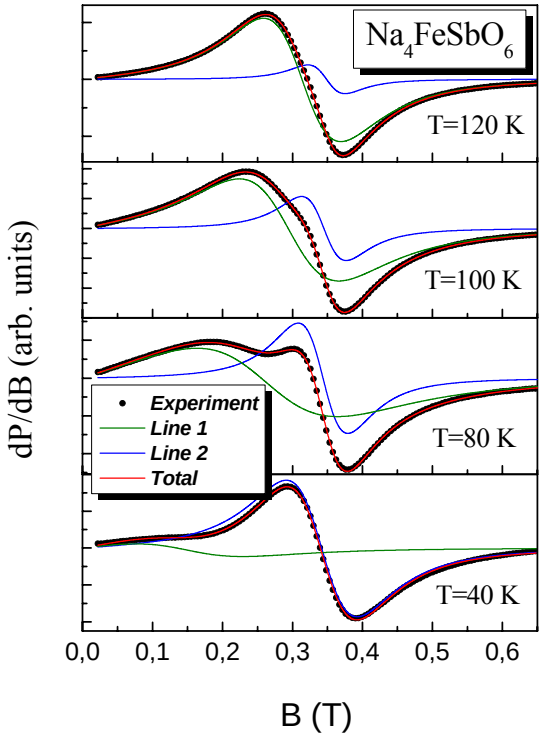

Fig.2. Temperature evolution of the ESR spectra for Na_4FeSbO_6 at low temperatures: black points – experimental data, green and blue dashed lines represent two resolved components in ESR spectra, red solid line – sum of two components.

while another L_2 strongly shifts to lower fields. This behavior indicates the presence of strong short-range magnetic fluctuations at T<Θ.

Both absorption lines broaden remarkably with T decreasing, but the linewidth and integral ESR intensity of the line L_2 demonstrated a maximum at temperature close to T_m. Thus ESR data are in aggrement with static magnetic properties.

Temperature dependencies of the effective *g*-factor, the linewidth and the integral ESR intensity derived from the fitting for both absorption components are presented in fig.3. Fitting χ_{esr}(T) in accordance with the Curie-Weiss law in the range 250 – 450 K (black solid

curve in upper frame of fig.3) results in $\Theta_{esr} \sim 145$ K being in reasonable agreement with the value obtained from the static magnetic susceptibility ($\Theta \sim 140$ K). An analysis of

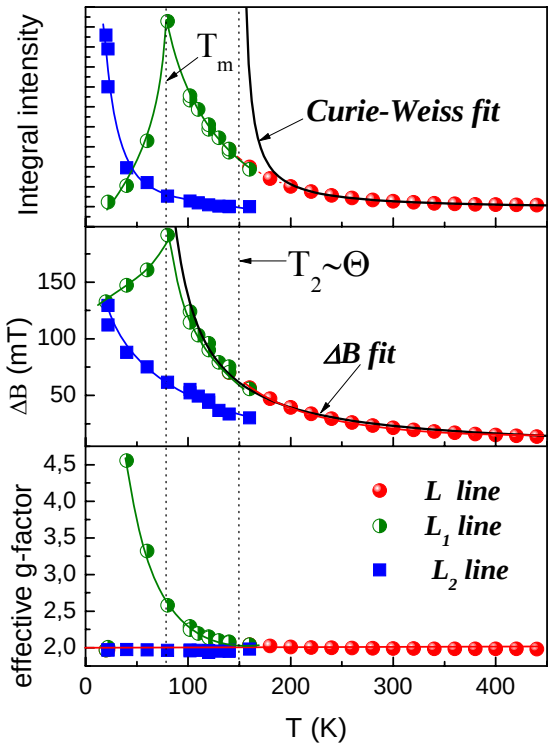

Fig.3. Temperature dependencies of the ESR integral intensity, the linewidth and effective g-factor for Na_4FeSbO_6.

temperature dependencies of the integral ESR intensities yeilds the picture of possible coexsistance of two magnetic sublattices driving the magnetic properties in the Na_4FeSbO_6.

The effective g-factor characterising the line L_1 (which obviously determined an absorption in the high temperature range) strongly increase with decreasing temperature. At the same time the effective g-factor of L_2 remains temperature independent and equal to $g_2=2.00\pm0.01$ over the whole temperature range studied. The $\Delta B(T)$ behavior observed resembles the behavior of spin glasses and the broadening observed we analyzed using the modified Huber expression:

$$\Delta B(T) = A\left(1+\frac{\Theta_{esr}}{T}\right)+B\left(\frac{T_m^{esr}}{T-T_m^{esr}}\right)^{\beta}.$$

The best agreement was achieved with the following parameters $\Theta_{esr} = 150 \pm 5$ K, $T_m^{esr} = 60 \pm 5$ K, that agree quite well with the static magnetization data.

References

[1] V. V. Politaev, V. B. Nalbandyan, *Sol. State Sci.*, **11**, 144 (2009).

Spin dynamics in one-dimensional magnet vanadyl acetate $VO(CH_3COO)_2$

M.I. Stratan, E.A. Zvereva, O.A. Savelieva, O.S. Volkova, A.N. Vasiliev

Faculty of Physics, M.V. Lomonosov Moscow State University, 119991 Moscow, Russia

e-mail: stratan@physics.msu.ru

Introduction

Searching and revealing of new low-dimensional systems with disordered magnetic ground states is one of the most exciting tasks of the modern physics of condensed matter. One of the candidates to find such a ground state at low temperatures is vanadyl acetate $VO(CH_3COO)_2$. According to the crystallographic data [1] it has non-centrosymmetric $Cmc2_1$ space group. Their structure contains VO_6 octahedra, forming an infinite one-dimensional (1D) chains of tetravalent vanadium ions V^{4+} with S = ½, as shown in fig.1. According to available data [1], neither long-range magnetic order nor spin-Peierls transition in this compound is detected, despite the fact that the scale of the exchange interaction in this compound is very high. The purpose of this work was studying the static and dynamic magnetic properties of $VO(CH_3COO)_2$ by means of magnetometry and electron paramagnetic resonance to clarify the ground state of interesting 1D compound.

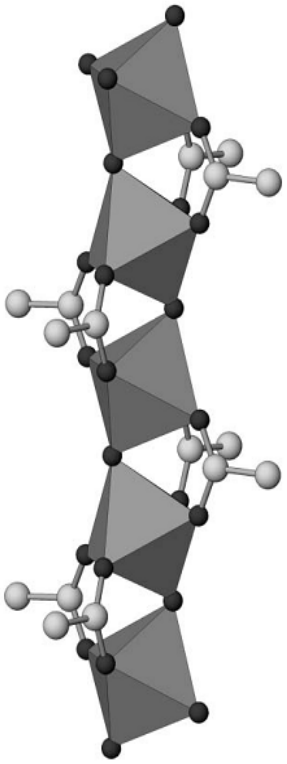

Fig.1. Infinite one-dimensional spin chain in the structure of $VO(CH_3COO)_2$.

Experimental

Temperature dependencies of the magnetic susceptibility and magnetic field dependencies of the magnetization have been measured by a Quantum Design SQUID magnetometer in the range T=2-300 K, $B \leq 5$ T, electron paramagnetic resonance (EPR) studies were carried out using X-band spectrometer (f≈9.4 GHz, B≤0.7 T, T=6-500 K).

Results and discussion

Similarly to the data of work [1] the temperature dependence of the magnetic susceptibility χ demonstrate a broad smooth maximum at about 200 K, accompanied by a noticeable low temperature Curie-Weiss-type increase of χ, which probably reflects to the presence of paramagnetic impurities and/or short chains. The experimental data were found to be equally well consistent with two models: (i) uniform Heisenberg antiferromagnetic chain (HAFC) with spin S = ½ and (ii) HAFC with Dzyaloshinskii-Moriya interaction. The magnetic susceptibility is well described by sum of Curie-Weiss and 1D magnetic contributions χ_{m1} or χ_{m2}, which for two cases are [2,3]:

$$\chi_{m1} = \frac{N_A g^2 \mu_B^2}{k_B T} \cdot \frac{A + B\frac{J}{k_B T} + C\left(\frac{J}{k_B T}\right)^2}{1 + D\frac{J}{k_B T} + E\left(\frac{J}{k_B T}\right)^2 + F\left(\frac{J}{k_B T}\right)^3}, \quad (1)$$

$$\chi_{m2}(T) = g^2 \left(\frac{N_A \mu_B}{4k_B} \right) F\left(\frac{J}{k_B T} \right) \frac{1}{T}, \qquad (2)$$

where J is the exchange integral, N_A, k_B and μ_B are the Avogadro, Boltzman and Bohr constants, S and g are the spin and g-factor $g = 1.96$ determined from our EPR data — see below, F(x) — empirical rational function, which can be expressed for $x = J/k_B T$ as: $F(x) = \left(1 + 0.08516x + 0.23351x^2\right) \Big/ \left(1 + 0.73382x + 0.13696x^2 + 0.535368x^3\right)$. The scale of the exchange interactions within the chain was found is large enough and is $J/k_B = 169 \pm 1$ K and $J/k_B = 154 \pm 1$ K for both models, respectively.

The evolution of the EPR spectra with variation of temperature is shown on fig.2. The thorough analysis shows that the experimental EPR spectra represent the superposition of the

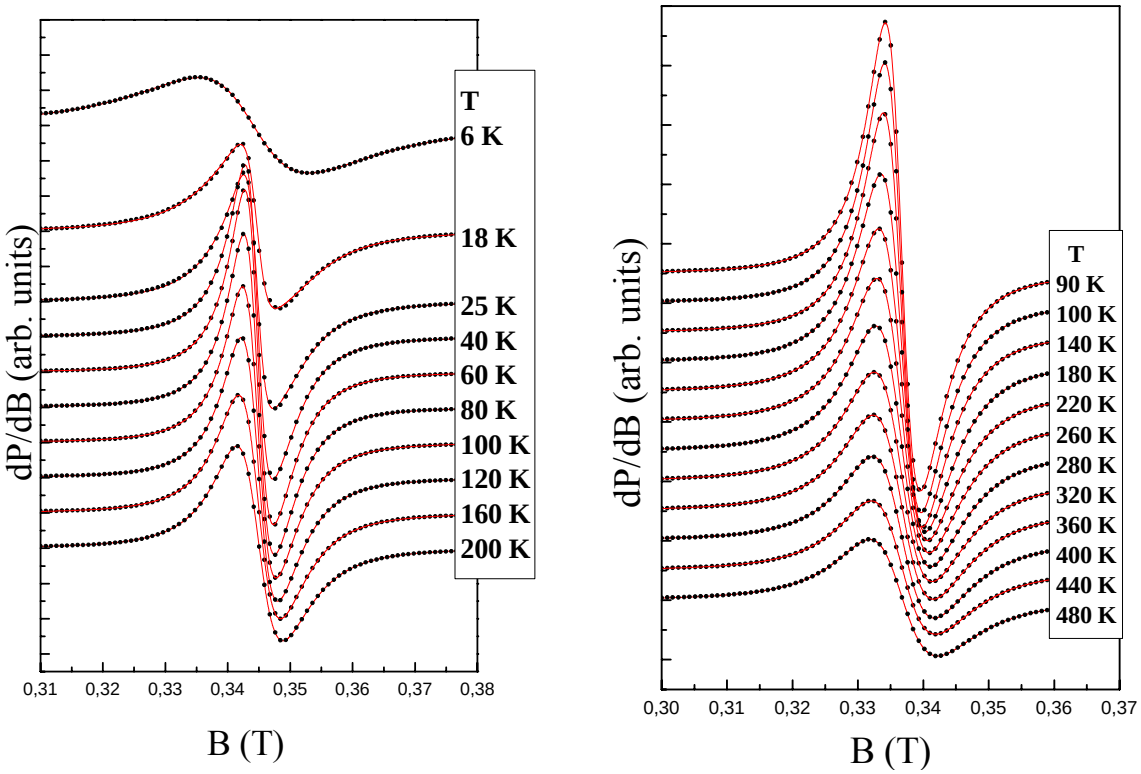

Fig.2. The evolution of the EPR spectra with temperature for the vanadyl acetate $VO(CH_3COO)_2$ at low and high temperatures. Points - experimental data, solid red lines - the result of approximation by sum of two Lorentzians.

two components of the Lorentzian lineshape and the behavior of main parameters for the components are significantly different (fig.3). Effective g-factor for Line 1 is 1.961 ± 0.002 and is almost independent of temperature up to the very low temperatures. This value is characteristic of the vanadium ions in a state V^{4+} ($S = 1/2$). At the same time, the effective g-factor for the Line 2 increases significantly (from 1.937 to 1.963) with decreasing temperature over the whole temperature range. EPR linewidth for both components varies non-monotonically: first is reduced with cooling, passes through a minimum and then increases rapidly. Integral intensities of the EPR (which is proportional to the number of magnetic spins and estimated by double integration of the first derivative ESR spectrum) show rather different behavior with temperature (fig.4). Line 1 demonstrates typical one-dimensional character over the whole temperature range: I_{esr1} passes through a broad maximum at about

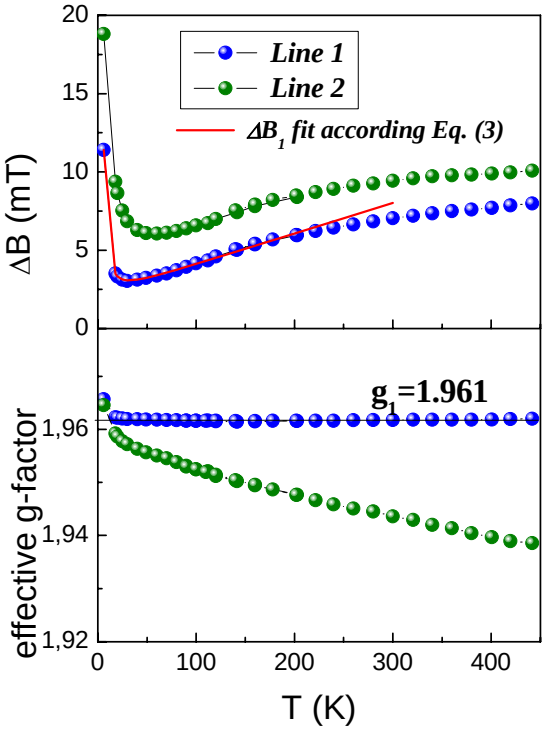

Fig.3. The temperature dependence of the effective g-factor and the linewidth for two resolved components in the EPR spectra of the vanadyl acetate.

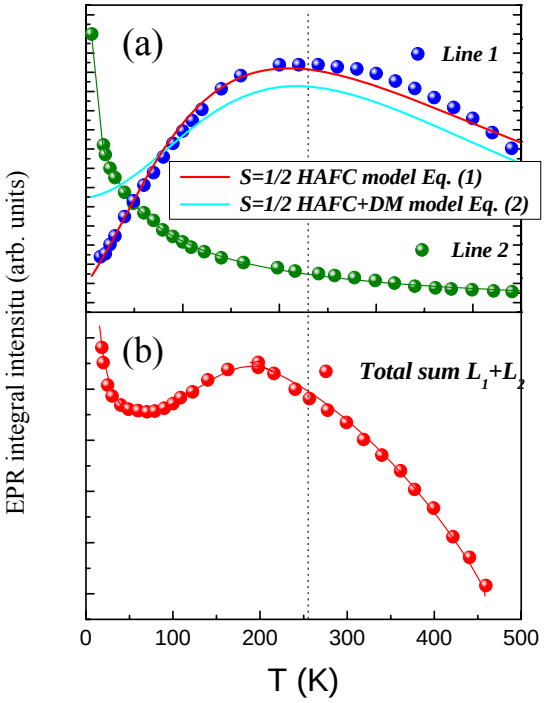

Fig.4. Temperature dependence of the integral EPR intensity I_{esr} for two resolved components (a) (two contributions to the magnetic susceptibility) and their sum (b), normalized to the corresponding constant in comparison with SQUID data for χ(T).

230 K. In contrast, I_{esr2} shows Curie-Weiss-type growth at lowering temperature and possibly reflects to the presence of paramagnetic impurities and/or short chains. Sum of two components gives the result, which is rather similar to $\chi(T)$ obtained from the SQUID data. Hence, EPR data has given us unique possibility to select pure low-dimensional contribution.

To estimate the exchange parameter in 1D chain $I_{esr1}(T)$ for the lower-dimensional components of the EPR spectra were analyzed in the frame of two mentioned above models. It was found that both models may reasonably account for the temperature evolution of the experimental curve $I_{esr1}(T)$, but some deviation occurs as temperature decreases as compared both with experimental points and with the product of fitting in accordance with Eggert model (2), especially at low temperatures. Nevertheless, the values of the exchange integral obtained in two different ways coincide with very high accuracy with each other ($J = 167 \pm 3$ K and $J = 168 \pm 9$ K for model (1) and (2), respectively) and with the estimation obtained from the static magnetic susceptibility data. So, we have found that the best agreement between experimental data and theoretical predictions is obtained by fitting in the frame of HAFC model (1). In addition, the value obtained for the alternation parameter $\alpha = J_1/J_2$ was with very good accuracy close to one, indicating that the 1D chain considered is uniform one. Moreover, we have got very reasonable value $g = 1.96$ if even setting it as a variable parameter during the fitting by (1). At the same time though, we have to note that the fall of $I_{esr1}(T)$ at $T \to 0$ is essentially larger than it would be expected χ for uniform $S = 1/2$ HAFC [2].

To clarify the latter fact we also tried to analyze the behavior of the linewidth ΔB_1 for low-dimensional component. It was found that the $\Delta B_1(T)$ dependence resembles those obtained previously for other 1D antiferromagnets, for example $BaCu_2Ge_2O_7$, $KCuF_3$ [4]. To describe the temperature dependence of the EPR linewidth Oshikawa-Affleck model for S=1/2 HAFC with Dzyaloshinskii-Moriya interaction interaction was used [5]:

$$\Delta H\left(T\right) = AT + B\left(T - T_N\right)^n, \tag{3}$$

where A and B — coefficients, T_N — Neel temperature, and n - parameter. According to this theory, the linewidth of the EPR signal for $S = 1/2$ HAFC should be directly proportional to the temperature at $T << J$. The second term in (3) becomes significant at low temperatures and is interpreted as the occurrence of 3D AF fluctuations on approaching T_N from above.

As one can see from fig.3 when the temperature below $T_{max}/2$, ΔB_1, in fact, follows a linear dependence $\Delta B \sim T$ in a wide range of temperatures, as predicted by theory [5]. At lower temperatures, the second contribution of so-called 3D component to ΔB becomes more important, so that $\Delta B_1(T)$ passes through minimum at certain temperature. Parameter $n \approx -1.16$ obtained from fitting agrees satisfactorily with the value $n = -1.1$ reported in [4].

Conclusion

Summarizing the results obtained we can conclude the following. The investigation of both static and dynamic magnetic properties of the vanadyl acetate $VO(CH_3COO)_2$ has shown that this compound represent 1D uniform antiferromagnetic Heisenberg chain with $S = 1/2$. The scale of the exchange interaction in the chain has been estimated as $J/k_B = 167$ K. According to our data, the long-range magnetic order in the system is not achieved down to 2 K. According to the evaluation $T_N = \sqrt{J \times J'}$, parameter of the interchain interaction $J' < 0.02\,\text{K}$, so that the ratio between the interchain and intrachain interactions in this compound reaches a record low value $k = J'/J \sim 10^{-4}$. Result of our EPR study indicates the presence of small Dzyaloshinskii-Moriya anisotropy in $VO(CH_3COO)_2$.

References

[1] C. Weeks, Ya. Song, M. Suzuki, N.A. Chernova, P.Y. Zavalij, and M.S. Whittingham, *J. Mater. Chem.* **13**, 1420-1423 (2003)

[2] J.W. Hall, W.E. Marsh, R.R. Weller, and W.E. Hatfield, *Inorg. Chem.* **20**, 1033-1037 (1981).

[3] S. Eggert, I. Affleck and M. Takahashi *Phys. Rev. Lett.* **73** 332(1994).

[4] S. Bertaina, V.A. Pashchenko, A. Stepanov, T. Masuda, and K. Uchinokura, *Pys. Rev. Lett.* **92** 057203 (2004).

[5] M. Oshikawa and I. Affleck, *Phys. Rev. Lett.* **79**, 2883 (1997); I. Affleck and M. Oshikawa, *Phys. Rev. B* **60**, 1038 (1999).

Aerobic oxidation of 5-hydroxy-6-methyluacil in alkaline solutions

S.F. Petrova, S.P. Ivanov, T.R. Nugumanov

Institute of Organic Chemistry Ufa Scientific Centre of RAS, 450054, Prospekt Oktyabrya, 71, Ufa, Russia.

e-mail: nugumanov_tr@anrb.ru

The 5-hydroxy-6-methyluracil's (**1**) oxidation by molecular oxygen has been demonstrated in our previous report [1]. In aqueous solutions in the presence of copper chloride it resulted to 5,5,6-trihydroxy-6-methyluracil-2,4-dione (2) which structure proved by X-ray diffraction. The uracil **1** has been oxidized to sodium salt of 4-hydroxy-6-methyl-2,5-dione (4) in aqueous solution of NaOH (pH ~10) [2]. The structure of **4** was proved using ^{13}C NMR technique: 165,12 C(2); 177,19 C(4); 183,82 C(5); 158,61 C(6); 25,65 C(7).

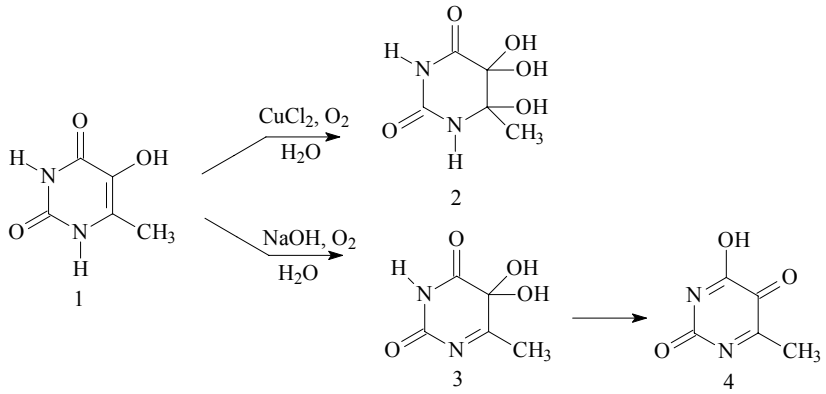

In this paper the 5-hydroxy-6-methyluracil's oxidation in aqueous solutions is reported (pH ~ 8-10). To avoid tracks of transition metal's ions Trilon B has been added. For the ascertainment of oxygen role the reaction has been carried out under argon. The uracil's **1** aerobic oxidation was followed by spectrophotometry and HPLC. There is an absorption of high intensity at 278 nm in UV spectra of initial uracil's solution. During the course of reaction the intensity of this maximum was decreased to nearly zero. As to chromatogram the signal of compound **1** almost disappeared with concomitant appearance a new one. This compound was isolated by preparative liquid chromatography and characterized by ^{13}C NMR technique as 5,5-dihydroxy-6-methylpyrimidine-2,4-dione (3). The chemical shifts of **3**'s carbon atoms are following: 154,03 C(2); 159,90 C(4); 79,23 C(5); 172,21 C(6); 23,62 C(7) [3]. For the time the **3**'s peak was transformed to the final products one.

On the basis of our results we suggest a reaction scheme according to which an oxidative transformation of uracil **1** → product **4** proceeds via the intermediate **3.**

This work was partially supported by RFBR, research project No. 12-03-31712.

References

[1] Nugumanov T.R., Ivanov S.P., Starikova Z.A., Murinov Yu.I. // Mend. Commun. – 2008. – V.18. – P. 223-224.

[2] S.P. Ivanov, I.G. Konkina, I.P. Baikova, L.V. Spirikhin, Yu.I. Murinov. // Chem. Heterocycl. Compounds. – 2002. – V. 38, №11. – C. 1424 - 1425.

[3] Petrova S.F., Ivanov S.P., Zimin Yu.S., Murinov Yu.I. // International conference "Fundamental Mathematics and its employment in Natural Science", Ufa, Russia – 2-6 October 2011. – P. 56-57.

Investigations of the locally compensated triclinic Fe^{3+} EPR centers in lead germinate

V.A. Vazhenin, A.P. Potapov, A.V. Fokin, M.Yu. Artyomov

Research Institute of Physics and Applied Mathematics, Ural Federal University, 19 Mira St., Ekaterinburg, 620002, Russia

e-mail: andrey.fokin@rambler.ru

The trigonal Fe^{3+} (S = 5/2) center in the uniaxial ferroelectric $Pb_5Ge_3O_{11}$ was studied in [1]. It was established that this center is formed by the single Fe^{3+} ion allocated in Pb7 [2] position. The charge compensation is carried out nonlocally.

The polar angular dependencies of the resonance positions of two allowed and five forbidden transitions for B||C_3 (B is the magnetic field induction) of the trigonal Fe^{3+} center (energy levels for B||C_3 are shown in fig.1) were measured and the spin-Hamiltonian parameters were determined at 170 K.

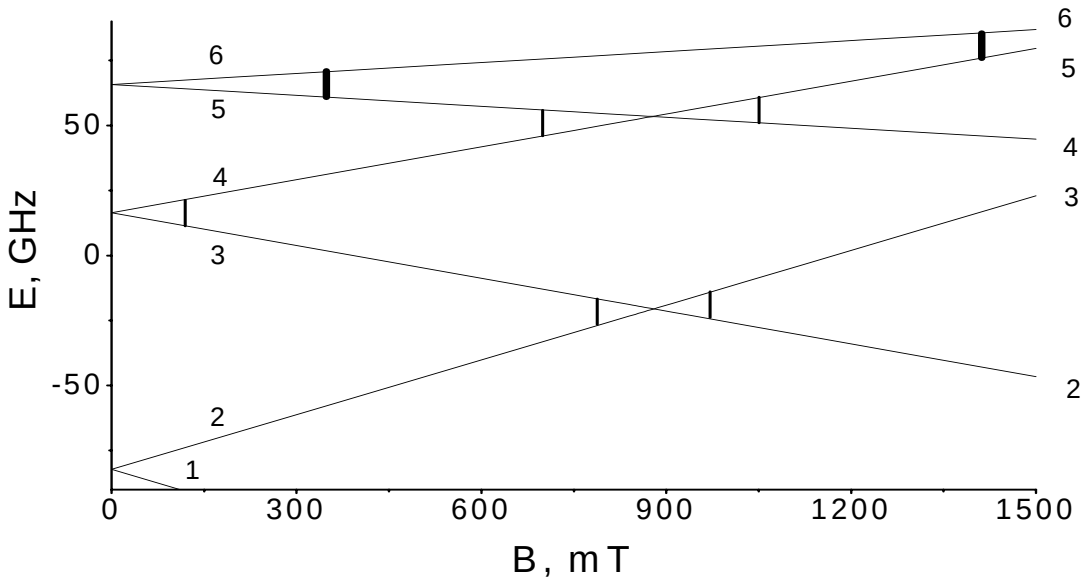

Fig.1. Energy levels 1-6 of the trigonal Fe^{3+} center for B||C_3. The vertical bars indicate the positions of the transitions which used for spin-Hamiltonian constants determination (thick lines represent the allowed transition; the thin lines show the forbidden transitions corresponding to 9.4 GHz)

It was discovered, that the EPR signal from the high-field transition 5-6 of the single Fe^{3+} ion has weak satellite signals (see fig.2a), which split into three components in the single-domain crystal at a deviation from the direction B||C_3. In an arbitrary orientation a similar satellites are observed in the area of the forbidden transitions for B||C_3.

Undoubtedly, the above-mentioned satellite signals correspond to the transitions of the locally compensated Fe^{3+} centers which have the point symmetry group C_1. The trigonal crystal always contain the three structurally equivalent centers with the C_3 symmetry. This centers turn into each other with rotation through 120° around C_3.

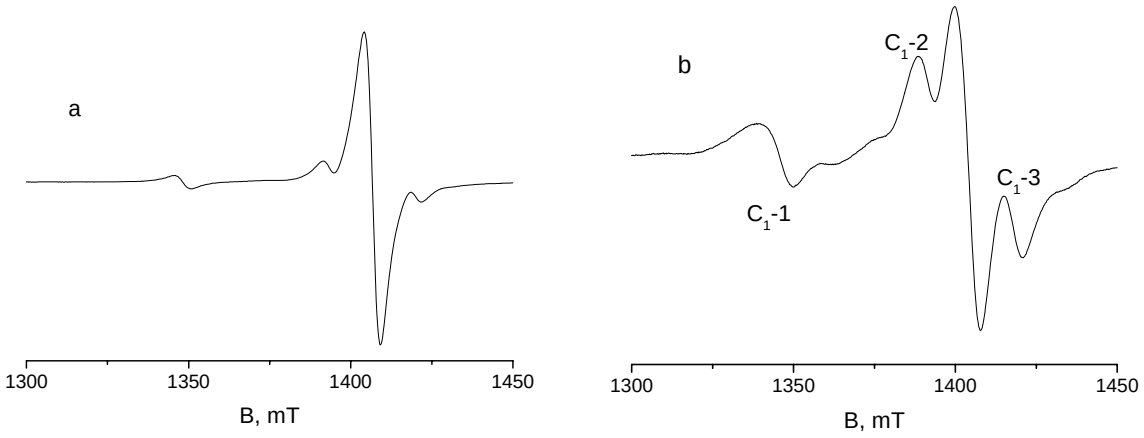

Fig.2. EPR spectrum in the area of 5-6 transition of the single Fe^{3+} ion (see fig.1) for $B||C_3$ at room temperature: a – before annealing, ν_{EPR} = 9829 MHz; b – after annealing, ν_{EPR} = 9864 MHz.

Annealing of the crystals in a chlorine-containing atmosphere (with $ZnCl_2$) appreciably increases the intensity of the satellite signals (fig.2b); the most intensive satellite signals are indicated by C_1-1, C_1-2, C_1-3. It is most likely that these signals are due to the transitions of the triclinic Fe^{3+}-Cl^- dimers which are similar to Gd^{3+}-Cl^- dipole clusters.

According to [3,4] the charge-compensating chlorine ions are disposed in closest to Gd^{3+} ion empty channels of the structure formed with lead ions (triangles) and passed along the C_3 axis.

The orientation behavior of the satellites of the trigonal Fe^{3+} center transitions was investigated in the ZX, ZY and XY planes in the crystals which were annealed in the chlorine atmosphere. The coordinate system is the same as for the trigonal Fe^{3+} center: $Z||C_3$, X-axis is orthogonal to the face of the unit cell or a side face of the crystal, which has hexagonal prism form. Each of the C_1-1, C_1-2, C_1-3 dimers represents by three differently oriented paramagnetic clusters. For the estimation of the spin-Hamiltonian parameters of the triclinic centers it is necessary to correlate the observed signals with EPR transitions of the nine discovered centers. The measurement data of the azimuthal angular dependence of the 3-4 transitions for $B\perp C_3$ (fig.3) assist us to solve the problem of this correlation in the first place. As it seems there are three centers in the fig.3. Each of these centers is represented by three sinusoidal dependences shifted on the 120 degrees. The position of the signal of the trigonal Fe^{3+} spectrum doesn't depend on an angle φ. The presence of this signal doesn't allow to measure a signal position of the triclinic centers in the range of magnetic field 620÷670mT. An amplitude and phase of the azimuthal angular dependences are determined by the spin-Hamiltonian constants b_{22}, c_{22} in the first instance. These dependences allow us to associate the polar angular dependences of each center and estimate other spin-Hamiltonian parameters. The final values of the spin-Hamiltonian parameters for the three triclinic centers with $g_{||} = g_{\perp} = 2$ were obtained by minimization of the root-mean-square error between the experimental and calculated EPR frequencies and are shown in table 1. It should be noted that for description of the spectra of the triclinic centers only the second-rank parameters are required.

It is most likely that chlorine$^-$ ions are situated in the nearest interstitial site of the structure channel. A farther compensators lead only to an broadening of observed signals.

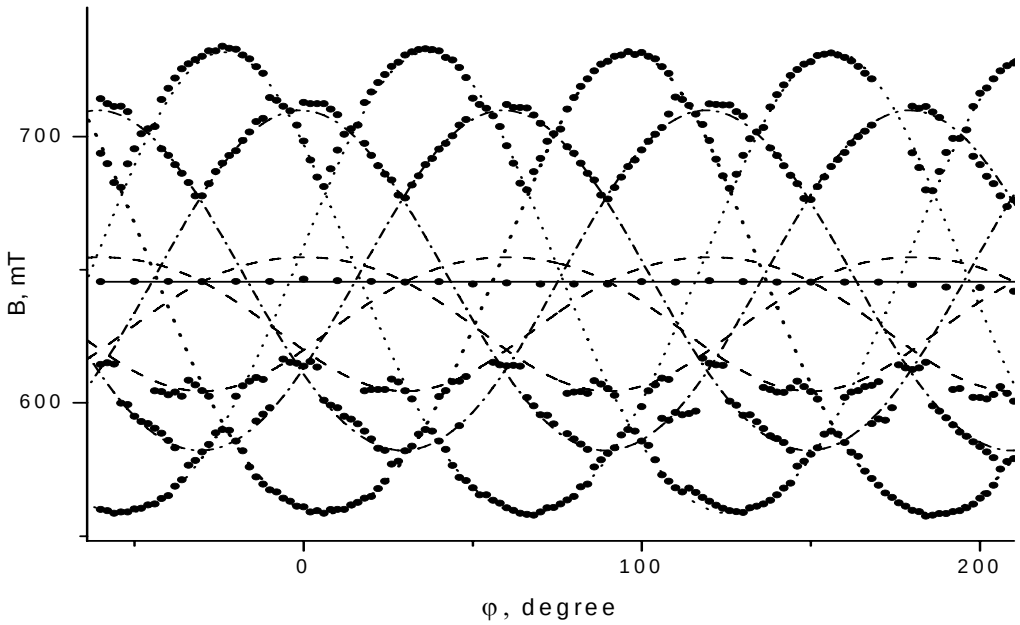

Fig.3. Azimuthal angular dependence of the positions of the transitions 3-4 for B||C_3 at 170 K. The points show the experimental data; the solid curves show the calculated data for trigonal center; the dashed curves: calculations for C_1-1 center; the dotted lines represent calculated data for C_1-2 center; the dash-dotted curves: for C_1-3.

Table 1. Spin-Hamiltonian parameters and the root-mean-square deviation S (in MHz) for the trigonal (C_3) and triclinic Fe^{3+} centers at 170 K.

	C_3	C_1-1	C_1-2	C_1-3
b_{20}	-25320(11)	-24233(11)	-25142(15)	-25342(13)
b_{21}		-680(100)	210(100)	-503(100)
b_{22}		416(18)	1025(12)	1072(13)
c_{21}		-19(100)	-204(100)	26(100)
c_{22}		15(18)	-1053(12)	-21(13)
b_{40}	-80(5)			
b_{43}	200(100)			
S	63	68	69	75

This work is supported by a grant for young scientists of UrFU.

References

[1] H.R. Asatryan, V.A.Vazhenin, A.D. Gorlov, A.A.Mirzahanyan, A.P.Potapov, Sov. Phys. Solid State **23**, 2463 (1981).

[2] Y. J. Iwata, J. Phys. Soc. Jpn. **43**, 961 (1977).

[3] V. A. Vazhenin and K. M. Starichenko, Sov. Phys. Solid State **28** (6), 1069 (1986).

[4] V. A. Vazhenin, K. M. Starichenko, and A. V. Gur'ev, Sov. Phys. Solid State **30** (5), 832 (1988).

Investigation of the magnetic resonance spectra of the nanocomposite thin films

I.N. Razmyslov[1], V.S. Vlasov[1], V.K. Turkov[1], Yu.E. Kalinin[2], A.V. Sitnikov[2]

[1]Syktyvkar State University, 167001 Syktyvkar, Oktybrsky 55, Russia

[2]Voronezh State Technical University, 394026 Voronezh, Moskovsky Pr. 14, Russia

e-mail: z-project@bk.ru

Nanocomposite metal-dielectric films are promising materials for applications and display unusual characteristics: giant magnetoresistance, intense magnetooptical response etc. [1]. These films can be applied as magnetic sensors and read heads. [2] The magnetic metal-dielectric nanocomposite films have high coercivity, weak noise and can be used as a medium for recording.

The ferromagnetic resonance (FMR) can be very useful tool to study of magnetic films. To study of the spectra obtained from the excitation of uniform precession or excited modes we can get important information about the effective fields, form and distribution of the grains, the ferromagnetic exchange coupling constant, etc. To solve the problems associated with the use of nanocomposite films is important to choose the model to describe the resonance films properties.

The aim of the work is the interpretation of experimental FMR spectra of metal-dielectric composite films and selection model to adequately describe FMR experiment.

Metal-dielectric composite films consist of many randomly oriented magnetic and dielectric particles with different size and shape. Thus, each composite film is a complex magnetic system and the FMR in such system is different from the resonance in homogeneous single-crystal films. The mean field model was used in the work because of large number of irregularities is in heterogeneous structures. The first model used in this work was proposed Nezelman. In this model, the magnetic particles are considered as ellipsoidal coupled by the dipole-dipole interaction [1]. The Nezelman model should be corrected in the case of films with small concentrations of the metal phase was shown by Dubovik [2]. We use the modified Dubovik model to describe the FMR characteristics of the composite films in present paper.

Fig.1 shows the geometry of the problem. We consider the magnetic particles of the film as rotation ellipsoids. The one film particle is shown on fig.1. The orientation of the axis of the particle and its magnetization is given by the following angles: φ – is the angle between the X axis and the magnetization vector $\vec{M}$ (field $\vec{H}$); θ – is the angle between the Z axis and the magnetization vector $\vec{M}$ (field $\vec{H}$); ε – is the angle between the X axis and the axis of the ellipsoid; β – is the angle between the axis Z and the axis of the particle.

Using the Dubovik model and the Smith-Suhl equation, we obtain the quadratic equation relatively to the resonance field, which is measured in the experiments [1-2]:

$$A_2 H^2 + A_1 H + A_0 = 0\,, \tag{1}$$

where H is the resonant magnetic field, A_i — coefficients which are expressed below and introduced for convenience:

$$A_2 = q_1 q_2\,, \tag{2}$$

$$A_1 = q_2 p_1 + q_1 p_2\,, \tag{3}$$

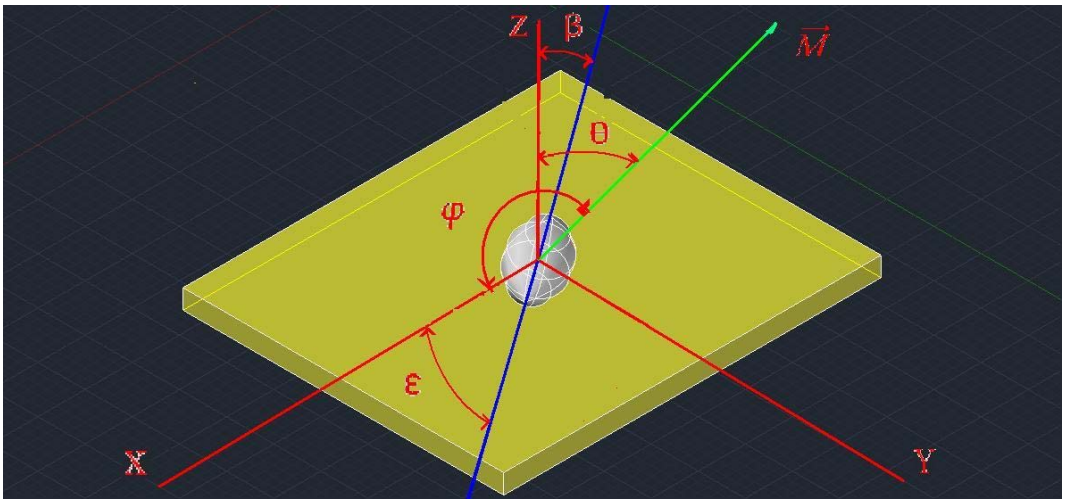

Fig.1. Definition of the systems of coordinates and the angles used for the theoretical description films FMR signal

$$A_0 = p_1 p_2 - k - \frac{(\omega M \sin\theta)^2}{\gamma^2 (1+\alpha^2)}. \tag{4}$$

Here M — magnetization, ω — the resonance frequency, α — the magnetic dissipation parameter, γ — gyromagnetic ratio. Expressions for p_i, q_i, k are given below:

$$k = (k^*)^2 \tag{5}$$

$$k^* = 2\pi(N_b - N_a)(1-x)xM^2\left[\sin^2\beta\sin 2(\phi-\varepsilon)\sin 2\theta + \sin 2\beta\cos 2\theta\sin(\phi-\varepsilon)\right] - \\ -2\pi xM^2\sin 2\theta\sin 2\phi \tag{6}$$

k^* is the expression for the mixed derivative of the energy on the θ and φ angles in the condition of energy minimum.

$$q_1 = M, \tag{7}$$

$$p_1 = 4\pi M^2 x\cos 2\theta\cos^2\phi - 2\pi(N_b - N_a)(1-x)xM^2 * \\ *\left[2\sin^2\beta\cos^2(\phi-\varepsilon)\cos 2\theta - 2\cos^2\beta\cos 2\theta - 2\sin 2\beta\sin 2\theta\cos(\phi-\varepsilon)\right], \tag{8}$$

$$q_2 = M\sin^2\theta \tag{9}$$

$$p_2 = 2\pi(N_b - N_a)(1-x)xM^2\left[2\sin^2\beta\cos 2(\phi-\varepsilon)\sin^2\theta + 0,5*\sin 2\beta\sin 2\theta\cos(\phi-\varepsilon)\right] \\ -4\pi M^2 x\cos 2\phi\sin^2\theta \tag{10}$$

The tensor of particles demagnetizing factors is diagonal and can be reduced to the form:

$$\overleftrightarrow{N} = \begin{pmatrix} N_a \\ N_a \\ N_b \end{pmatrix} \tag{11}$$

$$2N_a + N_b = 1 \tag{12}$$

The theoretical model developed in this paper was used for interpretation of the FMR characteristics of metal-dielectric composite films. The composite films were produced in the Voronezh State Technical University [3]. The FMR properties of the films were measured

experimentally in the Syktyvkar State University laboratory [3]. Analysis of experimental FMR spectra based on the resulting quadratic equation (1) allows reveal the structural characteristics of the films.

We were compared the resonance field experimental dependences on the metal phase concentration for single-layer and multilayer films and some calculations by formula (1). The compositions of monolayer and multilayer investigated films were as following: $(Co_{45}\text{-}Fe_{45}\text{-}Zr_{10})_x(Al_2O_3)_y$ (A-series); composite-composite - $\{(Co_{45}\text{-}Fe_{45}\text{-}Zr_{10})_x(Al_2O_3)_y\text{-}(Co_{45}\text{-}Fe_{45}\text{-}Zr_{10})_x(Al_2O_3)_y\}_{120}$ (C-series); composite-semiconductor - $\{[(Co_{45}\text{-}Fe_{45}\text{-}Zr_{10})_x(Al_2O_3)_y]\text{-}[\alpha\text{-}Si]\}_{120}$ (D-series), $\{[(Co_{45}\text{-}Fe_{45}\text{-}Zr_{10})_x(Al_2O_3)_y]\text{-}[\alpha\text{-}Si:H]\}_{120}$ (E-series); $0.3<x<0.62$, $3<y<12$, $y=21-30x$. Here 120 is the number of composite and semiconductor layers.

To simplify the analytical calculation the computer program was written in scilab environment. We calculate the concentration dependence of the resonance field by the program. The theoretical and experimental dependences of the resonance field were compared [3].

The model took into account the changes of the particle size and shape with increasing metal concentration. The metal concentration increase results in the demagnetizing tensor factors changing. Thus comparing the theoretical and experimental curves can determine the structural parameters of the film: the distribution of the directions of the particles and the shape of the magnetic particles.

Results of the comparison of experimental data and calculations based on formula (1) are shown in fig.2. We can see good agreement between theory and experiment. For the fig.2 were selected expression that defines the changes of the demagnetization factor N_b particles

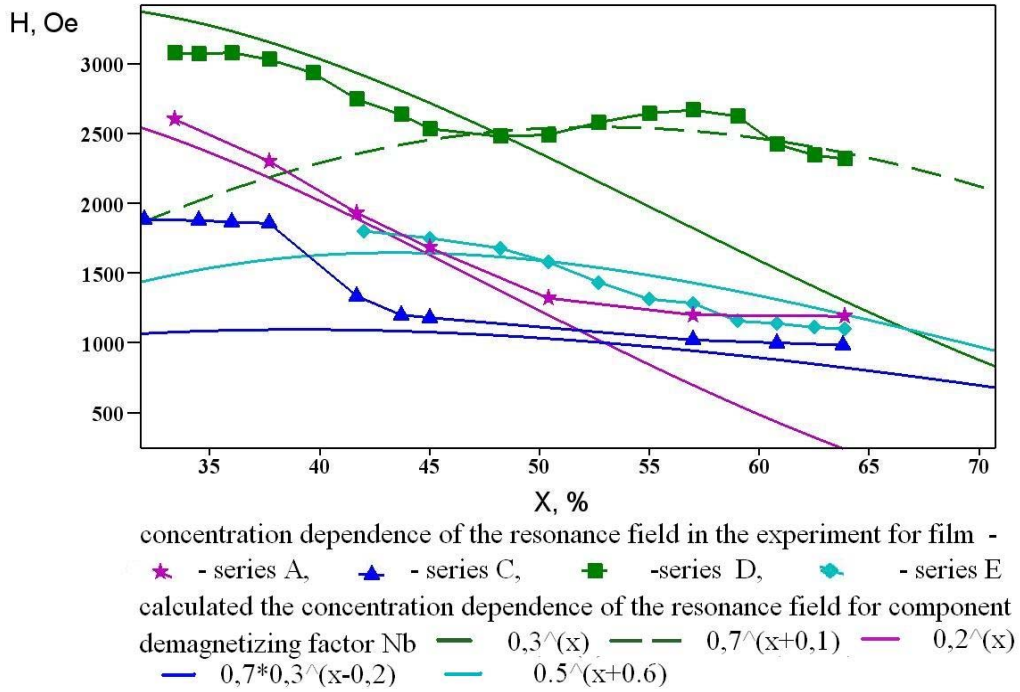

Fig.2. Experimental and theoretical concentrations dependence of the resonance field

by varying the concentration of the metal. The equation for the demagnetization factor N_b changing we consider on the form:

$$N_b = \lambda \cdot (\rho)^{f(x)}. \qquad (13)$$

Here ρ and λ are constants defining the range in which the component N_b is changed, f(x) - the linear function. For films of series D we use expression $N_b = 0{,}3^x$ for x changing from 0,35 to 0,5 and $N_b = 0{,}7^{x+0{,}1}$ for x changing from 0,5; for films of series A — $N_b = 0{,}2^x$; C — $N_b = 0{,}7 \cdot 0{,}3^{(x-0{,}2)}$, E — $N_b = 0{,}5^{(x+0{,}6)}$. It should be noted that changes in the shape of the particles can be described by more complex equations. For comparing experimental and theoretical results we assume the uniform angular particle distribution and that all particles have the same shape.

Thus in the work were considered model that can be used to describe experiments on the FMR for nanocomposite metal-dielectric films. The behavior of the metal phase concentration dependence of the resonance field was explained by the concentration dependences of the demagnetizing factors of film particles.

This work was supported by RFBR (grant № 12-02-01035a).

References

[1] Netzelmann U., J. Appl. Phys., **68**, 1800 (1990)

[2] Dubowik J., Phys. Rev., **54**, 1088 (1996)

[3] L.N. Kotov, V.K. Turkov, Vlasov, VS et. al. Nanomaterialy I Nanostructury 21 vek, **4**, 27 (2011)

EPR-monitored redox titration of RcXDH and mAOH1 variants

D. Kurzhunov[1], M. Mahro[2], C. Teutloff[1], S. Leimkühler[2]

[1]Freie Univertität Berlin, Physics Faculty, Arnimalle 14, 14195, Berlin, Germany

[2]Potsdam Univertität, Institute of biochemistry and biology, 14476, Postdam-Golm, Germany

e-mail: kurzhunov@gmail.com

Subfamily of mammalian molybdo–flavoenzymes (MFEs) consist of two members, i.e. xanthine oxidoreductase [XOR; xanthine dehydrogenase (XDH) form, xanthine oxidase (XO) form], aldehyde oxidase [AOX1 and aldehyde oxidase homologue (AOH)] [1]. All MFEs are homodimers consisting of two identical subunits that form a complex in the cellular cytosol. Protein subunit consists of a 20 kDa N-terminal domain, in which two EPR-distinct 2Fe/2S redox centers (FeSI and FeSII) are localized. This is linked to the 40 kDa FAD-binding domain and then to the 85 kDa domain containing the MoCo-binding site, which is located within the substrate pocket. The biochemical and physiological functions of AOX1 are still largely obscure. Several substrates of AOX1 and AOH are of toxicological or pharmacological interest. Although the crystal structures and the arrangements of cofactors of MFEs are similar, they have different properties, which could not assigned by crystal structure, yet EPR and kinetic study can help.

The use of chimeric enzymes revealed that 2Fe-2S/FAD and MoCo domains affect the rate and substrate binding properties of AO-catalyzed 2-oxidation, respectively [2]. Rate constant of the total reaction of mouse mAOX1 is about ten times higher than one of mAOH1 [3]. According to the conclusions of Itoh [2], the implementation of FeS domains of mAOX1 into mAOH1 should accelerate the reaction. For that purpose the following mutants were produced:

a) mAOH1 FeSI-mAOHX1 variant: mAOH1 protein , which FeSI domain was replaced by a FeSI domain of mAOX1,
b) mAOH1 FeSII-mAOHX1 variant: mAOH1 protein , which FeSII domain was replaced by a FeSII domain of mAOX1,
c) mAOH1 FeSIFeSII-mAOHX1 variant: mAOH1 protein , which FeSI and FeSII domains were replaced by FeSI and FeSII domains of mAOX1.

Kinetic analyses shows that the rate constant of the whole reaction (k_{kat}) of all the mutants is smaller than that of a mAOH1 wild type (WT) [9], whereas Michaelis Menten constants (k_M), which determine the affinity of the enzymes to the substrate, are the same, e.i. the substrate binding of all the mutants is the same as of a wild type. Two explanations are possible: either reaction is slower or enzymes are not active (do not have the cofactors). To confirm the integrity of the FeS centers the activity of the enzymes EPR should be applied. In the enzyme the electron transfer (ET) rate is one of the parameters, defining the total rate constant, which is proportional to the difference in the midpoint redox potentials between the cofactors. In order to compare the ET rates of mAOH1-WT and variants the midpoint redox potentials ΔE^0 of the cofactors are required. They can be determined by the EPR-monitored redox titrations.

mAOH1 xO2 variant posses the active side of bovine XDH, but show no activity toward xanthine [9]. In order to rule out an alteration of the redox properties, EPR-monitored redox titrations were also applied.

Similarity of the recorded EPR spectra of RcXDH and of the ΔE^0 of the cofactors (fig.1) to other XOR proteins [4,5] show the success of the established EPR-monitored titration

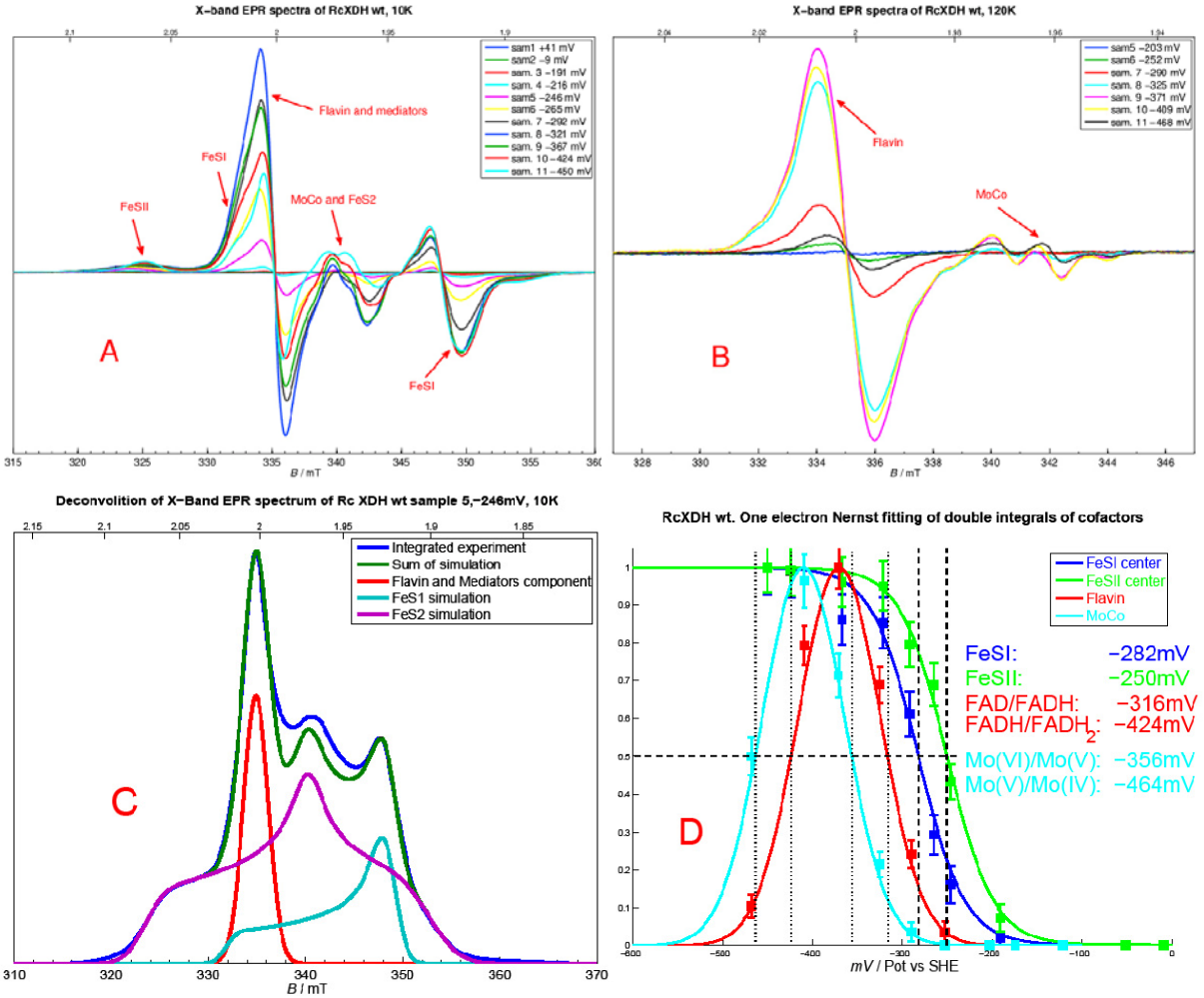

Fig.1. EPR spectra of RcXDH samples poisoned at different potential at 10K (A) and 120K (B); deconvolution of integrated 10K experiment to its components (C): axial FeSI (cyan, S=1/2, visible up to 80K), rhombic FeSII (violet, S=1/2, visible up to 40K) and axial S=1/2 with g=2.002 Flavin and Mediators signal (red, mediators having an EPR signal were later excluded from the mixture of mediators); one electron Nernst fitting of double

procedure in the presence of mediators under anaerobic conditions and of the designed titration cell. The cell has a closed pumping system (to equilibrate the potential within the cell) and is optimized for small sample volumes by having a small dead volume. Such a cell is required due to the difficuitl protein preparation with limited yield. 15 X-band EPR sample poisoned at different potential requires around 1.2 ml of most possible concentration.

Spectra of mAOH1 wild type and its variants are similar to those of RcXDH, besides the splitting of FeSI signal into two components (130MHz). It was previously observed in XOR proteins [6] and, as in our case, assigned to dipolar interactions between FeSI center and MoCo. Concentrations of the fully reduced centers of mAOH1 variants determined by spin quantitation with $CuSO_4$ as a reference are as small as 1-3 µM, which complicate the background correction and the spectra deconvolution, so that some FeSII signals are not analyzable due to their broadness and small intensities. Signals of FeSI and some FeSII centers (fig.2A) and Mo (fig.2B) are nicely visible and are analyzed. Reduction step FAD/FADH in mAOH1 is immediately followed by FADH/$FADH_2$ reduction, i.e. flavin

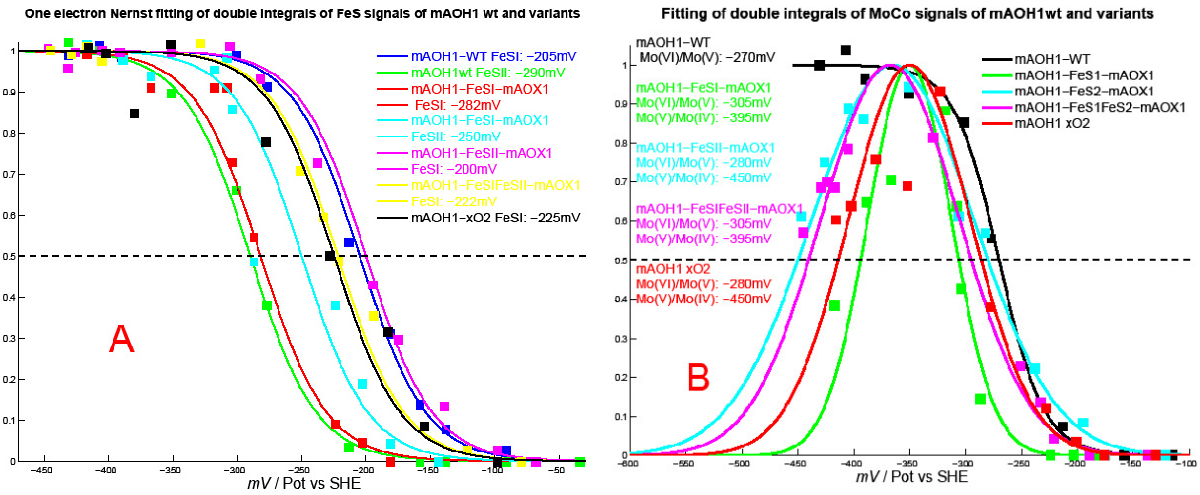

Fig.2. One electron Nernst fitting of double integrals of FeS (A) and Mo signals (B).

semiquinone (FADH) is not stabilized in the presence of sodium dithionite. In this case we cannot see any EPR signal from FAD, because both oxidized FAD and fully reduced $FADH_2$ don't have any unpaired electrons. Plotting of double integrals of signals from cofactors instead of peak intensities, which is common in literature [4,5,6], leads to the better precision and separation of highly overlaping signal of mAOH1 variants. Reduction potential of Mo(V)/Mo(IV) couple of mAOH1-WT is not reachable with sodium dithionite.

Although the known crystal structures of all XOR and AO are similar [8], the environment around the cofactors is different. That influences the ΔE^0, which are similar within AO and XOR groups, but differ between the groups. This discrepancy, especially of molybdenum potentials, may contribute to the differencies in substrate specificity, which is mainly defined by MoCo [2]. Since only one structure of AO is known [8], no general features of the environment around the cofactors can be assigned to the differencies in the redox potentials.

FeSI centers and the averaged FAD reduction potential of AO are more positive and FeSII are more negative than those of XOR. It is consistent with the conclusions of M. Barber [7]. The rate constant is measured by the chemical compounds, reduced by the electrons transferred from FAD to MoCo through FeS centers (FAD→FeSII→FeSI→MoCo). The potential barrier, caused by the fact that ΔE_0 of FeSI center of AO is higher than ΔE_0 of FeSII center (80mV for mAOH1 and 100mV for rabbit liver AO [7]), complicates the ET to MoCo. According to the Marcus theory, this barrier would decrease the k_{ET}. It is consistent with the comparative results of the kinetic studies of XOR and AO [9].

The implementation of FeSI domain from mAOX1 into mAOH1 leads to the decrease of the potential of FeSI center (around -70mV) and to the increase of the potential of FeSII center (around 30mV), i.e. the ΔE_0 of FeS centers of mAOH1-FeSI-mAOHX1 are similar to RcXDH-WT and other XOR. Potential barrier between FeS center, which is typical for AO, is now vanishes, so the k_{ET} is higher than in mAOH1-WT. The increase of the k_{ET}, which is one of the parameters defining the total rate constant k_{cat} in the redox reactions, will increase k_{cat}. According to the conclusions from [9], this means that the activity of the variant is smaller in comparison to WT. It corresponds with the results of spin quantitation, yielding that 30% less enzymes of the variant (around 4%) are active in comparison to the WT.

Introduction of FeSII or of both FeS domains, in contrast to the implementation of FeSI domain, do not change the potential of FeSI canter a lot, but the amount of active enzymes of mAOH1-FeSII-mAOHX1 and mAOH1-FeSIFeSII-mAOHX1 are still small: 4% and 5%

correspondingly. In order to understand the reasons for that, the ΔE_0 of other cofactors required. In this work only the potentials of both reduction steps of MoCo were determined: they are similar for these two variants and significantly smaller in comparison to the WT. It is not sufficient for the proper understanding of the ET process and the variations of k_{cat}.

The potentials of FeSI center and Mo(VI)/Mo(V) couple of mAOH1 xO2 variant, which possesses the active site of bovine XDH but the same environment of the cofactors, are similar to those of mAOH1-WT. It shows that the arrangements of the cofactors of AO and XDH are the same and that the potentials of the cofactors are determined by their environment. The same conclusions were obtained by M. Mahro in comparative kinetic studies of AO and AOR [8].

References

[1] E. Garatini at al., *Biochem*. J. **372**, 15-32 (2003).

[2] K. Itoh at al., *Biol. Pharm. Bull*. **32,** 31-35 (2009).

[3] S. Schumann at al., *PLoS One.*, **4** 5348 (2009).

[4] K. Parschat et al., Biochimica et *BiophysicaActa*, **1544** 151-165 (2001).

[5] R. Hille, *Chem. Rev*., **96,** 2757-2811 (1996).

[6] C. Canne at al., *Biochemistry***, 36**, 9780-9790 (1997).

[7] M. J. Barber at al., *Biochemistry*, **21**, 3561 (1982).

[8] M. Coelho et al., to be published.

[9] Mahro et al., to be published.

Structure of Cu(II) Alkyl Chlorocomplexes formed via tetrachlorocuprates photolysis: EPR, UV-Vis and DFT study

O.I. Gromov[1], E.M. Zubanova[1], E.N. Golubeva[1], G.M. Zhidomirov[1,2]

[1]Chemistry Department, Lomonosov Moscow State University, Leninskiye Gory 1-3, Moscow, Russia

[2]Boreskov Institute of Catalysis (BIC) SB RAS, 630090, Novosibirsk, Russia

e-mail: aalchm@gmail.com

Introduction

Investigation of structure and properties of complexes with Cu(II)-C(sp^3) bond is important as they could be intermediates [1] in radical reactions catalyzed by copper complexes [2], such as polyhalohydrocarbons addition to alkenes [3], living radical polymerization [4], cyclization [5]. Indeed Cu^+ forms organocopper(II) compounds with a wide variety of alkyl-type radicals, such as CH_3 [6 – 8], poly(acrylates) derivatives[9, 10], or CR^1R^2OH and $CH_2CR^1R^2OH$ radicals, produced from methanol, ethanol or propan-2-ol [11]. Though, they have short (10^{-2} – 10^{-6} s) lifetimes at ambient conditions, in a frozen matrix at 77 K organocuprates(II) are stable and could be studied by EPR and UV-Vis spectroscopy. On the tetrachlorocuprates of quaternary ammonium photolysis in frozen solvents alkyl-type radicals, Cu(I) compounds and two paramagnetic copper complexes are formed. New complexes were denoted as **1-Cu** and **2-Cu** [12**,** 13]. They are supposed to include alkyl fragments of ammonia cations or solvent [14]. The greatest advantage of EPR technique in application to the system under investigation is that complexes of Cu(I) are EPR silent as they are diamagnetic and do not introduce complications in the spectra interpretation. However, spectra of **1-Cu**, **2-Cu** and alkyl-type radicals strongly overlap that makes it difficult to obtain the individual spectra. On the annealing at 100 K complete conversion of **2-Cu** to **1-Cu** and alkyl-type radicals vanishing were observed [13]. As a result the individual EPR-spectrum and Spin-Hamiltonian parameters of **1-Cu** were obtained [15]. Though, it was difficult to separate out EPR spectrum of **2-Cu** since it was gained in presence of other paramagnetic products of photolysis [12]. This spectrum previously obtained by multiple subtractions gives rise to some doubts as we are still failing to interpret it [13].

Experimental and Calculation details

Anhydrous copper(II) chloride was prepared from $CuCl_2$ $2H_2O$ via azeotropic dehydration with benzene [16] followed by vacuum pumping at 10^{-3} torr. Tetrahexylammonium chloride $(C_6H_{13})_4N^+Cl^-$ from Sigma–Aldrich (Switzerland) was used without additional purification. 2-Chlorobutane from Merck (Germany) was purified by distillation over phosphoric anhydride. The solutions of $[(C_6H_{13})_4N^+]_2[Cu(II)Cl_4]^{2-}$ were prepared by successive dissolution of an excess of preliminarily evacuated $(C_6H_{13})_4N^+Cl^-$ and $CuCl_2$ in freshly distilled 2-chlorobutane. The copper concentration was 4.2×10^{-3} mol/l. The ratio $[(C_6H_{13})_4N^+Cl^-]$:$[CuCl_2]$ = 6:1 ($[Cl^-]$:[Cu(II)] = 8:1) was maintained constant in all the solutions in order to preclude the formation of bi- and polynuclear chlorocuprates [17]. The concentration of tetrachlorocuprate solutions and their purity were monitored by spectrophotometry [18]. The UV-Vis absorption spectra were recorded using HP 8453 spectrophotometer. The photolysis of the samples was carried out at 77 K in ESR cylindrical quartz ampules of 4 mm inner diameter. The ampules were preliminarily calcined at 500 K and freed of adsorbed water by connecting to a vacuum line of 10^{-3} torr. Each ampule was filled with 0.13 ml of solution with a certain copper(II) concentration, subjected to three

freezing–pumping (10^{-3} torr)– thawing cycles, and then sealed off. The photolysis was carried out with light from a DRSh-250 high-pressure mercury lamp equipped with a glass filter for isolation of the line at λ = 405 nm (T max = 27%, $\Delta\nu_{1/2}$ = 2400 cm^{-1}). The ESR spectra were recorded on a Varian-E3 X-band radiospectrometer (100 kHz magnetic field modulation) at 77 K. The measurement was performed under conditions that ruled out both saturation and modulation broadening of the signal. The spin Hamiltonian parameters were calculated as recommended in [19]. The invariability of the recording conditions in the resonator cavity was controlled via the simultaneous recording of the spectrum of as test sample and a certain component of the spectrum of ruby (Al_2O_3 containing Cr^{3+}) single crystal as an internal standard.

Unrestricted DFT calculations of the geometry model Cu (II)-alkyl chlorocomplexes were performed using ORCA program package [20] on B(38HF)P86 [21]/def2-TZVPP [22] level with RIJCOSX approximation [23]. Vibrational frequencies were calculated in order to prove the potential energy surface minima achievement. EPR parameters calculations were done using B(38HF)P86 functional with CP(PPP) basis set for Cu, IGLO-III for Cl and C atom bonded with Cu, and with IGLO-II basis set for other atoms. All calculations were performed employing COSMO [24] solvation model with 2-chlorobutane as the solvent.

Results and discussion

The principal values of *g*-tensor and hyperfine coupling (HFC) tensor *A*(Cu) of **1-Cu** are as follows: $g_1 = 2.082\pm0.003$, $g_2 = 2.033\pm0.001$, $g_3 = 2.024\pm0.001$, $A(^{63}Cu)_1 = 4.1\pm0.2$ mT, $A(^{63}Cu)_2 = 3.8\pm0.1$ mT, $A(^{63}Cu)_3 = 11.0\pm0.2$ mT [15]. These values are typical for non-symmetrical Cu (II) compounds [25]. We calculated principal g-tensor values of different model compounds with the DFT approach and compared them with experimentally acquired g-tensor values of **1-Cu**. For the model compounds of **I** type (fig.1) we got agreement of calculated g-tensor values with experimental ones: 2.021; 2.029; 2.088 in our calculation versus 2.024; 2.033; 2.082 in experiment. For more information see [26].

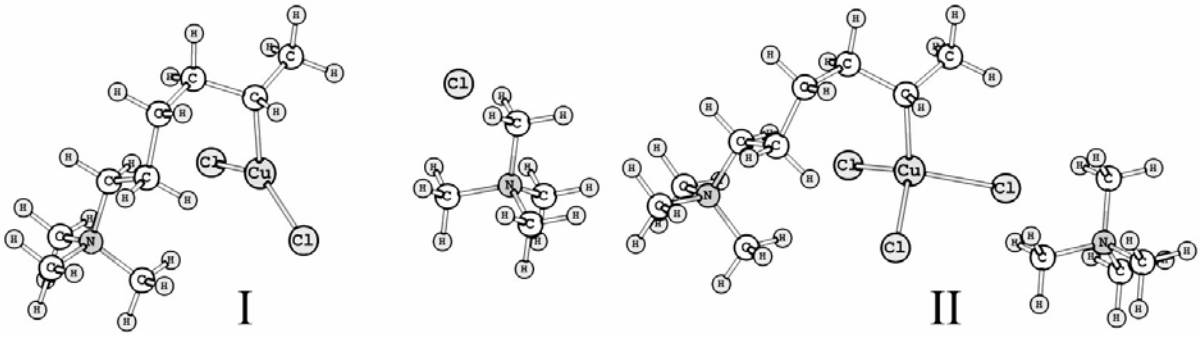

Fig.1. Model structures corresponding to **1-Cu** (**I**) and **2-Cu**(**II**).

Though it was difficult to interpret whole spectrum with multiple particles therein (fig.2). Thus UV-Vis spectrum of photolysed tetrahexylammonia tetrachlorocuprate was analyzed. TD-DFT calculated UV-Vis spectrum of the model structure **I** being scaled by 0.91 factor matches the experimental spectrum of **1-Cu**. This agreement confirms our previous conclusion on the structure of **1-Cu** based on comparison of experimental and calculated EPR parameters of **1-Cu**. **2-Cu** is known to form during the photolysis of $((N(C_6H_{13})_4)_2[CuCl_4])$ at 77 K and to transform into **1-Cu** on annealing, hence it may have structure intermediate between $CuCl_4^{2-}$ and **1-Cu**. Thus, it is suggested to contain three chlorine atoms instead of two chlorine atoms in **1-Cu** and alkyl-type fragment in copper coordination sphere. The model structure for **2-Cu** is presented at fig.1 (**II**). Indeed, TD-DFT calculated UV-Vis spectrum of **II** being scaled by 0.91 factor is in agreement with the experimental spectrum of

2-Cu. Therefore, **1-Cu** and **2-Cu** are concluded to have $Cu(II)Cl_2R$ and $Cu(II)Cl_3R$ general formulae, respectively, and the structures similar to model compounds **I** and **II**. For more information see [27].

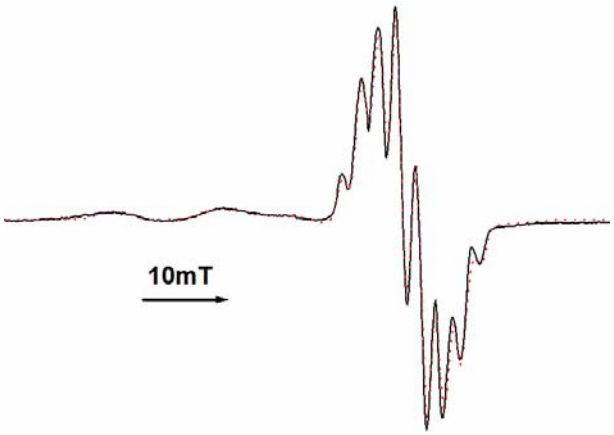

Fig.2. EPR spectrum of photolysed tetrahexylammonia tetrachlorocuprate in 2-chlorobutane at 77 K (Solid line) and simulated spectrum (Dot line)

DFT calculated parameters of model compound **II** are as follows: $g_1 = 2.005$, $g_2 = 2.084$, $g_3 = 2.112$, $A(Cu)_1 = 22.1$ mT, $A(Cu)_2 = 6.9$ mT, $A(Cu)_3 = 3.9$ mT. These parameters were taken as the first approximation for the **2-Cu** experimental spectrum simulation. Alkyl type radicals spectrum was simulated as the superposition of spectra of $CH_3CH(\cdot)CH_2\sim$ radical in potential energy surface minimum and $CH_3CH(\cdot)CH_2\sim$ radical in CH_3-group rotation transition state. First approximations for radical HFCs were also taken from calculation (DFT/PBE0/def2-SVP). **1-Cu** EPR parameters were taken from the literature [15] and were not varied (fig.3, Dash line). The results of simulation are presented in fig.1 (Dot line). **2-Cu** simulated spectrum (fig.3, Solid line) parameters are as follows: $g_1 = 2.005$, $g_2 = 2.084$, $g_3 = 2.112$, $A(Cu)_1 = 22.2$ mT, $A(Cu)_2 = 7.6$ mT, $A(Cu)_3 = 6.8$ mT and are in agreement with the results of DFT calculation.

The comparison of UV-Vis and EPR data, as well as results of DFT and TD-DFT calculations evidences that two paramagnetic compounds produced under photolysis of tetrahexylammonia tetrachlorocuprate solutions earlier denoted as **1-Cu** and **2-Cu** appear to be organochlorocuprates(II): **1-Cu** has general formula $Cu(II)Cl_2R$, where R is $(\text{-}C_6H_{12})N(C_6H_{13})_3^+$, and structure similar to model compound **I** (fig.1, I), **2-Cu** has general formula $Cu(II)Cl_3R$ and structure similar to model compound **II** (fig.1, II)

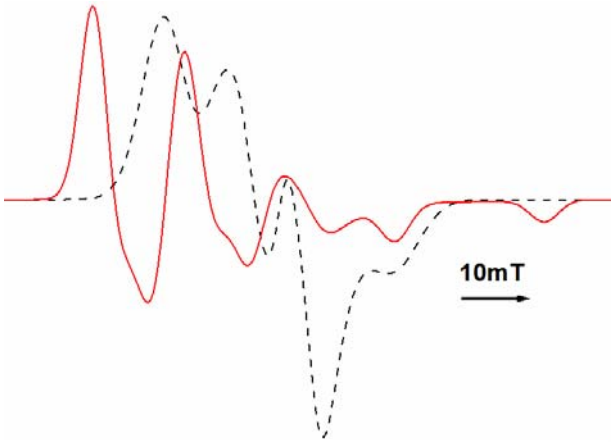

Fig.3. Simulated EPR spectrum of **1-Cu** (Dash line) and **2-Cu** (Solid line)

Acknowledgements

Authors want to acknowledge Prof A.Kh Vorobiev for kindly providing the computer programs for the processing of ESR spectra, Prof. V.F. Plyusnin, , Dr. A.V. Lobanov, Prof. M.Ya. Melnikov, Dr. V.I. Pergushov and Dr. N.A. Chumakova for the help with experiment and useful discussions

The research is partially supported by RFBR Grants 10-03-00603a and 12-03-31130

References

[1] Burg, A.; Meyerstein, D. Inorganic/Bioinorganic Reaction Mechanisms **2012**, 64, 219-261.

[2] Golubeva, E. N.; Kharitonov, D. N.; Kochubey, D. I.; Ikorskii, V. N.; Kriventsov, V. V.; Kokorin, A. I.; Stoetsner, J.; Bahnemann, D. W. *J. Phys. Chem. A* **2009**, 113, 10219-10223.

[3] Eckenhoff, W. T.; Pintauer, T. *Catalysis Reviews.* **2010**, 52, 1-59.

[4] Braunecker, W. A., Matyjaszewski, K. *Prog. Polym. Sci.* **2007**, 32, 93–146.

[5] Clark, A. J. *Chem. Soc. Rev.* **2002**, 31, 1–11.

[6] Ferraudi, G. *Inorg. Chem.* **1978**, 17, 2506-2508.

[7] Cohen, H.; Meyerstein, D. *Inorg. Chem.* **1986**, 25, 1505-1506.

[8] Navon, N.; Golub, G.; Cohen, H.; Meyerstein, D. *Organometallics* **1995**, 14, 5670-5676.

[9] Baumgartner, E.; Ronco, S.; Ferraudi, G. *Inorg. Chem*. **1990**, 29, 4747-4750.

[10] Das, S.; Ferraudi, G. *Inorg. Chem*. **1986**, 25, 1066-1068.

[11] Freiberg, M.; Mulac, W.A.; Schmidt, K.H. *J.C.S. Faraday I* **1980**, 76, 1838-1848.

[12] Golubeva, E. N.; Lobanov, A. V.; Kokorin, A. I. *Russ. J. Phys. Chem. B* **2009**, 3, 179.

[13] Lobanov, A. V.; Golubeva, E. N.; Mel'nikov, M. Ya. *Mendeleev Commun.,* **2010**, 20, 343.

[14] Plyusnin, V. F.; Bazhin, N. M.; Kiseleva, O. B. *Zh. Khim. Fiz.* **1980**, 54, 672-675 (in Russian).

[15] Golubeva, E. N.; Lobanov, A. V.; Pergushov, V. I.; Chumakova, N. A.; Kokorin, I. A. *Dokl. Chem.* (Engl. Transl.) **2008**, 421, 171; *Dokl. Akad. Nauk* **2008**, 421, 630-633.

[16] Karyakin, Yu.V. and Angelov, I.I., Chistye Khimicheskie Veshchestva (Purity Chemicals), Moscow: Khimiya, 1974.

[17] Kharitonov, D.N. and Golubeva, E.N., *Kinet. Katal*. **2003**, 44, 595.

[18] Golubeva, E.N., Kokorin, A.I., Kochubei, D.I., Pergushov, V.I., and Kriventsov, V.V., *Kinet. Katal*. **2002**, 43, 440.

[19] Vorobiev, A.Kh.; Chumakova, N.A. in Nitroxides – Theory, Experiment and Applications, Ed. A. I. Kokorin, InTech, **2012**.

[20] Neese, F. ORCA - an ab initio, DFT and semiemperical programpackage, 2.8 ed.; University of Bonn: Bonn, Germany, 2010.

[21] Szilagyi, R. K.; Metz, M.; Solomon, E. I. *J. Phys.Chem. A* **2002**, 106, 2994–3007.

[22] Weigend, F.; Ahlrichs, R. *Phys. Chem. Chem. Phys.* **2005**, 7, 3297.

[23] Neese, F.; Wennmohs, F.; Hansen, A.; Becker, U. *Chem. Phys.* **2009**, 356, 98–109.

[24] Sinnecker, S.; Rajendran, A.; Klamt, A.; Diedenhofen, M.; Neese, F. *J. Phys. Chem. A* **2006**, 110, 2235-2245.

[25] Abragam, A.; Bleaney, B. Electron paramagnetic resonance of transitionions; Oxford University Press: Oxford, 1970.

[26] Golubeva, E. N.; Gromov, O. I.; Zhidomirov, G. M. *J. Phys. Chem. A* **2011**, 115, 8147–8154.

[27] Gromov, O.I.; Zubanova, E.M.; Golubeva, E.N.; Plyusnin, V.F.; Zhidomirov, G.M.; Melnikov M.Ya. *J. Phys. Chem. A* **2012** *in press*

Hydrophobic and hydrophilic interactions in carboxylic acid aqueous solutions

R.G. Dzhambulatov, A.V. Donets

Faculty of Physics, Saint-Petersburg State University, 198504, Ulyanovskaya Street 1, Petrodvorets, Saint-Petersburg, Russia

e-mail: ren6415@yandex.ru

Introduction

Aqueous solution of ions and organic molecules is a basis of a living tissue. Hydrophobic and hydrophilic interactions play an important role in formation of structure of organic molecules. For example, the carboxylic acids are characterized by uncharged hydrophobic methyl and methylene groups and hydrophilic carboxylic group. One of the most informative techniques of investigation of the hydration characteristic is analysis of concentration and temperature dependences of the spin-lattice relaxation rates.

Experiment and methods

The samples of solution of acetic acid and propionic acid(CH_3-COOH and CH_3-CH_2-COOH respectively)in heavy water were prepared. Measurements of spin-lattice and spin-spin relaxation times of deuterium nuclei were taken on Bruker SPX 4-100.

The water forms ordered structure around acid molecules. In case of the fast exchange of solvent molecules in the solution the relaxation rate of the solvent nucleiis given by the formula [1]

$$\frac{1}{T_1}=\sum_{i=1}^{N-1}\frac{mn_i}{M}\frac{1}{T_{1i}}+\left(1-\sum_{i=1}^{N-1}\frac{mn_i}{M}\right)\frac{1}{T_{10}}, \qquad (1)$$

where m is the molality, M is the number of moles in 1000 grams of solvent, T_{1i} is the solvent nuclei relaxation time in the structure number i, T_{10} is the relaxation timeof free solvent, n_i is the number of molecules in the structure (coordination number).

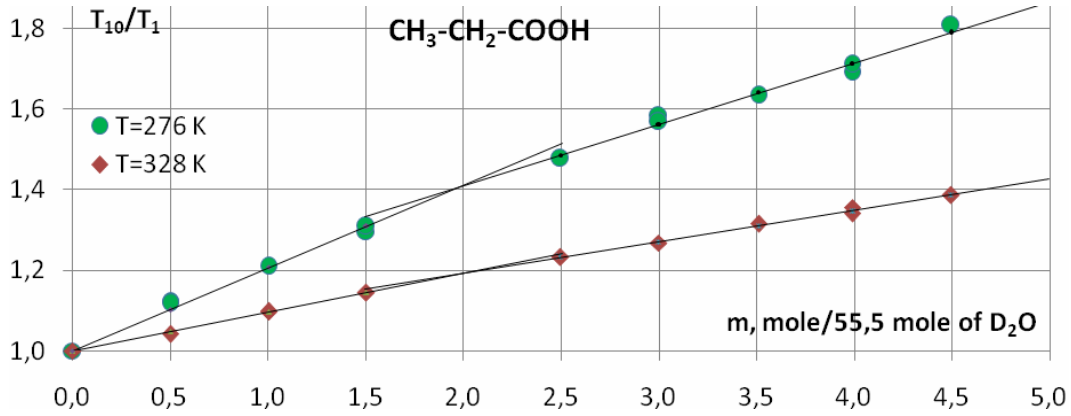

Fig.1. The concentration dependence of deuteron relative spin-lattice relaxation rates in solution of propionic acid.

The temperature dependence of relaxation rate is described by the Arrhenius equation

$$\frac{1}{T_1}=A\cdot\exp\left(\frac{E_a}{RT}\right), \qquad (2)$$

where Ea is the activation energy.

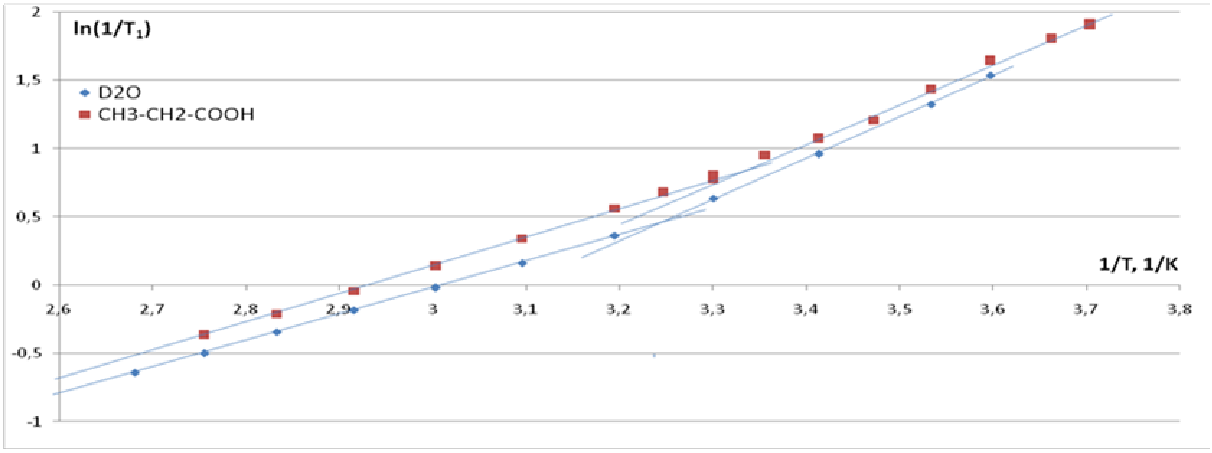

Fig.2. The temperature dependence of deuteron spin-lattice relaxation rates in solution of propionic acid.

Analysis of concentration and temperature dependences gives us information about microstructure of solution: the number of water molecules in hydration shellsof the acids functional groups, activation energy of water molecules in different structures of the solution.For example, the propionic acid differs from the acetic only in themethylene group, we may obtain information about water structure near this group: relaxation and correlation times, coordination number and activation energy.

Results

The result of this work is obtaining of following significant numeral characteristics of hydration of carboxylic acids:

- An acetic acid molecule coordinates 20 molecules of D_2O and propionic acid coordinates 27 ones.
- The coordination number of the CH_2 group is 7. This result agrees with result for amino acids obtained by NMR-relaxation data and quantum chemical calculation.
- For temperature t=5°C and concentration m=1 mole/55.5 moles the relative relaxation rate and relaxation time in structure near CH_2-group are $T_{10}/T_{12}=1.31$ and $T_{12}=164\ ms$. For t=50°C $T_{10}/T_{12}=1.64$ and $T_{12}=518\ ms$.
- Activation energies are

	Low temperature	High temperature
D2O	25,2	16,1
CH3-CH2-COOH	24,4	17,6
CH3-COOH	24,2	18,2

The obtained structure parameters allow us to study the temperature and concentration features of the hydrophobic and hydrophilic interactions between the functional groups and water molecules inthe acid solutions.

References

[1] V. I. Chizhik, NMR relaxation and microstructure of aqueous electrolyte solutions, Mol. Phys., 1997, Vol. 90, No. 4, p. 653-659

Development of New Se-based Chiral Derivatization Reagent for Determination of Enantiomeric Purity of α-Chiral Carboxylic Acids by NMR Spectroscopy

N.V. Orlov, V.P. Ananikov

Zelinsky Institute of Organic Chemistry RAS, Leninsky prosp. 47, 119991, Moscow, Russia.

e-mail: onv@ioc.ac.ru

Determination of enantiomeric purity and absolute configuration of chiral molecules is an important task in modern asymmetric synthesis and catalysis as well as in drug design and investigation of natural compounds [1]. Nowadays NMR spectroscopy has become a powerful tool for analysis of chirality. Though enantiomers cannot be distinguished by NMR spectroscopy itself, they can be converted into magnetically nonequivalent diastereomers by means of chiral derivatizing agents (CDAs), followed by reliable spectral analysis [2]. Recently we have developed convenient derivatization procedure using both well-appreciated CDAs such as MTPA or MPA and newly synthesized Se-based chiral acid for analysis of chiral alcohols and amines which can be performed directly in an NMR tube [3]. No preliminary purification of diastereomers formed is required to obtain various NMR spectra (both 1D and 2D) of high quality which allows determination of enantiomeric purity of chiral alcohols and amines with high accuracy within several minutes including sample preparation time.

Here we wish to present synthesis of novel Selenium-based reagent **1** and its application for determination of enantiomeric purity of α-chiral carboxylic acids. Usually ^{1}H and ^{13}C NMR spectra are quite complicated especially when crude mixtures are to be analyzed. ^{77}Se NMR spectra are superior in assignment of signals, because only peaks of diastereomers are present, and in determination of enantiomeric purity of chiral samples, because NMR scale of ^{77}Se nucleus is much larger compared to ^{1}H and ^{13}C nuclei.

Target CDA **1** was easily synthesized from cheap and readily available (*R*)-2-amino-1-butanol in one step. Derivatization of α-chiral carboxylic acids with **1** was performed directly in an NMR-tube using N,N'-dicyclohexylcarbodiimide (DCC) as a coupling agent (scheme 1). Insoluble particles of dicyclohexylurea formed floated to the top of solution upon centrifugation thus they having no influence on the quality of NMR spectra. Scope and limitations of the procedure developed as well as comparison of spectral data will be presented.

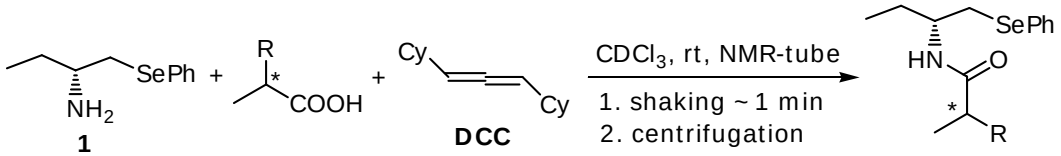

Scheme 1. Derivatization of α-chiral carboxylic acids with modified amine **1** directly in NMR tube.

Acknowledgments

The work was supported by the RFBR grant No. 12-03-01094.

References

[1] A.P., Jin. D., Lee Y.-I., *Appl. Spectroscopy Rev.*, **2009**, *44*, 267–316.

[2] SecoJ.M., Quinoa E., Riguera, R. *Chem Rev.*, **2004**, 104, 17–117; Wenzel T.J., Chisholm C.D., *Progr. Nucl. Magn. Reson. Spectrosc.*, **2011**, *59*, 1–63.

[3] Orlov N.V., Ananikov V.P., *Chem. Commun.*, **2010**, *46*, 3212–3214; Orlov N.V., Ananikov V.P., *Green Chem.*, **2011**, *13*, 1735–1744.

Study of electric field gradients in ZnO by means of high-frequency EPR/ENDOR spectroscopy

Yu.S. Kutin[1], G.V. Mamin[1], S.B. Orlinskii[1], A.P. Bundakova[2], P.G. Baranov[2]

[1]Kazan Federal University, 420008, Kremlyovskaya St.18, Kazan, Russia.

[2]A.F. Ioffe Physico-Technical Institute, 194021, Polytekhnicheskaya 26, St. Petersburg, Russia.

e-mail: yuri_kutin@mail.com

Semiconductor materials with wurtzite structure, e.g., ZnO, typically have intrinsic crystal field gradients that originate within the crystals due to hexagonal symmetry of the lattice [1]. Value of the electric field gradient is a fundamental characteristic of the crystal. It is directly connected to the lattice parameters and the degree of covalence of the crystal bonds. Electron nuclear double resonance (ENDOR) is a sensitive method for measuring crystal field gradients, which is required in case of a low concentration of the nuclei with $I > 1/2$. It is based on observing quadrupole splitting in spectra of paramagnetic ions. Dopant ions with nuclear spins $I > 1/2$ can be used as probes, when introduced into crystallographic sites where the electric field gradient is to be measured. It is important, however, that the distortion of the crystal lattice caused by dopant ions be minimal. In the present work we analyse electric field gradients in ZnO single crystals calculated from ENDOR measurements, as well as some of our results published in [2, 3].

Fig.1 shows EPR spectra of a ZnO single crystal recorded with the magnetic field parallel and perpendicular to the *c* axis. The multitude of narrow EPR lines corresponds to the Mn^{2+} ion. The broader line with the g-tensor values $g_{\|}$=1.9584, $g_{\perp}$=1.9569 originates from the Al shallow donor (SD).

The Hamiltonian used to analyze EPR and ENDOR spectra is

$$\hat{H} = \mu_B \mathbf{B}\mathbf{g}\hat{\mathbf{S}} - g_N \mu_N \mathbf{B}\hat{\mathbf{I}} + A\hat{\mathbf{S}}\hat{\mathbf{I}} + \hat{\mathbf{I}}\mathbf{P}\hat{\mathbf{I}}, \qquad (1)$$

where $\hat{\mathbf{S}}$ and $\hat{\mathbf{I}}$ are the operators of the electron and nuclear spin respectively, **g**-tensor denotes the anisotropic g-factor. The second, third and forth terms stand, respectively, for the Zeeman interaction of the nuclear magnetic moment, the hyperfine (HF) interaction with the isotropic constant *A*, and the quadrupole interaction represented by the **P** tensor; μ_B is the Bohr magneton, μ_N and g_N are the nuclear magneton and the nuclear *g*-factor, respectively. In the case of the axial symmetry the quadrupole term in (1) can be written as $P\left[I_Z^2 - (1/3)I(I+1)\right]$, where $P = 3/2P_{ZZ} = 3q$.

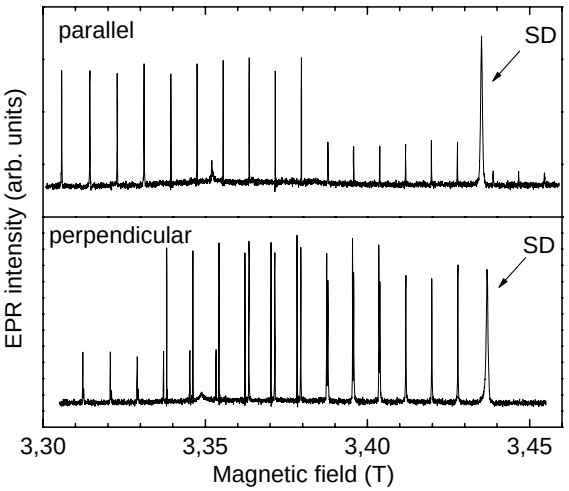

Fig.1. EPR spectrum of the Mn^{2+} ion a ZnO single crystal recorded with the magnetic field parallel and perpendicular to the *c* axis. T = 6 K, f ~ 94.1 GHz.

Conditions of ENDOR with the selection rules $\Delta M_S = 0, \Delta m_I = \pm 1$ for the

isotropic HF interaction and the axial symmetry of the quadrupole interaction, which is the case in our experiments, are given by

$$hf_E = \left| g_N \mu_N B_0 \pm M_S A + 3 m_q q (3\cos^2\theta - 1) \right|, \quad (2)$$

where the first term is the nuclear Zeeman energy, A is the isotropic HF interaction constant, m_q=1/2(m_I+$m_{I'}$) is the average value of the two nuclear angular momentum projections m_I and $m_{I'}$, between which the nuclear transition takes place, θ is the angle between the c axis of the crystal and the external magnetic field direction;

$$q = eQ_0 V_{ZZ}(r_i)/[4I(2I-1)] \quad (3)$$

where Q_0 is the electric quadrupole moment of the nucleus in multiples of $|e|$x10^{-24} cm^2 and $V_{ZZ}(r_i)$ is the electric field gradient. Therefore, experimental determination of the quadrupole splitting in ENDOR spectra makes it possible to directly obtain the electric field gradient at the position of the nucleus under study. In the present work we examine quadrupole interactions of the ^{27}Al, ^{67}Zn, and ^{55}Mn nuclei, whose nuclear spin I = 5/2, and there are five m_q values: $m_q = \pm 2, \pm 1$ and 0.

To account for the fine structure of the EPR spectrum, the following term should be added to the Hamiltonian (1) in the case of an axial crystal field: $\hat{\mathbf{S}}\mathbf{D}\hat{\mathbf{S}} = D\left[S_Z^2 - (1/3)S(S+1)\right]$, where $D = (3/2)D_{ZZ}$.

The electron spin of the Mn^{2+} ion $S = 5/2$ and the nuclear spin of ^{55}Mn (natural abundance 100%) $I = 5/2$. Thus, the Mn^{2+} EPR spectrum consists of 5 groups of fine structure; each of them is composed out of 6 lines of hyperfine structure. Fig.1 shows parts of this spectrum. The angular dependence of the spectrum is consistent with the results for the axial symmetry of the crystal field.

Fig.2 shows ENDOR spectra of the Mn^{2+} ions in the ZnO single crystal. The spectra were recorded in the electron transition $M_S = -1/2 \leftrightarrow M_S = 1/2$ for the three values of the nuclear spin projections: $m_I = -5/2, +1/2, +5/2$. The left part of fig.2 shows a fragment of the EPR spectrum of Mn^{2+} recorded with the magnetic field parallel to the c axis. Arrows show the EPR lines of the manganese hyperfine structure, on which the ENDOR spectra were recorded.

In the spectra recorded on the first and last EPR lines of the $M_S = -1/2 \leftrightarrow M_S = 1/2$ sextet (i.e. on the lines with $m_I = -5/2$ and $m_I = +5/2$), only two ENDOR lines are present. This is because in these two cases there is only one radiofrequency transition that is allowed under the selection rule $\Delta M_S = 0, \Delta m_I = \pm 1$ for each of the M_S values. The energy level

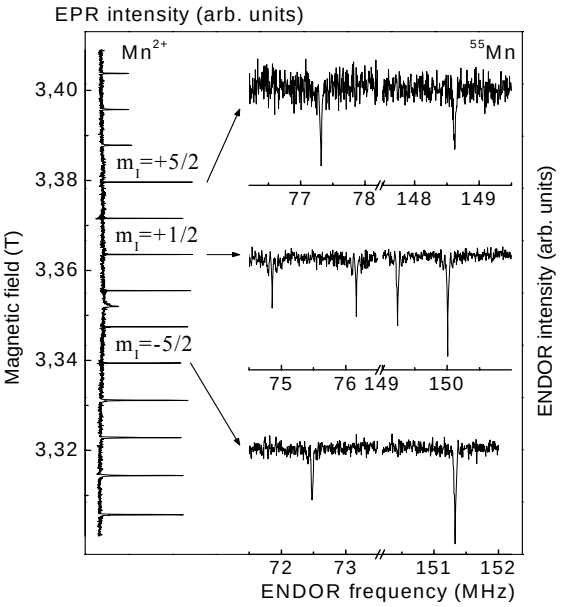

Fig.2. (Right) ENDOR spectra of Mn^{2+} in ZnO, recorded in the electron transition $M_S = -1/2 \leftrightarrow M_S = 1/2$ for m_I= -5/2, 1/2, 5/2. (Left) Fragment of the EPR spectrum of Mn^{2+} recorded at around 94.1GHz at T = 6 K (the magnetic field is parallel to the c axis).

diagram is shown in fig.3. In the ENDOR spectrum recorded on the $m_I = +1/2$ line, the quadrupole splitting is present, since in this case four radiofrequency transitions are allowed (two for each of the M_S values).

The diagram successively takes into account Hamiltonian terms of decreasing magnitude. The absolute value of the HF interaction constant of Mn^{2+} in ZnO is 220 MHz [4]. The sign of the constant is assumed to be negative based on the known effect of core polarization, which leads to an incomplete coupling of s-electrons of inner shells [5]. The Larmor frequency $f_L(^{55}Mn)$ in W-band is around 37 MHz. Solid arrows show EPR transitions at which the ENDOR spectra of ^{55}Mn were recorded. Dashed arrows within the M_S manifolds show the corresponding ENDOR transitions.

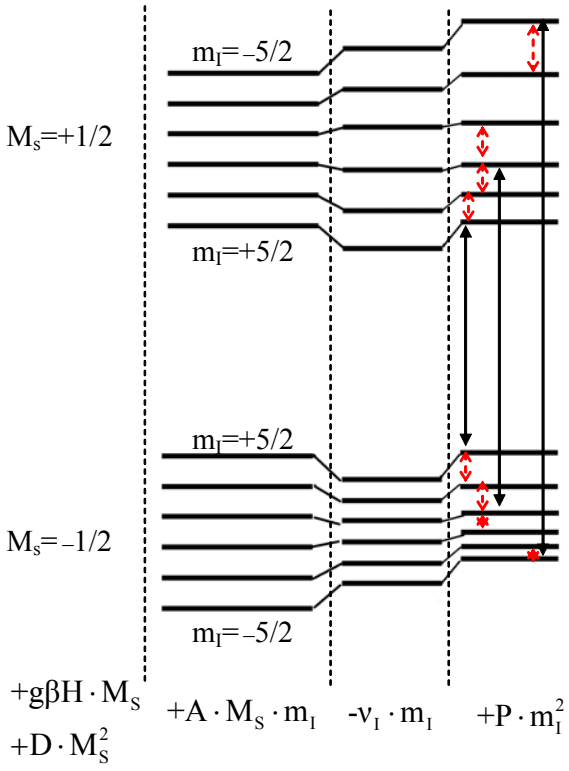

Fig.3. Part of the energy level diagram of Mn^{2+} (S=5/2, I=5/2) in ZnO.

In first-order calculations based on the expression (2) the quadrupole splitting between the ENDOR lines should be $2P$ for both $M_S = -1/2$ and $M_S = +1/2$. In our measurements, however, the splitting values are different: 0.774 and 1.308 MHz. Therefore, the second order corrections should be taken into account:

$$E^{(2)}(M_S, m_I) = \frac{A^2}{2g\beta H}\left[M_S\left(I(I+1) - m_I^2\right) - m_I\left(S(S+1) - M_S^2\right)\right] \qquad (4)$$

These corrections have the opposite signs for $M_S = -1/2$ and $M_S = +1/2$: $2F + A^2/2g\beta H$ and $2F - A^2/2g\beta H$. Thus $4P$=(0.774+1.308) MHz, i.e. $2P$=1.041 MHz. From these considerations it also follows that $A^2/g\beta H = (1.308 - 0.774)\text{MHz} = 0.534\,\text{MHz}$ (which corresponds well with $|A| \sim 220$ MHz and $f \sim 94.1$ MHz). The electric field gradient at the manganese nuclei substituting zinc is calculated from the expression (3) using $Q(^{55}Mn)$=0.33: $V_{ZZ}(^{55}Mn) = 8.697 \cdot 10^{20}$ V/m^2.

Now consider the Al shallow donor line also present in fig.1. Fig.4 shows ENDOR spectra recorded in this EPR signal. These spectra reveal interaction of the shallow donor electron with its own ^{27}Al nucleus (a) and with the magnetic ^{67}Zn nuclei (b) placed at distances up to several nanometers around the SD core. These spectra were previously discussed in [2]. The quintet structure of the ENDOR spectrum in fig.4 (a) is due to the quadrupole interaction

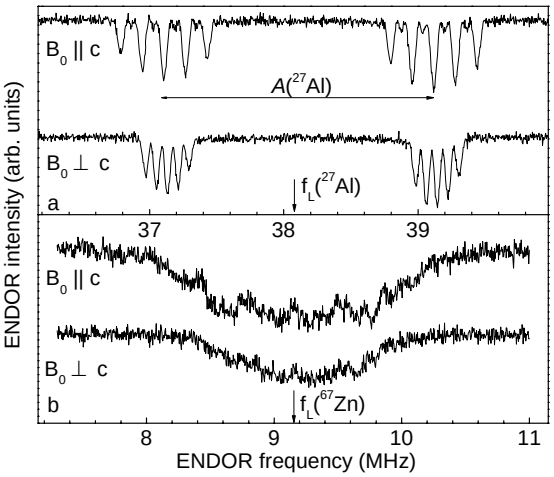

Fig.4. ENDOR spectra of (a) ^{27}Al and (b) the ^{67}Zn nuclei recorded via ESE signal of the shallow Al donor in two orientations of the magnetic field at W-band. $T = 15$ K.

with the ^{27}Al nuclei (I = 5/2). For the electron spin S = 1/2 there are two quadrupole quintets placed symmetrically around the nuclear Zeeman frequency, whose centers of gravity are separated by a distance equal to the isotropic HF interaction constant. The angular dependence of the observed quadrupole structure is typical for the case of the axial symmetry along the c axis. The quadrupole splitting goes to zero at the angle $\theta = 54.7°$, as seen from the expression (2).

It was shown in [2] that in the parallel spectrum of ^{27}Al, the spacing between the lines equals $\nu_Q = \frac{3eQ_{Al}V_{ZZ}(\mathrm{Al})}{2I(2I-1)h} = 161\ \mathrm{kHz}$, where $Q(^{27}\mathrm{Al})$=0.1466 and I = 5/2. From this, the electric field gradient at the ^{27}Al nucleus can be calculated: $V_{ZZ}(^{27}\mathrm{Al}) = 3.027 \cdot 10^{20}\ \mathrm{V/m^2}$.

The ENDOR spectrum of ^{67}Zn shown in fig.4 (b) can be used in a similar manner to calculate the electric field gradient at the zinc site. The obtained value is $V_{ZZ}(^{67}\mathrm{Zn}) \approx 6.51 \cdot 10^{20}\ \mathrm{V/m^2}$.

Experimental results are shown in the table. It contains the HF and quadrupole interaction constants, and the electric field gradients, calculated based on the expression (3). The gradient at the ^{55}Mn nuclei is only around 30% higher than that on ^{67}Zn. At the same time, the electric field gradient value on ^{55}Mn is 2.9 times larger then that on the ^{27}Al nuclei.

	nucleus	A (MHz)	$2P$ (MHz)	eQ_0V_{ZZ}/h (MHz)	V_{ZZ} (V/m^2)
ZnO, single crystal	^{27}Al	2.01	0.161	1.073	$3.027 \cdot 10^{20}$
	^{55}Mn	~220	1.041	6.940	$8.697 \cdot 10^{20}$
	^{67}Zn		0.354	2.360	$\sim 6.51 \cdot 10^{20}$

It is shown, therefore, that the Mn^{2+} ions with a stable half-filled 3d shell in the ^{6}S state can be used to probe crystal field gradients. Substitution of Zn^{2+}, an ion with a filled shell (1s state), by Mn^{2+} does not result in a significant change in the electric field gradient at the zinc site, since both systems have a zero orbital momentum. It is likely that the Mn^{2+} ion, which is easily incorporated into condensed materials, including biological systems, can be used as a probe to measure crystal field gradients. Substitution of Zn by Al results in a formation of a shallow donor bearing an excess charge of the unpaired electron. In ZnO single crystals this leads to reduction of the electric field gradient more than by the factor of two, compared to the intrinsic gradient at the zinc position in a ZnO single crystal.

This work was supported in part by the Ministry of Education and Science of the Russian Federation (contract nos. 14.740.11.0048 and 16.513.12.3007), by the Russian Academy of Sciences (programs “Spin Phenomena in Solid State Nanostructures and Spintronics” and “Foundations of Nanotechnologies and Nanomaterials”), and by the Russian Foundation for Basic Research. The measurements were partly carried out in the Federal Center of Shared Facilities, Kazan Federal University, in the framework of the federal program “Research and Development in Priority Fields of the Russian Scientific and Technological Complex for 2007–2012.” The authors thank Edward Lavrov and Jörg Weber for supplying the ZnO samples.

References

[1] G. Denninger and D. Reiser, Phys. Rev. B **55**, 5073 (1997).
[2] F. Herklotz, E.V. Lavrov, J. Weber, et al., physica status solidi (b), Vol. 248, Issue 6, pp. 1532–1537, (2011).
[3] Yu.S. Kutin, G.V. Mamin, S.B. Orlinskii, A.P. Bundakova, P.G. Baranov JETP Letters V 95, Issue 9, 2012, P. 471-475
[4] A. Hausmann and H. Huppertz, J. Phys. Chem. Solids 29, 1369 (1968)
[5] A. Abragam, B. Bleaney, *Electron Paramagnetic Resonance of Transition Ions* (Clarendon, Oxford, 1970).

Nuclear pseudo quadrupole resonance of ^{141}Pr in Van Vleck paramagnet PrF_3

A.S. Alexandrov, A.V. Egorov

Kazan Federal University, 420008, Kremlevskaja st. 18, Kazan, Russia Federation.

e-mail: alexandrov.artem.sergeevich@gmail.com

By present time were done several investigations of PrF_3 Van Vleck paramagnet nuclear magnetism. NMR [1] and NAR [2] of ^{141}Pr nucleus in PrF_3 were observed in 1979. Then in 2006 the temperature dependence of magnetic susceptibility in wide range of temperatures were obtained [3] and the crystal field parameters were calculated. Recently there were done investigations of magnetic coupling between ^{141}Pr and ^{3}He nuclei in the "PrF_3 – liquid ^{3}He" system. In 2007 it was discovered [4]. The magnitude of such coupling has a strong dependence from a contact surface [4]. Possibility of synthesizing a micro- and nano-sized powders without defects [4] and a large nuclear magnetic moment of Pr makes PrF_3 a good system for dynamic nuclear polarization of ^{3}He [5], which is applied in the lungs MRI. However, NMR in PrF_3 nanocrystals [6] didn't show that coupling.

In the case of the Van Vleck ion the enhanced nuclear magnetism is observed [1]. The effective Hamiltonian containing only nuclear spin operators then looks like [1]

$$H = -\hbar\sum_{\alpha}\gamma_{I\alpha}H_{\alpha}I_{\alpha} + D\left(I_z - \frac{1}{3}I(I+1)\right) + E\left(I_x^2 - I_y^2\right), \qquad (1)$$

where $\alpha = x, y, z$, $\gamma_{I\alpha}$ is the effective gyromagnetic ratio, the D and E parameters contains two contributions: $D = D_{hf} + D_Q$, $E = E_{hf} + E_Q$, the Q index is corresponded to the quadrupole contribution, *hf* — the pseudo quadrupole, which is defined by the hyperfine interaction.

An NMR spectrum of ^{141}Pr in PrF_3 is characterized by a strong anisotropy of ^{141}Pr effective magnetic moment and by a zero-field splitting, which is due to the quadrupole and the pseudo quadrupole interactions. The parameters of the ^{141}Pr spin Hamiltonian in PrF_3 single crystal were carried out in [1]. These parameters are defined by the CEF. Calculations of spectra [6], which were done using these parameters tell that the CEF in the nanocrystals is different from the macrocrystals. In paper [1] also is shown that in the zero field the pseudo quadrupole interaction is dominate. It seems reasonable to call zero-field NMR of ^{141}Pr in PrF_3 nuclear pseudo quadrupole resonance (NPQR).

The NPQR of ^{141}Pr in PrF_3 was not observed later. The cause of this is apparently a very fast spin-spin relaxation. The NPQR investigations of ^{141}Pr in PrF_3 allow us to directly determine the parameters of the pseudo quadrupole Hamiltonian, spin-lattice and spin-spin relaxation times, which will be useful to correct NMR spectra simulations and help to find a magnetic coupling between ^{3}He and ^{141}Pr nuclei in nanocrystals. Either, the frequency of transitions and the line widths are presented in this work. They allow us characterize the CEF.

There is no one solution about the space group of PrF_3 crystal. The neutron scattering tells about C_{6v}^3 (P 6_3 c m) group and C_s local symmetry of Pr^{3+} ion [7, 8]. The x-ray scattering suggests D_{3d}^4 (P $\bar{3}$ c 1) group and C_2 local symmetry [9, 10]. The CEF of a low symmetry splits the ground multiplet $^{3}H_4$ of Pr^{3+} ion into nine singlets. The energy gap between the ground state and the first exited state measured by neutron scattering equals 59.5 cm^{-1} [5]. There is one natural isotope of a praseodymium — ^{141}Pr, with 100% abundance, nuclear spin

I = 5/2, and gyromagnetic ratio $\gamma_I / 2\pi = 1.26$ kHz/Oe. An NMR spectrum is described by the Hamiltonian (2) with the parameters $D/h = 4.31(1)$ MHz, $E/h = 0.30(1)$ MHz; $\gamma_x / 2\pi = 3.32(2)$ kHz/Oe, $\gamma_y / 2\pi = 3.24(2)$ kHz/Oe, $\gamma_z / 2\pi = 10.03(5)$ kHz/Oe [1]. In the zero external magnetic field the system Hamiltonian contains only two last terms of (2). There should be three energy levels with mixed wave functions (if E = 0 they are $|\pm 1/2\rangle$, $|\pm 3/2\rangle$, $|\pm 5/2\rangle$). So we will call the transitions by low frequency transition (LF) and high frequency transition (HF).

Three samples of PrF_3 were studied in present work by the NPQR method. The sample A is a single crystal grown by Bridgmen-Stockbagger method in the magnetic-resonance spectroscopy laboratory (MRS) of Kazan Federal University (KFU). The sample B is a micro-sized polycrystalline powder obtained by a mechanical fragmentation of the single crystal in a sapphire mortar and then bolting (bolt cell diameter — 45 μm). The crystallites size — 10 – 45 μm. The sample C is a nano-sized poly-crystal powder synthesized from a praseodymium oxide by the method described in [6]. The crystallites size — 22 – 40 nm.

All experiments were done at 4.2 K on the spectrometer, built in the MRS laboratory of KFU. The spectra were measured by spin echo intensity with help of a standard Hahn sequence. Spin-lattice and spin-spin relaxation times were measured with help of well known pulse sequences. The spectral lines have Gauss shape, so in order to obtain the parameters, they were approximated with a gauss functions. As the line width parameter we use dispersion σ.

Measured data for the all samples is presented in the table 1. The NPQR spectrum of ^{141}Pr in the sample A is presented at the fig.1. The lines widths are equal for both LF an HF. So it is reasonable to assume, that this width is defined by a dipole-dipole interaction with the 11 neighbouring fluorine nuclei. The fluorine nucleus has a big magnetic moment $^{19}\gamma / 2\pi = 4.007$kHz/Oe, I=1/2. Moreover, this assumption is confirmed by the fact, that the relaxation of a transverse magnetization is well fitted by a gauss-like function $A(2\tau) = A(0)\exp\left(-(2\tau)^2 / 2T_2^2\right)$, where τ is an interval between scanning pulses.

Table 1. The spectra parameters.

Sample	Line	f, MHz	σ, MHz	T_1, ms	T_2, μs	D, MHz	E, MHz
A	LF	9,063 ± 0,009	0,134±0,003	2,26 ± 0,42	10,37 ± 0,07	4,311±0,000	0,314±0,006
	HF	17,083 ± 0,003	0,128±0,001	10,49 ± 0,75	13,79 ± 0,06		
B	LF	9,036 ± 0,015	0,135±0,001	2,89 ± 0,40	9,88 ± 0,09	4,31±0,01	0,31±0,01
	HF	17,072 ± 0,006	0,130±0,002	10,20 ± 0,31	13,04 ± 0,05		
C	LF	9,9±0,2	1,16±0,05	2,21 ± 0,96	14,78 ± 0.05	4,2±0,1	0,6±0,1
	HF	16,4± 0,3	1,74±0,08	7,25 ± 0,54	17,87 ± 0,27		

The spectra for the B and C samples are presented at the fig.2. It is clearly seen that the sample B is almost equal to the sample A by the all parameters. On the other hand the spectrum of the sample C is completely different. The lines peaks are shifted. This may be explained by lowering Pr^{3+} local symmetry. The line widths in the sample C are wider more than 10 times. This could be explained only by increased the CEF inhomogeneity. Nevertheless, spin-spin relaxation time T_2 in the sample C is longer quite a bit. This fact tells that the CEF changes smoothly along the crystallite, so the neighbouring nuclear spins lay in the equal CEFs. Moreover, the lines are asymmetric. We don't have any model for the line

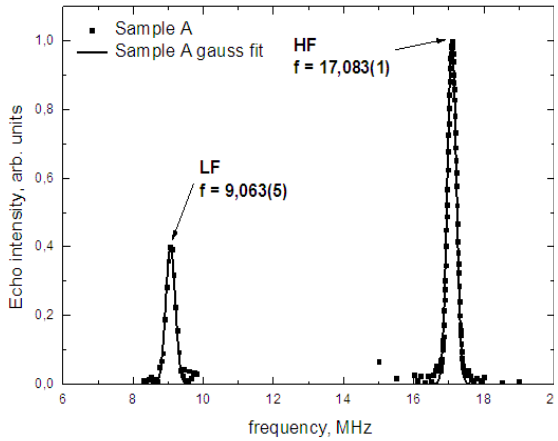

Fig.1. Sample A ^{141}Pr NPQR spectra

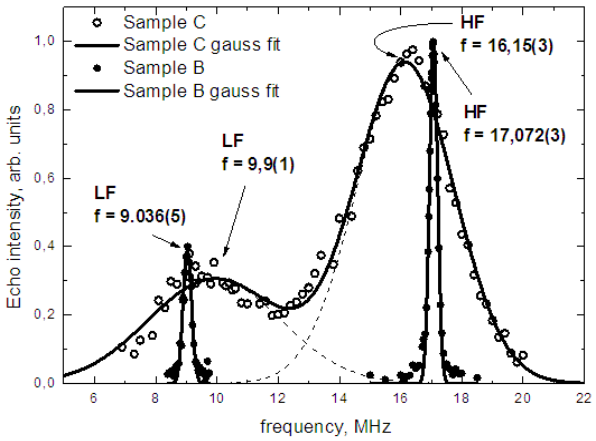

Fig.2. Sample B and C ^{141}Pr NPQR spectra

widen by CEF inhomogeneity, so the sample C spectra were also fitted with the Gauss function.

The relaxation of longitudinal magnetization is well fitted by a "stretched" exponent $A(t) = A(\infty)\exp\left(-\sqrt{t/T_1}\right)$, where t is an interval between the saturation pulse and the scanning sequence. This tells that spin-lattice relaxation is probably goes through the impurity paramagnetic centers Nd^{3+}, Gd^{3+}, Er^{3+}, Dy^{3+} and others. The EPR investigation of PrF_3 [11] determine that the impurity concentration is about 0,01%.

Although, temperature dependence of spin-lattice relaxation rate in the sample A was carried out. It is shown at the fig.3. The main feature of this dependence is the constant rate below 4K at both transitions. For the LF transition (filled rounds) dependence is well fitted by

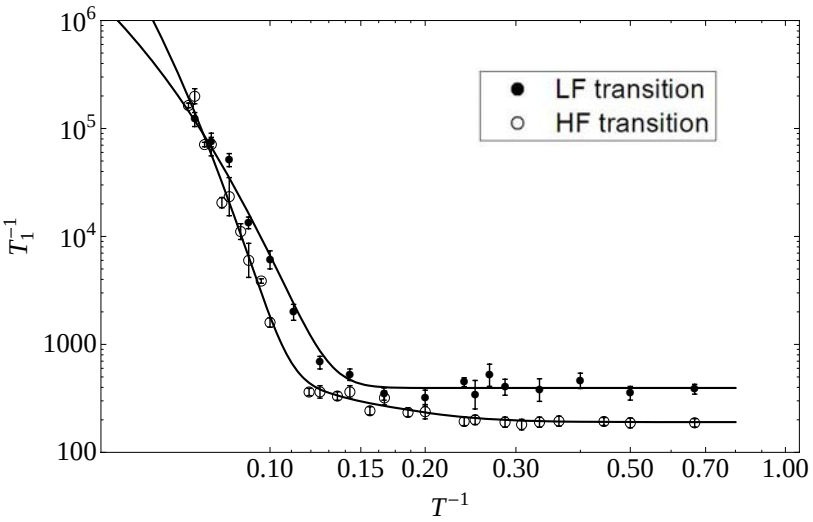

Fig.3. Temperature dependence of spin-lattice relaxation rate in sample A

$T_1^{-1} = A + B\exp\left(-\Delta/T\right)$ function with parameters A = 395 ± 19 c^{-1}, B = (1.8 ± 0.1)·10^8 c^{-1}, Δ = 103 ± 6 K (solid line). So the relaxation rate is determined by the Orbach-Aminov process. The Δ parameter is well agreed with the energy of the first exited CEF level [12]. For the HF transition (blank rounds), however there is another growth, which could be described with one more exponent term only (A = 191 ± 2 c^{-1}, B = (1.5 ± 0.1)·10^{10} c^{-1}, Δ = 163 ± 9 K, C = (1.7 ± 0.2)·10^3 c^{-1}, Λ = 18 ± 5 K. Further investigations is needed to determine cause of this growth

The NPQR in the Van Vleck paramagnet PrF_3 were observed for the first time. The spectra were obtained for the three samples that have different dispersity. The peak frequencies, the line widths, relaxation times T_1, T_2 were measured. Using these, the D, E, parameters of the spin Hamiltonian were calculated. Were shown, that the line width in the samples A and B is defined by a dipole-dipole interaction with the ^{19}F nuclei. The both line width in the sample C may only be defined by the CEF inhomogeneity. Further investigations are needed to find out this mechanism and the CEF dependence by the crystallite size.

References

[1] Большаков И.Г., Теплов М.А. *Ядерный магнитный резонанс ^{141}Pr в PrF_3* / Большаков И.Г., Теплов М.А. // – Казань, 1979 – 19 с. – Деп. в ВИНИТИ № 1274-79.

[2] Альтшулер С.А., Дуглав А.В., Хасанов А.Х. *Ядерный акустический резонанс ^{141}Pr в Ван-флековском парамагнетике PrF_3* / Альтшулер С.А., Дуглав А.В., Хасанов А.Х.// Письма в ЖЭТФ – 1979. – Т. **29** – С. 680-683.

[3] *PrF_3 Van Vleck paramagnet as a promising material for the nuclear dynamic polarization of ^3He* / Savinkov A.V., Suzuki H., Egorov A.V., Tagirov M.S., Tayurskii D.A., Safiullin K.R., Irisov D.S. // Journal of Physics: Conference Series – 2006 – Vol. **51** – P. 79-82.

[4] *Observation of magnetic coupling between the nuclei of liquid ^3He and the ^{141}Pr nuclei of PrF_3 crystalline powder* / Egorov A.V., Irisov D.S.,Klochkov A.V., Savinkov A.V., Safiullin K.R., Tagirov M.S., Tayurskii D.A., Yudin A.N. //, JEPT Letters, – 2007 – Vol. **86** – P. 475–478.

[5] Tagirov M.S., Tayurskii D.A. *A possibility of dynamic nuclear polarization by using of Van Vieck paramagnets* / Tagirov M.S., Tayurskii D.A. // JETP Lett., 1995,V.61,P.652-656.

[6] *Spin Kinetics of ^3He in Contact with Synthesized PrF_3 nanoparticles* / Tagirov M.S., Alakshin E.M, Gazizulin R.R., Egorov A.V.,·Klochkov A.V., Korableva S.L., Kuzmin V.V.,·Nizamutdinov A.S., Kono K., Nakao A., Gubaidullin A.T. // Journal of Low Temperature Physics – 2011 – Vol. **162** – P. 645-652.

[7] C. De Rango, G. Tsoucaris, C. Zelwer, *Determination de la structure du fluorure de lanthane LaF_3* // C.R. Acad. Sci. Paris – 1966 – ser. C **263** – P. 64-66.

[8] *The structure of LaF_3 – a single-crystal neutron diffraction study at room temperature* / Gregson D., Catlow C.R.A., Chadwick A.V., Lander G.H., Cormack A.N., Fender B.E.F. // *Acta Cryst.* – 1983 – Vol. **39 –** P. 687-691.

[9] Zalkin, A. *The atomic parameters in LaF3 structure* / Zalkin A., Templeton D.H., Hopkins T. E. // Inorg. Chem. – 1966 – Vol .5, №8. - P. 1466-1470.

[10] Zalkin A., Templeton D.H. *Refinement of the trigonal crystal structure of lanthanum trifluoride with neutron diffraction data* / Zalkin A., Templeton D.H. // Acta Cryst. – 1985 – Vol. **41** – P. 91-93.

[11] *The Study of the System "Van Vleck Paramagnet PrF3 – Helium-3"* / Egorov A.V., Irisova D.S., Klochkov A.V., Konoc K., Kuzmin V.V., Safiullin K.R., Tagirov M.S., Tayurskii D.A., Yudina A.N. // Journal of Physics: Conference Series – 2009 – Vol. **150** – 032019.

[12] M. Dahl, G. Schaack, *Tysonite Structure and Crystal-Field Analysis of the Pr^{3+} Ion in PrF_3* / M. Dahl, G. Schaack // Z.Phys.Cond.Matt – 1984 – Vol. **56**, P. 279.

Magnetic system for NMR logging tool using cryogenic technologies

E.M. Alakshin, R.R. Gazizulin, A.V. Klochkov, V.E. Kosarev, V.V. Kuzmin,
D.K. Nourgaliev, A.M. Sabitova, T.R. Safin, V.D. Skirda, M.S. Tagirov

Kazan (Volga region) Federal University, 420008, Kremlevskaya 18, Kazan, Russia

e-mail: imfador@gmail.com

The magnetic system for NMR logging tool using cryogenic technologies is used in the geophysical methods of the borehole explorations. The main idea of our invention is using material with high specific heat material at low temperatures for supporting low temperature required to maintain the solenoid in the superconducting state. NMR logging tool based on high-field of superconducting magnet using cryogenic technologies is designed for determination the composition and the amount of fluid in the area outside the borehole by recording and processing the NMR signal. With the using cryogenic technologies the intensity of the magnetic field produced by superconducting magnet will be increased. In consequence, the depth of borehole exploration (the distance from the axis of the borehole) will be increased, too.

There are some technical solutions that were proposed to use trapped field magnets (TFMs) on an NMR logging tool. Such magnets are used to produce a static magnetic field in a formation surrounding a borehole. The TFMs are made of material having a high T_c, so that the magnetic field can be sustained for the duration of the well logging by enclosing the TFMs within a cryostat containing liqiud nitrogen as a coolant. By using the TMFs, the field strength within this region is much higher than is attainable with conventional magnets, giving an improved signal to noise (S/N) ratio for the NMR signals. The magnetic field strength within the TFMs is kept at a low enough value that instability problems associated with these materials do not arise. The field strength may be selected based upon knowledge of the resistivity and dielectric constant of the formation and the associated skin depth for electromagnetic signals. This makes it possible to use the TFMs in both wireline and measurement while drilling (MWD) environments [1].

The proposed solution is in implementation of logging tool in the field of a superconducting magnet with cryogenic technologies. Magnetic system consists of one or two solenoids, which are wound by a high-temperature superconductor, placed in a cryostat, operating on the principle of cryo-accumulator. The magnetic system is being pre-cooled to liquid helium temperature (-269 ^{0}C or 4 K) before the descent in borehole. The magnetic field is frozen by a superconducting key, which is also made of high-temperature superconductor. After that, liquid helium is being extracted from the system, cryostat is being evacuated and lowered into the borehole.

It is proposed to use the substance with the lowest Debye temperature as a material for cryo-accumulator. The Debye temperature for the different materials is shown in Table 1.

Table 1 shows, that the lead has the lowest Debye temperature. Consequently, this substance has the highest specific heat at low temperatures. It is confirmed by the reference data[2]. The experimental warm-up plot for the lead sample is presented in fig.1. The photo of the model of the lead cryo-accumulator is shown in fig.2.

Table 1.

Substance	θ_D, K
Diamond	1860
Silica	647
Iron	420
Aluminum	390
Copper	315
Germanium	290
Silver	215
Lead	88

The presented results are claimed as intellectual property (Patent № 117648. Magnetic system for NMR logging tool using cryogenic technologies. Patentees: KFU and "TNG-GROUP" Authors: Alakshin E.M., Gazizulin R.R., Klochkov A.V., Kosarev V.E., Kuzmin V.V., Nourgaliev D.K., Skirda V.D., Tagirov M.S., Application for invention № 2011127783, 06.07.2011. Magnetic system for NMR logging tool using cryogenic

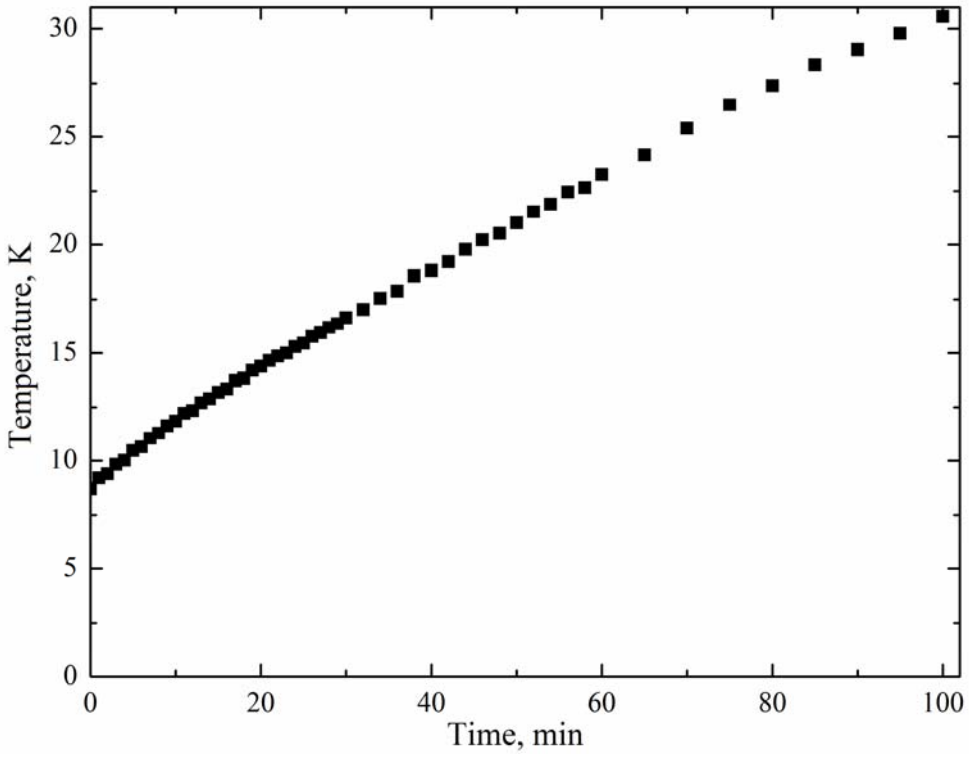

Fig.1. Temperature dependence of lead sample (weight 2.8 kg) warm-up time, pre-cooled down to 7 K

technologies, the application for invention 2011127783, 06.07.2011. Authors: Alakshin E.M., Gazizulin R.R., Klochkov A.V., Kosarev V.E., Kuzmin V.V., Nourgaliev D.K., Skirda V.D., Tagirov M.S.).

Fig.2. The model of the lead cryo-accumulator

Acknowledgments

This work was supported by the Ministry of Education and Science of the Russian Federation (project no.13.G25.31.0025).

References

[1] Patent US № 6,411,087 B1, 25.06.2002.

[2] M.P. Malkov, I.B. Danilov, A.G. Zeldovich, A.B. Fradkov, Reference book of physical-technical basis of deep cooling - state energy publishing. 1963.

Temperature dependence of the magnetic penetration depth and multicomponent order parameter in the $YBa_2Cu_3O_{7-\delta}$

D.A. Sunyaev, M.V. Eremin

Kazan (Volga region) Federal University, Institute of Physics, Kremlevskaya 18, Kazan 420008, Russian Federation.

e-mail: dasforrum@rambler.ru

Abstract

We have analyzed the temperature dependencies of the superfluid density in $YBa_2Cu_3O_7$ along a- and b- crystallographic axes using the multicomponent order parameter for the superconducting gap. Estimated values of the gap components for the d-wave and the isotropic s-wave are $\Delta_d = 29$ meV and $\Delta_s = 5$meV correspondently. Band structure parameters were taken accordingly ARPES and neutron scattering data.

Keywords: Superconductivity, multicomponent order parameter, superfluid density

Introduction

Intensive studies of HTSC cuprates by different experimental methods displayed the unbelievable complexity of these materials [1]. Telplov et al. [2, 3] at early stages of HTSC activity have demonstrated that even most perfect compounds $TmBa_2Cu_4O_8$ show an anomalies in Tm –NMR line width at $T<T^*$. Afterwards, Müller and Keller [4] pointed some evidence that HTSC cuprates are unconventional superconductors with multicomponent order parameter. For now this intriguing phenomena is under debate of many studies [5, 6]. In this paper we focus on the temperature dependence of the superfluid density in orthorhombic $YBa_2Cu_3O_{6.98}$ reported in [7] and show that this data allows us to extract the relative value of s- and d- component of superconducting gap. It is clear that in addition to other possibilities to measure the multicomponent order parameter (via ARPES [8], by neutron scattering [9, 10] tunneling experiments [11, 12], or via Raman [13] spectroscopy) it will give us a new information about the nature of interactions yielding the superconducting pairing.

Temperature dependencies of the superfluid density

Our calculations are based on the energy dispersion for carriers in CuO_2 plane, which has been extracted from ARPES data [9]. The general expression for the superfluid density was discussed for details in paper [14]. It is written as follows

$$\frac{1}{\lambda^2} = 4\pi\left(\frac{e}{c\hbar}\right)^2 \left\{\sum_k \frac{\partial\varepsilon_k}{\partial k_x}\left[\frac{|\Delta_k|^2}{E_k^2}\frac{\partial\varepsilon_k}{\partial k_x} - \frac{(\varepsilon_k-\mu)}{2E_k^2}\frac{\partial|\Delta_k|^2}{\partial k_x}\right]\left[\frac{1}{E_k} - \frac{\partial}{\partial E_k}\right]\tanh\left(\frac{E_k}{2k_BT}\right)\right\}. \quad (1)$$

Here it is assumed that the field is applied along the *x*-axis in CuO_2-plane (ab). ε_k is the energy dispersion for quasiparticles in the normal state, μ — chemical potential, $E_k = \sqrt{(\varepsilon_k-\mu)^2 + |\Delta_k|^2}$ — Bogolubov's quasiparticles energy in the superconducting state, Δ_k is the energy gap, which depends on wave vector and temperature. Energy dispersion has been taken in form [9]:

$$\varepsilon_k = \mu + \frac{t_1}{2}(1+\delta)\cos k_x + \frac{t_1}{2}(1-\delta)\cos k_y + t_2 \cos k_x \cos k_y + \frac{t_3}{2}(1+\delta)\cos 2k_x + \\ + \frac{t_3}{2}(1-\delta)\cos 2k_y + \frac{t_4}{2}\left(\cos 2k_x \cos k_y + \cos k_x \cos 2k_y\right) + t_5 \cos 2k_x \cos 2k_y \quad (2)$$

The temperature dependence of the Δ_d was taken in accordance to analyses of temperature dependence of Knight Shift and nuclear relaxation rate [15]:

$$\Delta_d(T) = \Delta_d(0)\tanh\left[1.75\sqrt{\frac{T_c}{T}-1}\right], \quad (3)$$

whereas the full gap taken in the form:

$$\Delta_k = \Delta_d\left(\cos k_x - \cos k_y\right) + \Delta_{2s}\left(\cos k_x + \cos k_y\right) + \Delta_s . \quad (4)$$

In fig.1 we show results of our fit with a single d-wave gap parameter. As one sees there is essential deviation from the experimental data. fig.2 displays variant when both s- and d-wave components were taken. As one can see, the multicomponent superconducting gap

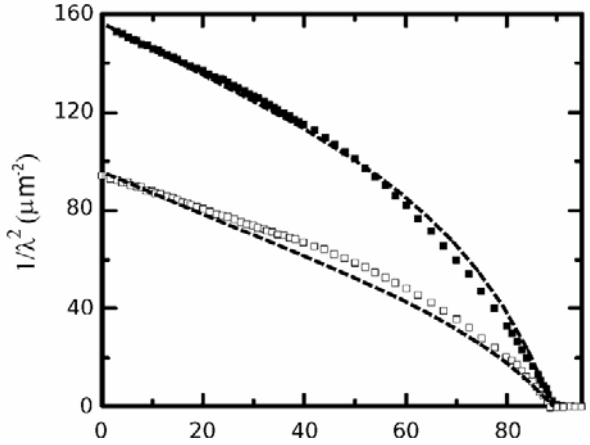

Fig.1. The temperature dependencies of the superfluid density in ab plane for $YBa_2Cu_3O_{6.98}$. Solid symbols correspond to experimental data [7]. Dashed lines – best fit using the energy dispersion (2) with following set of parameters: t_1=588.1 meV, t_2=146.1 meV, t_3=9.5 meV, t_4=-129.8, t_5=6.9 meV, mu=110 meV, δ=-0.037, Δ_d=29 meV, Δ_{2s}=0, Δ_s=0 meV. The lowest curve corresponds to a-axis, whereas highest – to b-axis.

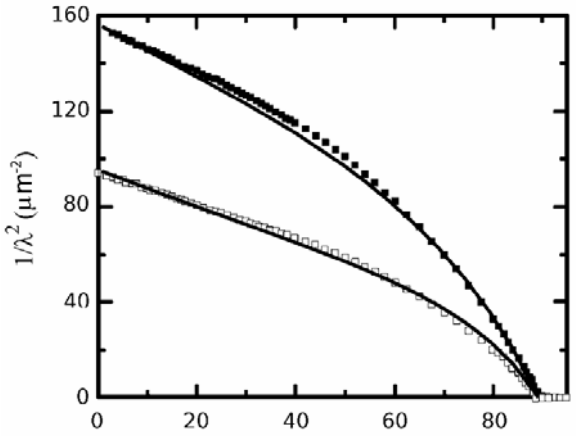

Fig.2. The temperature dependencies of the superfluid density in ab plane for $YBa_2Cu_3O_{6.98}$. Solid symbols correspond to experimental data [7]. Solid lines demonstrate our calculations using the energy dispersion (2) with next parameters: t_1=588.1 meV, t_2=146.1 meV, t_3=9.5 meV, t_4=-129.8, t_5=6.9 meV, mu=110 meV, δ=-0.037, Δ_d=29 meV, Δ_{2s}=0, Δ_s=5 meV. The lowest curve corresponds to a-axis, whereas highest – to b-axis.

describes the experimental data much better. Going on, we added Δ_{2s}-component in the fit procedure. However, this admixture of anisotropic s-wave gap yields a small effect on the temperature dependence of superfluid density.

In this respect our result is in agreement with analysis of ref. [12], where relative value of anisotropic s-component was estimated as 2%.

Summary

We have analyzed the temperature dependence of the superfluid density in orthorhombic HTSC compound $YBa_2Cu_3O_{6.98}$, along a and b crystallographic axes. We show

that temperature dependencies are very sensitive to relative value of d- and s- components of the superconducting energy gap and were able to extract their values from available experimental data [7]. Our results are in agreement with previous study of the multicomponent gap problem by ARPES [8], neutron scattering experiments [9, 10], tunneling experiments [11, 12] and Raman spectroscopy [13]. We note that from two possible types of s-components – isotropic or extended s-wave $\Delta_{2s}\left(\cos k_x + \cos k_y\right)/2$ – the superfluid density is most sensitive to the first one, whereas the last one seems to be relatively small. This information might be essential for understanding the relative role of the short (superexchange, spin fluctuation, optical phonon mediated interaction et al.) and long range interaction (acoustic phonons or plasmons, etc.) in HTSC compounds. In this connection the additional experimental measurements of the isotope effect on the superfluid density (and therefore on Δ_s and Δ_d) in orthorhombic HTSC compounds would be very informative and desirable.

References

[1] Bianconi, A., Poccia, N.: Superstripes and complexity in high-temperature superconductors, Journal of -Superconductivity and Novel Magnetism, **25**, 1403–1412 (2012).

[2] Teplov, M.A., Kryukov, E.V., Duglav, A.V., et al.: Electronic phase separation in $TmBa_2Cu_4O_8$, JETP Letters, **63**, 227–233 (1996).

[3] Teplov, M.A., Bakharev, O.N., Dooglav, A.V., et al.: Inhomogeneity of charge and spin distribution in CuO_2 layers of high-T_c superconductors: NQR/NMR studies of 1-2-3 compounds, Journal of -Superconductivity and Novel Magnetism, **12**, 113–115 (1999).

[4] Müller, K.A., Keller, H.: In: High-*T*c Superconductivity: Ten Years after the Discovery. NATO ASI Ser. E, **343**. Kluwer, Dordrecht (1996).

[5] Khasanov, R., Shengelaya, A., Bussmann-Holder, A., Karpinski, J, Keller, H., Müller, K.A.: S-wave symmetry along the c-axis and a+d in-plane superconductivity in bulk $YBa_2Cu_4O_8$, Journal of Superconductivity and Novel Magnetism **21**, 1557 (2008).

[6] Bussmann-Holder, A.: Evidence for s+d wave pairing in copper oxide superconductors from an analysis of NMR and NQR data, Journal of Superconductivity and Novel Magnetism, **25,** 155–157 (2012).

[7] Bonn, D.A., Hardy, W.N., in Handbook of High-Temperature Superconductivity, Theory and Experiment, Ed. J. Robert Schrieer, James S. Brooks, Springer Science + Business Media, LLC, 2007, p.145.

[8] Lu, D.H., Feng, D.L., Armitage, N.P., Shen, K.M., et al.: Superconducting gap and strong in-plane anisotropy in untwinned $YBa_2Cu_3O_{7-\delta}$, Phys. Rev. Lett. **86**, 4370–4373 (2001).

[9] Shnyder, A.P., Manske, D., Murdy, C., Sigrist, M.:Theory for inelastic neutron scattering in orthorhombic high-T_c superconductors, Phys. Rev. B **73**, 224523 (2006).

[10] Eremin, I., Manske, D.: Fermi-liquid based theory for the in-plane magnetic anisotropy in untwined high-T_c superconductors, Phys.Rev.Lett. **94**, 067006 (2005).

[11] Kirtley, J.R., Tsuei, C.C., Ariando, Verwijs, C.J.M., et al.: Angle resolved phase-sensitive determination of the in-plane gap symmetry in $YBa_2Cu_3O_{7-\delta}$, Nature Physics, **2**, 190 (2006).

[12] Smilde, H.J.H., Golubov, A.A., Ariando, Rijnders, G., et al.: Admixtures to d-wave gap symmetry in untwined $YBa_2Cu_3O_7$ superconducting films measured by angle-resolved electron tunneling, Phys. Rev. Lett. **95**, 257001 (2005).

[13] Bakr, M., Schnyder, A.P., Klam, L., Manske, D., et al.: Electronic and phononic Raman scattering in detwinned $YBa_2Cu_3O_{6.95}$ and $Y_{0.85}Ca_{0.15}Ba_2Cu_3O_{6.95}$: s-wave admixture to the d_{x2-y2}-wave oreder parameter, Phys.Rev.B **80**, 064505 (2009).

[14] Eremin, M.V., Larionov, I.A., Lyubin, I.E.: London penetration depth in the tight binding approximation: orthorhombic distortion and oxygen isotope effects in cuprates, J. Phys.: Condens.Matter **22**, 185704 (2010).

[15] Mayer, T., Eremin, M., Eremin, I., Meier, P.F.: Spin dynamics of itinerant holes in HTSC cuprates: the singlet-correlated band model and its applications, 2007 J. Phys.:Condens. Matter, **19**, 116209 (2007).

Magnetic and magnetoelastic properties of lithium-rare-earth tetra-fluoride single crystals

I.V. Romanova[1], A.V. Klochkov[1], S.L. Korableva[1], V.V. Kuzmin[1], B.Z. Malkin[1], I.R. Mukhamedshin[1], H. Suzuki[2], M.S. Tagirov[1]

[1]Kazan Federal University, Kremlevskaya 18, Kazan 420008, Russian Federation

[2]Kanazawa University, Kanazawa 920-11, Kakuma-machi, Japan

e-mail: Irina.Choustova@ksu.ru

Abstract

Temperature and magnetic field dependences of the magnetization of $LiHoF_4$ and $LiDyF_4$ single crystals were measured with a dc-SQUID magnetometer MPSM-2 (Quantum Design) and by the inductance method with the magnetic field applied along and perpendicular to the c-axis. The results of measurements are compared with the results of simulations.

Introduction

Double lithium-rare-earth fluorides which crystallize in the tetragonal scheelite structure attract a lot of interest as model objects in physics of dipolar magnets [1]. The unit cell of $LiRF_4$ contains two magnetically equivalent lanthanide R^{3+} ions at sites with the S_4 point symmetry. Earlier we studied the magnetization of the $LiTbF_4$ single crystal and NMR of ^{19}F in $LiTbF_4$ [2,3] and found the set of crystal field parameters for Tb^{3+} ions and parameters of the superhyperfine interaction between the Tb^{3+} ions and the nearest fluorine nuclei. $LiErF_4$ and $LiTmF_4$ exhibit a giant forced magnetostriction at liquid helium temperatures which has been studied earlier [4,5]. $LiDyF_4$ is a dipolar antiferromagnet with Dy^{3+} magnetic moments normal to the crystal symmetry axis (T_N=0.62 K), $LiHoF_4$ is a dipolar Ising-like ferromagnet with T_c=1.53 K [1]. The main goal of the present study was to elucidate the role of magnetoelastic interactions in formation of the magnetization and the energy level structure of R^{3+} ions in $LiRF_4$ crystals in the external magnetic fields.

Experimental details and the results of measurements

Single crystals of $LiDyF_4$ and $LiHoF_4$ were grown by Bridgeman-Stockbarger method. The samples were oriented by means of X-ray diffractometer. The samples used for magnetization measurements were shaped by polishing as spheres to acquire a definite demagnetizing factor. To prevent rotation of the sample in the strong magnetic field, it was fixed in Stycast 1266 epoxy (the accuracy of orientation was ±3°). The temperature dependences of the magnetization of single crystals in the temperature range of 2-300 K and the dependences of the magnetization on the magnetic field in the interval 0-5 T applied along and perpendicular to the c-axis were measured with a dc-SQUID. Some experimental dependences of the magnetization as well as the results of simulations described below are presented in fig.1.

Angular dependences of the magnetization in the basis plane of $LiDyF_4$ and $LiHoF_4$ were measured by the inductance method with the magnetic field (up to 2 T) applied perpendicular to the c-axis at the temperature 4.2 K. The inductance of the coil with the sample was measured on a forward and backward field sweeps by LCR-meter E7-14 using the inductance bridge circuit balanced at zero fields on the 1 kHz frequency.

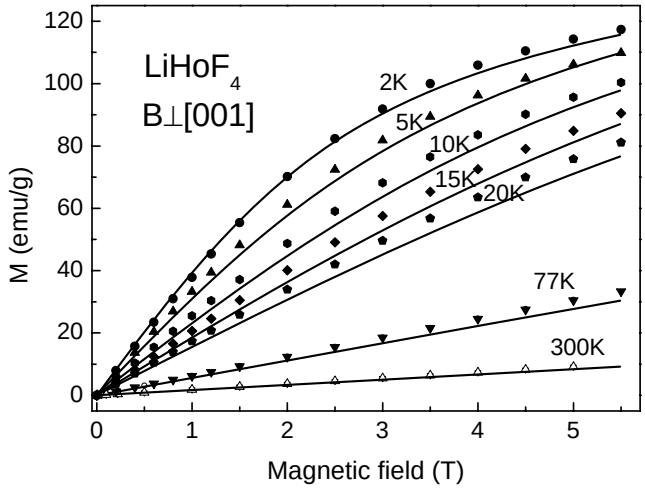

Fig.1. Magnetic field dependences of the $LiHoF_4$ magnetization. Solid lines – theory, points– experiment.

The background from the empty coil was measured independently and subtracted from the total signal. The sample was glued inside the capsule and could be rotated inside the coil with the accuracy of ±5°. Magnetization curves $M(B)$ were extracted from the experimental data by integrating the field scans of the derivatives dM/dB (in arbitrary units) at various sample orientations. The obtained curves were calibrated using magnetization data for $LiDyF_4$ and $LiHoF_4$ single crystals measured with a dc-SQUID [6].

At the first step, we studied theoretically the behavior of the magnetization in the external magnetic field rotating around an arbitrary axis (the orientation of the rotation axis was defined by the angle θ between the rotation axis and the crystallographic c-axis and the angle α between the projection of the rotation axis on the crystal *ab* plane and the *a*-axis). The results of calculations are presented in fig.2. The measured angular dependence of the magnetization in the basis plane of $LiDyF_4$ in the magnetic field $B = 2$ T is compared in fig.3 with the results of calculations, the experimental and theoretical results agree satisfactorily.

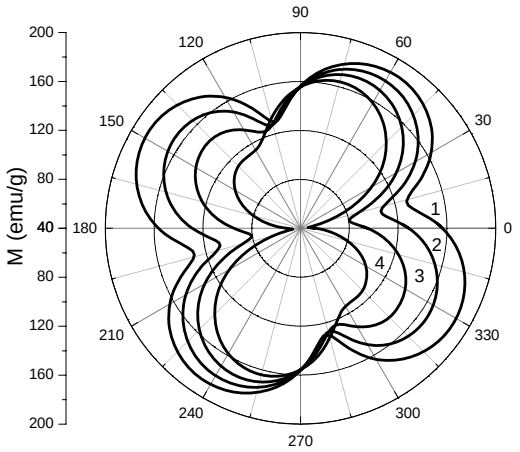

Fig.2. Calculated angular dependences of the magnetization of $LiDyF_4$ single crystal at T=4.2 K in different planes containing the external magnetic field (B=2 T): 1 – $\theta = 0$, α = 0; 2 – $\theta = 5^o$, α = 30°; 3 – $\theta = 5^o$, α = 45°; 4 – $\theta = 5^o$, α = 60°.

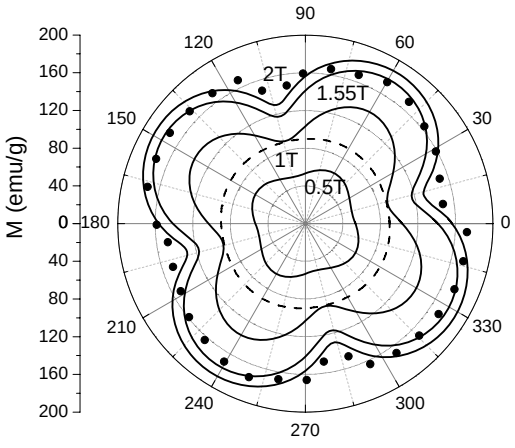

Fig.3. Angular dependences of the magnetization in the basis plane of $LiDyF_4$ single crystal at T=4.2 K. Solid lines - theory, symbols – experiment (B=2 T). The dashed curve (for B=1 T) corresponds to zero magnetoelastic coupling.

Discussion

In the presence of an applied magnetic field $\boldsymbol{B}$, in the framework of the mean field approximation, we write the Hamiltonian of a single R^{3+} ion in the following form:

$$H = H_0 + H_{cf} + \sum_{\alpha\beta} V_{\alpha\beta} e_{\alpha\beta} + \sum_{\alpha,s} V_\alpha(s) w_\alpha(s) + \sum_j [\mu_B(\boldsymbol{B} + \tilde{Q}\boldsymbol{M})(\boldsymbol{l}_j + 2\boldsymbol{s}_j) - \sum_{pkp'k'} \lambda_{pp'}^{kk'} < O_p^k > O_{p'}^{k'}] \quad (1)$$

Here, the first term is the free ion energy, the second term is the crystal field Hamiltonian:

$$H_{cf} = B_2^0 O_2^0 + B_4^0 O_4^0 + B_4^4 O_4^4 + B_4^{-4} O_4^{-4} + B_6^0 O_6^0 + B_6^4 O_6^4 + B_6^{-4} O_6^{-4} \quad (2)$$

determined in the crystallographic system of coordinates by the set of seven crystal field parameters B_p^k (O_p^k are the Stevens operators). The third and fourth terms correspond to linear interactions of rare-earth ions with the homogeneous macro- and microdeformations, respectively, where $\boldsymbol{e}$ is the deformation tensor, and $\boldsymbol{w(s)}$ is the vector of the s-sublattice displacement. The electronic operators V' and $V''(s)$ can be presented, similar to the crystal field energy, through the linear combinations of Stevens operators with the parameters which have been calculated earlier in the framework of the exchange charge model (see [7,8,9]).

The fifth term in (1) is the electronic Zeeman energy where μ_B is the Bohr magneton, $\boldsymbol{l_j}$ and $\boldsymbol{s_j}$ are operators of orbital and spin moments, $\boldsymbol{M}$ is the equilibrium magnetization, the tensor $\boldsymbol{Q}$ defines magnetic dipole-dipole interactions between the rare-earth ions, and the sum is taken over $4f$ electrons. The last term corresponds to the energy of interaction between paramagnetic ions via the phonon field, parameters $\lambda_{pp'}^{kk'}$ were calculated by making use of the characteristics of the lattice dynamics of the $LiRF_4$ crystal lattices. Calculations of the magnetic properties were carried out considering the matrix of the Hamiltonian (1) in the subspace of the lower 146 states of the $4f^9$ configuration of the Dy^{3+} ion and in the total space of 1001 states of the $4f^{10}$ configuration of the Ho^{3+} ion.

The crystal free energy (per unit cell) is written as:

$$F = \frac{v}{2}(\boldsymbol{eC'e} + \boldsymbol{waw} + 2\boldsymbol{ebw}) + < \boldsymbol{O} > \boldsymbol{\lambda} < \boldsymbol{O} > - v\boldsymbol{MB} - nk_BT \ln Tr \exp(-H / k_BT), \quad (3)$$

where v is the volume of the unit cell, k_B is the Boltzman constant, $\boldsymbol{C} = \boldsymbol{C'} - \boldsymbol{ba}^{-1}\boldsymbol{b}$ is the tensor of elastic constants, $\boldsymbol{a}$ is the dynamic matrix of the lattice at the Brillouin zone centre, the tensor $\boldsymbol{b}$ determines linear coupling between macro- and microdeformations, n=2 is the number of rare-earth ions in the unit cell, and angular brackets <…> mean the thermal averaging. From the equilibrium conditions for the coupled paramagnetic ions and the elastic crystal lattice

$$\partial F / \partial < O_p^k > = \partial F / \partial e_{\alpha\beta} = \partial F / \partial w_\alpha(s) = \partial F / \partial B_\alpha = 0\,, \quad (4)$$

we obtain self-consistent equations for the magnetization vector and the deformation tensor components. In particular, the lattice macro-deformation induced by the external magnetic field is determined by the expression:

$$\boldsymbol{e}(\boldsymbol{B}) = -\frac{n}{v}\boldsymbol{S}[\langle \boldsymbol{V} \rangle_B - \langle \boldsymbol{V} \rangle_0] \quad (5)$$

and the sublattice displacements, which define the internal magnetostriction, equal

$$\boldsymbol{w}(\boldsymbol{B}) = -\frac{n}{v}\boldsymbol{a}^{-1}[\langle \boldsymbol{V''} \rangle_B - \langle \boldsymbol{V''} \rangle_0] - \boldsymbol{a}^{-1}\boldsymbol{be}(\boldsymbol{B})\,. \quad (6)$$

Here $\boldsymbol{S}$ is the compliance tensor of the lattice, and angular brackets $<...>_B$, $<...>_0$ indicate thermal averages for $B \neq 0$ and B=0, respectively. Operators $\boldsymbol{V}$ in the expression (5) equal to

operators $\boldsymbol{V}'$ renormalized due to linear coupling of macro- and micro-deformations ($\boldsymbol{V} = \boldsymbol{V}' - \boldsymbol{b}\boldsymbol{a}^{-1}\boldsymbol{V}''$).

The system of equations (4) was solved by making use of the method of successive approximations at fixed values of the temperature and the external magnetic field. The procedure involved the following steps: first, the matrix of the Hamiltonian (1) with $\boldsymbol{M}=0$, $\boldsymbol{e}=0$, $\boldsymbol{w}=0$ is diagonalized, and the macro- and micro-deformations ($\boldsymbol{e}(\boldsymbol{B})$ and $\boldsymbol{w}(\boldsymbol{B})$), and the magnetization $\boldsymbol{M}$ are calculated. At the next step, the obtained values of $\boldsymbol{M}$, $\boldsymbol{e}$, $\boldsymbol{w}$ are substituted into the Hamiltonian and the calculations are repeated. Considering the expansion of the free energy in power series in deformation parameters up to second order, we find corrections to the elastic constants depending on the magnetic field and temperature. At the last step, the obtained values of $\boldsymbol{M}$, $\boldsymbol{e}$, $\boldsymbol{w}$ and $\boldsymbol{C}(\boldsymbol{B})$ are substituted into the Hamiltonian and the values of $\boldsymbol{M}$ are calculated. The results of calculations are presented in figures 1-3.

Conclusion

The measured temperature, field and angular dependences of the magnetization in $LiDyF_4$ and $LiHoF_4$ single crystals are compared with the results of simulations. The simulated temperature, magnetic field and angular dependences of the magnetization are in good agreement with the experimental results. It follows from calculations that magnetoelastic interactions in lithium-rare earth tetra-fluorides contribute essentially to the magnetization in external magnetic fields at liquid helium temperatures.

Acknowledgements

The authors are grateful to V.A. Shustov for the X-Ray orientation of the samples, to A.N. Yudin and K.R. Safiullin for help in experimental measurements. This work was partially supported by RFBR grant №12-02-00372-a.

References

[1] L.K. Aminov et al., Handbook on the Physics and Chemistry of Rare Earths, vol. 22, ed. by K.A. Gschneidner and LeRoy Eyring, North Holland, Amsterdam, 1996.

[2] I.V. Romanova et al., Sol. St. Phys. 44, 1475 (2002).

[3] I.V. Romanova et al., Journ. of Phys.: Conf. Series 324, 012034 (2011).

[4] L.A. Bumagina et al., Sov. Phys. JETP 54, 792 (1981).

[5] V.I. Krotov et al., Sol. St. Phys. 24, 542 (1982).

[6] I.V. Romanova et al., Magn. Resonance in Solids. EJ. 8, 1 (2006).

[7] R.Y. Abdulsabirov et al., J. Lumin. 117, 225 (2006).

[8] R.Y. Abdulsabirov et al., SPIE Proceedings 4766, 59 (2002).

[9] L.K. Aminov, B.Z. Malkin, Dynamics and kinetics of electronic and spin excitations in paramagnetic crystals, Kazan State University, 2008.

NMR of ^{141}Pr, ^{19}F and ^{3}He of PrF_3 nanoparticles at low temperature

E.M. Alakshin, R.R. Gazizulin, A.V. Klochkov, S.L. Korableva, V.V. Kuzmin, A.M. Sabitova, T.R. Safin, K.R. Safiullin, M.S. Tagirov

Kazan (Volga region) Federal University, 420008, Kremlevskaya 18, Kazan, Russia

e-mail: alakshin@gmail.com

Five samples of PrF_3 nanoparticles by varying the time of hydrothermal reaction were syntesized [1, 2]. The series of X-ray and HRTEM experiments were made, the size distribution of nanoparticles were obtained. The effect of cross-relaxation between the nuclear spins of ^{141}Pr (powder PrF_3 with particle size 10-45 microns) and ^{3}He at the Larmor frequency of ^{3}He (6.63 MHz) in the system "^{141}Pr–^{3}He" was observed earlier [3, 4]. This system is of interest because of the possibility for dynamic nuclear polarization of liquid ^{3}He. The transition from micron to nanoscale powders PrF_3 could help in creation of highly correlated spin system "^{141}Pr – ^{3}He" and improving cross-relaxation. Time of hydrothermal reaction for prepared samples of PrF_3 nanoparticles of its size dependence is presented in Table 1.

Table 1.

Time of hydrothermal reaction, min	0	20	40	60	420
d, nm	21±9	31±10	27±10	37±10	34±13

The experimental measurements of the spin-lattice relaxation ^{141}Pr and ^{19}F were done at 1.5 K. The relaxation times of the ^{141}Pr, ^{19}F and ^{3}He nuclei for five samples were obtained. It was shown that the longitudinal relaxation time of the nuclei of ^{141}Pr and ^{19}F is increasing with the time of hydrothermal reaction (fig.1).

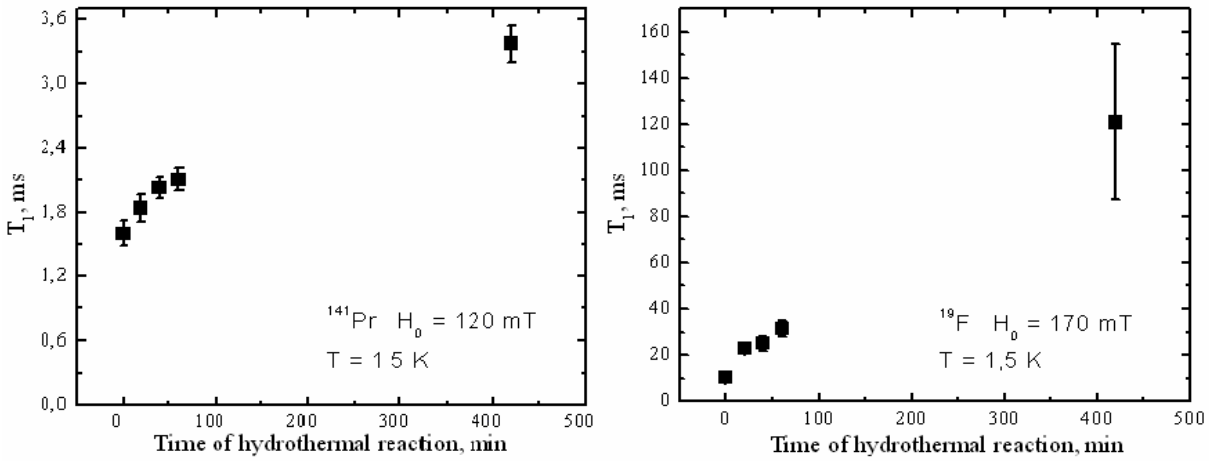

Fig.1. Relaxation time T_1 of ^{141}Pr and ^{19}F in PrF_3 nanoparticles

The graph indicates changes in the crystal structure of the samples, which depends on the time of hydrothermal reaction. During the reaction time nanoparticles are becoming more monocrystalline.

The measurements of the spin-lattice relaxation of ^{3}He in contact with synthesized samples were also done. Previously, a model of relaxation of the longitudinal magnetization

of the ^{3}He nuclei [2], according to the adsorbed film on the surface of ^{3}He (first term in equation (1)) [6, 7, 8], and due to the Fatkullin's relaxation (modulation of the dipole-dipole interaction in a strongly inhomogeneous magnetic field, generated by nanoparticles PrF_3) [9].

$$\frac{1}{T_1} = \frac{A}{H_0} + BH_0 \qquad (1)$$

The relaxation rates of ^{3}He in contact with synthesized samples were measured. The correlation of the relaxation rate with the particles size was observed (fig.2.). For example, the rate of relaxation of ^{3}He in contact with the sample 2 is less than in contact with the sample 1 in about half, as the size of the particles.

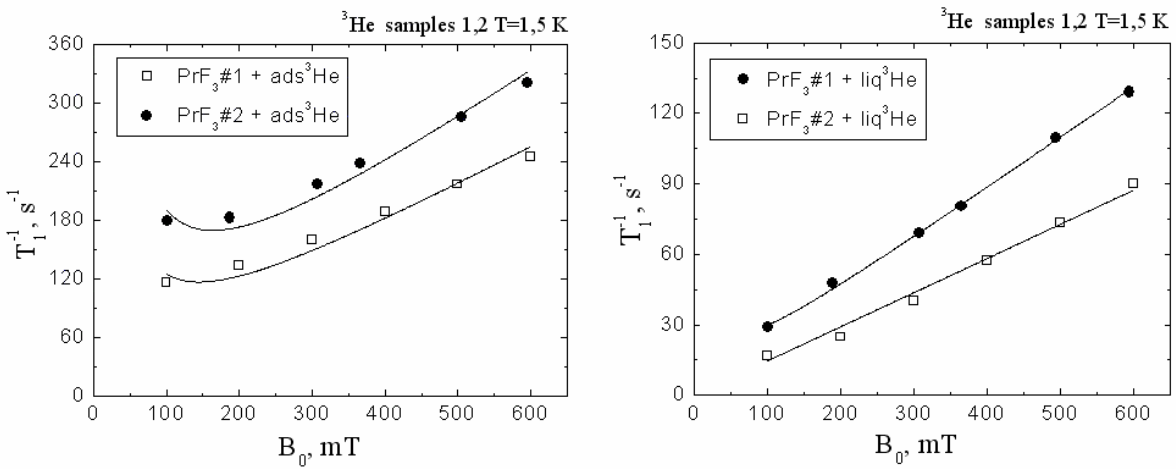

Fig.2. The relaxation rate dependence of the longitudinal magnetization of ^{3}He nuclei in systems "PrF_3 – adsorbed ^{3}He" and "PrF_3 – liquid ^{3}He" in magnetic field for samples 1, 2

Let's discuss the relaxation mechanism of adsorbed film in details. From the experimental data of relaxation rate of ^{3}He Fatkullin's mechanism was subtracted. There is a correlation between the calculation of ^{141}Pr NMR signal intensity of a non-oriented PrF_3 powder (on Larmor frequency of ^{3}He) and our results (fig.3).

In this way, the experimental data can be interpreted as cross-relaxation. There are two facts: the spin-lattice relaxation time for ^{141}Pr comparable with the spin-lattice relaxation time for the ^{3}He and relaxation mechanism through the surface should be hundreds of milliseconds, but we have seen tens of milliseconds.

Results of measurements of the ^{3}He relaxation rates in contact with synthesized samples were presented in fig.4. It seems that the proposed model for sample 5 is not suitable. On HRTEM images (fig.5) it is shown that the particles exposed to liquid nitrogen temperature have been destroyed, by the expansion of freezing water inside of nano-cavities [10].

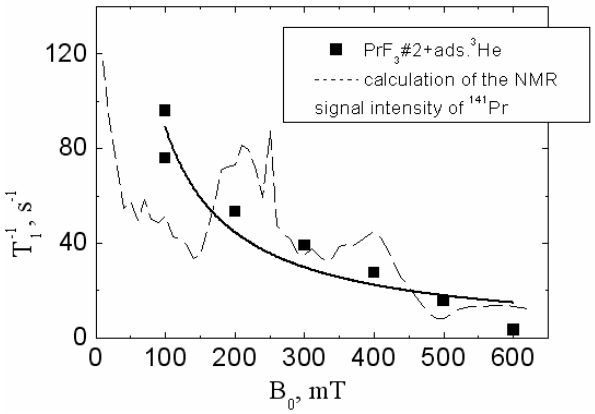

Fig.3. The relaxation rate dependence of the ^{3}He nuclei longitudinal magnetization in system «PrF_3 - adsorbed ^{3}He» without Fatkullin's mehanism

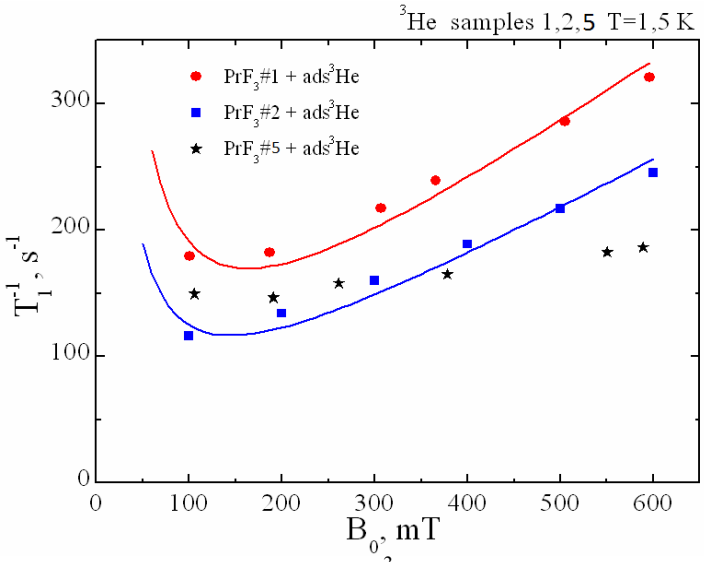

Fig.4. The relaxation rate dependence of the ^{3}He nuclei longitudinal magnetization in system" PrF_3 – adsorbed ^{3}He" in the magnetic field for the samples № 1,2,5.

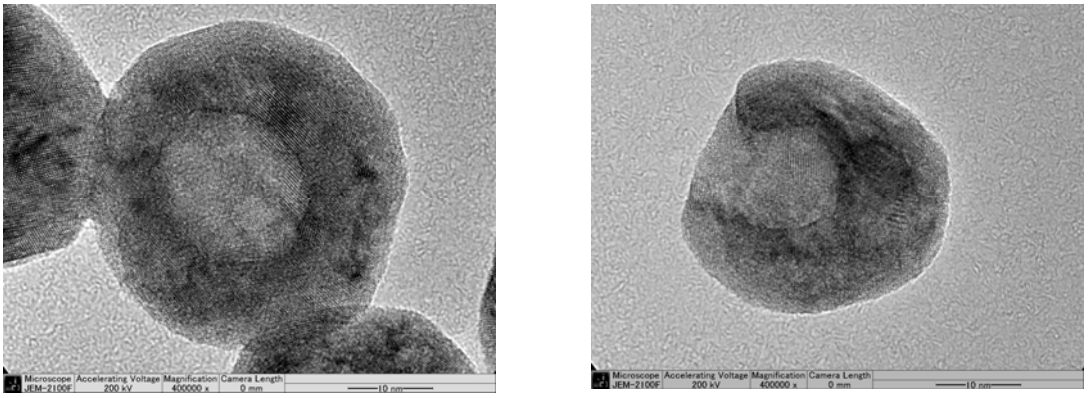

Fig.5. HRTEM of the sample 5: on the left – sample 5, on the right - sample 5 after cooling to liquid nitrogen temperature.

Acknowledgments

This work is partially supported by the Ministry of Education and Science of the Russian Federation (FTP "Scientific and scientific - pedagogical personnel of the innovative Russia" GK- P900).

References

[1] E.M. Alakshin and al., arXiv:condmat, Vol.1104, p.0208 (2011)
[2] E.M. Alakshin and al., J. Low. Temp. Phys., Vol.162, n. 5/6, p.645–652 (2011)
[3] A.V. Egorov et al., JETP Letters, 86, n.6, c.416 (2007)
[4] A.V. Egorov and al., J. Phys.: Conf. Series, 150, 032019 (2009)
[5] E.M. Alakshin and al., JETP Letters, Vol.94, n.3, p.259-261 (2011)
[6] Cowan B.P., J. Low Temp. Phys., Vol.50, № 1-2, p.135-142 (1983)
[7] Richardson R.C., Physics B., Vol.126, Is.1-3, p.298-305 (1984)
[8] Klochkov A.V. et al., JETP Letters, v.88, P.944 (2008)
[9] Fatkullin N.F., Sov. Phys. JETP, v.74, p.833 (1992)
[10] E.M. Alakshin and al., JETP Letters, Vol.96, n.3, p.194 (2012)

Study of the exchange interaction in relation to the concentration of spin labels in different solutions

S.B. Orlinskii, G.V. Mamin, M.A. Volodin

Kazan Federal Unoversity, Federal center of physical and chemical measurements, 420008, Kremlyovskaya St. 18, Kazan, Russian Federation

e-mail: volodinmikhail@yandex.ru

Spin labels are widely used as tools for probing different materials using EPR spectroscopy. One of their applications is wet gas measuring. In wells producing natural gas, free liquid is almost always present. This free liquid consists of a mixture of water (condensed water vapour and possibly also formation water containing dissolved salts) and liquid hydrocarbons (usually referred to as “condensate” and with a composition similar to gasoline or light kerosene). The designation for well fluids typically containing 0-10% liquid is wet gas, and accurate measurement of wet gas is both important and difficult. One accurate way of measuring wet gas is to inject known concentrations of tracers at known flow rates into the unseparated flow, with one tracer for the water, and another for the light fractions of liquid hydrocarbons. An appropriate distance downstream a sample of the liquid is withdrawn, and measurement of the concentrations of the tracers in the sampled water and condensate allows their flow rates to be calculated. The meter measuring total flow can then be corrected for the liquids to give the gas flow measurement. Different spin labels can be used as tracers for aforesaid purposes and tracer concentration could be determined from EPR spectrums of water and gasoline mixture analysis [1-3].

A cuprum sulfate was used as a tracer for water and TEMPON (based on NO nytroxil radical) spin label was used as a tracer for gasoline. Desirable spin labels concentrations were achieved by means of mixing with water or gasoline in ultrasonic band. Mass of components was controlled with balance. Samples were placed into glass capillary with 1 mm diameter, overall sample volume did not exceed 0,5 ml.

All experiments were performed at room temperature with a Bruker Elexsys 680 EPR spectrometer with the microwave frequency 9,5 GHz, modulation magnitude — 0,5 G. EPR spectrums of spin labels in different solutions were recorded. The integrated intensities of these spectrums in dependence of spin label concentration are shown in fig.1 and fig.2.

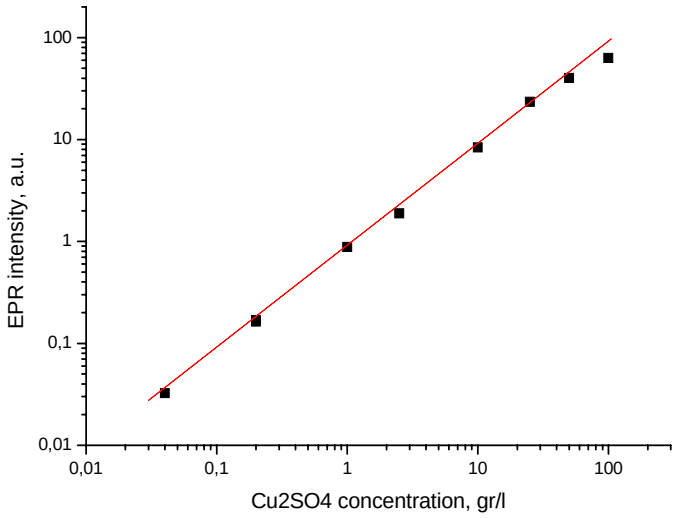

Fig.1. Cuprum sulfate diluted in water EPR signal intensity from cuprum sulfate concentration dependence.

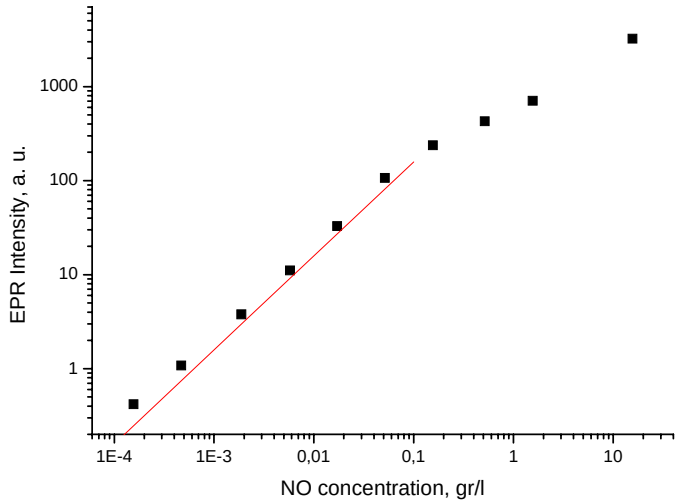

Fig.2. NO spin label diluted in gasoline EPR signal intensity from NO spin label concentration dependence.

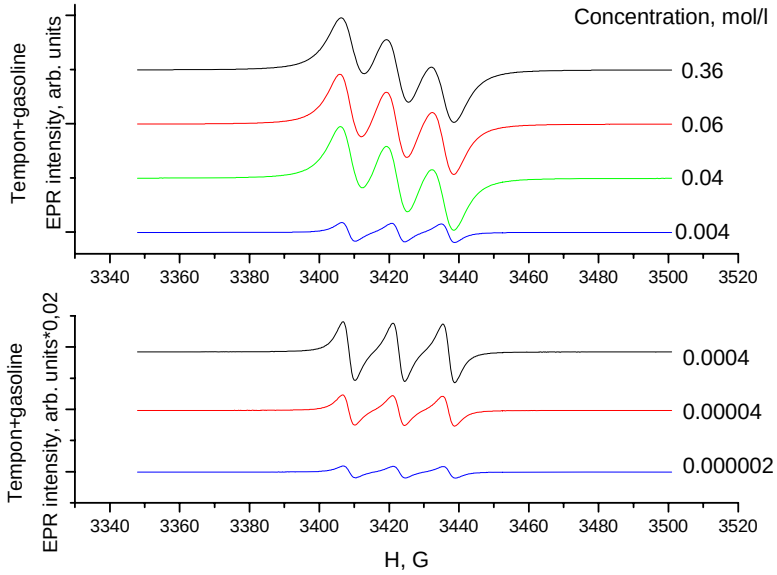

Fig.3. EPR spectrums of NO spin label diluted in gasoline in different concentrations.

Conclusion

Additional contributions to EPR spectra depend on the parameters of the spin–spin interactions and the diffusion kinematics, molecular-kinetic parameters. From the EPR experimental data, we can obtain the limit of linear regime.

References

[1] R.S. Alger, Electron paramagnetic resonance: techniques and applications, New York, (1971), pp 201-221.

[2] S.S Eaton, G.R Eaton, L.J Berliner, Biomedical EPR – Part B: methodology, instrumentation and dynamics, New York, (2005).

[3] H. de Leeuw, Wet gas flow measurement by means of a Venturi meter and a tracer technique, North Sea Measurement Workshop, (1994).

[4] K. M. Salikhov Contributions of Exchange and Dipole–Dipole Interactions to the Shape of EPR Spectra of Free Radicals in Diluted SolutionsAppl Magn Reson (2010) 38:237–256

Index

Table of Contents

TABLE OF CONTENTS

TABLE OF CONTENTS

TABLE OF CONTENTS

ACTUAL PROBLEMS OF MAGNETIC RESONANCE AND ITS APPLICATION

XV International Youth Scientific School

Program
Lecture Notes
Proceedings

Kazan
22 – 26 October 2012

Подписано в печать 18.10.12.
Бумага офсетная. Печать ризографическая.
Формат 60x84 1/16. Гарнитура «Times New Roman». Печ. л. 24,4
Уч.-изд. л. 26,3. Тираж 100 экз. Заказ 3/10

Отпечатано с готового оригинал-макета
в типографии Издательства Казанского университета

420008, г. Казань, ул. Профессора Нужина, 1/37
тел. (843) 233-73-59, 292-65-60

ISBN 978-5-905787-85-0